University
of Basel

Swiss Nanoscience Institute

Swiss Nanoscience Institute
Center of Excellence supported
by the University of Basel
and the Canton of Aargau

Annual Report 2025 Supplement

Swiss Nanoscience Institute

Content

PhD Projects

From Protein Aggregation to Cellular Dysfunction in Parkinson’s Disease ... 1

Applying nanowire MFM to 2D materials ... 3

Surface chemistry of hafnium oxide nanocrystals as X-ray computed tomography contrast agents ... 5

Investigating the biomechanical properties of the T6SS speargun ... 7

The surface phases of epitaxial altermagnetic MnTe ... 9

Synthetic Membranes as Functional Platforms Shaped by Protein Interactions ... 11

Two-Dimensional Frameworks from Metal Oxo Clusters at Liquid Interfaces ... 13

Coupled Kerr-cat qubit modes in a tantalum-based planar architecture ... 15

Functional nanofilaments in biology ... 17

Raman Microscopy: Targeting EGFR of Ovarian Cancer Cells by the Effective Surface Modification of Gold Nanoparticles ... 19

X-ray crystallography as a tool to explain the mechanism of metabolite biodegradation ... 21

Combined transport-optics characterisation of a gated semiconductor monolayer ... 23

Bioorthogonal uncaging following ring-closing metathesis (RCM) ... 25

Torque transducers for the study of nanoscale and low-dimensional vdW systems ... 27

Optical and transport experiments in atomically thin semiconductor devices ... 29

Unraveling room temperature ferromagnetism and magnetic orders coexistence in Cr_3Te_4 ... 31

Towards Controlling the Surface Chemistry of Cobalt Phosphide Nanocatalysts ... 33

In situ cryo-ET reveals tunable phases of Rubisco condensates ... 35

Developments in metal assisted chemical etching ... 37

Towards NIR-light triggered nanocarriers ... 39

Biofunctionalizing scintillating HfO_2 nanoparticles for X-ray mediated optogenetics ... 41

NANO-PHOTO: NANOstructured protein material for PHOTOcatalysis ... 43

Osteogenesis on the nanoscale – an in vitro model based on electrospun PCL/chitosan scaffolds ... 45

Vertical Quantum Dots in Coupled Ge Quantum Wells ... 47

Programmable Origami for Regulated Exchange (PORE-X): Nuclear Pore Complex-Inspired DNA Nanopores ... 49

Synthesis of a novel carcerand suitable for metal ion encapsulation ... 51

Optical coherent feedback control of a nanomechanical oscillator ... 53

Low-noise diamond membranes in an optical cavity ... 55

Coupled phonons in graphene nanoribbons ... 57

Induced quantum dot microscopy of germanium and graphene quantum devices ... 59

Spin wave imaging and control at the nanoscale ... 61

Quantum Sensing Towards Direct Observation of Dynamics in Biomolecules ... 63

Engineering proteins with multinuclear metal complexes as cofactors ... 65

Lipid-core polymer-shell hybrid nanoparticles for the delivery of mRNA against bacterial infections ... 67

Enzymatic reactions in subzero liquid water by lipidic mesophase nanoconfinement ... 69

Nano-Argovia Projects

Smooth focusing mirrors for X-rays ... 71

Development of functional nano-layers for Gen 4 anode-less all-solid-state batteries ... 73

Nano-structured zirconia - do cells like rice crackers? ... 75

Pushing the limits of electron microscopy with high-Z sensors ... 77

Nanobiocatalysts for PET Recycling ... 79

Advancing Electron Diffraction ... 81

Nano structured Fresnel axicon lens for ultrahigh resolution Optical Coherence Tomography (OCT) and large size, high efficiency gratings for ultrafast chirped pulse amplified lasers ... 83

Nano-Optimized Carrier System for Efficient Laser Tissue Soldering ... 85

Nano-structured absorbable implants for pediatric neurosurgery ... 87

Quantum-Limited Microwave Amplifier ... 89

Selective Nano Magnetic Detector for Water Pollution ... 91

Publications

Publications ... 93

From Protein Aggregation to Cellular Dysfunction in Parkinson’s Disease

Project P1901: Microfluidics to Study Huntington’s Disease by Visual Proteomics
Project leader: T. Braun
Collaborator: A. Fränkl (SNI PhD Student)

Introduction

We investigated the cellular effects of infecting (“seeding”) eukaryotic cells with disease-associated fibrillar aggregates of α-synuclein (α-syn), which are linked to synucleopathies such as Parkinson’s disease (PD). Specifically, we employed three complementary methodological approaches: (i) analysis of cellular and mitochondrial ultrastructural alterations by EM, (ii) structural proteomics using limited proteolysis coupled to mass spectrometry (LiP-MS), and (iii) microfluidics-enabled extraction of α-syn seeds from single cells for high-resolution cryo-EM analysis using the cryoWriter system.

Biological background

Synucleopathies, including PD, are characterized by a close interplay between α-syn pathology and mitochondrial dysfunction. Pathological aggregation of α-syn into amyloid fibrils and Lewy bodies is a defining feature of PD, with mitochondrial impairment acting both as a driver and a downstream consequence of α-syn accumulation. Environmental toxins such as rotenone and MPTP ('sloppy drugs') further underscore this link, as they induce PD-like pathology by disrupting mitochondrial respiration, increasing oxidative stress, and promoting α-syn aggregation.

Recent ultrastructural studies of PD patient brains reveal that Lewy bodies are frequently surrounded by damaged mitochondria, highlighting a spatial and functional association between α-syn inclusions and mitochondrial pathology. Beyond aggregation, α-syn directly influences mitochondrial biology in a conformation-dependent manner, affecting mitochondrial fusion and fission, ATP production, and microtubule-based transport. While monomeric α-syn can translocate into mitochondria and may play a physiological role in ATP regulation, the impact of aggregated α-syn species—particularly fibrils—on mitochondrial structure and function remains poorly understood. Elucidating this pathological cross-talk between α-syn and mitochondria is therefore central to understanding PD disease mechanisms.

Advanced microfluidic sample preparation for electron microscopy

Over the past years, we have developed *cryoWriter*, a microfluidic sample preparation system for electron microscopy [1], which is now commercialized (*www.cryowrite.com*). By reducing the required sample volume to the nanoliter (nL) range, cryoWriter enables experiments that were previously not feasible with conventional approaches. This includes, for example, structural analysis of proteins produced *in vitro* and high-resolution electron microscopy of extracts from individual cells (Fig. 1). These capabilities open new opportunities for studying rare, precious, or otherwise inaccessible biological samples.

Early ultrastructural mitochondria alteration and pathway activation

We used electron microscopy (EM) to examine how α-syn fibrils affect mitochondria. We focused on three main features: mitochondrial size, the shape of cristae, and the formation of mitochondrial-derived vesicles (MDVs). Compared to unseeded cells, α-syn-seeded cells showed mitochondria with a significantly larger area and perimeter, suggesting that α-syn fibrils cause mitochondrial swelling.

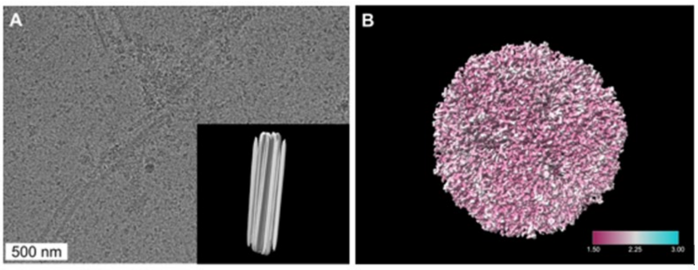

Fig. 1: Advanced microfluidic sample preparation workflows for electron microscopy (EM). A) Extraction of disease-associated α-syn fibrils from a single eukaryotic cell followed by direct cryo-EM imaging. Inset: 3.8 Å reconstruction of a single-cell–derived α-syn fibril fragment.B) Cell-free expression of apo-ferritin, followed by microfluidic protein isolation and cryo-EM sample preparation. Single-particle analysis yielded a 3D reconstruction at 1.9 Å resolution. Color coding indicates local resolution.

Looking more closely, mitochondria in α-syn-treated cells often showed abnormal cristae. These defects included unusual cristae shapes or a strong reduction, and sometimes complete loss, of cristae structure. Mitochondria with depleted cristae were frequently much larger than normal ones, indicating severe structural damage.

We also observed clear differences in mitochondrial membrane budding. Cells treated with α-syn fibrils produced about twice as many MDVs as control cells. Since MDVs are part of mitochondrial quality control, this increase suggests that α-syn fibrils induce mitochondrial stress, triggering attempts by the cell to remove damaged mitochondrial components before full mitophagy is required.

To support these structural observations at the molecular level, we performed LiP-MS, a novel, unbiased method that detects protein structural changes. LiP-MS identified 130 proteins whose structure changed after α-syn treatment, with strong enrichment of mitochondrial proteins. Many of these proteins are involved in maintaining cristae structure and mitochondrial membrane organization, including components of the MICOS complex (Mic60, Mic19, Mic26), as well as TOM40, TOM70, and TIM23.

Importantly, LiP-MS also revealed structural changes in Tollip, a protein required for TOM-positive MDV formation, supporting our EM observation of increased MDVs. In addition, we detected changes in several MICOS subunits and in MIRO2, a protein linked to mitochondrial dynamics and MDV formation. *Together, these results show that α-syn fibrils strongly disrupt mitochondrial structure, particularly cristae organization, and activate mitochondrial stress and quality-control pathways.*

Conclusions

The microfluidics of the cryoWriter systems enables new workflows for biological exoeriments. Our results demonstrate single cell visual proteomics, and enables cell-free protein characterization at high resolution.

Furthemore, our biomedical results demonstrate that fibrilar α-syn aggregates are sufficient to trigger increased MDV formation, linking pathological protein aggregation to activation of mitochondrial quality-control pathways. An important open question is whether other aggregation-prone proteins associated with neurodegenerative diseases, such as tau or amyloid-β, similarly induce MDV formation. Addressing this will help clarify whether enhanced MDV production represents a shared cellular response to protein aggregation or a mechanism specific to synucleinopathies.

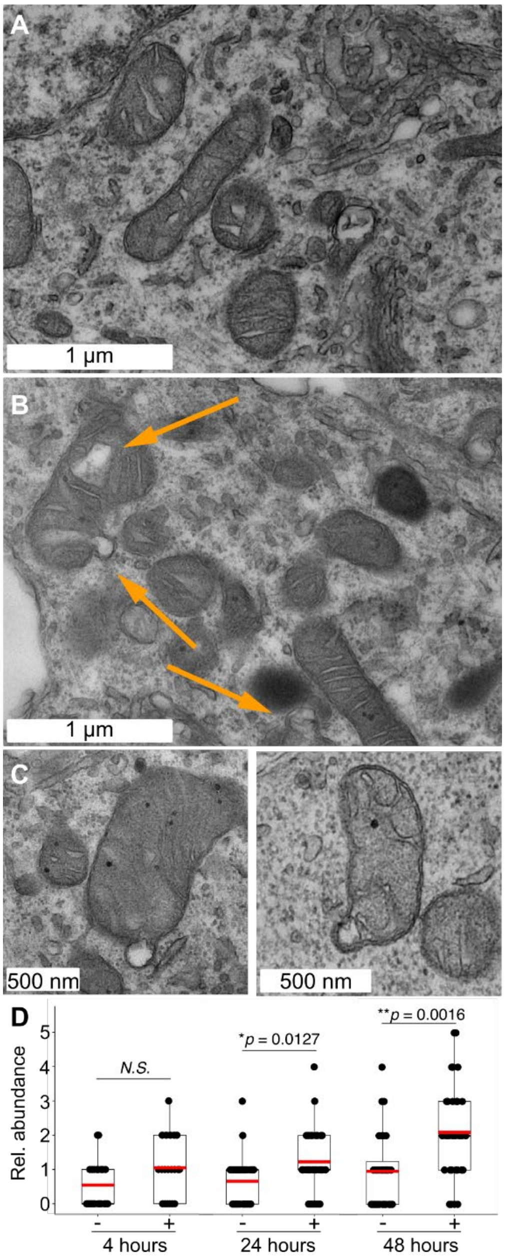

Fig. 2: α-syn fibrils induce mitochondrial defects. A) Negative control without seeding. B) cells treated with α-syn fibrils (250 nM monomer equivalents) for 24 h. C) Representative EM images showing budding of MDVs. D) Number of MDVs detected per cell for control and α-syn treated condition. P values were calculated using two tailed t test (revision submitted).

References

C. Schmidli, S. Albiez, L. Rima, R. Righetto, I. Mohammed, et al., "Microfluidic Protein Isolation and Sample Preparation for High-Resolution Cryo-EM", Proc. Natl. Acad. Sci. U.S.A. 116(30), 15007 (2019)

Applying nanowire MFM to 2D materials

Project P1905: Magnetic force microscopy with nanowire transducers
Project leaders: M. Poggio and E. Meyer
Collaborator: L. Schneider (SNI PhD Student)

Introduction

Recent years have seen rapid progress in nanometer-scale magnetic imaging technology, with scanning probe microscopy driving remarkable improvements in both sensitivity and resolution. Among the most successful tools are magnetic force microscopy (MFM), spin-polarized scanning tunneling microscopy, as well as scanning magnetometers based on nitrogen-vacancy centers in diamond, Hall-bars, and superconducting quantum interference devices. Over the past 5 years, we have been using nanowire (NW) force sensors as ultra-sensitive MFM probes. Using NWs functionalized with magnetic tips, we strive to map magnetic fields and dissipation with enhanced sensitivity and resolution compared to the state of the art and to apply these new capabilities to study magnetization in 2D materials.

The key component of a force microscope is the force sensor, which consists of a mechanical transducer, used to convert force into displacement, and an optical or electrical displacement detector. In MFM, "top-down" Si cantilevers with sharp tips coated by a magnetic material have been the standard transducer for years. Under ideal conditions, state-of-the-art MFM can reach spatial resolutions down to 10 nm, although more typically around 100 nm. These cantilevers are well-suited for the measurement of the large forces and force gradients produced by strongly magnetized samples. The advent of NWs and carbon nanotubes grown by "bottom-up" techniques now gives researchers access to much smaller force transducers than ever before. This reduction in size implies both a better force sensitivity and potentially a finer spatial resolution. Sensitivity to small forces provides the ability to detect weak magnetic fields and therefore to image subtle magnetic patterns; tiny concentrated magnetic tips have the potential to achieve nanometer-scale spatial resolution, while also reducing the invasiveness of the tip on the sample under investigation. Such improvements are crucial for imaging nanometer-scale magnetization textures in 2D systems.

Recent efforts have demonstrated the use of single NWs as sensitive scanning force sensors [1]. When clamped on one end and arranged in the pendulum geometry, i.e. with their long axes perpendicular to the sample surface to prevent snapping into contact, they probe both the size and direction of weak tip-sample interactions. NWs have been demonstrated to maintain excellent force sensitivities around 1 aN/√Hz near sample surfaces (<100 nm), due to extremely low noncontact friction. As a result, NW sensors have been used as transducers in force-detected nanometer-scale magnetic resonance imaging and in the measurement of tiny optical and electrical forces. In a proof-of-principle microscopy experiment in the Poggio lab, we showed that a magnet-tipped NW can be sensitive to magnetic field gradients of just a few mT/(m √Hz), equivalent to the gradient produced by a few tens of Bohr magnetons or a few nA of flowing current at a distance of a few hundred nanometers [2]. Such sensitivity compares favorably to that of other magnetic microscopies, including scanning Hall microscopy, scanning SQUID microscopy, and scanning nitrogen-vacancy magnetometry [3].

Despite these promising features, until now, few NW MFM experiments have been carried out, mostly as proofs-of-principle [4-6]. We have moved past this stage by: 1. optimizing the magnet-tipped NW transducers to achieve the highest possible sensitivity and resolution; 2. using the new scanning probes to image magnetism in 2D, chiral, and superconducting systems.

Main Results

In the fifth year of work, we used NW MFM to study the magnetically-controlled vortex dynamics in a ferromagnetic superconductor, using our NW MFM. In particular, we investigated the material $\mathrm{EuFe_2(As_{1-x}P_x)_2}$, which is an iron-based superconductor with a maximum critical temperature of 25 K. It is unique in that it exhibits full coexistence with ferromagnetic order below 19 K. We study the interplay between superconductivity and magnetism in this regime by imaging the magnetic field gradients at the sample surface via NW MFM, as shown in Fig. 1. The results are summarized in a manuscript published with our collaborators [6].

At the same time, we have been working on improvements to the NW MFM probes themselves. In a collaboration with Prof. Marco Stampanoni (ETH & PSI) and Dr. Lucia Romano (PSI) we have been applying metal assisted chemical etching (MacEtch) to fabricate NWs intended as MFM probes. Unlike previous NWs, which were fabricated via crystal growth techniques, such as molecular beam epitaxy or chemical vapor deposition, MacEtch can produce wafer-scale ordered arrays of Si NWs with extreme aspect ratios, e.g. NWs which are 100-nm-thick and 100-μm-long. This extreme aspect ratio can boost sensitivity to small forces – and therefore to small magnetic fields – and could make possible the imaging of subtle contrast that was not visible until now. Furthermore, the cross-

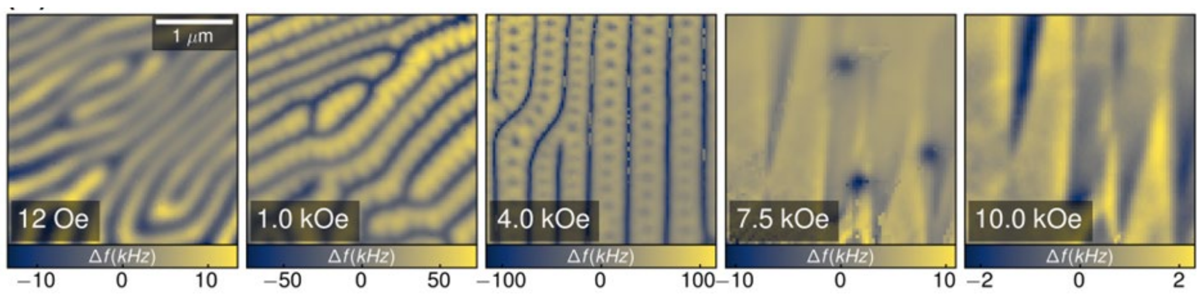

Fig. 1: Evolution of the domain vortex state in EuFe2(As1-xPx)2 with applied field 3 µm x 3 µm NW MFM images captured at T = 4.3 K.

section of the NWs can be patterned to have a specific shape, allowing us to precisely design the mode splitting of the NW's fundamental flexural mode. This additional control will allow us to obtain the most robust and easy-to-use NW MFM sensors to-date. Initial NW devices are pictured in Fig. 2. Deposition of magnetic Co tips by focused-electron-beam-induced deposition is the next step in making these NWs into MFM probes.

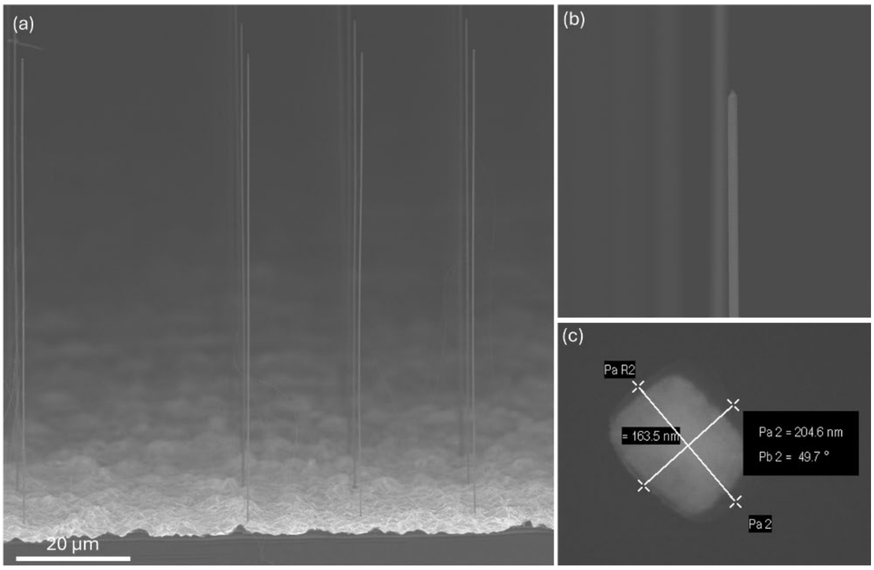

Fig. 2: NWs fabricated by MacEtch. (a) Array of NWs. (b) Zoomed-in view. (c) Top-view of single NW showing patterned rectangular cross-section.

Finally, in this last year of the Lukas Schneider's Ph.D., he spent significant amount of time plotting data, analyzing it, and writing up his interpretation for his dissertation. The result was a well-organized and extremely well-written thesis. It begins with an impressive theoretical section, laying down the foundations of the technique. Analysis of the mechanical and magnetic interactions of the NW MFM with the sample follows, yielding important new insights, which were ignored in past analyses. The thesis also analyzes the special case of the NW MFM strongly interacting with the magnetic sample and shows how the magnetic susceptibility of the sample can be inferred from the NW MFM measurement. This important new measurement modality in MW MFM is likely to be extremely important in future measurements of 2D magnets and perhaps superconducting systems. The second part of the thesis describes the experimental setup. A third section covers the magnetic imaging results on 3 separate samples: the surface of a chiral magnet Cu_2OSeO_3, and two 2D magnets: $Cr_2Ge_2Te_6$ and $EuGe_2$. The dissertation distinguishes itself because of its theoretical sophistication and fluency. In the next months, parts of this thesis will be reworked for publication in a peer-reviewed journal.

References

[1] *N. Rossi, F. R. Braakman, D. Cadeddu, Denis Vasyukov, G. Tütüncüoglu, A. Fontcuberta i Morral, and M. Poggio, "Vectorial scanning force microscopy using a nanowire sensor", Nat. Nanotechnol. 12, 150 (2017).*

[2] *N. Rossi, B. Gross, F. Dirnberger, D. Bougeard, and M. Poggio, "Magnetic Force Sensing Using a Self-Assembled Nanowire", Nano Lett. 19, 930 (2019).*

[3] *E. Marchiori, L. Ceccarelli, N. Rossi, L. Lorenzelli, C. L. Degen, and M. Poggio, "Nanoscale magnetic field imaging for 2D materials", Nat. Rev. Phys. 4, 49 (2022).*

[4] *H. Mattiat, L. Schneider, P. Reiser, M. Poggio, P. Sahafi, A. Jordan, R. Budakian, D. V. Averyanov, I. S. Sokolov, A. N. Taldenkov, O. E. Parfenov, O. A. Kondratev, A. M. Tokmachev, and V. G. Storchak, "Mapping the phase-separated state in a 2D magnet", Nanoscale 16, 5302 (2024).*

[5] *E. Marchiori, G. Romagnoli, L. Schneider, B. Gross, P. Sahafi, A. Jordan, R. Budakian, P. R. Baral, A. Magrez, J. S. White, and M. Poggio, "Imaging magnetic spiral phases, skyrmion clusters, and skyrmion displacements at the surface of bulk Cu2OSeO3", Commun. Mater. 5, 202 (2024).*

[6] *J. A. Wilcox, L. Schneider, E. Marchiori, V. Plastovets, A. Buzdin, P. Sahafi, A. Jordan, R. Budakian, T. Ren, I. Veshchunov, T. Tamegai, S. Friedemann, M. Poggio, and S. J. Bending, "Magnetically-controlled vortex dynamics in a ferromagnetic superconductor", Commun. Mater. 6, 108 (2025).*

Surface chemistry of hafnium oxide nanocrystals as X-ray computed tomography contrast agents

Project P2001: Imaging cardiovascular macro- and micro-structure using HfO_2 nanocrystals as X-ray tomography

Project leaders: J. De Roo and A. Bonnin
Collaborator: E. Maksimova (SNI PhD Student)

Introduction

Nanoparticles (NPs) play a crucial role in modern medicine, offering versatile platforms for targeted drug delivery, diagnostic imaging and therapeutic applications. While the core composition of the NP dictates its functionality and application (magnetic, optical, or catalytic property), the surface modification of the nanomaterials affectts their performance by providing colloidal stability in solution, enabling selective whatargeting and preventing the adsorption of serum proteins. [1-3]

Polyethylene glycol (PEG) has become a gold standard for the design of NPs for biomedical applications. An overall neutral charge of these capping ligands provides NPs with excellent steric stabilization and high hydrophilicity that allow PEGylated NPs to be extensively used in various biomedical applications. This results in suppressed protein corona formation that prolongs the circulation time of NPs in blood but at the same time results in low cellular internalization preventing the NPs from reaching their final target. Together with the development of immunological reactions, this is known as "PEG dilemma". [4] To address and minimize this phenomenon, alternative engineered surface chemistries need to be developed.

In this work, we investigate the surface chemistry of hafnium oxide HfO_2 nanocrystals as they have been previously reported as promising contrast agents for x-ray computed tomography. [5] We synthesized a novel catechol-based zwitterionic (NDA ZW) ligand as an alternative to PEGylated nitrocatechol (NDA PEG), which has been proven to provide excellent colloidal stability in aqueous solutions. The nanoparticles with PEGylated or ZW surfaces were prepared and compared in terms of colloidal stability in a wide pH range, in phosphate buffered solution (PBS) and in bovine serum albumin (BSA) solution.

Ligand synthesis

The synthesis of zwitterionic nitrodopamine (NDA ZW) is shown in Fig. 1.

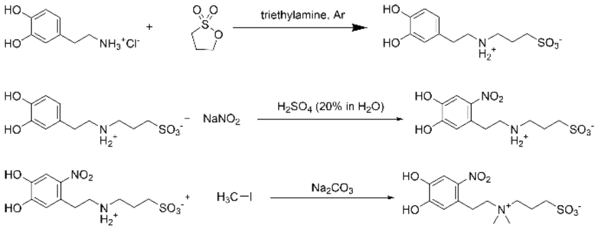

Fig. 1. The synthesis route of zwitterionic nitrodopamine (NDA ZW) in three steps: 1) sultone-ring opening to yield dopamine sulfonate; 2) nitration of the benzene ring to form nitrodopamine sulfonate; 3) methylation of the amino group to form the final product

The introduction of an electron-withdrawing nitro-group nto the benzene ring not only protects the catechol from oxidation, but also improves the binding of the ligand to the metal oxide surface. The first step is identical to the previously published sultone ring opening. Next, a nitro-group is introduced into the catechol ring to achieve the desired binding capabilities. Finally, deprotonation of the tertiary amine is followed by its methylated, yielding NDA-ZW. The last step becomes challenging due to the electron-withdrawing effects of nitro-group, which increases the acidity of the catechol groups, which upon deprotonation compete for the methylation with the tertiary amine. The ratio of base and methyliodide and the reaction time had to be carefully optimized to increase the yield of the final product formation and enable its isolation.

Colloidal stability of NPs with different surface composition

The HfO_2 NPs were synthesized via a standard autoclave synthesis and initially stabilized by a carboxylic acid (MEEAA). Then, the HfO_2 NPs were stabilized either with NDA-PEG or NDA-ZW and functionalized with 2 azide groups per NP by introducing NDA-PEG_4-N_3 (Fig.2) according to previously published methods.

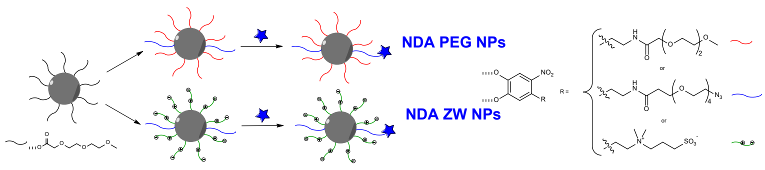

Fig. 2. Preparation of HfO_2 NPs with different surface chemistry: ligand exchange of carboxylic acid to NDA PEG (top) and NDA ZW (bottom). Both formulations have 2 molecules of NDA-PEG_4-N_3 per NP. Blue star symbol corresponds to the fluorescent dye sulfoCy5-DBCO.

Next, we prepared dye-labeled NPs with the aim of having one dye/NP to have comparable formulations with the same fluorescent brightness. For all further experiments, the solutions with the same particle concentration ($7{\cdot}10^{15}$ mL^{-1}) were used.

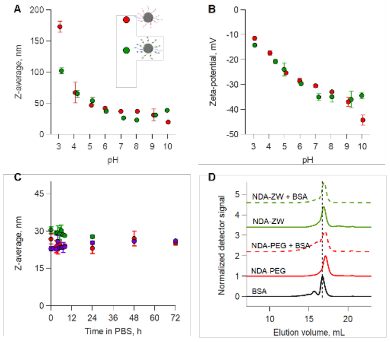

Fig.3. Comparison of colloidal stability of NPs stabilized by NDA PEG or NDA ZW: dependence of a Z-average and b) Zeta-potential over pH range; c) size distribution of NPs over incubation time in PBS; d) composition of mixtures after incubation of NPs in BSA solution

To compare the colloidal stability of different formulations the dynamic light scattering (DLS) was used. It is clear from both size and zeta potential distribution (Fig.3A-B), that both ligands follow the same trend over the pH range providing excellent colloidal stability at pH > 5 and slowly aggregating at lower acidic pH due to protonation of catechols and their resulting desorption from the surface.

Next, we incubated the NPs in PBS to mimic the dynamic system of the bloodstream and followed their collodal stability by DLS (Fig. 3C). Phosphate ions are abundant in blood serum and can compete for the binding sites on the surface of NPs and thus decrease the colloidal stability of NPs. It is clearly visible, that the colloidal stability for both ligands is preserved, proving the impeccability of catecholate binding group.

Finally, we incubated the NPs in BSA solution to gain insights into protein corona formation (Fig. 3D). As our nanoparticles are very small, it was impossible to isolate the NPs with a formed corona by centrifugation. The DLS is not strong enough to differentiate between free BSA, free NPs and NPs with protein corona, that is why size exclusion chromatography was used to analyze the composition of the solution after incubation. Note that only the hard corona can be studied as the soft corona is not bound tight enough to stay on the surface during any purification. Interestingly, ZW NPs did not adsorb BSA on the surface (green dashed line), whereas for PEGylated NPs an additional peak of aggregates or particles of bigger size appeared (red dashed line).

Conclusions and outlook

In this work, we synthesized a new organic ligand (NDA ZW) to stabilize HfO_2 NPs for biomedical applications. We showed that the colloidal stability provided by this ligand is comparable to that of NDA PEG over different pH range and in PBS. Interestingly, we have observed higher degree of BSA adsorption onto PEGylated NPs compared to zwitterionic ones, which is a promising sign of protein repelling behavior of ZW NPs. However, further thorough *in vitro* and *in vivo* investigation is needed to confirm the translation and applicability of the current findings.

References

[1] S.V.Kaymaz, H.M.Nobar, H.Sarigül, C.Soylukan, L.Akyüz, et al., "Nanomaterial surface modification toolkit: Principles, components, recipes, and applications", Adv. Colloid Interface Sci ***322****, 103035 (2023)*

[2] E. Amstad, M. Textor and E. Reimhult "Stabilization and functionalization of iron oxide nanoparticles for biomedical applications." Nanoscale, ***3(7),*** *2819-2843 (2011).*

[3] R. Bilardo, F.Traldi, A.Vdovchenko, M.Resmini "Influence of surface chemistry and morphology of nanoparticles on protein corona formation", ***14(4)****, 1788 (2022).*

[4] S.Zalba, T. Ten Hagen, C.Burgui, M.Garrido "Stealth nanoparticles in oncology: Facing the PEG dilemma",J.Control Release ***351****, 22-36 (2022).*

[5] J.Marill, N.M.Anesary, P.Zhang, S.Vivet, E.Borghi, et al., "Hafnium oxide nanoparticles: toward an in vitro predictive biological effect? ", Radiat.Oncol. ***9****, 150 (2014)*

Investigating the biomechanical properties of the T6SS speargun

Project P2002: A Death-Dealing Nanomachine
Project leaders: R. Y. H. Lim and M. Basler
Collaborator: M. Brüderlin (SNI PhD Student)

Introduction

Secretion systems allow bacteria to survive in mixed communities by sensing external threats and delivering toxin to combat those threats. In *Pseudomonas aeruginosa*, the H1-type VI secretion system (H1-T6SS) plays a central role in such antagonistic interactions. This system assembles a contractile sheath only as a defense mechanism and fires toxic effectors into neighboring cells with remarkable precision. A key outstanding question is how the bacterium senses physical damage and converts that signal into a rapid, targeted H1-T6SS response.

At the same time, the effectiveness of the H1-T6SS depends on the mechanical performance of its spike protein, VgrG1b, which forms the penetrating tip that must withstand large contractile forces and efficiently puncture multiple membrane barriers. To address these questions, we have combined correlative atomic force microscopy (AFM)–fluorescence microscopy, biophysical characterization, and single-protein force spectroscopy to investigate:

1. how *P. aeruginosa* detects and responds to outer-membrane damage, and
2. how the VgrG1b spike behaves mechanically and contributes to membrane penetration.

Together, these studies provide a unified mechanical view of T6SS activation and function — from damage sensing to membrane puncture.

Main Results

To resolve how individual cells perceive and respond to physical insults, correlative AFM–fluorescence microscopy [1] was used to apply controlled forces at defined positions on single cells, while simultaneous fluorescence imaging tracked assembly of fluorescently tagged T6SS sheaths in real time.

Indentation forces above a reproducible threshold triggered the formation of bright TssB1-mNeonGreen foci within seconds. Frequently, multiple rounds of assembly occurred at the same site, consistent with the known ability of *P. aeruginosa* to mount repeated retaliatory responses. Importantly, assemblies aligned with the direction of the incoming AFM tip, illustrating that the bacterium localizes its response to the damaged region.

Detailed analysis of AFM force–distance curves revealed discrete force drops associated with puncture of the outer membrane and, at higher loads, deeper layers of the envelope. H1-T6SS activation strongly correlated with the first rupture event, indicating that breach of a single envelope layer is both necessary and sufficient to initiate the response.

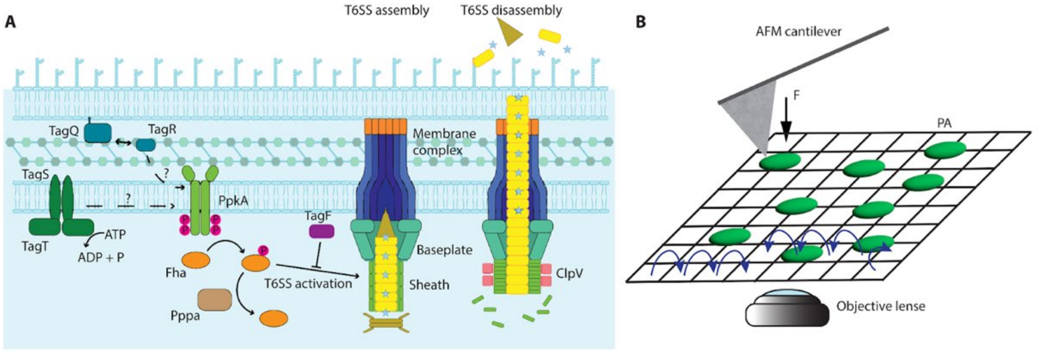

Fig. 1: Mechanical force triggers H1-T6SS assembly in P. aeruginosa cells.

*(**A**) Simplified model of H1-T6SS regulation and assembly. The proteins known to be required for initiation of T6SS assembly include TagQ, TagR, TagS, TagT, Fha, and PpkA. Inhibition and deactivation are mediated by TagF and PppA, respectively. The unfoldase (ClpV) is responsible for disassembly of the contracted sheath. (**B**) The green rods represent P. aeruginosa (PA) cells, and the blue arrows show the path of the AFM tip during a force mapping experiment. The direction of applied force exerted by the AFM tip is indicated by the black arrow (adapted from Brüderlin et al., 2025.)*

Mutants lacking TagQ or the kinase PpkA failed to assemble H1-T6SS upon mechanical impact, demonstrating that the mechanically induced response feeds into the canonical regulatory pathway responsible for retaliatory firing. Similarly, chemical destabilisation of the outer membrane using polymyxin B nonapeptide induced a comparable burst of assemblies. These results identify outer-membrane damage as a unifying input that activates the H1-T6SS via TagQRST–PpkA signalling.

This project established a quantitative single-event framework for studying how *P. aeruginosa* interprets physical threats and converts them into precisely targeted retaliatory T6SS activity.

Complementing the cellular studies, we examined the mechanical properties of the spike protein complex— the actual needle the T6SS uses to puncture neighboring cells [2]. Understanding its behavior under load is essential for interpreting how T6SS contraction translates into membrane penetration.

We performed biophysical characterizations (SEC-MALS, mass photometry, EM) to confirm the VgrG1b oligomeric state. We also used bioinformatic tools to compare its oligomeric state with other know spike complexes. To probe the mechanics directly, we developed a method to attach individual VgrG1b trimers to the apex of AFM tips. We then compressed these VgrG1b-decorated tips against a hard substrate, showing them to display distinct, reproducible mechanical responses across many loading cycles. Using an AFM-based single-spike puncture assay, we compared how different tips break a model lipid bilayer. We compared bare AFM tips with our VgrG1b-decorated tips to elucidate how the mechanical forces during puncture are altered. Our results show the importance of the VgrG spike complex for successful T6SS activity and its crucial role in membrane puncture.

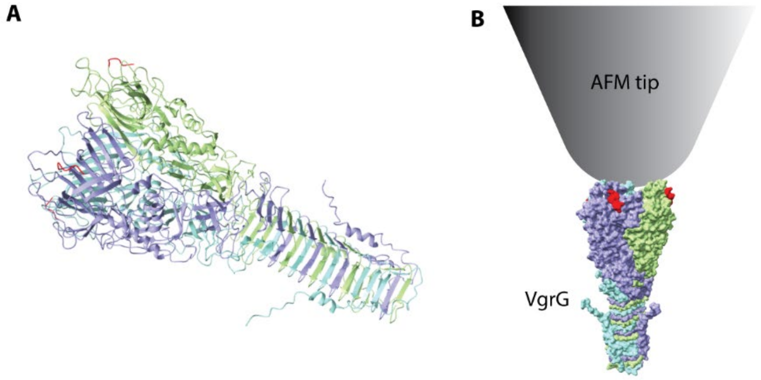

Fig. 2: Characterization of the VgrG spike protein

*(**A**) Cartoon representation of the VgrG1b trimer structure. Each chain is shown in different colors to show its intertwined structure.*
*(**B**) Presentation of the attachment of the Spike protein to the AFM tip.*

Together, these results represent the first experimental characterization of a T6SS spike under load and establish a powerful platform for probing the mechanics of single protein complexes during membrane penetration.

Conclusion

These two projects establish a cohesive mechanical picture of T6SS function in *P. aeruginosa* at the single-event level. The cell senses outer-membrane damage via the TagQRST–PpkA pathway and responds with rapid, spatially focused assembly of the H1-T6SS. At the same time, the VgrG1b spike possesses the stiffness, resilience and geometry needed to puncture membranes efficiently and withstand repeated mechanical loading.

By combining single-cell mechano-stimulation with single-spike force spectroscopy, this work provides an integrated view of how T6SS retaliation is triggered and how it physically succeeds, while also introducing experimental tools applicable to a broad range of bacterial injection systems.

References

[1] M. Brüderlin, et al, "Pseudomonas aeruginosa assembles H1-T6SS in response to physical and chemical damage of the outer membrane ", Science Advances ***11****, Issue 10 (2025).*

[2] M. Brüderlin, et al., "VgrG1b of Pseudomonas aeruginosa facilitates lipid membrane puncture by reducing the required force", In preparation.

The surface phases of epitaxial altermagnetic MnTe

Project P2004: Local manipulation of spin domains in a multiferroic Rashba semiconductor
Project leaders: M. Muntwiler and T. Jung
Collaborator: M. Heinrich (SNI PhD Student)

Introduction

Besides the well-known ferromagnetism and antiferromagnetism, altermagnetism was recently postulated as a third paradigm of magnetic order, characterized by a non-relativistic momentum-dependent spin splitting in the electronic band structure and collinear compensated magnetic moments in real space [1]. The spin sublattices are connected by rotational symmetry while lacking translational symmetry or inversion centers. Altermagnetic materials bear a great potential in spintronic applications as they can carry spin polarized currents in a system with net zero magnetization, effectively combining the benefits of ferromagnetic and antiferromagnetic properties. The absence of a magnetic stray field enables their use in thin film transistors and tightly integrated spintronic circuits.

In this project, we study the surface of altermagnetic α-MnTe(0001). α-MnTe received a lot of recent attention as the first demonstrated altermagnetic material hosting a relatively large spin band splitting (up to 0.8 eV) [2]. As modern electronic devices consist of sandwiched layers of multiple materials interfacing with a large surface to volume ratio, the surface properties of a material can play a critical role to the device performance. In addition, the modeling of complex surface structures in ab initio theories remains a formidable task. The situation is complicated by the occurrence of multiple structural phases depending on the choice of substrate, growth conditions and post-growth annealing steps. We investigate the surface structure and composition of α-MnTe(0001) epitaxial thin films by low-energy electron diffraction (LEED), scanning tunneling microscopy (STM) and X-ray photoelectron spectroscopy (XPS).

Results

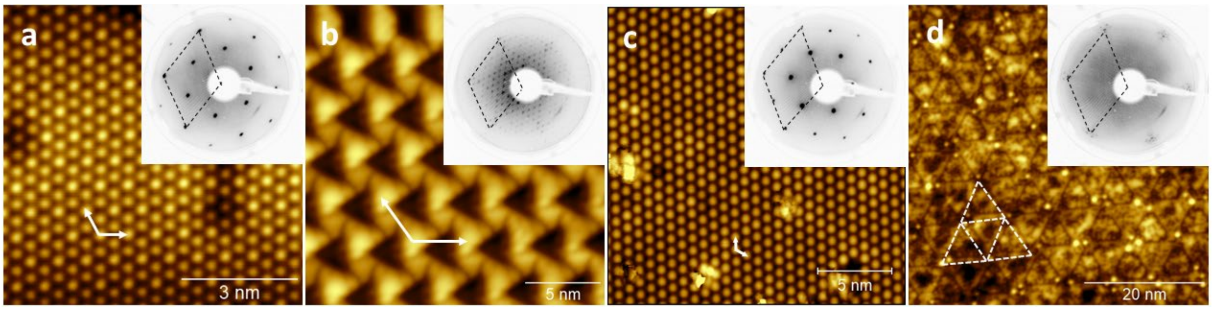

Fig. 1: STM topography and LEED patterns of the reconstructed surface phases of α-MnTe(0001): (a) $(\sqrt{3} \times \sqrt{3})$ R30°, (b) $(5\sqrt{3} \times 5\sqrt{3})$ R30°, (c) 2 × 2 and (d) quasi-1 × 1

We start by growing 400 nm thick epitaxial α-MnTe(0001) thin films on SrF_2 substrates. The surface initially exhibits a $(\sqrt{3} \times \sqrt{3})$ R30° reconstruction as shown by the LEED pattern in Fig. 1a. STM topography measurements on the same sample reveal a well-ordered hexagonal surface lattice with a lattice constant of 7.2 Å which corresponds to $\sqrt{3}$ times the MnTe bulk lattice constant of 4.15 Å. Subsequent annealing of the sample at 200 °C causes the surface to change to a $(5 \times 5)\sqrt{3}$ R30° reconstruction observable in LEED (Fig. 1b). The corresponding STM data reveals a large scale array of connected small and large triangular pyramids. The superstructure has a lattice constant of 3.6 nm. Further annealing at 260 °C causes another phase transition to a 2 × 2 surface phase with a lattice constant of 8.3 Å as shown in Fig. 1c. A third annealing step at 350 °C finally results in a complex surface where small patches of a 1 × 1 surface lattice are resolved in STM, tiled in a triangular superstructure with a lattice constant of 8 nm, as evident in the STM data of Fig. 1d and by the satellite peaks in the LEED pattern.

The progression of phases shown in Fig. 1 a-d is accompanied by decreasing Te content at the surface of the epitaxial film indicating that thermal desorption and reconfiguration of Te atoms are at the origin of the observed reconstructions. MnTe is often grown with slightly higher Te flux, leading to excess Te at the surface as seen in XPS measurements. In all phases a-c the surface is terminated by one or more monolayers of tellurium. With careful adjustment of the growth conditions, the 2 × 2 phase is identified as the thermodynamically stable phase. The final quasi-1 × 1 phase has a precise stoichiometric composition with a Mn termination. However, the high defect density and missing rows in the superstructure are a clear sign that the surface is energetically unfavourable.

The quality of thin films grown in molecular beam epitaxy (MBE) often depends on the choice of a suitable substrate. A large lattice mismatch between film and underlying substrate may lead to a high defect density or cause the formation of disjunct islands. InP as a substrate offers several advantages for applications due to its semiconducting nature and high carrier concentration. The surface lattice constant of InP(111) is almost identical to the bulk in-plane lattice constant of MnTe(0001) (4.14 Å vs 4.15 Å) promising a high quality growth. However, when we grow MnTe on InP substrates, surprisingly, the surface looks very different from samples grown on SrF_2 substrates. XPS measurements as shown in Fig. 2a reveal additional In photoemission peaks originating from the top few atomic layers suggesting the presence of about 1.5 monolayers of InTe at the surface. This InTe layer is very stable under annealing and retains a 1 × 1 surface lattice even after heating the sample to 500 °C, as indicated by the LEED data in Fig. 2b. A closer look at the LEED diffraction spots reveals the presence of additional satellite peaks indicative of a superstructure. The superstructure is also evident in STM data in Fig. 2c as a large scale triangular tiling. The tiling is the result of dislocation lines due to the lattice mismatch between InTe and MnTe.

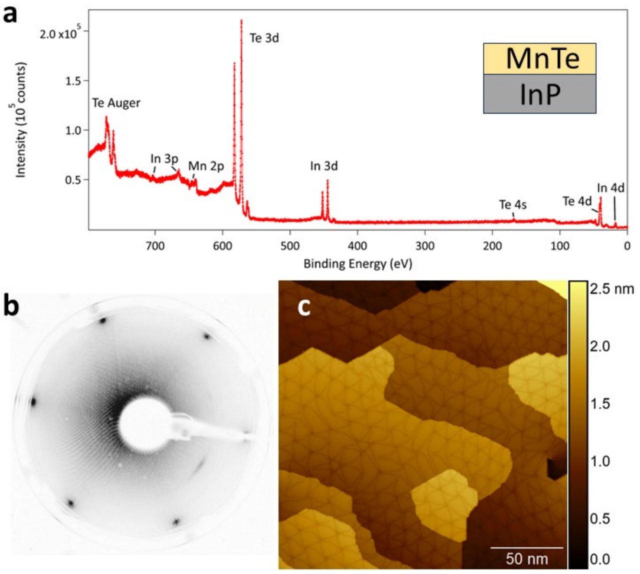

Fig. 2: The surface of MnTe grown epitaxially on InP(111) substrates. (a) XPS, (b) LEED and (c) STM data.

The presence of indium at the surface after deposition of another material, MnTe, may seem surprising. However, such «surfactant» behaviour is well known from the heteroepitaxy of other materials as well as from the chemistry of tensides. InTe as a surfactant lowers the surface energy compared to the pure MnTe surface. As the work in Fig. 1 shows, the pure MnTe surface is difficult to grow and contains many defects due to the lower atomic coordination at the surface.

Conclusion

We conclude that the epitaxial growth of α-MnTe(0001) can yield a range of surface terminations and reconstructions depending on the choice of substrate and post-growth conditioning, resulting in a rich surface phase diagram. The understanding of the actual surface structure is essential for surface sensitive measurements and the interpretation of altermagnetic properties.

Acknowledgements

The samples used in this study were provided by Gunther Springholz of the Johannes Kepler University of Linz, Austria.

References

[1] L. Šmejkal, J. Sinova, and T. Jungwirth, "Beyond conventional ferromagnetism and antiferromagnetism: A phase with nonrelativistic spin and crystal rotation symmetry", Phys. Rev. X 12, 031042 (2022).

[2] D. Kriegner, K. Výborný, K. Olejník, H. Reichlová, V. Novák, X. Marti, J. Gazquez, V. Saidl, P. Němec, V. V. Volobuev, G. Springholz, V. Holý, and T. Jungwirth, "Multiple-stable anisotropic magnetoresistance memory in antiferromagnetic MnTe", Nat. Commun. 7, 11623 (2016).

Synthetic Membranes as Functional Platforms Shaped by Protein Interactions

Project P2005: Transmembrane protein-mediated loading of synthetic compartments
Project leaders: C. G. Palivan, R. A. Kammerer, S. Gros
Collaborator: P. Jasko (SNI PhD Student)

Introduction

Compartmentalization is a fundamental principle underlying the spatiotemporal regulation of biochemical pathways in living cells and provides an important framework for biomedical and technological materials development. Synthetic nano- and micro-compartments (NCs and MCs) offer chemically versatile and mechanically robust platforms for the construction of catalytic compartments, artificial organelles, and cell mimics [1]. Despite significant progress, the development of integrated systems that more closely emulate cellular processes remains challenging, particularly with respect to controlled compartment growth, stability, and regulated material flow across the compartment membrane. Addressing these challenges requires simple and reliable strategies for membrane remodeling, fusion, and permeability control.

Protein-Mediated Compartment Fusion Using Bacterial Toxin Domain

To address controlled compartment growth and fusion, we investigated the use of bacterial toxin component as membrane-active element in synthetic systems. Bacterial toxins naturally remodel cellular membranes during intoxication, making them attractive candidates for protein-mediated manipulation of synthetic vesicles [2]. In this work, we focused on the isolated translocation T-domain of diphtheria toxin and examined its interaction with native-like lipid membranes under neutral (physiological) pH conditions.

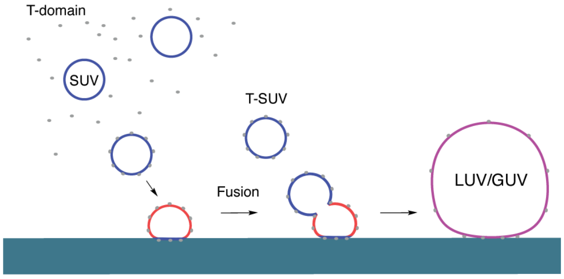

Fig. 1: Model of compartment fusion mediated by bacterial toxin-based. Our engineered bacterial toxin component (T-domain) binds to anionic small unilamellar vesicles (T-SUV) simultaneously mediating the surface adsorption of our vesicular systems inducing tension on the membrane that we found to be a trigger for the vesicle fusion and formation of MCs – giant unilamellar vesicles (GUV).

Contrary to prior assumptions that the T-domain exhibits only weak membrane interactions at neutral pH, we demonstrated that it binds selectively to anionic small unilamellar vesicles (SUVs) without causing membrane disruption. Using a combination of biophysical and imaging techniques, we showed that surface adsorption of T-domain–decorated SUVs induces membrane tension, which acts as a trigger for vesicle fusion and the formation of larger compartments, including large and giant unilamellar vesicles (LUVs and GUVs) (Fig. 1 and 2).

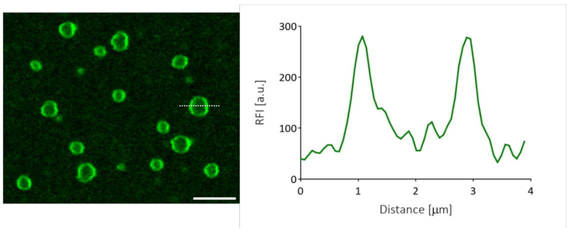

Fig. 2: The presence of DOPG ensures a negative charge whereas NBD-PC fluorescent signal is further recorded by CLSM (bottom left panel) in fused liposomes upon toxin addition. Emerged GUVs are of homogenous size with a typical 2 μm diameter. Scale bar 5 μm.

Recombinant protein variants carrying mutations in key basic residues exhibited reduced vesicle binding and surface adsorption, confirming the role of electrostatic interactions in this process. Importantly, fusion was not observed in bulk solution but emerged only upon surface-mediated tension generation, revealing a novel, protein-driven fusion mechanism at neutral pH. These findings establish a new role for the diphtheria toxin T-domain in controlled vesicle fusion without prior membrane functionalization or external stimuli [3].

Functional Reconstitution of Light-Driven Ion Pumps in Polymer Membranes

A second major focus of this work was the integration of functional membrane proteins into mechanically robust synthetic membranes. We investigated the reconstitution of the light-driven sodium/proton pump KR2 [4] into block copolymer membranes, aiming to preserve protein activity in non-biological environments.

Using a mild detergent-mediated insertion strategy, we successfully incorporated KR2 into planar polymer membranes and polymersomes (Fig. 3). Comparative analysis revealed that membrane geometry influences KR2 insertion density, with functional ion-pumping activity observed specifically in vesicular architectures. These results demonstrate that functional preservation of energy-transducing membrane proteins is achievable when detergent compatibility, membrane integrity, and geometry are appropriately matched.

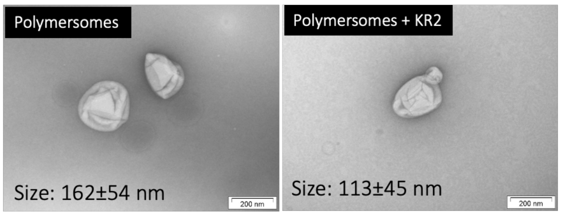

Fig. 3: Negative-stain transmission electron microscopy (TEM) micrographs of polymersomes prepared in the absence (left) and presence (right) of KR2. Both samples exhibit well-defined vesicular morphologies. The mean hydrodynamic diameters are indicated for each condition. Scale bar: 200 nm.

This work provides insight into how synthetic polymer membranes can sustain repeated photocycles and active ion transport, highlighting their potential as stable platforms for bioenergetic and biomimetic applications.

Outlook

This work highlights how protein-membrane interactions can be exploited to modulate membrane performance in synthetic systems, from controlled vesicle fusion to the functional reconstitution of energy-transducing membrane proteins. Together, these studies establish proteins as programmable elements for membrane remodeling, compartment growth, and functionality in non-biological membranes.

The finding that the diphtheria toxin T-domain mediates vesicle fusion at neutral pH through surface-induced membrane tension introduces a simple protein-driven route to compartment assembly without prior membrane functionalization or external triggers. Future studies may explore the generality of this mechanism across other membrane-active protein domains, surface chemistries, and geometries, as well as its potential reversibility for dynamically reconfigurable synthetic compartments.

In parallel, the successful reconstitution of the light-driven ion pump KR2 into polymer membranes shows that complex membrane protein functions can be preserved in mechanically robust synthetic environments. Extending this approach to additional transporters and pumps could establish general guidelines for integrating bioenergetic functionality into synthetic membranes.

Overall, the combination of protein-mediated membrane remodeling and functional membrane protein reconstitution provides a foundation for constructing higher-order biomimetic membrane systems with controllable architecture and activity, supporting future developments in nanotechnology, and materials science.

References

[1] V. Maffeis, A. Belluati, I. Craciun, D. Wu, S. Novak, C. A. Schoenenberger, and C. G. Palivan, "Clustering of catalytic nanocompartments for enhancing an extracellular non-native cascade reaction," Chemical Science, vol. 12, no. 37, 2021.

[2] R. A. Kammerer and R. M. Benoit, "Botulinum neurotoxins: new questions arising from structural biology," Trends in Biochemical Sciences, vol. 39, no. 11, 2014.

[3] P. Jasko, M. Bina, D. Frey, C. A. Schoenenberger, C. G. Palivan, and R. A. Kammerer, "Diphtheria toxin T-domain as a tool for inducing lipid vesicle fusion," Communications Chemistry, vol. 8, p. 355, 2025.

[4] K. Kovalev, R. Astashkin, I. Gushchin, P. Orekhov, D. Volkov, E. Zinovev, V. Marshanskiy, T. Balandin, D. Bratanov, V. Borshchevskiy, I. Chizhov, D. Kirilovsky, and V. Gordeliy, "Structure and mechanisms of sodium-pumping KR2 rhodopsin," Science Advances, vol. 5, p. eaav2671, 2019.

Two-Dimensional Frameworks from Metal Oxo Clusters at Liquid Interfaces

Project P2006: RESTRAIN – Reticular chemistry at interfaces as a form of nanotechnology
Project leaders: P. Shahgaldian and J. De Roo
Collaborator: A. R. Unniram Parambil (SNI PhD Student)

Introduction

Efforts devoted by scientists in the late 20th century toward crystal engineering sparked the discovery of metal-organic frameworks (MOFs), an exceptional class of crystalline materials with unparalleled physical properties including high porosity and large surface area, as well as tunable architectures-a significance underscored by their recognition in the 2025 Nobel Prize in Chemistry [1]. MOF chemistry rapidly transitioned from laboratory research to commercial applications, with several products now employing MOFs in areas ranging from gas storage to molecular separations. Despite these advances, their full potential remains constrained by technical bottlenecks primarily attributed to the poor utilization of metal sites, limited accessible surface area, and limited mass transport within MOFs. To tackle these challenges, MOFs can be size-tuned to 0D, 1D, or 2D supramolecular architectures while maintaining crystallinity. Among them, 2D MOF nanosheets are an interesting class of materials due to their milder reaction conditions and more controllable synthesis approach, and properties that differ from bulk analogs. Here, through RESTRAIN, we report the first synthesis of a 2D metal-organic coordination network (MOCN) at the air-water interface using tailor-made metal oxo clusters, achieved under mild, room temperature conditions.

Main Results

Acetate-capped zirconium oxo clusters (Figure 1A) were synthesized from their corresponding metal alkoxides under inert conditions and employed as secondary building units (SBUs). We target a two-dimensional analogue of UiO-66, a well-known MOF in which terephthalic acid linkers connect **Zr6** SBUs. To confine the growth of 2D MOCN at the surface, we designed amphiphilic terephthalates with hydrophobic alkyl chains and hydrophilic carboxylate groups (Figure 1B), which can readily form rigid monolayers at the surface of aqueous solutions containing low concentrations of clusters. The monolayer formation was studied using Langmuir balance technique. The self-assembly process upon barrier compression can be followed by the large surface pressures on Langmuir isotherms. The surface pressure-area compression isotherm of 2,3-bis(octyloxy)terephthalic acid with zirconium acetate cluster was shown in Figure 1D. Although the terephthalate possesses both hydrophilic carboxylates and hydrophobic aliphatic chains, it failed to form stable monolayers on pure water as evidenced by the absence of surface pressure increased upon compression. In contrast, when the subphase was supplemented with a low

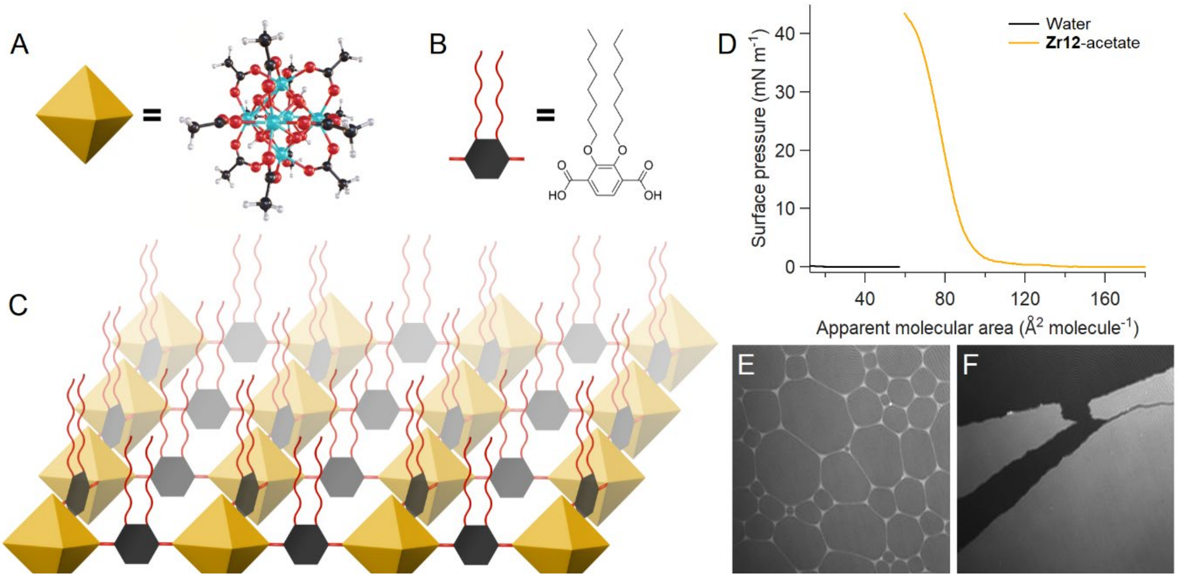

Fig. 1: (A) Structure of ***Zr6****-acetate cluster ($Zr_6O_4(OH)_4(OOCMe)_{12}$), where the $M_6O_8H_4$ core is capped with twelve acetate ligands. Cyan atoms represent zirconium, all other atoms follow conventional CPK coloring. (B) Structure of synthesized amphiphilic terephthalate. (C) Schematic model of 2D MOCN at the air-water interface. (D) Surface pressure-area compression isotherms of 2,3-bis(octyloxy)terephthalic acid on pure water and on aqueous solutions containing 10 µM of* ***Zr12****-acetate. BAM micrographs on pure water (E) and 10 µM of* ***Zr12****-acetate (F) are also shown. Scale bar: 100 µm.*

concentration of oxo clusters (i.e., 10 μM), the terephthalate derivative formed a stable Langmuir monolayer, displaying a collapse pressure as high as 40 mN m^{-1}. Monolayer formation was further studied by means of Brewster angle microscopy (BAM). The lack of contrast on micrographs of terephthalate acquired on pure water confirmed its inability to form monolayers at the interface (Figure 1E). The presence of zirconium clusters in the subphase led to the spontaneous formation of a self-assembled monolayer even before barrier compression as evidenced by the presence of bright islands (Figure 1F), further confirming a ligand exchange-driven assembly mechanism.

The MOCN prepared was transferred onto solid substrates at a surface pressure of 25 mN m^{-1} through the Langmuir-Schaefer (LS) method. The incorporation of **Zr12** clusters into the monolayer was studied by X-ray photoelectron spectroscopy. The Zr3d region exhibited two peaks corresponding to $Zr3d_{5/2}$ and $Zr3d_{3/2}$ located at 182.7 eV and 185 eV, respectively (Figure 2A). Deconvolution of the C1s spectrum revealed peaks assigned to carbonyl carbon (C=O) at 288.8 eV, Zr-O-C at 286.0 eV, and aliphatic C-C at 284.3 eV, consistent with the expected chemical composition of the layer (Figure 2B). The thickness of the monolayer was evaluated by atomic force microscopy (AFM) following transfer, as well as by synchrotron X-ray reflectivity (XRR) measurements at the air–water interface. AFM height profiles confirmed a uniform layer with an average thickness of approximately 3 nm (Figure 2C). XRR analysis yielded a thickness of 11.41 ± 0.16 Å for the portion of the monolayer protruding above the aqueous subphase, while the model does not fully capture contributions from the cluster core extending into the water (Figure 2D). By combining compositional information from XPS with height analysis from AFM and XRR, we propose a structural packing model for the self-assembled MOCN monolayer (Figure 2E-F). The model is derived from the hexagonal close-packed (*hcp*) UiO-66 topology, in which oxo-bridged **Zr12** cluster nodes are interconnected by terephthalate linkers. Unlike **Zr6**-UiO-66, a single layer of *hcp*-UiO-66 can be confined within a plane as a monolayer. In this configuration, the long aliphatic chains extend outward from the interface, while the planar *hcp*-UiO-66 framework constitutes the observed MOCN monolayer.

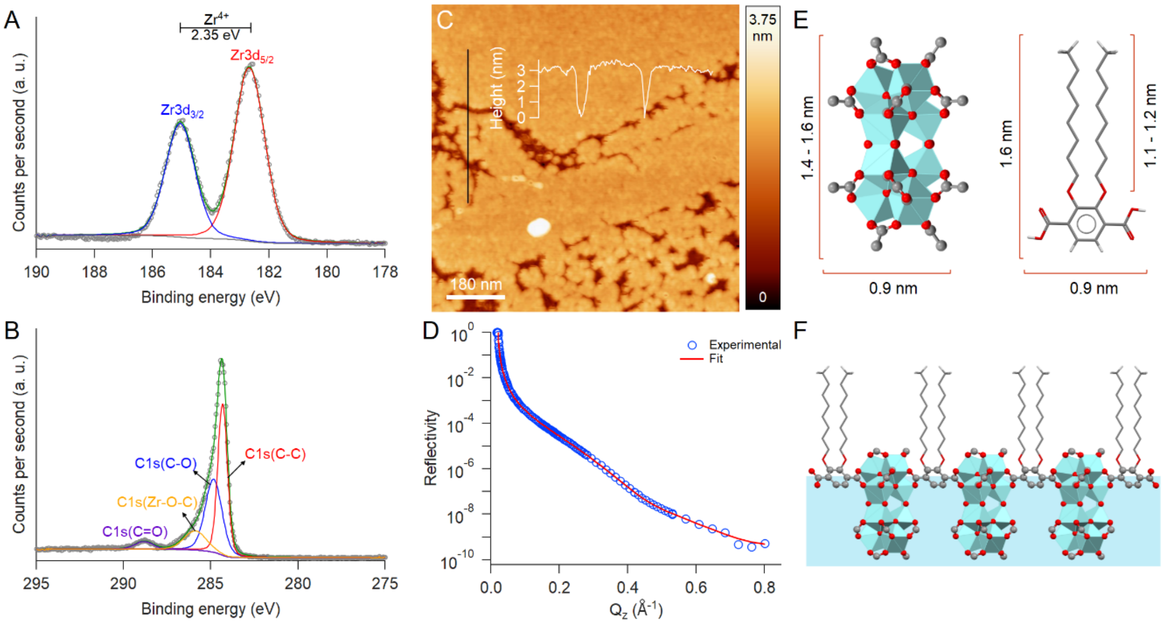

Fig. 2: (A) Zr3d and (B) C1s X-ray photoelectron spectra of the monolayer of 2,3-bis(octyloxy)terephthalic acid prepared on ***Zr12****-acetate, transferred onto highly oriented pyrolytic graphite. (C) AFM micrograph of the monolayer transferred onto an OTS-coated silicon wafer. The overlaid lines indicate the positions of the line profiles, highlighting the height variations across the monolayer. (D) X-ray reflectivity curve and fit of the monolayer of 2,3-bis(octyloxy)terephthalic acid on 10 μM* ***Zr12****-acetate subphase at a surface pressure of 10 mN m^{-1}. (E) Molecular dimensions of oxo-bridged* ***Zr12*** *cluster node and amphiphile. (F) Side view of the proposed packing model for the monolayer.*

Conclusion

In this work, we employed preformed **Zr12** clusters, the secondary building units of *hcp*-UiO-66, to achieve the first 2D metal-organic coordination network comprising a single *hcp*-UiO-66 sheet assembled at the air-water interface. Notably, this represents the first example of a Langmuir monolayer incorporating metal oxo clusters, rather than single metal ions. The monolayers were successfully transferred onto various solid substrates using Langmuir-Schaefer technique, preserving their structural integrity. These findings offer a foundation for the interfacial fabrication of 2D MOF-like networks using preformed oxo clusters and open new directions in the design of self-assembled monolayers.

References

[1] *H. Furukawa, K.E. Cordova, M. O'Keeffe & O. M. Yaghi. The chemistry and applications of metal-organic frameworks. Science* ***341****, 1230444-1230456 (2013).*

[2] *G. Chakraborty, I.-H. Park, R. Medishetty, & J. J. Vittal. Two-Dimensional Metal-Organic Framework Materials: Synthesis, Structures, Properties and Applications. Chem. Rev.* ***121****, 3751 (2021).*

Coupled Kerr-cat qubit modes in a tantalum-based planar architecture

Project P2101: A planar nanofabrication process for coupled Schrödinger-cat qubits in parametrically-driven nonlinear superconducting resonators
Project leaders: A. Grimm and C. Bruder
Collaborator: A. Bruno (SNI PhD Student)

Introduction

Quantum two-level systems are routinely used to encode qubits but tend to be inherently fragile, leading to errors in the encoded information. Quantum error correction (QEC) addresses this challenge by encoding effective qubits into more complex quantum systems. Unfortunately, the hardware overhead associated with QEC can quickly become very large. In contrast, a qubit that is intrinsically protected against a subset of quantum errors can be encoded into superpositions of two opposite-phase oscillations in a resonator, so-called Schrödinger-cat states. This "Schrödinger-cat qubit" has the potential to significantly reduce the complexity of QEC, because it can replace a large number of two-level-system qubits in a QEC code [1].

In a recent experiment, we have demonstrated the stabilization and operation of such a qubit through the interplay between Kerr nonlinearity and single-mode squeezing in a superconducting microwave resonator [2]. This type of Schrödinger-cat qubit is typically referred to as the "Kerr-cat qubit". Previous implementations of Kerr-cat qubits (KCQs) relied on three-dimensional microwave cavities. This counteracts the reduction in hardware complexity achievable with this system and is not fundamentally required. In this project, we are developing a nanofabrication process for fully planar KCQs using the low-loss superconducting material tantalum [3]. This will result in an easily scalable, high-coherence, platform enabling us to investigate interactions between several such qubits. In the first year of this SNI project, we built up the basics required for the fabrication, measurement, and operation of KCQs in line with the ramping up of the research activities of the host group. In addition to experimental tasks, such as building a measurement and control setup, we implemented an Al/AlO$_x$/Al Josephson junction fabrication process for standard superconducting transmon qubits and benchmarked it by characterizing the coherence times of these devices. We furthermore reported on building a first prototype of a quantum-limited parametric amplifier in our group. In the second year of this project we implemented a fabrication process for tantalum-based superconducting resonators. We performed all fabrication steps except for the thin-film deposition in-house. We furthermore designed the resonator test chips and measured them in our dilution refrigerator showing state-of-the-art quality factors.In the third year, we then integrated Al-AlO$_x$-Al Josephson junctions with tantalum structures to form superconducting tantalum transmon qubits. After this initial benchmarking step, we proceeded to design, fabricate, and measure a planar KCQ. This allowed us to perform a "smoking-gun" experiment demonstrating that we can indeed create a KCQ in our planar sample.

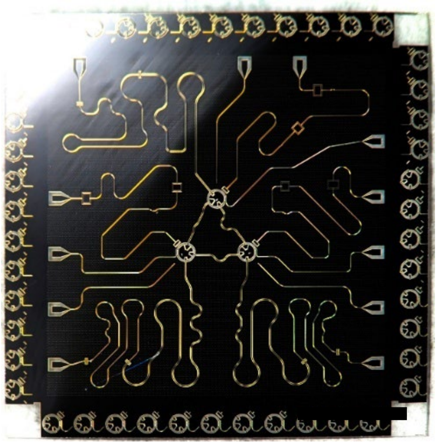

Fig. 1: Optical microscope image of a representative example chip showing three coupled KCQ devices (islands in the middle of the image), several drive lines (e.g. line entering the image from top center), as well as readout resonators and filtering structures. The tantalum film (dark color) has been etched away in some regions of the chip (light color) to define the device structures. All resonators and transmission lines are coplanar waveguides.

This year, we continued with the characterization of this sample and performed a full set of single-qubit operations as well as coherence measurements on the KCQ. The latter confirmed the expected long lifetime of hundreds of microseconds of the protected KCQ states. We then designed and fabricated samples with several KCQ devices where we have achieved controlled coupling between two KCQ modes. Additionally, the SNI-funded student has participated in work aimed at improving overall KCQ performance. We will describe our results in more detail in the following.

A device coupling three planar KCQs

We designed and fabricated a device coupling three KCQs shown in Figure 1. This involved careful microwave engineering of additional coupling resonators, drive lines, and filter structures. A particular challenge consisted in implementing local magnetic flux-bias lines on or chips, as these lines need to be compatible with the comparative complex circuit elements used in our work while minimizing cross-talk and induced losses. This task required several rounds of feedback. While we continue to work on this aspect, we now have access to working samples in which we can engineer an *in-situ* tunable coupling between two KCQ modes.

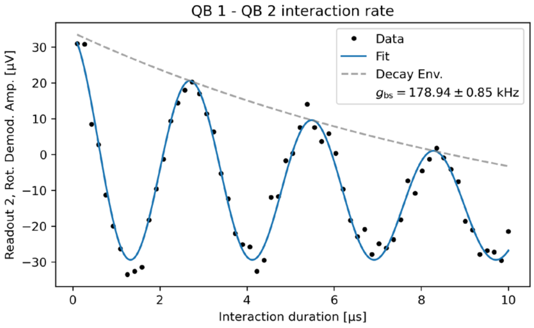

Fig. 2: Swapping of a photon between two KCQ modes. The y-axis shows the analog-to-digital converter voltage of the measured signal, which is proportional to the population of mode 2. The x-axis gives the time for which the interaction is switched on. See text for description of measurement sequence and fit.

Interactions between KCQ modes

An example dataset showing this coupling is presented in Figure 2. To obtain this data, we first initialized one of the two qubit modes in Fock state |1> (one photon) and then activated an exchange interaction between the modes. The latter is achieved through a parametric process in which the three-wave mixing capability of the circuit is leveraged: a drive at the difference frequency between the modes combines with this mixing capability to make them quasi-resonant. This results in swapping of the photon between the modes, which can then be detected by measuring the population of either mode over time. The oscillations in the measured population of mode 2, shown in Figure 2, indicate that this process was successful. From a fit to a decaying sinusoidal we extract an interaction rate of ~180 kHz. Note that this does not yet constitute an interaction between the KCQs themselves as the required squeezing drive was not active in this experiment. However, it demonstrates the required parametric process between the modes of the device in which we have created KCQs in an independent measurement. The measured interaction rate is larger than the decoherence rates of either mode, as evidenced by the fact that several coherent oscillations take place. This is a crucial prerequisite for engineering interactions between stabilized KCQs and a very encouraging result.

Enhancing the KCQ with single-photon dissipation

Finally, we addressed a long-standing challenge for KCQs in an experiment that the SNI-funded PhD student participated in. We investigated spurious processes which can promote the population of the KCQ to higher excited states, corresponding to leakage outside of the computational manifold. This effect was suspected to severely impact the lifetime of the protected states and overall qubit performance. In a work we recently published on the arxiv [4], we experimentally demonstrate an enhancement in the protected-state lifetime of a KCQ to 3.6 milliseconds by suppressing leakage out of the ground-state manifold. We used coherent control of the KCQ spectrum to quantify the population in the first excited states. We then introduced engineered dissipation that selectively targets transitions between the first excited states and the KCQ computational manifold. We moreover identified conditions under which this dissipation increases the coherent-state lifetime and show that lifetime enhancement is correlated to a decrease in excited-state population. This work is currently under review. We expect it to be published in a peer-reviewed journal over the course of this year.

Outlook

We have obtained a cost-neutral project extension of two months until end of May 2026 from the SNI to finish ongoing experiments related to this project. The PhD student will continue to be employed with us at no extra cost to the SNI. In the coming months, we will finalize our measurements on coupled KCQs and prepare a publication on them.

References

[1] A.S. Darmawan, B.J. Brown, A.L. Grimsmo, D.K Tuckett, S. Puri, Practical Quantum Error Correction with the XZZX Code and Kerr-Cat Qubits. PRX Quantum 2, 030345 (2021).

[2] A. Grimm, N.E. Frattini, S. Puri, S.O. Mundhada, S. Touzard, et al. Stabilization and operation of a Kerr-cat qubit. Nature 584, 205-209 (2020).

[3] A.P.M. Place, L.V.H Rodgers, P. Mundada, B.M. Smitham, M. Fitzpatrick, et al. New material platform for superconducting transmon qubits with coherence times exceeding 0.3 milliseconds. Nature Communications 12, 1779 (2021).

[4] F. Adinolfi, D.Z. Haxell, A. Bruno, L. Michaud, V.H. Kamrul, et al. Enhancing Kerr-Cat Qubit Coherence with Controlled Dissipation. arXiv:2511.01027 [quant-ph] (2025).

Functional nanofilaments in biology

Project P2102: Structure and Assembly Mechanism of the Ninjurin-1 Membrane Perforation Pore in Executing Cell Death
Project leaders: S. Hiller and D. J. Müller
Collaborator: M. Degen (SNI PhD Student)

Introduction

This project deepens our understanding of how nanofilaments play a role in cellular life and death. Eukaryotic cells can naturally undergo a process called Programmed Cell Death (PCD), which is vital for maintaining healthy tissues. However, when PCD goes awry, it can cause serious illnesses like cancer, neurodegenerative diseases, autoimmune disorders, and chronic inflammation. The 16 kDa protein Ninjurin-1 (NINJ1) plays a pivotal role in the final stages of lytic PCDs such as pyroptosis and secondary necrosis. Elucidation of its structure and function are crucial.

Main Results

Structure determination of NINJ1 nanofilaments

NINJ1 was produced by expression in *Escherichia coli*. We solubilized it from the bacterial membranes using detergents and then utilized a combination of chromatography-based techniques for its purification. Two types of electron microscopy were used to study NINJ1 nanofilament structure [1]. Negative stain transmission electron microscopy helped us understand the size and overall arrangement of NINJ1 assemblies at a basic and low-resolution level. Cryogenic electron microscopy (cryo-EM) resolved the three-dimensional structure of NINJ1 at atomic resolution (Fig. 1A).

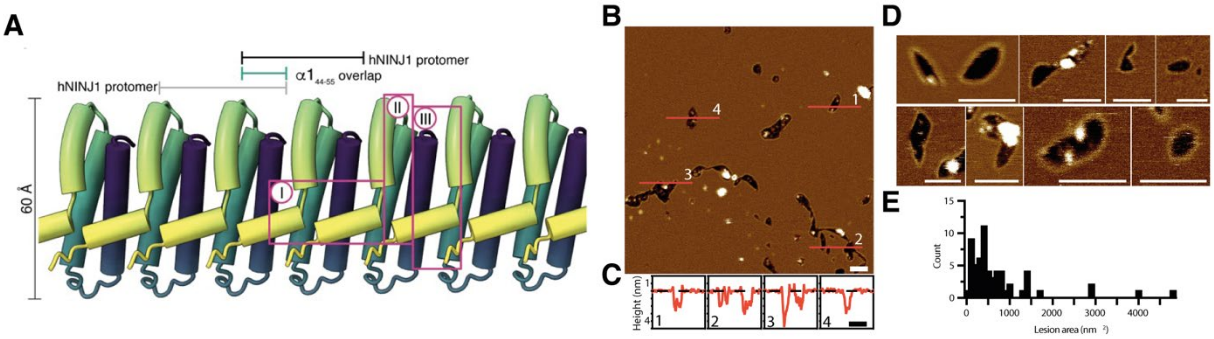

*Fig. 1: **A** Cryo-EM Structure of the NINJ1 filament. Individual protomers are colored by gradient (yellow-green-purple). Main interfaces of NINJ1 protomers are indicated by magenta boxes. **B** AFM topograph of NINJ1 proteoliposomes adsorbed on freshly cleaved mica. **C** Height profiles of the membrane lesions corresponding to the red lines from (B). **D** Gallery of AFM topographs showing NINJ1 lesions in lipid membranes, prepared and analyzed as in (B). **E** Population analysis showing the size distribution of NINJ1 lesions in liposomal membranes.*

NINJ1 caps membrane edges in reconstituted proteoliposomes

To understand how NINJ1 assembles into higher-order oligomers that engage membrane edges and promote plasma membrane rupture during lytic cell death, we used atomic force microscopy (AFM) on supported lipid bilayers reconstituted with recombinant NINJ1. We could thus directly visualize large, irregular membrane lesions (Fig. 1B-E). In these recordings, the edges of the lesions are capped by oligomeric NINJ1 nanofilaments, whereas control bilayers without NINJ1 remain intact. Together, these data provide direct topographical evidence that NINJ1 forms extended, rim-like structures at membrane discontinuities, supporting a model in which NINJ1 oligomers stabilize pore-like openings in the plasma membrane during lytic cell death and can remain associated with membrane edges rather than being released as free nanodisc-like structures or vesicles.

Structural basis for cooperative ssDNA binding by bacteriophage nanofilament P12

Nanofilaments also play a crucial role in phage-pathogen interactions. The single-stranded DNA-binding protein P12 from bacteriophage PRD1 is essential for protein-primed DNA replication and so far had lacked a defined molecular model. Cooperative binding of single-stranded DNA (ssDNA) is a central requirement for efficient genome replication and protection in many viruses. Defining the structural basis of P12 assembly therefore provides critical insight into how bacteriophages safeguard their genomes during replication, while simultaneously exerting toxic effects on host cells. Using single-particle cryo-EM, we found that P12 assembles into a continuous filament along ssDNA, and that two such filaments associate to form an anti-parallel double-filament arrangement. Using poly(dT)$_{80}$ as a well-defined ssDNA substrate, we obtained a 2.75 Å cryo-EM reconstruction resolving both P12 protein and the bound ssDNA, enabling an atomistic description of the nanofilament (*Fig. 2A, B*).

The structure shows that each P12 protomer covers an approximately 6-nucleotide segment of ssDNA, with binding dominated by electrostatic and hydrogen-bonding interactions to the phosphate backbone within a positively charged, pincer-like cleft (*Fig. 2C*). This binding mode is consistent with largely sequence-independent recognition, while still allowing tight wrapping of the ssDNA within the filament architecture. At the same time, the maps reveal how cooperativity emerges from the assembly itself: a C-terminal α-helix of each protomer forms stabilizing contacts with the neighboring subunit, effectively coupling ssDNA engagement to inter-protomer packing and promoting processive nanofilament growth (Fig. 2D, E). In contrast, a further C-terminal extension is not resolved in the density, which is consistent with a flexible, intrinsically disordered tail.

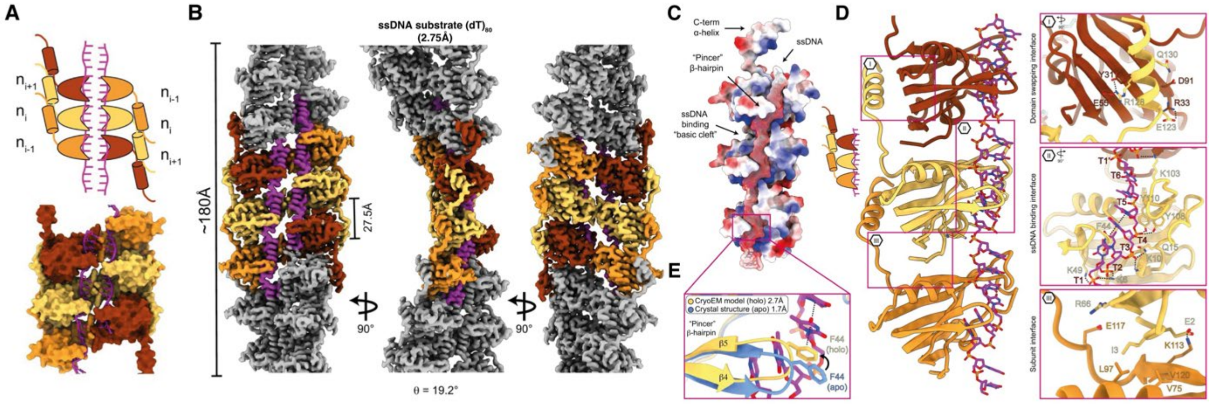

Fig. 2: ***A*** *Modelled structure of the anti-parallel double-filament of the P12–ssDNA complex, highlighting the arrangement of P12 subunits (colored by protomer) and the ssDNA threaded through the central cleft of each filament (pink).* ***B*** *3D reconstruction of P12 bound to (dT)$_{80}$ at 2.75 Å resolution.* ***C*** *Surface electrostatic representation of P12 upon ssDNA binding. The ssDNA threads through the positively charged cleft formed by the pincer β-hairpin and the core of each P12 protomer.* ***D*** *Structural representation of the P12 filament bound to ssDNA. Three key interaction sites are marked with pink boxes: (I) Domain-swapping interface between P12 protomers. (II) ssDNA-binding interface showing interactions between P12 and the ssDNA backbone. (III) Subunit interface illustrating interactions between neighboring P12 protomers.* ***E*** *Overlay of the crystal structure (apo, blue) and the cryo-EM model (holo, yellow), illustrating the position of the F44 residue at the tip of the pincer loop between β-strands 4 and 5.*

To connect the structural model to function, we combined structure-guided mutations and truncations targeting both the ssDNA-binding cleft and the C-terminal assembly interface. Disrupting these features weakened ssDNA binding and compromised filament formation, and, in cellular assays, reduced the toxicity observed upon P12 expression in host bacteria, linking strong ssDNA engagement and cooperative assembly to a measurable biological outcome. Complementary biochemical assays further showed that intact P12 filaments protect ssDNA against nuclease digestion, consistent with the continuous protein "sheath" seen in the cryo-EM structure [2].

Conclusion

Together, our results highlight filamentous protein assemblies as a unifying molecular principle that underpins diverse biological outcomes at the nanoscale. Despite acting in fundamentally different biological contexts—eukaryotic cell death versus phage replication—both NINJ1 and P12 rely on higher-order homooligomeric assemblies that transform local molecular interactions into large-scale structural and functional effects. These findings underscore the versatility of nanofilament architectures as emergent biological modules that stabilize membranes, reshape nucleic acids, and enforce irreversible cellular decisions. Looking ahead, the mechanistic principles uncovered here open several new avenues for future research. For NINJ1, understanding how filament formation is regulated in space and time, and how it interfaces with adhesion molecules or immune signaling pathways, may enable targeted modulation of membrane rupture in inflammatory diseases. For P12 and related viral filaments, the structural framework established here provides a blueprint for exploring how cooperative ssDNA binding can be tuned to balance genome protection, replication efficiency, and host toxicity. This work establishes proteinaceous nanofilaments as tractable targets for structural, biophysical, and therapeutic investigation, reinforcing their importance as fundamental effectors in both cellular and viral biology.

References

[1] *M. Degen, J.C. Santos, K. Pluhackova, et al., "Structural basis of NINJ1-mediated plasma membrane rupture in cell death", Nature* ***618****, 1065 (2023).*

[2] *L.K. Träger, M. Degen, et al., "Structural basis for cooperative ssDNA binding by bacteriophage protein filament P12", Nucleic Acids Research* ***53****, gkaf132 (2025).*

Raman Microscopy: Targeting EGFR of Ovarian Cancer Cells by the Effective Surface Modification of Gold Nanoparticles

Project P2103: Gold nanoparticle assemblies for SERS based detection of EGFR expressing ovarian cancer cells in tumor xenografts.
Project leaders: S. Saxer, J. De Roo, V. Heinzelmann, and F. Jacob
Collaborator: Alessandro Stumpo (SNI PhD Student)

Introduction

Surface-Enhanced Raman Scattering (SERS) combined with Raman microscopy has emerged as a powerful imaging technique, increasingly used for cancer visualization both in vivo and ex vivo [1]. This approach relies on SERS-active nanotags [2] that specifically target cancer biomarkers, enabling differentiation between cancerous and healthy cells via Raman imaging.

Ovarian Cancer (OC) is the gynecologic malignancy with the highest mortality due to silent symptoms which are often misattributed to other diseases, leading to late-stage diagnoses. Epidermal growth factor receptor (EGFR) overexpression in OC has been associated with poorer patient outcomes, playing a key role in tumor growth and resistance to radiotherapy and chemotherapy [3].

We developed two types of SERS-active nanotags to target OC cells expressing EGFR: anti-human EGFR single gold nanoparticles (anti-EGFR AuNPs), and anti-human EGFR gold nanoparticle assemblies (anti-EGFR aAuNPs). For the single gold nanotags, 60 nm anti-EGFR AuNPs are functionalized on the surface with a two-step protocol, achieving an effective balance between Raman sensitivity, binding specificity and nanoparticles stability. The functionalized nanoparticles were characterized for their physicochemical properties, including EGFR-binding capability and Raman signal intensity, and then their capability to discriminate between EGFR-positive and EGFR-negative OC cells was demonstrated. Due to the relatively weak SERS signal of spherical nanoparticles [2], we have also developed nanoparticle assembly nanotags. These assemblies were linked using Cucurbit[7]uril/Methyl Viologen (CB[7]/MV) host-guest complex, which served as molecular linker and Raman reporter, with an interparticle gap of approximately 1 nm. Such small gaps are high intensity electromagnetic regions, the so-called “hotspots”, which promote strong plasmonic coupling and maximization of SERS signal.

Main Results

In the first part of the project antibodies were immobilized on 60nm gold nanoparticles with a defined two steps functionalization, resulting in controlled surface chemistry that enabled to overcome antibody induced aggregation [4] and unspecific adsorption and allows for reproducible and stable SERS measurement on fixed cells. The AuNPs were functionalized with anti-human EGFR antibodies with the ideal orientation to ensure both binding sites to be functioning. Benzene-1.4 dithiol, a Raman marker, was immobilized via thiol-gold bond, while PEG is used to stabilize our nanoparticles. Anti-EGFR AuNPs and chemistry were characterized with NMR, HPLC, DLS and Raman. Moreover, nanoanalyzer (nanoFCM) measurements showed that 79% of nanoparticles display anti-EGFR antibodies on the surface. The specificity of our anti-EGFR AuNPs towards EGFR was measured by quartz crystal microbalance (QCM-D). Flow cytometry measurements proved that anti-EGFR AuNPs selectively bind to EGFR-positive ovarian cancer cells (OVCAR5 and OVCAR8) but not to EGFR-negative cells (TOV112D), with only minimal, non-specific binding observed. However, EGFR-knockout OVCAR8 cells exhibited a small secondary fluorescence peak, that corresponds to the residual cells (27%) that retained EGFR expression after genome editing. Finally, the SERS signal of anti-EGFR AuNPs was detected by Raman microscopy on EGFR-positive OVCAR8 cancer cells (Figure 1).

In the second part of the project, anti-human EGFR gold nanoparticle assemblies (anti-EGFR aAuNPs) were synthesized with the aim of an increased SERS signal due to the defined “hotspots” between the linked nanoparticles. Anti-EGFR aAuNPs were synthesized using an adapted Turkevich method, with CB[7]/MV added as linker molecules. Within 15 minutes, the solution turned black, indicating the formation of nanoparticles assemblies, in contrast to the bright red solution observed for monodispersed AuNPs (Figure 2a). Statistical analysis of TEM images (Figure 2b) showed that, on average, each assembly is made of 9 nanoparticles. SERS measurements confirmed the presence of methyl viologen within the plasmonic “hotspots”, with characteristic peaks clearly detectable at 835, 1190, 1297, and 1645 cm^{-1} (Figure 2c). A peak corresponding to cucurbit[7]uril was also observed at 448 cm^{-1}. It must be noted that, in comparison to monodispersed AuNPs, the SERS signal of anti-EGFR aAuNPs is strong enough to be detected in liquid. Nanoanalyzer confirmed the functionalization of 93% of the assemblies with anti-EGFR antibodies. Subsequent backfilling with PEG resulted in highly stable assemblies, likely due to the increased surface area, which allows PEG chains to be fully extended and densely packed on the assemblies’ surface. QCM-D experiments showed that the assemblies selectively bind the EGFR receptor.

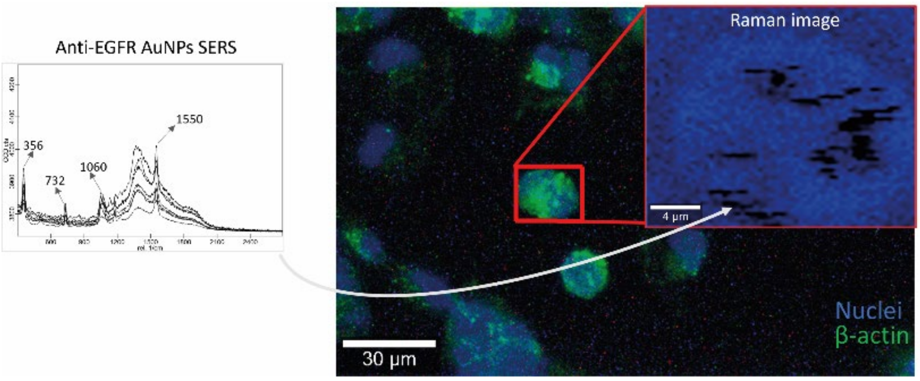

Fig. 1: Fluorescence microscopy image (Confocal laser scanning microscope FV3000, Olympus) of OVCAR8 cancer cells (blue: nuclei; green: actine). Inset shows a Raman image of an EGFR-positive OVCAR8 cell with SERS signal of anti-EGFR AuNPs (black stripes) bound to the cell (Raman Microscope alpha 500, WITEC)

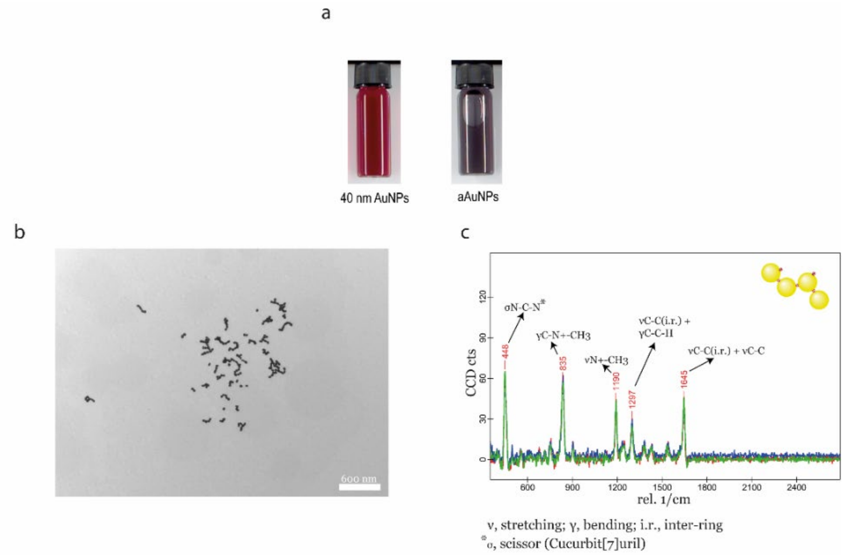

Fig. 2: a) Color change of single and assembled AuNPs, b) Trasmission electron microscope of assemblies dried on Formvar Cu-grid (Zeiss EM900), c) Raman spectra of anti-EGFR aAuNPs in PBS.

Conclusion

In SERS-based cancer visualization, SERS-active nanotags are employed to selectively bind cancer-associated biomarkers. AuNPs as SERS-active nanotags face several challenges, including limited stability and fast agglomeration, which might result in false positive signal. Thus, the stable robust chemistry and adequate cell measurement process are both crucial. In this study we have developed two types of nanotags targeting the EGF receptor expressed by ovarian cancer cells: anti-EGFR AuNPs and anti-EGFR aAuNPs. The surface of anti-EGFR AuNPs was functionalized and fully characterized, demonstrating their selectivity for EGFR-positive ovarian cancer cells, as well as their stability and SERS activity. To enhance the SERS signal, anti-EGFR aAuNPs were synthesized and characterized in a similar way, showing an improved stability and increased SERS signal in comparison to anti-EGFR AuNPs. Initial experiments on EGFR selectivity underscore the need for in vitro studies to evaluate their ability to discriminate between EGFR-positive and EGFR-negative ovarian cancer cells.

References

[1] Sangyeop Lee, et al., "Rapid and sensitive phenotypic marker detection on breast cancer cells using surface-enhanced Raman scattering (SERS) imaging", Biosensors and Bioelectronics 51, 238 (2014).

*[2] Alexandre Verdin et al., "Designing SERS nanotags for profiling overexpressed surface markers on single cancer cells: A review", Talanta **276**, 126225 (2024).*

*[3] Q Sheng & J Liu, "The therapeutic potential of targeting the EGFR family in epithelial ovarian cancer", British Journal of Cancer **104**, 1241 (2011).*

*[4] Samuel Okyem et al., "Probing the mechanism of antibody-triggered aggregation of gold nanoparticles", Langmuir **37**, 2993 (2021).*

X-ray crystallography as a tool to explain the mechanism of metabolite biodegradation

Project P2104: Methods to understand the role of ordered waters and disordered residues in enzyme catalysis using macromolecular crystallography at physiological temperatures

Project leaders: F. P. Seebeck and J. H. Beale
Collaborator: S. B. Bolotova (SNI PhD Student)

Introduction

Certain compatible solutes are abundant sulfur-containing non-proteinogenic amino acids. In humans, 2-aminoethanesulfonic acid (2AES) acts as an osmolyte, antioxidant, bile salt conjugate, and neuroprotective agent. While it can be synthesized endogenously from cysteine via 2-aminoethanesulfinic acid (2AESi), mammals lack the enzymes for degradation of this sulfonated amino acid, and excess amounts are excreted. In contrast, various bacteria utilize this molecule as a source of carbon, nitrogen, sulfur, and energy. This study focuses on the structural characterization of the first enzyme in the catabolic pathway for this compound (Fig. 1): 2AES:pyruvate aminotransferase (Tpa) from opportunistic pathogen Bilophila wadsworthia. B. wadsworthia is a sulfite-reducing bacterium and a common member of human gut microbiota; it has been associated with inflammatory bowel diseases, such as colitis and colorectal cancer [1]. Degradation of this sulfonated amino acid by B. wadsworthia leads to the production of hydrogen sulfide (H_2S), which negatively impacts gut microbiome dynamics. A better understanding of the mechanism by which human gut bacteria catabolize this compound would allow us to gain more insights into their regulation of its levels, which is crucial for cellular function and health.

Fig. 1: Transaminase-catalyzed degradation of 2AES.

Main Results

2AES aminotransferase is a pyridoxal 5'-phosphate (PLP) dependent enzyme, catalyzing sequestration of the 2AES amino group with formation of sulfoacetaldehyde. As an amino group acceptor, 2AES aminotransferases utilize prochiral pyruvate or 2-oxoglutarate, converting them to chiral metabolites, alanine and glutamate. Generated sulfoacetaldehyde is subsequently either desulfonated by sulfoacetaldehyde acetyltransferase (Xsc) or reduced to isethionate by sulfoacetaldehyde reductase (SarD). 2AES aminotransferases belong to the class III aminotransferase family (IPR005814), so-called ω-transaminases, acting on substrates with terminal amines. The cofactor PLP serves as an amino group shuttle in the transamination reaction following the ping-pong mechanism.

The 2AES:pyruvate aminotransferase from *Bilophila wadsworthia* (BwTpa) has been biochemically characterized previously [2]. BwTpa was found to be co-encoded in the 2AES-inducible gene cluster, together with alanine dehydrogenase, producing BwTpa's substrate, pyruvate, and SarD. As 2AES is a widespread compound and its metabolism is commonly initiated by Tpa, identification of 2AES-dissimilating bacteria can be done by *tpa* gene-specific PCR; the method was proven successful in faecal samples for *B. wadsworthia* [3]. Recently, Y. Zhang's group described 2AES:2-oxoglutarate aminotransferase (Toa) from human gut bifidobacteria and proposed that all 2AES-specific aminotransferases share the same set of active site residues [4]. As there is little structural information available for any proteins in bacterial sulfonate metabolism, we decided to contribute to their characterization by working on the key enzyme BwTpa.

BwTpa was recombinantly produced in *E. coli* with a C-terminal His-tag and purified with NiNTA chromatography. The protein was further crystallized in Morpheus® screen (Molecular Dimensions), and the crystals diffracted to the resolution of 1.3 Å. Further data processing resulted in the first ever structure of 2AES:pyruvate aminotransferase (Fig. 2, A). BwTpa forms a lung-shaped homotetramer as a dimer of dimers. The dimer unit is organized by interface contacts with 22% of monomer residues involved; the identical catalytic sites include residues from both subunits in the dimer. Each monomer has a classic type I PLP-dependent enzyme fold (CATH 3.40.640.10) with the PLP-binding site located between large and small domains. BwTpa was crystallized with PLP, covalently bound to a conserved lysine, in full occupancy within all monomers. The nitrogen of the PLP pyridine ring interacts with an aspartate side chain, while the phosphate group forms multiple hydrogen bonds with residues in a serine-glycine-serine sequence and threonine from another subunit. These interactions also stabilize the reaction intermediate pyridoxamine-5`-phosphate (PMP), which is generated as a product of 2AES deamination. Interestingly, in the crystal structure of Tpa, we also observed molecules of 1,5-pentanediol, which is present in the crystallization screen. The ligand was located in a wide channel, leading to the PLP-bound active site. A terminal hydroxyl group of 1,5-pentanediol is located in a putative position of a sulfonate group of 2AES during the catalytic cycle and is coordinated by active site arginine and threonine via hydrogen bonding (Fig. 2, B). To find the actual substrate binding mode, the available Tpa crystals were soaked with 2AES. Despite reported difficulties in obtaining co-crystal structures, we were able to obtain the Tpa structure with 2AES-bound PLP with a resolution of 2.5 Å (Fig. 2, C). 2AES-PLP was found in all monomers with 80-100% occupancy; no structural differences between "apo" and 2AES-bound structure were observed (RMSD: 0.239 Å between 454 pruned atom pairs). Presumably, BwTpa doesn`t require structural rearrangement for accommodating the substrate, as the wide channel leading to the PLP remains open in the 2AES-bound structure. 2AES`s sulfonate group is coordinated by a hydrogen-bonding network with arginine, threonine, and serine, as it was observed with 1,5-pentane-diol. The structural evidence allows us to propose that Tpa doesn`t require challenging dehydratation of the charged sulfonate group for performing the enzymatic reaction.

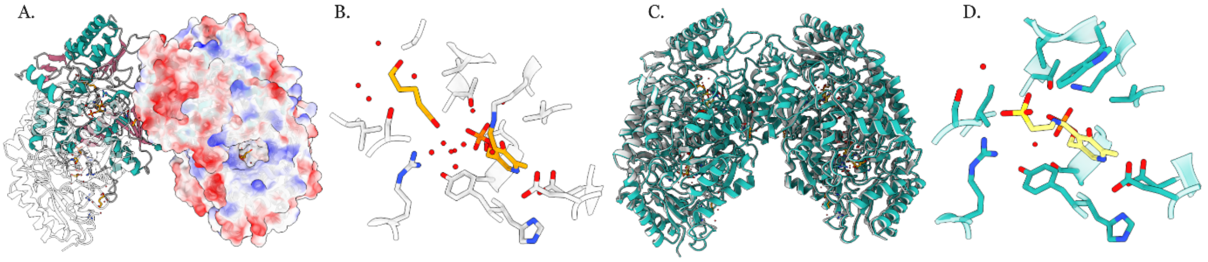

Fig. 2: A. Crystal structure of Tpa, resolution 1.3 Å. B. Active site of Tpa with co-crystallized ligand 1,5-pentane-diol in the substrate-binding channel. PLP and 1,5-pentane-diol are colored orange. C. Alignment of the 2AES-soaked (resolution 2.5 Å) and apo-structures of Tpa. D. Active site of Tpa with internal 2AES aldimine. 2AES-bound PLP is colored yellow.

Based on the analysis of ligand binding, we could propose the following mechanism of transamination (Fig. 3). The 2AES and PLP-coordinating residues of BwTpa show high homology to other 2AES-specific transaminases [4]. The positioning of 2AES-binding residues also explains the narrow substrate scope of BwTpa: the most active amino group donors, 2AES and hypo2AES, have an optimal length for coordination with arginine for sulfonate charge compensation, while longer substrate homo2AES is reported to be 30% less efficient [2].

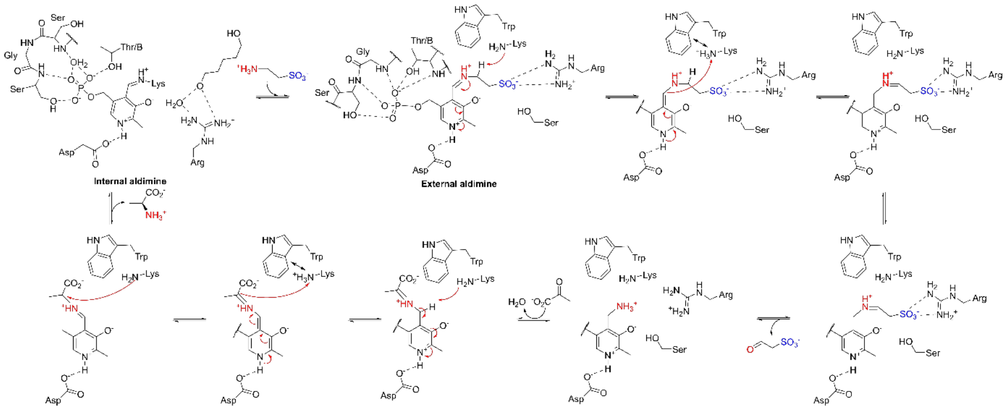

Fig. 3: Proposed mechanism of Tpa-mediated 2AES transamination.

Conclusion

Structural analysis by X-ray crystallography resulted in the first structures of 2AES:pyruvate aminotransferase with PLP and 2AES-PLP bound state. The analysis of ligand-binding site and interactions confirmed the conservation of residues specific for 2AES transaminases and explained the enzyme`s mechanism. The characteristic sequence patterns of Tpa could be used for bioinformatic search for other 2AES-degrading bacteria, including the species in the human gut microbiota.

References

[1] A. G. Burrichter, S. Dörr, P. Bergmann, S. Haiß, A. Keller, et al. Bacterial Microcompartments for Isethionate Desulfonation in the 2AES-Degrading Human-Gut Bacterium Bilophila Wadsworthia. BMC Microbiol. ***21*** *(1), 340. (2021).*

[2] H. Laue, A. M. Cook, Biochemical and Molecular Characterization of 2AES:Pyruvate Aminotransferase from the Anaerobe Bilophila Wadsworthia. Eur. J. Biochem. ***267*** *(23), 6841–6848. (2000).*

[3] H. Laue, T. H. M. Smits, U. K. Schumacher, M. C. Claros, R. Hartemink, A. M. Cook. Identification of Bilophila Wadsworthia by Specific PCR Which Targets the 2AES:Pyruvate Aminotransferase Gene. FEMS Microbiol. Lett. ***261*** *(1), 74–79. (2006).*

[4] M. Li, Y. Wei, J. Yin, L. Lin, Y. Zhou, et al. Biochemical and Structural Investigation of 2AES:2-Oxoglutarate Aminotransferase from Bifidobacterium Kashiwanohense. Biochem. J. ***476*** *(11), 1605–1619. (2019).*

Combined transport-optics characterisation of a gated semiconductor monolayer

Project P2105: Ferromagnetism of mobile electrons in a two dimensional semiconductor
Project leaders: R. J. Warburton and Martino Poggio
Collaborator: R. M. Kaier (SNI PhD Student) and J. N. Sunil (SNI PhD Student)

Introduction

Modulation spectroscopy has a long history in semiconductor physics as it enables picking out delicate signals from the noise. The general idea is to modulate the response of the semiconductor at a specific frequency, measuring the response at exactly the same frequency. One important example is to modulate the carrier density. This requires low-resistance contacts. Such contacts are of course routine with standard semiconductors. The contacts rely on local doping of the material to very high levels. It is much more challenging to create low-resistance contacts to monolayer semiconductors such as transition-metal dichalcogenides, for instance MoS_2, as other techniques are required. One promising approach uses a conducting material in direct contact with the monolayer. The work function of the conducting material should be very close to the electron affinity of the semiconductor [1,2]. Example materials include the semi-metals bismuth [1], graphene and few-layer graphene [2]. In our case, the motivation is to develop low-resistance contacts in order to switch monolayer MoS_2 electrically from a ferromagnetic state (low to medium density) to a paramagnetic state (high density) [3]. This will allow modulation spectroscopy to be applied in the context of magnetometry, a potentially direct way to control the ferromagnetism.

Main Results

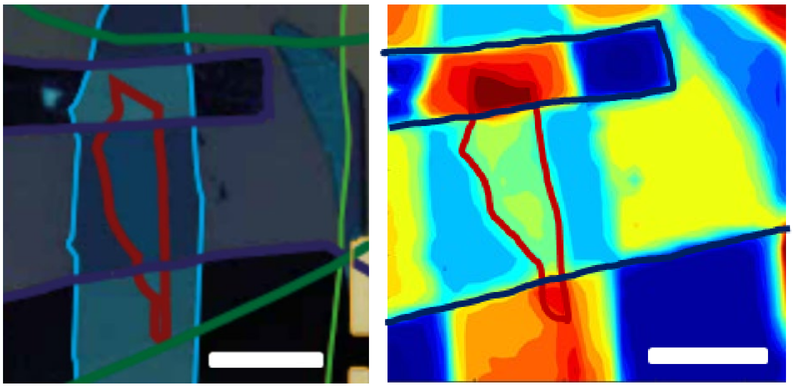

Fig. 1: Images of the MoS_2 device. Left: microscopy image, right: reflection image. Few-layer graphene is shown in blue, contacted MoS_2 in red. The scale bars are 10 μm.

The sample is shown in Fig. 1. Monolayer MoS_2 was embedded in h-BN, an insulator, to ensure that the MoS_2 surfaces are pristine. Parts of the MoS_2 stick out from the h-BN layers, and these are used for the contacts. Two separate few-layer graphene layers were placed directly onto the MoS_2. The two few-layer graphene layers are connected to gold bond pads on the sample substrate using gold wires defined lithographically.

Combined transport-optics characterization was carried out at low temperature, 4 K, Fig. 2. The transport measures the entire conductivity of the device, the conductivity of the two contacts and the MoS_2-layer in series. Conversely, the optics measures the reflectivity, a local probe of the electron density. The optical characterization shows a clear transition from the neutral (X^0) to the charged exciton (X^-) at a bias voltage of 1.0 V. This shows that in terms of conductivity, the MoS_2 layer is above any Mott insulator-metal transition at 1.0 V. The transport shows a clear step in the conductivity at higher bias, 2.1 V. For voltages below 2.1 V the conductivity is small: this means that although the MoS_2 layer itself is conducting, the entire conductivity remains low, limited by the MoS_2 regions close to the contacts. At higher biases, 3.0 V, the conductivity exhibits a second step upwards. This corresponds to the occupation of the second set of conduction bands: the number of bands contributing to the transport increases from 2 to 4. At voltages between 1 V and 2 V, a series of small peaks are observed in the conductivity. These correspond to disorder-related resonances in the contact regions.

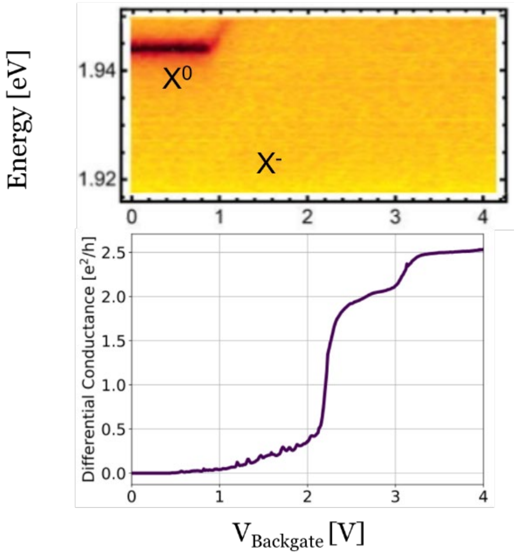

Fig. 2: Characterisation of gated MoS$_2$ at low temperature, 4 K. Top: reflectivity showing photon energy versus bias voltage. Bottom: conductance from source to drain versus bias voltage.

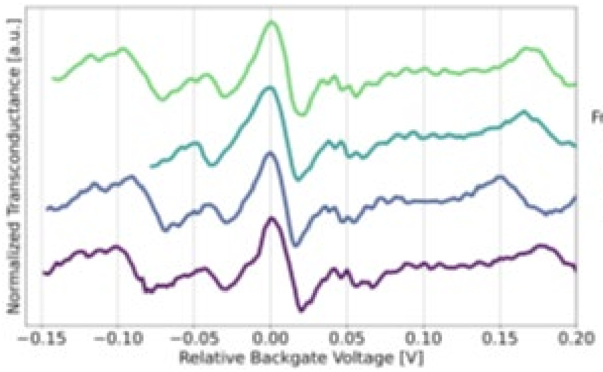

Fig. 3: Transconductance versus bias voltage for four different modulation frequencies.

The dc measurements were complemented with ac measurements, Fig. 3. The contacts enable the transconductance to be measured up to about 500 Hz. Higher frequencies are possible, but increasing the frequency results in an increasing heat dissipation in the high-resistance contact regions.

Conclusion

A scheme has been developed with which MoS$_2$ can be modulated at frequencies up to 500 Hz using few-layer graphene contacts. The electron density is controlled by applying a bias to the MoS$_2$ via the contacts. The combined transport-optics characterisation shows that the sample regions surrounding the contacts only become conducting at bias voltages for which the carrier concentration is high. The next step is to replace few-layer graphene with bismuth.

References

[1] P. Shen et al., "Ultralow contact resistance between semimetal and monolayer semiconductors", Nature ***593****, 211 (2021).*

[2] Y. Liu et al., "Toward barrier free contact to molybdenum disulfide using graphene electrodes", Nano Letters ***15****, 3030 (2015).*

[3] J. G. Roch et al, "First-Order Magnetic Phase Transition of Mobile Electrons in Monolayer MoS$_2$", Physical Review Letters ***124****, 187602 (2020).*

Bioorthogonal uncaging following ring-closing metathesis (RCM)

Project P2106: Innovative Catalytic Strategies to Combat Cancer
Project leaders: T. R. Ward and M. Fani
Collaborator: D. A. Graf

Introduction

Bioorthogonal chemistry offers powerful tools for controlling molecular function within complex biological environments. Metal-catalyzed reactions, particularly those involving ruthenium, have shown promise for selective activation of caged substrates in cells and living organisms [1,2]. While ruthenium(*N*-heterocyclic carbene) complexes (Ru(NHC)) are prone to rapid decomposition in aqueous media, ruthenium(cyclic(alkyl)(amino)carbene) complexes (Ru(CAAC-5)) have been reported to be much more stable under such conditions, making them highly suitable for bioorthogonal applications [3]. In this project, we aim to use Ru(CAAC-5) complexes to site-selectively trigger the uncaging of prodrugs via ring-closing metathesis (RCM). In this "close-to-release" approach, RCM of a tethered diolefin induces a spontaneous 1,4-elimination that liberates the active cargo (Figure 1) [4]. By combining the stability and bioorthogonal character of Ru(CAAC-5) with an RCM-driven release mechanism, this strategy provides a versatile platform for chemical biology, targeted therapeutics, and synthetic bioengineering.

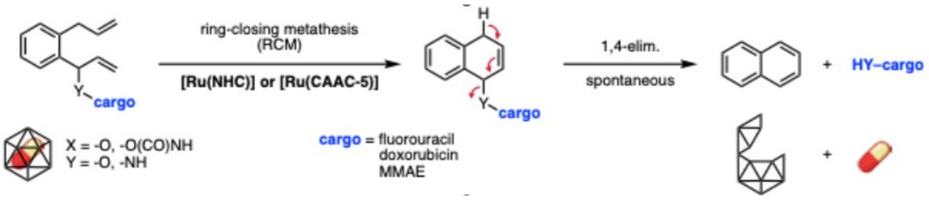

Fig. 1: Ring-closing metathesis (RCM) catalyzed by Ru(NHC) or Ru(CAAC-5), followed by 1,4-elimination to release a cargo.

Main Results

To the best of our knowledge, no anchoring groups have previously been reported for CAAC-5 ligands. Nevertheless, several studies have highlighted that functionalization of this scaffold is feasible, albeit challenging. One established strategy relies on alkylation of the enamine intermediate **1** [5]. Building on this approach, we synthesized the benzyl bromide derivative **2** that reacts with enamine **2** to afford the CAAC-5$^+$ BF$_4^-$ salt **3** in moderate yield. Following deprotonation and ligand exchange with the Hoveyda–Grubbs first-generation catalyst (HG-I), the Boc protecting group is removed using gaseous HCl in DCM. The resulting secondary amine can then be functionalized with acyl chlorides to generate either Ru(CAAC-5_ArSO$_2$NH$_2$), which binds to human carbonic anhydrase II (hCA II), or Ru(CAAC-5_azide), which enables click-type coupling with alkynes (Figure 2).

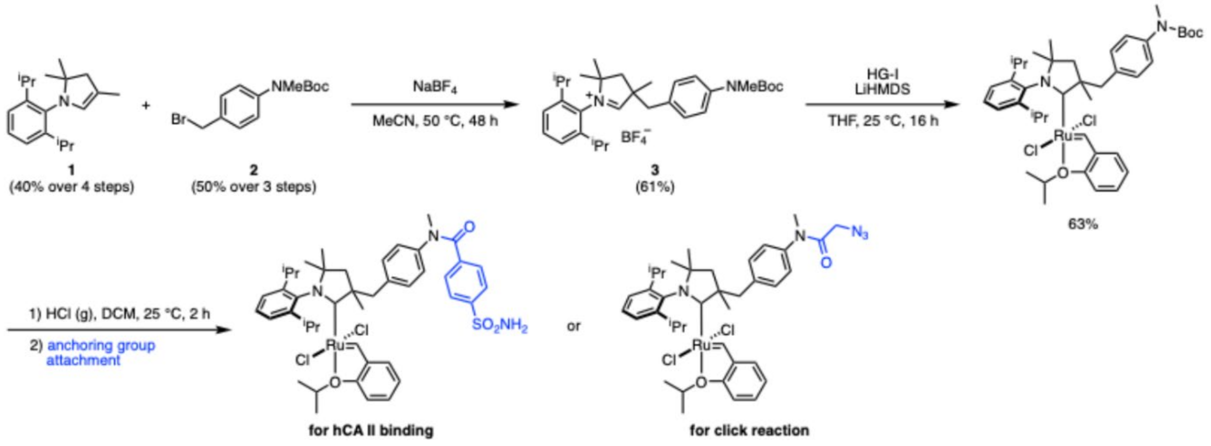

Fig. 2: Synthesis and functionalization of Ru(CAAC-5) with an aryl sulfonamide for hCA II binding and an azide for click reaction.

After the synthesis of the Ru(CAAC-5) cofactor, its catalytic performance was evaluated and compared with the previously developed Ru(NHC) system (Figure 3a). In the benchmark RCM of the tosyl diolefin to the cyclized product, the Ru(CAAC-5) cofactor exhibited a 10-fold increase in turnover number (TON) and retained catalytic activity at elevated pH, where the Ru(NHC) complex typically deactivates. These results confirm that the Ru(CAAC-5) complex is a robust candidate for *in cellulo* prodrug activation, providing a stable and bioorthogonal platform for further functionalization. Building on this, the cofactor was then modified to enable targeted delivery.

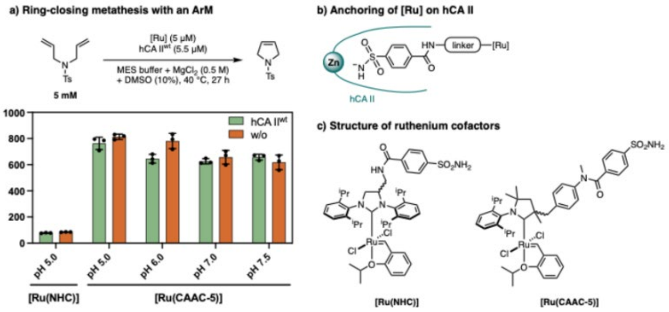

Fig. 3: a) Comparison of Ru(NHC) and Ru(CAAC-5) artificial metalloenzymes (ArM) using a benchmark reaction. b) The sulfonamide moiety of the ruthenium cofactor binds to the zinc inside the active site of hCA II. c) Structure of the two different ruthenium cofactors.

Functionalization was achieved by coupling the Ru(CAAC-5_azide) cofactor to the SSTR antagonist peptide SS01 via CuAAC click chemistry. Somatostatin receptors (SSTRs), particularly SSTR2, are overexpressed in neuroendocrine tumor (NET) cells, and both SSTR agonists and antagonists have been clinically validated for tumor imaging and targeting.[6] The SS01 peptide, with the sequence "H_2N-*p*-Cl-Phe-cyclo(*D*-Cys-Tyr-*D*-Trp-Lys-Thr-Cys)-*D*-Tyr-NH_2", was synthesized using automated solid-phase peptide synthesis (SPPS), with hexynoic acid installed at the *N*-terminus as a handle for conjugation to Ru(CAAC-5_azide). This modification preserves the peptide's receptor-binding properties while anchoring the catalytic cofactor to create a targeted system for prodrug activation in NET cells.

The peptide-functionalized Ru(CAAC-5) cofactor was then assessed for its ability to uncage the doxorubicin prodrug (proDox), which can be synthesized in four steps from readily available starting materials. Following RCM, the dihydronaphthalene intermediate is expected to undergo 1,4-elimination, generating aromatic naphthalene, releasing CO_2, and liberating doxorubicin (Fig. 1). However, only trace amounts of doxorubicin were detected under all tested conditions. This limitation is attributed to an initial [2+2]-cycloaddition between the terminal olefin of proDox and the Ru(CAAC-5) cofactor, which severely limits the productive RCM. Literature reports indicate that substituting the *ortho*-diisopropyl aniline with *ortho*-diethyl groups and introducing a nitro substituent on the benzylidene moiety significantly lowers the activation barrier of the reaction [7]. Guided by these insights, next-generation cofactors that incorporate both modifications are currently being synthesized to enhance metathesis efficiency and enable effective prodrug uncaging.

Conclusion

A new class of Ru(CAAC-5) complexes that can be functionalized with anchoring groups to bind either hCA II or alkyne-containing peptides has been developed. These cofactors exhibit enhanced stability under aqueous and basic conditions compared to conventional Ru(NHC) complexes. Current efforts are focused on improving the catalytic efficiency of Ru(CAAC-5) under physiological conditions. Once an optimized cofactor is obtained, the system will be evaluated *in cellulo*, and ultimately *in vivo* in tumor-bearing mouse models, leveraging somatostatin receptor targeting for selective delivery and proDox uncaging via ring-closing metathesis.

References

[1] I. Nasibullin, I. Smirnov, P. Ahmadi, K. Vong, A. Kurbangalieva, K. Tanaka, "Synthetic prodrug design enables biocatalytic activation in mice to elicit tumor growth suppression", Nat. Commun. ***13*** *(2022).*

[2] R. Hamaguchi, D. A. Graf, K. Kinbara, T. R. Ward, "Programmable Artificial-Cellular Membrane Dynamics via Ring-Closing Metathesis", J. Am. Chem. Soc. ***147****, 39204–39211 (2025).*

[3] C. O. Blanco, D. E. Fogg, "Water-Accelerated Decomposition of Olefin Metathesis Catalysts", ACS Catal. ***13****, 1097-1102 (2023).*

[4] V. Sabatino, J. G. Rebelein, T. R. Ward, ""Close-to-Release": Spontaneous Bioorthogonal Uncaging Resulting from Ring-Closing Metathesis", J. Am. Chem. Soc. ***141****, 17048–17052 (2019).*

[5] J. Chu, D. Munz, R. Jazzar, M. Melaimi, G. Bertrand, "Synthesis of Hemilabile Cyclic (Alkyl)(amino)carbenes (CAACs) and Applications in Organometallic Chemistry", J. Am. Chem. Soc. ***138****, 7884–7887 (2016).*

[6] R. Mansi, M. Fani, "Radiolabeled Peptides for Cancer Imaging and Therapy: From Bench-to-Bedside", Chimia ***75****, 500–504 (2021).*

[7] X. Ou, G. Occhipinti, E. Y. Boisvert, V. R. Jensen, D. E. Fogg, "Mesomeric Acceleration Counters Slow Initiation of Ruthenium–CAAC Catalysts for Olefin Metathesis", ACS Catal. ***13****, 5315–5325 (2023).*

Torque transducers for the study of nanoscale and low-dimensional vdW systems

Project P2107: High-sensitive torque magnetometry for 2D materials
Project leaders: I. Zardo and M. Poggio
Collaborator: M. Claus (SNI PhD Student)

Introduction

The investigation of magnetic and superconducting phenomena in nanoscale and low-dimensional systems is fundamentally limited by the extremely small magnetic moments involved. Conventional techniques such as SQUID magnetometry, neutron scattering, or X-ray-based probes lack the sensitivity required to study individual or magnetic few-layer van der Waals (vdW) systems. As a result, many predicted and experimentally observed phases in low-dimensional systems remain difficult to characterize quantitatively.

Over the last decades, nanomechanical torque magnetometry has emerged as a powerful alternative, offering exceptional sensitivity by transducing magnetic signals into mechanical motion. The dramatic reduction in size and mass of mechanical resonators, combined with advances in nanofabrication, has enabled the detection of minute magnetic torques and frequency shifts associated with magnetic anisotropy, phase transitions, and collective magnetic behavior [1].

The goal of this project was to develop ultra-sensitive nanomechanical torque sensors tailored for the study of two-dimensional (2D) materials and other nanoscale magnetic systems. In particular, the project aimed to combine advanced nanofabrication with phononic engineering to reduce mechanical dissipation, while enabling the integration of electrically contacted samples [2,3]. By extending dynamic torque magnetometry to new material classes and systems, this work sought to establish a versatile experimental platform capable of probing magnetic phase transitions, anisotropies, and magnetization dynamics at the nanoscale.

Main Results

During the first phase of the project, fabrication techniques were developed to realize silicon nitride torsional resonators embedded in phononic crystal structures. These devices were designed to suppress phonon radiation losses by placing the mechanical resonance within a band gap of the supporting structure, while maintaining compatibility with future electrical contacting schemes. Optical inspection and frequency-response measurements confirmed the presence of well-defined phononic band gaps and torsional resonances located within them.

Despite the successful realization of these structures with examples shown in Fig. 1, no substantial improvement in the mechanical quality factor was observed compared to devices without phononic crystal surrounds. This result indicated that mechanical dissipation was dominated by intrinsic loss mechanisms rather than clamping losses, providing an important constraint for future resonator designs.

In the second phase, this insight motivated a systematic study of alternative resonator geometries. Doubly clamped flexural beams integrated into phononic bandgap structures were fabricated and characterized. While these devices showed clear suppression of substrate-driven excitation—demonstrating effective phonon isolation—their quality factors again did not substantially exceed those of comparable devices without bandgap supports. These results established surface and material losses as the dominant limitation in the realized structures and highlighted the need for strategies beyond phononic engineering alone.

In parallel, significant progress was made toward preparation of vdW samples in the few- to monolayer limit. Exfoliation and encapsulation protocols were developed and we found that magnetic vdW crystals can be stamped directly onto suspended silicon nitride membranes. Focused ion beam milling or reactive-ion etching can then be used to define predetermined breaking points and the SiN platform can be used as a carrier to transfer a vdW sample to an already suspended SiN resonator. This approach may enable torque magnetometry measurements on individual ultrathin magnetic specimens and represented a key step toward studying intrinsic magnetic properties of 2D materials.

In the final phase of the project, our dynamic torque magnetometry platform was used for the study of a biological nanosystem. By performing dynamic cantilever magnetometry with an ultrasensitive SiN cantilever, magnetic hysteresis and field rotations were measured of a single *Magnetospirillum gryphiswaldense* bacterium. By combining these measurements with transmission electron microscopy, tomography, and micromagnetic simulations, key magnetic parameters of the magnetosome chain were extracted, including the remanent magnetic moment, the saturation moment, and the effective easy-axis anisotropy. These results quantitatively demonstrated how the collective anisotropy of the magnetosome chain stabilizes the bacterium's magnetic moment in Earth's magnetic field, providing direct physical insight into the mechanism of magnetotaxis at the single-cell level.

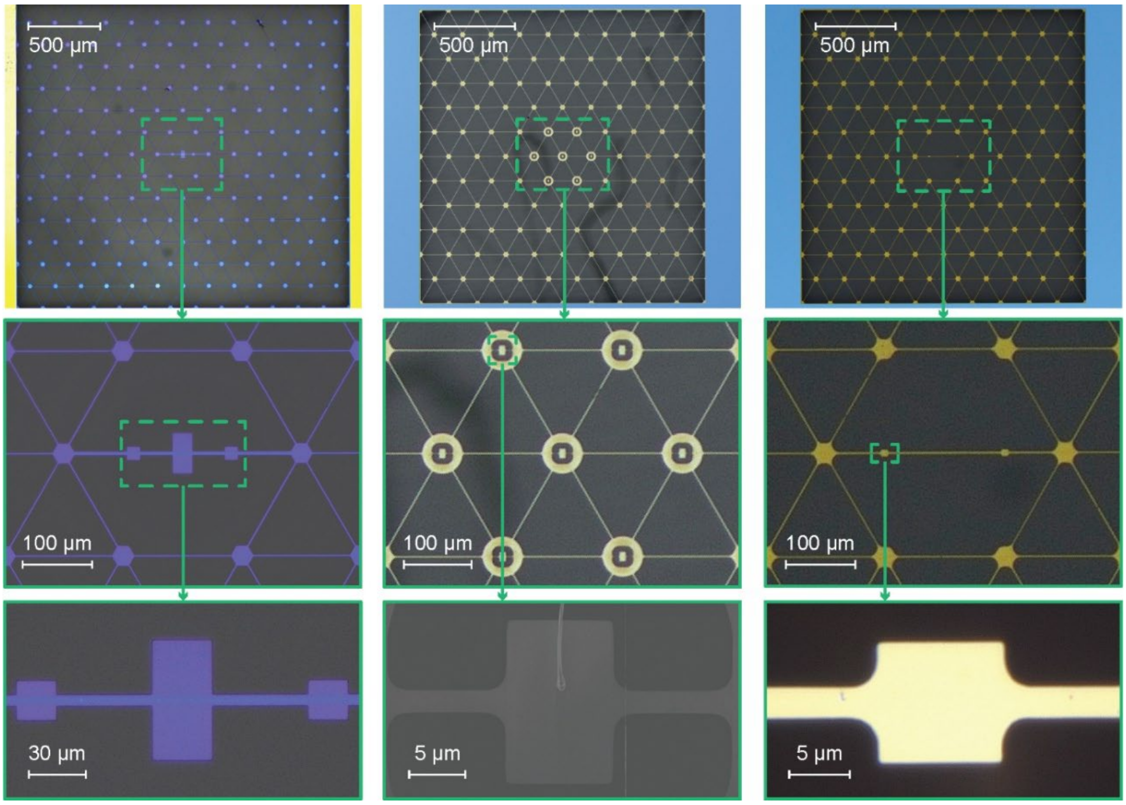

Fig. 1: Torque transducers with phononic crystal surrounds made from silicon nitride.

Conclusion

Over the course of this project, nanomechanical torque sensors with a phononic crystal surround based on amorphous silicon nitride were developed, fabricated, and characterized with the aim of advancing dynamic torque magnetometry toward the study of nanoscale and low-dimensional vdW systems. By systematically comparing plain torsional and flexural resonators with devices embedded in phononic crystal structures, this project provided a detailed assessment of the mechanical dissipation mechanisms that ultimately limit torque sensitivity under cryogenic, high-vacuum conditions.

Although phononic bandgap engineering successfully suppressed acoustic radiation into the substrate and enabled strong mechanical isolation, the measurements demonstrated that, for the investigated device geometries, the overall quality factor is not limited by clamping losses. Instead, intrinsic material dissipation and surface-related losses were identified as the dominant contributions. These findings place clear constraints on the effectiveness of phononic shielding alone and highlight the necessity of addressing internal loss channels in order to further improve sensitivity.

Beyond sensor development, the work established dynamic torque magnetometry as a quantitative and versatile probe for nanoscale magnetism. This was demonstrated most prominently through measurements on a single *Magnetospirillum gryphiswaldense* cell, where the magnetic moment, anisotropy, and switching behavior of an individual magnetosome chain were extracted by combining torque magnetometry with electron microscopy and micromagnetic modeling. This study validates the technique's capability to resolve magnetic properties in systems with extremely small magnetic volumes.

Looking forward, the results motivate future efforts that combine acoustic isolation with dissipation dilution, soft-clamping, and surface engineering strategies. Such approaches are expected to unlock substantially higher quality factors and improved torque sensitivity, paving the way toward quantitative dynamic torque magnetometry of ultrathin two-dimensional magnets and van der Waals heterostructures.

References

[1] F. R. Braakman and M. Poggio, Force sensing with nanowire cantilevers, Nanotechnology ***30****, 332001 (2019).*

[2] Y. Tsaturyan, A. Barg, E. S. Polzik, and A. Schliesser, Ultra-coherent nanomechanical resonators via soft-clamping and dissipation dilution, Nat. Nanotechnol. ***12****, 776 (2017).*

[3] Wollack, E. A. et al. Loss channels affecting lithium niobate phononic crystal resonators at cryogenic temperature, Appl. Phys. Lett. 118, 123501 (2021).

Optical and transport experiments in atomically thin semiconductor devices

Project P2201: Strongly correlated electronic phases in twisted and stretched bilayer semiconductor nanostructures
Project leaders: A. Baumgartner and P. Maletinsky
Collaborators: J. N. Sunil (SNI PhD Student)

Introduction

Atomically thin, optically active semiconducting transition metal dichalcogenides (TMDCs), for example MoS_2, can be used as ultimately thin transistors [1], but can also contain novel electronic phases due to strong electron-electron interactions [2,3]. The latter are expected to occur in artificially fabricated twisted bilayer devices, which we aim to investigate in this project. However, progress is often hindered by highly resistive contacts, and badly known material properties, like the electron effective mass, and by various issues in integrating these materials into more complex electronic devices with more than two contacts. In previous work, we improved the contacts with very clean interfaces [4] and by using semimetal contacts [5], and we already discussed in the previous report that also the contact geometry needs to be optimized [6]. The aim of the second year of this project was to establish good electrical contacts and to develop fabrication routes for twisted bilayer and multi-terminal devices.

Main Results

In this reporting period, we initially faced the problem that the device fabrication yield was reduced to zero, which we were able to trace back to MoS_2 crystals we bought from a new supplier at the start of the year. In spite of reproducibly very large exfoliated monolayer (ML) flakes (up to >60 μm diagonals), we obtained 0 out of 11 working devices. Reverting back to the previous crystals, we obtained again good results for all 4 since then tested devices.

In the process of finding the reason for the excessively low yield, we established Raman spectroscopy to assess the number of atomic layers of a given crystal flake. By comparing the spacing of the two emission lines shown in Fig. 1(a) or 1(b) to Ref. 7, one can reliably determine the layer number, consistent with the contrast in optical microscopy images, with examples shown as insets in Figs. 1(a) and 1(b), and with photoluminescence (PL) experiments (not shown). Surprisingly, the low-yield “new” crystal flakes do *not* exhibit significantly different spectra, except for a slight, but reproducible overall shift of the discussed Raman peaks. In addition, we established a method to optically measure the density of states and with it the effective mass of the carriers in the conduction band: in Fig. 1(c), we plot the change in the charge neutral exciton energy, ΔE_{X^0}, extracted from standard PL experiments, as a function of the backgate voltage V_{BG}. As long as the Fermi energy resides in the energy gap of the semiconductor, the emission energy is essentially constant, given by the energy gap and the exciton binding energy. In contrast, if the Fermi energy lies in the conduction band, the lower states are filled and not available for the exciton formation, resulting in a linear increase in the emission energy with the Fermi energy E_F of the 2D system, pointed out by the blue dashed line in Fig. 1(c). Since E_F is determined by the carrier density, known from electrostatics, and by the density of states, the latter can be extracted directly. For the corresponding electron effective mass we find $m^* \approx 0.6 m_e$ [6], slightly smaller than in recent transport experiments [8], and slightly larger than predicted [9].

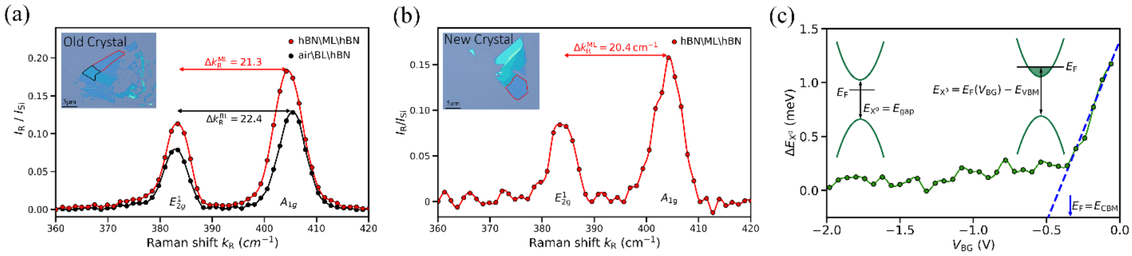

*Fig. 1: **Optics on MoS_2.** (a) and (b) Room temperature Raman spectra of mololayer (ML) MoS_2 recorded on flakes indicated in the optical microscopy images in the insets. The number of MoS_2 layers was achieved according to Ref. 7, here MLs and a bilayer (BL), which relates very well to the optical impression, as well as to PL experiments (not shown). (c) Change in the PL emission energy of the charge neutral exciton (X^0) plotted as a function of the backgate voltage V_{BG} (T=1.6K). The inset shows the bandstructure for two different Fermi energies E_F, namely in-gap (left) and in the conduction band (right), and the minimum exciton excitation energy, which requires a valance band electron to be excited to an empty conduction band state. For a 2D system like ML MoS_2, this allows one to directly extract the effective mass of the conduction band electrons (described in the text).*

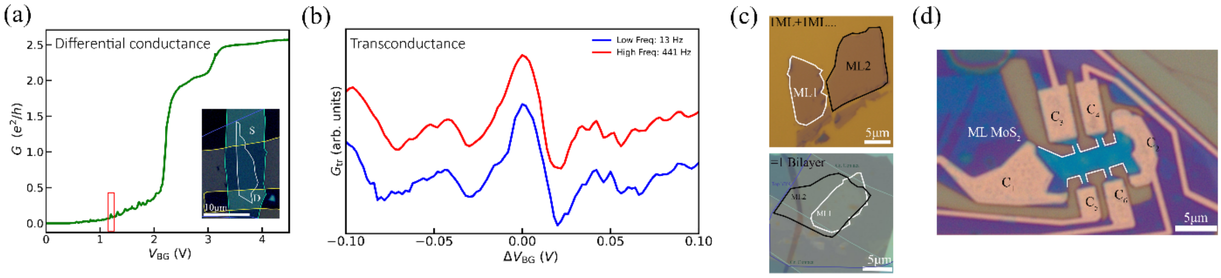

Fig. 2: ***Electrical transport and first steps towards next generation devices.*** *(a) Differential conductance G plotted as a function of the backgate voltage V_{BG} for the two-terminal device shown in the inset. (b) High-resolution transconductance, G_{tr} (described in the text), directly measured as a function of the gate voltage in the range pointed out by the red rectangle in (a). The blue and the red curves show G_{tr} measured using two different gate modulation frequencies, offset for clarity, showing no significant detoriation of the signal up to at least 400 Hz (temperature $T \approx 5$ K). (c) Optical microscopy images of two monolayer (ML) MoS$_2$ flakes before and after deterministically stacking them into an MoS$_2$ bilayer structure, with a twist angle of 3°. (c) First fully hBN-encapsulated 6-terminal Hall bar device on a ML MoS$_2$ flake in our group.*

Our progress towards electronic (and optical) devices with improved contacts and beyond monolayer and simple two-terminal devices is illustrated in Fig. 2. In Fig. 2(a), the differential conductance $G=dI_{SD}/dV_{SD}$ is plotted as a function of the backgate voltage V_{BG} (with I_{SD} and V_{SD} the measured current and applied bias voltage, respectively, between the source (S) and drain (D) contacts). To investigate the very faint conductance features highlighted by the red rectangle, it is advantageous to employ a high-resolution technique known as (differential) transconductance (G_{tr}) experiments [10], in which a constant bias voltage is applied between the source and drain contacts, while the backgate voltage is modulated by a small sinusoidal oscillation, resulting in a modulation of the conductance at the same frequency, $G_{tr}=V_{SD}^{-1} \cdot dI_{SD}/dV_{BG}$. This technique requires a fast enough charging of the 2D electron system through low enough contact resistances. As illustrated in Fig. 2(b), we do not find significant deviations between the transconductance curves of the faint features [red rectangle in Fig. 2(a)] at low-frequency (13 Hz) and higher-frequency modulations (400 Hz, the largest frequency we tested). In addition, we also started to develop more complex devices: figure 2(c) shows a first fully hBN (boron nitride) encapsulated twisted bilayer structure, for which one part of a MoS$_2$ ML flake cut in two parts was picked up, rotated by 3°, and used to pick up the remaining partial flake. In addition, Fig. 2(d) shows a first 6-terminal Hall bar device on another MoS$_2$ ML flake, also fully hBN encapsulated. No characterization experiments were done on these devices, yet.

Conclusions

In spite of severe problems with material qualities this year, we were able to advance the project in several directions. First, we established Raman spectroscopy to determine the number of layers of promising semiconductor flakes, making the fabrication process more reliable. We also analysed and modelled photoluminescence experiments, for example establishing a new method to extract the electron effective mass in the conduction band, one of the most crucial parameters in device physics. In other experiments, we were able to perform so-called transconductance experiments, which show that our contact quality is now good enough to modulate the carrier density fast enough to perform high-resolution transport, optical, or NV-center-based experiments using lock-in techniques. In addition, we started the development of bilayer and multi-terminal MoS$_2$ electronic devices, which, together with multi-gate designs [11,12] expand the scope of this material platforms tremendously.

References

[1] B. Radisavljevic and A. Kis, "Mobility engineering and a metal–insulator transition in monolayer MoS2", Nature Materials 12, 815 (2013).

[2] J. Roch et al., "Spin-polarized electrons in monolayer MoS$_2$", Nature Nanotechnology 14, 432 (2019).

[3] N. Leisgang et al., "Exchange energy of the ferromagnetic electronic ground state in a monolayer semiconductor", Phys. Rev. Lett. 133, 026501 (2024).

[4] M. Ramezani et al., "Superconducting contacts to a monolayer semiconductor", Nano Lett. 21, 5614 (2021).

[5] P.-C. Shen et al., "Ultralow contact resistance between semimetal and monolayer semiconductors", Nature 593, 211 (2021).

[6] J.N. Sunil et al., working title "Screened region as the origin of reduced contact resistance in monolayer semiconductor devices", in preparation (2026).

[7] D.H. Lee et al., "hBN encapsulation effects on the phonon modes of MoS$_2$ with a thickness of 1 to 10 layers", Advanced Materials Interfaces 10, 2300002 (2023)

[8] R. Pisoni et al., "Interactions and magnetotransport through spin-valley coupled Landau levels in monolayer MoS$_2$" Phys. Rev. Lett. 121, 247701 (2018).

[9] A. Kormányos, V. Zólyomi, N.D. Drummond and G. Burkard, "Spin-orbit coupling, quantum dots, and qubits in monolayer transition metal dichalcogenides", Phys. Rev. X 4, 011034 (2014).

[10] Bordoloi et al., " Spin cross-correlation experiments in an electron entangler ", Nature 612, 454 (2022).

[11] I. Corea-Sampaio et al., working title "Quantization values in monolayer semiconductor quantum point contacts", in preparation (2026).

[12] M. Niese et al., " Time-resolved charge detection in transition metal dichalcogenide quantum dots", arXiv:2512.15842 (2026).

Unraveling room temperature ferromagnetism and magnetic orders coexistence in Cr_3Te_4

Project P2202: Search for 2D ferromagnetism at room temperature
Project leaders: M. Ciomaga Hatnean and M. Kenzelmann
Collaborator: E. D. Bervas-Soloview (SNI PhD Student)

Introduction

Spintronics exploits the spin polarization and magnetic properties of electrons, in addition to their charge, to achieve faster, more energy-efficient devices, paving thus the way for breakthroughs in computing, data storage, and quantum information technologies. Nevertheless, several challenges remain to be solved before integrating quantum spin phenomena into practical applications.

One of the key issues is related to the availability of ferromagnetic (FM) materials with a high Curie temperature (T_C) and good air stability, that could be used in ambient conditions in devices. Additionally, this FM material should retain these qualities when scaled down towards the 2D limit for practical applications. The discovery of a material meeting all these criteria is far from straightforward. Recently, 2D ferromagnets have been discovered in van der Waals (vdW) materials (e.g. CrI_3, $Cr_2Ge_2Te_6$), however, the low temperatures at which the ferromagnetic orders exist limit their potential for applications [1].

In the last years, the $Cr_{1+x}Te_2$ system has attracted considerable attention as a promising candidate for spintronic applications, primarily due to its tunable magnetic transition temperature. The T_C of this family of materials varies with the increasing Cr content ($x \rightarrow 1$), up to a maximum of 360 K [2]. Moreover, owing to the interplay of magnetic interactions in this system, the $Cr_{1+x}Te_2$ family is of particular interest from a fundamental perspective. The parent vdW material $CrTe_2$ exhibits a FM Cr-Te-Cr superexchange and a direct antiferromagnetic (AFM) Cr-Cr exchange; the AFM component induces spin frustration in the triangular lattice [3]. The increase of the Cr content, x, additional Cr is intercalated between the vdW layers (see figure 1), leading to the emergence of an extra FM double exchange interaction between the layers, which is considered to be the dominant FM pathway. Furthermore, the reduced magnetic moments observed relative to the theoretical expectations suggest the presence of a canted spin structure of unknown origin, superimposed on these three magnetic interactions. The origins and implications of the coexistence of these interactions remain poorly explored and insufficiently understood.

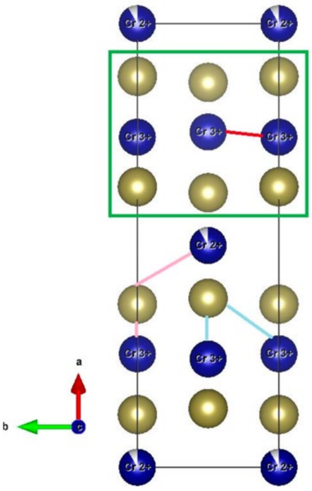

Fig. 1: Crystallographic structure of Cr_3Te_4 in comparison to its parent compound $CrTe_2$ (highlighted in green). The Cr-Cr direct exchange is shown in red, the Cr-Te-Cr superexchange in blue, and the Cr-Te-Cr double exchange in pink colour. Adapted from [4].

Main Results

Through a fundamental investigation of members of the $Cr_{1+x}Te_2$ system, this work aims to shed light on the interplay between the different magnetic interactions existing in these materials and clarify how these phenomena evolve when transitioning from bulk to the 2D regime.

A first member of the family, Cr_3Te_4 (i = 0.5), was synthesized in powder form, by the solid-state synthesis method, in a sealed quartz ampoule. Chemical composition analysis was performed using powder X-ray diffraction, and despite the existence of a small amount of Cr_2O_3 impurity (reported previously in the literature and unavoidable), the majority of the sample (~ 95%) belongs to the desired Cr_3Te_4 phase. The magnetic properties of the sample were measured using a Magnetic Properties Measurement System (MPMS) and the data show a paramagnetic (PM) to FM transition around 320 K and an AFM transition around 80 K (see figure 2).

Neutron diffraction data was collected on the DMC instrument at the Paul Scherrer Institute (PSI). The measurements involved continuous data acquisition during a temperature ramp to capture the variation of magnetic order parameters and magnetic moment with the temperature. Additionally, complementary long duration measurements were carried out at specific temperatures corresponding to distinct magnetic phase. In a first instance, data were collected in the temperature range 250 K - 350 K using a cryo-furnace. A second data set was acquired in the temperature range 2 K-110 K using a cryostat.

The long duration pattern collected at 350 K was refined, using the FullProf software suite, and confirmed the presence of nuclear Bragg peaks belonging to both the main phase, Cr_3Te_4, as well as the Cr_2O_3 impurity. Below 320 K, additional signal is observed due to the onset of magnetic orders of the two phases. Moreover, below 80 K, new strong peaks belonging to the AFM phase of Cr_3Te_4 appear in the collected patterns. Figure 2 highlights the distinct characteristics of the patterns obtained in the PM, FM and AFM phases. The superposition of the nuclear Bragg peaks corresponding to the Cr_3Te_4 and Cr_2O_3 phases, as well as the magnetic signal of the two compounds complicate the analysis of the data. Additional measurements were performed on the HRPT instrument at PSI in the second half of December, which will allow us to determine the crystallographic structure of the two phases, as well as their precise contribution to the pattern. The analysis of the data is ongoing.

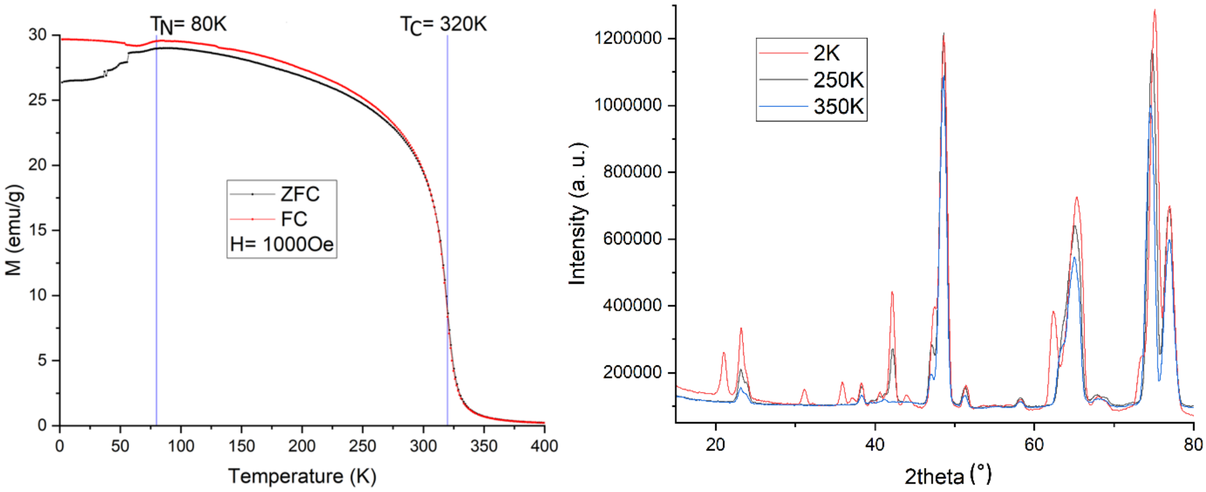

Fig. 2: (left panel) Evolution of the magnetization as a function of temperature for the Cr_3Te_4 polycrystalline sample. The FM transition temperature is 320 K, while the AFM transition temperature is 80 K. (right panel) Powder neutron diffraction patterns collected at 2 K, 250 K and 350 K on the Cr_3Te_4 polycrystalline sample, revealing Bragg reflections corresponding to three distinct magnetic regimes: PM, FM and AFM..

Conclusion

Complete, precise refinements of the neutron diffraction data will allow us to determine the magnitude and orientations of the Cr moments, and how these change with the temperature in the Cr_3Te_4 system. Additionally, the shape of the evolution of magnetic integrated intensities as a function of temperature can be used to infer the nature of magnetic interactions at play, the magnetic intensity being proportional to the square of the magnetic moment.

The next step is to prepare single crystal of Cr_3Te_4 by the chemical vapour transport method to study them using neutron diffraction and spectroscopy. Furthermore, mechanical exfoliation of these crystal samples will be attempted to prepare atomically thin layers. If mechanical or chemical exfoliation would prove unsuccessful due to the interlayer bonds through the intercalated Cr ions, thin films can be prepared via magnetron sputtering. This will allow us to understand the magnetic properties of this material towards the 2D limit.

References

[1] Zhang, et al., "Tunable Curie temperature in layered ferromagnetic $Cr_{5+x}Te_8$ single crystals", APL Materials ***8****, 031101 (2020)*

[2] Shimada, et al., "Photoemission study of itinerant ferromagnet $Cr_{1-\delta}Te$", Physical Review B ***53****, 7673 (1996)*

[3] Lukoschus, et al., "Magnetic properties and low temperature X-ray studies of the weal ferromagnetic monoclinic and trigonal chromium tellurides Cr_5Te_8", Journal of Solid State Chemistry ***177****, 951 (2004)*

[4] Goswami, et al., "Critical behavior in monoclinic Cr_3Te_4", Physical Review B ***109****, 054413 (2024)*

Towards Controlling the Surface Chemistry of Cobalt Phosphide Nanocatalysts

Project P2203: Towards Earth-Abundant Nanocatalysts for Hydrogenation Reactions: Understanding the Promoting Role of Sulfur in Cobalt Phosphide Nanocatalysts

Project leaders: M. F. Delley and M. Nachtegaal
Collaborator: C. Yuan (SNI PhD Student)

Introduction

For the development of sustainable chemical industrial processes earth-abundant catalysts are needed. Transition metal phosphide nanomaterials have shown promising catalytic activity for some chemical transformations, especially for water splitting and hydrogenation reactions [1],[2]. These materials may hence replace noble metal-based catalysts in these applications if their catalytic properties can be further improved. Prior work suggests that the catalytic activity of transition metal phosphides can be enhanced when a small amount of sulfur is incorporated in the catalyst (e.g. by doping) [3],[4],[5]. However, implementation of this approach is limited by a lack of understanding of the structure-reactivity relationships responsible for the observed catalytic effects. Obtaining a better understanding is made difficult by the complexity of the surface chemistry of metal phosphide nanomaterials where active sites may be influenced by the sulfur content as well as any other interfacial component, for instance, the organic ligands typically used to ensure colloidal stability. We aim to develop a controlled sulfur modification strategy for transition metal phosphide nanoparticles and will use X-ray based spectroscopic analysis under catalytic conditions to obtain insight into the surface structure – performance relationships of sulfur-based cobalt phosphide catalysts for the rational design of next generation earth abundant catalysts.

Main Results

By adapting a previously reported method [6], we synthesized cobalt phosphide (CoP) nanoparticles using cobalt chloride as Co-precursor, triphenyl phosphite as P-precursor, hexadecylamine (HDA) as ligand, and hexadecane as solvent. We adapted our previously reported method [7] and mixed sulfur-transfer reagents and the CoP particles in *d*-benzene and monitored the reaction at 80 °C by Nuclear Magnetic Resonance (NMR) spectroscopy. After the reaction, the particles were separated, washed and dried. Analysis of the reaction mixture by NMR and of the S-doped CoP particles by X-ray photoelectron spectroscopy (XPS) suggested the successful doping of the CoP particles at the surface with sulfur. The size of the nanoparticles remained 4±1 nm before and after sulfur modification.

A significant decrease of density of organic ligands at the surface of the S-doped CoP nanoparticles was observed compared to what was obtained before S-modification. This was shown by characterization of as-prepared and S-modified CoP nanoparticles by High Resolution Mass Spectrometry (HRMS), Thermogravimetric Analysis (TGA), XPS, and by NMR analysis of the modification reaction. However, while the loss of ligands was reproducible, the extent of this ligand loss was not, which led to variable ligand density from batch to batch for S-doped CoP nanoparticles in the range of 0.05 to 0.48 ligands per surface Co (Fig. 1a). This could be connected to the presence of strongly and weakly-bound ligands as suggested by our Diffusion-Ordered Spectroscopy NMR (DOSY-NMR) results (Fig. 1b). Organic ligands are known to influence hydrogenation catalysis [8],[9]. The batch-to-batch variation in ligand density hence made it challenging to understand the catalytic effect of sulfur on CoP nanoparticles.

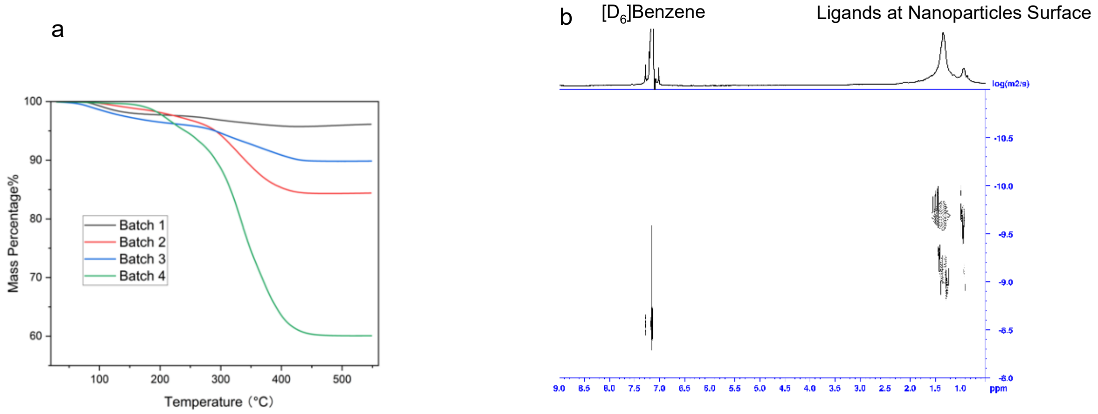

Fig. 1: a). TGA results showing a variable mass loss from the CoP nanoparticle surface from batch to batch associated with a variable density of organic ligands. b). DOSY-NMR pattern of CoP nanoparticles in de where two diffusion coefficients are measured, likely associated with strongly- and weakly-bound ligands.

To address this challenge, we tried different methods to improve the reproducibility of the surface chemistry of CoP nanoparticles from batch to batch. For instance, we tried to obtain more reproducible ligand densities between different batches by adapting our purification method of the as-synthesized CoP nanoparticles and included toluene/acetonitrile as solvent/anti-solvent in the purification cycles. However, even with the improved purification method, the uncertainty of the ligand density between different batches was 50% of the average amount based on NMR and TGA analysis. We also tried to remove all ligands from the surface using different reagents, but this was also not successful so far. As an alternative strategy, we are also pursuing the use of one single batch of CoP nanoparticles that could be used for a directly comparable data set of particles with identical ligand density and different amounts of sulfur. For this, we upscaled the synthesis by a factor of three in order to have enough material to do multiple different transformations and catalytic reactions within one single batch. The upscaled synthesis yielded particles of sizes of 4±1nm based on TEM characterization with a cobalt to phosphorus ratio of roughly 1:2 based on EDX and XPS results. Sulfur transfer led to incorporation of sulfur as shown by NMR and XPS with a sulfur to cobalt ratio of ca. 0.06:1.

Conclusion and Outlook

Our research highlighted the complexity of deriving clear structure-reactivity relationships for transition metal phosphide nanoparticles due to the presence of both inorganic dopants and organic ligands with densities that are difficult to control experimentally. We have been pursuing different strategies to improve the reproducibility of the cobalt phosphide surface chemistry. Currently, we are testing the utility of different approaches to obtain a data set that would allow clear insight into the effect of sulfur on catalysis. With reproducible batches of sulfur-doped CoP nanoparticles in hand, we hope to finally bring this chemistry to SLS 2.0 .

References

[1] *T. Shi, B. Zhang, "Recent advances in transition metal phosphide nanomaterials: synthesis and applications in hydrogen evolution reaction", Chem. Soc. Rev.,* ***45****, 1529-1541 (2016).*

[2] *S. Oyama, T. Gott, H. Zhao, Y. Lee, "Transition metal phosphide hydroprocessing catalysts: A review", Catal. Today,* ***143****, 94– 107, (2009).*

[3] *W. Chen, Y. Che, J. Xia, L. Zheng, H. Lv, et al., "Metal-Sulfur Interfaces as the Primary Active Sites for Catalytic Hydrogenations", J. Am. Chem. Soc.* ***146,*** *11542-11552, (2024).*

[4] *J. Kibsgaard, T. Jaramillo, "Molybdenum Phosphosulfide: An Active, Acid-Stable, Earth-Abudant Catalyst for the Hydrogen Evolution Reaction", Angew. Chem. Int. Ed.* ***53****, 14433-14437, (2014).*

[5] *X. Duan, Y. Teng, A. Wang, V. Kogan, X. Li, Y. Wang, "Role of sulfur in hydrotreating catalysis over nickel phosphide" J. Catal.* ***261****, 232– 240, (2009).*

[6] *J. Liu, M. Meyns, T. Zhang, J. Arbiol, A. Cabot, A. Shavel, "Triphenyl Phosphite as the Phosphorus Source for the Scalable and Cost-Effective Production of Transition Metal Phosphides", Chem. Mater.* ***30****, 1799-1807, (2018)*

[7] *N. Arnosti, V. Wyss, M. Delley, "Controlled Surface Modification of Cobalt Phosphide with Sulfur Tunes Hydrogenation Catalysis", J. Am. Chem. Soc.* ***145,*** *23556-23567, (2023).*

[8] *C. Schroder, M. Schmidt, P. Haugg, A. Baumann, J. Smyczek, et al., "Understanding Ligand-Directed Heterogeneous Catalysis: When the Dynamically Changing Nature of the Ligand Layer Controls the Hydrogenation Selectivity", Angew. Chem. Int. Ed.* ***60****, 16349-16354, (2021).*

[9] *S. G. Kwon, G. Krylova, A. Sumer, M. Schwartz, E. Bunel, et al., "Capping ligands as selectivity switchers in hydrogenation reactions", Nano Lett.* ***12****, 5382-5388, (2012).*

In situ cryo-ET reveals tunable phases of Rubisco condensates

Project P2204: NanoPhase
Project Leaders: B. Engel and M. Hondele
Colaborator: P. Van der Stappen (SNI PhD Student)

Pyrenoids: the ubiquitous CCM organelle in algae

Rubisco is central to photosynthesis, catalyzing the carboxylation reaction within the Calvin cycle. However, this reaction is intrinsically rate-limiting. Rubisco evolved in an atmosphere rich in CO_2 and essentially devoid of O_2; as a result, modern Rubisco shows poor discrimination between the two gasses [1]. This results in frequent oxygenation reactions that waste energy and generate toxic intermediates [2]. To sustain efficient carbon fixation, photosynthetic organisms therefore rely on a CCM that locally elevates CO_2 levels in the vicinity of Rubisco. This requirement is even more acute in aquatic environments where CO_2 is poorly soluble.

Despite the importance of photosynthetic marine systems, the underlying molecular basis of CCMs is poorly understood [3]. Pyrenoids across algal lineages differ strikingly in morphology (see Fig. 1). The repeated, independent emergence of pyrenoids suggests that evolution has converged on similar functional requirements while allowing architectural flexibility.

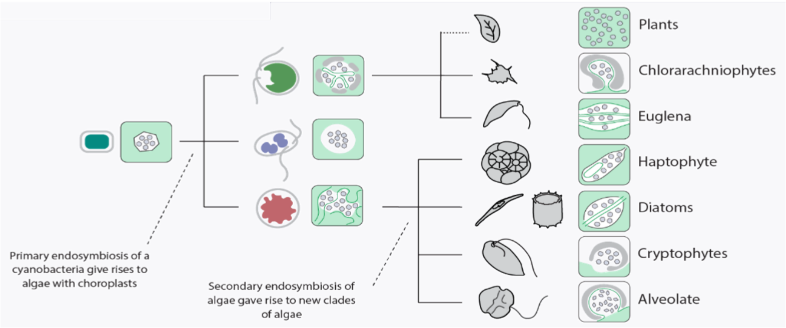

Fig. 1: The convergent and complex evolution of pyrenoids and their respective plastids were subject to multiple endosymbiotic events and deep branching of various lineages.

All eukaryotic chloroplasts originated from a primary endosymbiotic event in which a cyanobacterium was stably integrated into a heterotrophic host. This event gave rise to three lineages with primary plastids: chlorophytes (green algae), glaucophytes (blue algae), and rhodophytes (red algae). Subsequent rounds of secondary and tertiary endosymbiotic events increased the algal tree and pyrenoid diversity. Electron microscopy has revealed the vast morphological diversity of the core components, such as a Rubisco matrix (condensate), specialized thylakoid membranes which can traverse the matrix, and “barriers” surrounding the matrix such as starch or proteinaceous shells. A deep mechanistic understanding has so far only been developed in *Chlamydomonas reinhardtii* (Chlamy), a model organism from the green algal lineage.

Chlamy and the pyrenoid

In 2016, an intrinsically disordered protein was discovered in Chlamy pyrenoid [4]. This protein interacts with Rubisco and is essential for phase separation and pyrenoid formation. It is named EPYC1 (Essential Pyrenoid Component 1) and it is a ~30 kDa repeat protein containing five Rubisco binding motifs. These motifs are the so-called “stickers”, which are separated by repeat sequences called “spacers” (see Fig. 2). However, EPYC1 presents no sequence homology in other algae, which complicates the discovery of other Rubisco linker proteins. In the last decade, only three other potential Rubisco linkers have been identified and characterized. It seems that only functional analogy exists between those linkers (such as multivalency, disorder, high hydrophilicity, and sequence repeats), suggesting that Rubisco linkers seem to follow certain sticker and spacer configurations and low structural complexity [5, 6]. Naturally, the question arises what the role of this configuration is and how applying engineering approaches to linker proteins affect Rubisco condensation, pyrenoid morphology, and physiology. Little is known about how tuning the valency of a single component in a heterotypic condensate impacts mesoscale organization and function. In particular, it remains unclear how variation in sticker number alters packing density and material properties in a defined condensate, and how such physical changes feed through to enzymatic performance, cellular fitness, and survival.

Critical concentration, partitioning, and packing is affected by linker valency

We were able to show in vitro that increasing the valency of the sticker lowers the critical concentration needed to phase separate Rubisco (1 µM). Moreover, the minimum required sticker number for droplet formation was 3 whereas the WT sequence has 5. This was verified through fluorescence microscopy of reconstituted condensates as well as sedimentation assays. In Chlamy cells expressing different linker variants, this minimal sticker number for Rubisco condensation changed to 4. The 4x EPYC1 cell line showed a wide range of Rubisco partitioning coefficients, indicating a transition of proper pyrenoid formation from 3x to 5x. In situ cryo-electron tomography (cryo-ET) together with template matching revealed a gradual increase in Rubisco density for higher valency linkers (e.g., 9x). A possible explanation for this is the increase in Rubisco crosslinking of higher valency linkers. We did not observe increased partitioning in light microscopy probably because the differences lie within the measurement error from the intrinsic diffraction resolution limit. For more information, see our recent preprint: https://doi.org/10.64898/2026.01.27.701992.

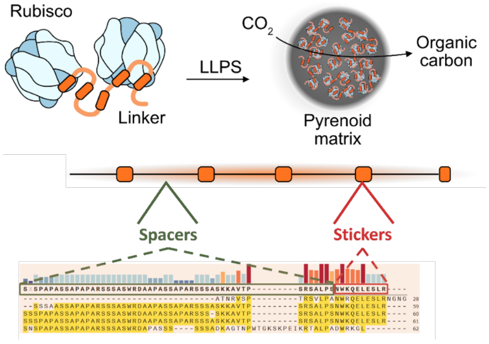

Fig. 2: Rubisco phase separation through linker proteins with EPYC1 stickers and spacers. The sequence is aligned to its repeating units vertically, corresponding to the horizontal cartoon depiction.

Turning the pyrenoid crystalline?

Through serendipitous circumstances, one of the many Chlamy strains we generated by chloroplast transformation was showing a peculiar phenotype. In these cells, the small subunit of Rubisco as well was EPYC1 were knocked out and complemented with *Chlorella sorokiniana* Rubisco small subunit (CsRbcS) and the 9x sticker variant of the CsLinker tagged with the fluorescent protein mVenus. When screening this strain in the fluorescence microscope, we noticed an unusual rod-like pyrenoid shape which initially was thought to be an artifact. Upon closer inspection, it was noted that this elongated pyrenoid can span over multiple cells. Some of the cells seem to show an impaired cytokinesis (stuck together), but their growth in mixotrophic (TAP) conditions was similar to WT.

Naturally, cryo-ET of this cell line was performed to see what is causing this phenotype. We observed long filaments of Rubisco tightly packed, arranged in a hexagonal lattice (see Fig. 3). Rarely, this lattice was interrupted by pyrenoid tubes and the apparent matrix in close vicinity showed a more random-like distribution similar to WT cells.

This is the first time Rubisco has been engineered to different phases. The ability to tune the condensate phases provides a foundation for the rational design of natural and synthetic pyrenoids.

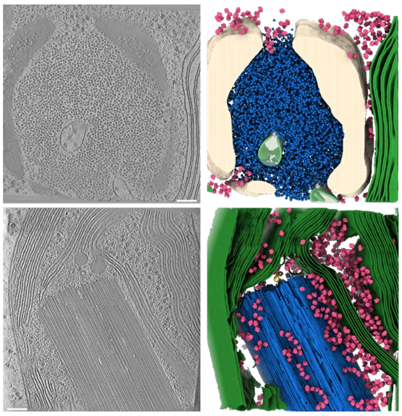

Fig. 3: Cryo-ET of a pyrenoid in wild-type cells (top row) and a Rubisco crystal in Cr–ΔRbcSΔEPYC1::CsRbcS::Cs9x-mVenus mutant cells (bottom row). Images show slices through cryo-ET volumes (left) and corresponding segmentations (right) of Rubisco (blue), tubules (green), starch (light brown) and ribosomes (pink).

References

[1] Prywes, Noam, et al. "A map of the rubisco biochemical landscape." Nature 638.8051 (2025): 823-828.

[2] Schulz, Luca, et al. "Evolution of increased complexity and specificity at the dawn of form I Rubiscos." Science 378.6616 (2022): 155-160.

[3] He, Shan, Victoria L. Crans, and Martin C. Jonikas. "The pyrenoid: the eukaryotic CO2-concentrating organelle." The Plant Cell 35.9 (2023): 3236-3259.

[4] Mackinder, Luke CM, et al. "A repeat protein links Rubisco to form the eukaryotic carbon-concentrating organelle." Proceedings of the National Academy of Sciences 113.21 (2016).

[5] Oh, Zhen Guo, et al. "A linker protein from a red-type pyrenoid phase separates with Rubisco via oligomerizing sticker motifs." Proceedings of the National Academy of Sciences 120.25 (2023): e2304833120.

[6] Barrett, James, et al. "A promiscuous mechanism to phase separate eukaryotic carbon fixation in the green lineage." Nature Plants 10.11 (2024): 1801-1813.

Developments in metal assisted chemical etching

Project P2205: MAGNET MacEtch based nAnofabrication of hiGh aspect ratio silicon Nanowires with magnEtic Tips

Project Leaders: M. Stampanoni, M. Poggio and L. Romano
Collaborator: B. Benz (SNI PhD Student)

Introduction

Metal assisted chemical etching (MacEtch) [1] can be used to create Si nanostructures with ultra-high aspect ratio [2]. Its applications cover a broad spectrum, including solar cells, batteries, X-ray optics [2], bio-surfaces, and sensors [1]. Our work focuses on X-ray gratings and nanowires for magnetic force measurements (MFM). Both applications stand to benefit greatly from very high-aspect-ratio structures with sections at the nanometer scale. Here, we present our recent development in the systematic fabrication of such nanostructures using a small lab tool and the preliminary observations in a new advanced tool, as part of a research collaboration of our team at PSI with the company memsstar Ltd. in UK and Fraunhofer Enas Institute in Germany.

MacEtch is a plasma-free, anisotropic chemical etching method that uniquely defies the isotropic nature of conventional wet etching through local catalyzed electrochemistry. An oxidant is reduced at the catalyst surface, and the silicon substrate underneath the catalyst layer is oxidized and subsequently removed by an etchant, usually HF. Inspired by vapor phase HF etching of SiO2 releasing structures for micro electromechanical systems, vapor-MacEtch delivers the etchant to the substrate surface in the vapor phase instead of the liquid phase.[2] Oxygen from the air is used as an oxidant with platinum as a catalyst for the oxygen reduction reaction. Since it is a “dry” process, it can be used for stiction sensitive applications without the need for supercritical drying steps. This is particularly relevant for nanowires and nanochannels, where stiction and capillary forces can lead to defects and deformations. Currently, we create such structures in our lab with a simple setup. The sample was placed in air and suspended on a hotplate above a beaker containing aqueous HF. In such a system, the oxygen is provided by the air and the HF in is supplied in vapor phase by evaporation of the liquid HF.[2] A massive downside of such a system is that the exact concentration of reactants cannot be determined. The continuous evaporation of HF also continuously changes the etching conditions. These effects make the investigation of the process challenging, with relevant limitations in the size of the chip that can be processed with uniform etching depth, reproducibility and process parameters range. The technical limitations motivated to explore the processing in an advanced tool with gas flow control.

Main Results

Magnetic force measurements greatly benefit from a reduction in the size of their cantilevers [3]. For an ideal cantilever, the minimum force sensitivity increases by increasing the length and decreasing the width of the cantilever. Additionally, the cantilever possesses a quality factor that quantifies how quickly it loses energy during oscillation. Having a high-quality factor, and hence, low loss, also improves the sensitivity and should therefore be maximized. The main components determining the quality factor are the surface effects and clamping. MacEtch is a promising candidate for solving both challenges. The smooth sidewalls that can be achieved with this method minimize the surface defects and hence lead to high-quality factors. Compared with a plasma-based approach, where scallops are inherent in the process, this is a major benefit. The clamping is solved itself, since the wire will be naturally connected to the substrate, due to the top-down nature of the etching. Both effects lead to high measured quality factors at room temperature of approximately 14000. An additional advantage of the top-down fabrication approach is the precise control of the wire location and shape. Figure 1 shows an array of nanowires fabricated in this manner. All the wires are spaced out by 20 µm, which allows them to freely oscillate without collision. A set-up like this allows for the measurement of multiple wires and hence improved statistics, as well as the opportunity to measure multiple wires at once for faster scanning of probes.

The wires presented here are suitable for force measurements but still require a magnet to become sensitive to the magnetic field. Placing a magnet on the tip is the next step of fabrication and is programmed for next year. Owing to the small diameter, the direct placement will come with significant challenges. A promising solution is focused electron beam induced deposition, as has been done previously.[4] The smaller diameter and hence stronger thermal motion will likely make the deposition more challenging.

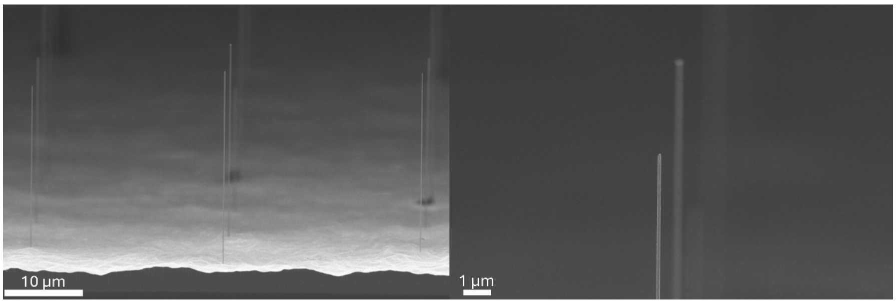

Fig. 1: Cross-sectional SEM image of the etched nanowires array and a zoom in on the top. The wires had a diameter of 120 nm and height of 25 µm, resulting in an aspect ratio of approximately 200:1.

X-ray optics is another field that stands to gain significantly from improvements in grating manufacturing. We concentrated our work to realize gratings with circular geometry suitable as optics for X-ray tensor tomography at TOMCAT beamline of PSI. The new gratings have been processed using our patterning method followed by MacEtch in HF and O_2 and are going to be tested at synchrotron facilities next year [5]. Grating defects and limitations are cited as one of the main inhibitors.[6] MacEtch can help by realizing gratings with smaller pitch and larger aspect ratio. A major limitation of this research is the consistency of the etching process and the lack of uniformity over large area. So far, our work has been conducted in an IDONUS system. It consists of a minimal setup that allows HF to flow in and then evaporate, and air to enter and supply oxygen. The system has no way of monitoring the exact concentration of the reactants and no control over oxygen concentration. This lack of control limits the available etching regimes, long-term control, and most importantly, repeatability. To overcome these limitations, a new tool has been recently prototyped by the company memsstar Ltd. and installed at Fraunhofer Enas Institute. Together with the corresponding teams, we are currently exploring the processing capabilities for MacEtch using Pt as catalyst. The preliminary results are very promising, showing high levels of uniformity and large-area capabilities. Figure 2 shows the first etched grating on a full 4-inch silicon wafer. The etching depth is around 2.5 µm with a good uniformity over the entre grating area, the aspect ratio is approximately 1:1. We are focusing now on a systematic study of the process parameters, such as etchant composition, gas flows and temperature.

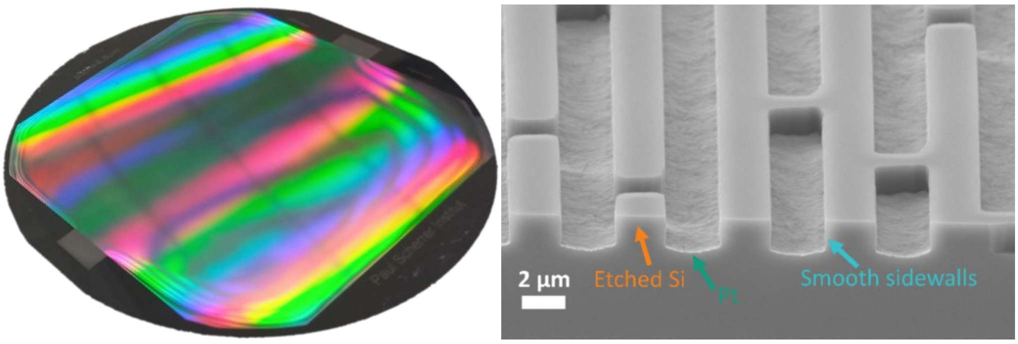

Fig. 2: Full 4 inch wafer with a 4.8 um pitch grating etched in MacEtch with memsstar tool (credits from B. Benz et al. First results on vacuum-gas-controlled metal assisted chemical etching., poster at MNE 2025 conference in Southhampton, UK). Cross sectional SEM image of the grating. The results demonstrate the large-scale capabilities that can be achieved with the new tool.

Conclusion

The last year has seen significant improvements in MacEtch technology. We have further reinforced the capabilities of etching targeted nanostructures to achieve high aspect ratio. Aspect ratio of over 200:1 is now reliably achieved with patterned nanowires. A series of selected chips with wires array is going to be tested in MFM. In parallel, we are exploring the processing possibilities of a new dedicated etching tool, which will enable additional process control and uniformity over larger area.

References

[1] R.P. Srivastava and D.-Y.Khang, "Structuring of Si into Multiple Scales by Metal-Assisted Chemical Etching", Adv. Mater. ***33****, 2005932 (2021).*

[2] L. Romano, M. Kagias, J .Vila-Comamala, K.Jefimovs, L. Tseng et al., "Metal assisted chemical etching of silicon in the gas phase: a nanofabrication platform for X-ray optics", Nanoscale Horiz. ***5****, 869 (2020).*

[3] F. R. Braakman and M. Poggio., "Force sensing with magnetic cantilevers", Nanotechnology ***30****, 332001 (2019).*

[4] H. Mattiat, L.Schneider, P.Reiser, M.Poggio, P.Sahafi et al., "Mapping the phase-separated state in a 2D magnet", Nanoscale ***16****, 5302-5312 (2024).*

*[5] J. Kim, M.Kagias, F.Marone and M.Stampanoni, "X-ray scattering tensor tomography with circular gratings", Appl. Phys. Lett. 1****16****, 134102 (2020).*

[6] M. Rawlik, A.Pereira, S. Spindler, Z. Wang, L.Romano et al.., "Increased dose efficiency of breast CT with grating interferometry", Optica ***10****, 938 (2023).*

Towards NIR-light triggered nanocarriers

Project P2206: Multi-compartment nanofactories for on-site and on-demand drug synthesis and delivery
Project leaders: O. Tagit and C. G. Palivan
Collaborator: A. Nikoletić (SNI PhD Student)

Introduction

Stimuli-responsive polymeric self-assemblies are promising drug delivery platforms offering on-demand release with dose and spatiotemporal control over delivery. Thermoresponsive polymers with a lower critical solution temperature (LCST) are widely explored as building blocks for such drug delivery systems. These polymers have hydrated polymer chains and remain soluble below the critical temperature (cloud point), but once heated beyond it they undergo entropy-driven hydrophobic chain collapse and aggregation [1]. Since temperature rarely acts as an endogenous stimulus in physiological settings, external stimuli capable of inducing localized heating are required to activate thermoresponsive materials [2].

In this context, inorganic nanoparticles are of particular interest due to their size-dependent optical, electrical, thermal, or magnetic properties, which allow them to efficiently convert external stimuli into heat. Among these, plasmonic nanoparticles have been extensively investigated for photothermal conversion. Gold nanorods (AuNRs) display localized surface plasmon resonance (LSPR) and efficiently generate heat upon excitation with near-infrared (NIR) light. By adjusting their size and aspect ratio, the LSPR wavelength can be precisely tuned within the NIR window, which is particularly suitable for biomedical applications due to its deep tissue penetration, biocompatibility, and low phototoxicity [2].

The goal of this project is the development of AuNR–thermoresponsive polymer hybrid nanoassemblies that enable NIR-light-triggered cargo release (Fig. 1A), and their incorporation into giant unilamellar vesicles to form compartmentalized nanofactories (Fig. 1B). To this end, novel thermoresponsive block copolymers are synthesized that self-assemble into defined nanostructures and allow for the covalent attachment of AuNRs via appropriate end-group functionalization. Since the performance of such hybrid systems critically depends on the precise thermal response of the polymeric component, we systematically investigated the thermoresponsive behavior of homo- and copolymers under complex conditions to reliably predict their behavior in physiological settings.

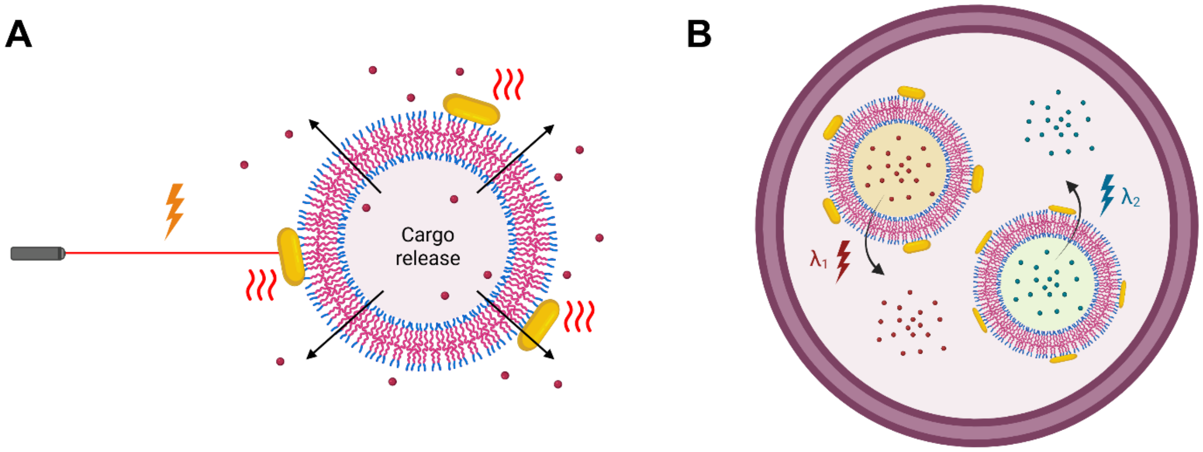

Fig. 1: Schematic illustration of the (A) NIR light triggered release from thermoresponsive assemblies and (B) compartments with different AuNRs triggered with light of different wavelengths.

Main Results

We have synthesized a series of well-defined thermoresponsive block copolymers based on hydrophobic poly(butylacrylate) (PBA) and hydrophilic poly(diethylene glycol acrylate) (PDEGA). We used the photoinitiated reversible addition-fragmentation chain transfer (RAFT) polymerization to synthesize both blocks, allowing us to obtain a library of PBA-*b*-PDEGA polymers in a straightforward manner. Starting from different RAFT chain transfer agents (CTAs), we introduce three end-groups of varying polarity onto the hydrophilic PDEGA block to investigate their influence on polymer's LCST, as well as the effect of varying block lengths. Nanoprecipitation allowed us to obtain nanoassemblies with good control over size and size distribution, while ensuring high encapsulation efficiency for further experiments.

The thermoresponsive behavior of PDEGA and PBA-*b*-PDEGA was evaluated through dynamic light scattering (DLS) and turbidimetry (cloud point) experiments conducted in aqueous solutions. Upon heating, the PDEGA block undergoes a reversible collapse, becoming hydrophobic and leading to destabilization of dissolved polymer chain or block copolymer assemblies. The cloud point temperature (T_{cp}) increased with the degree of polymerization for homopolymers (Fig. 2A). Additionally, polymers bearing more polar end-group functionalities exhibited higher T_{cp} values. All polymers exhibited lower T_{cp} in PBS compared to H_2O, but more importantly presence of model small molecule (Fig. 2B) or macromolecule (Fig. 2C) further decreases the $T_{cp.}$ For the thermoresponsive nanoassemblies in the presence of physiological concentration of macromolecular crowder, T_{cp} is decreased by 8 °C.

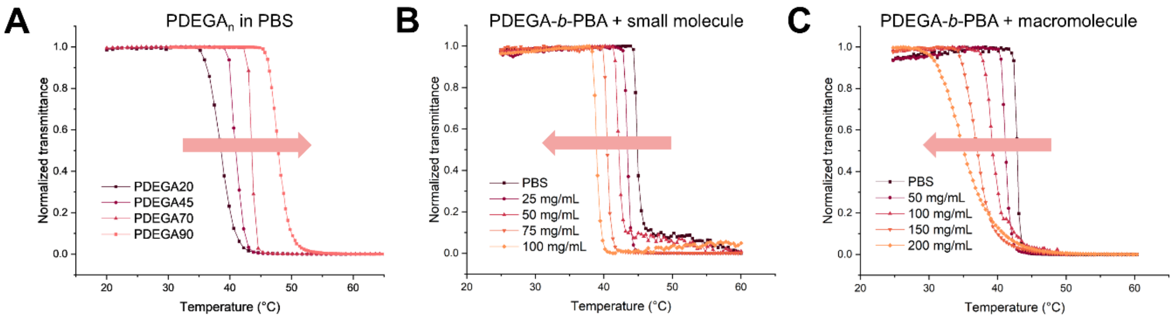

Fig. 2: Cloud point determination in PBS using turbidimetry. (A) Longer PDEGA homopolymers have higher T_{cp}. (B) Presence of model small molecule and (C) macromolecule decreases T_{cp} of PDEGA-b-PBA assemblies.

AuNRs, our photothermal counterpart, were prepared using a two-step seed-mediated growth method. The resulting CTAB-stabilized AuNRs exhibited near-infrared localized surface plasmon resonance around 800 nm (Fig. 3A), as determined by UV-Vis-NIR spectroscopy, with minor tuning achieved by adjusting seed aging and growth conditions. The dimensions and aspect ratios of the AuNRs were assessed by scanning and transmission electron microscopy, yielding nanorods with typical dimensions of approximately 50 × 15 nm and an aspect ratio of ~3.5 (Fig. 3B). Ligand exchange during liquid–liquid phase transfer enabled tuning of AuNR hydrophilicity.

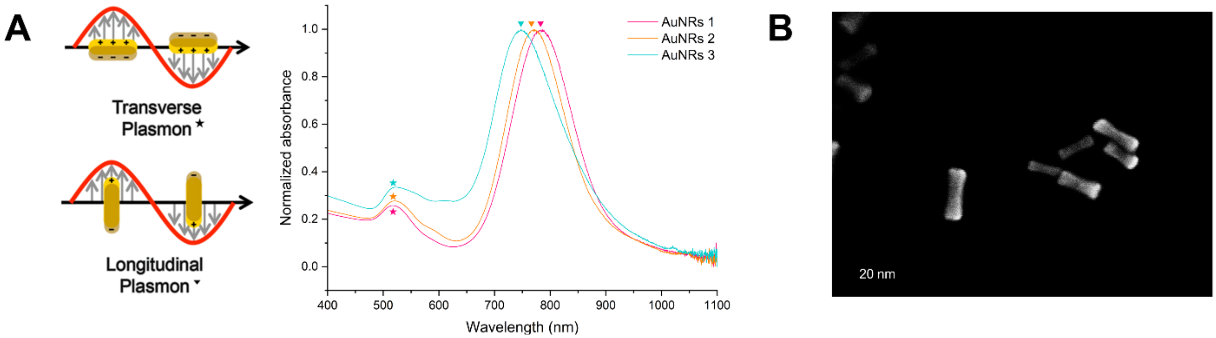

Fig. 3: Characterization of CTAB-stabilized AuNRs. (A) UV-vis spectra of AuNRs with schematic illustration of corresponding plasmon resonances. (B) SEM micrograph of AuNRs synthesized from 2h-aged seeds (aspect ratio 3.6).

Conclusion

We have developed a series of thermoresponsive polymers and gold nanorods for the design of NIR-triggered hybrid nanocarriers. Systematic studies revealed how block length, and end-group functionality influence thermoresponsive behavior, while ligand exchange on AuNRs allowed controlled modulation of hydrophilicity for integration into polymer assemblies. Importantly, critical temperature of polymers was significantly altered by biologically relevant solutes, highlighting the importance of testing thermoresponsive polymers in complex media to better predict their behavior in physiological environments. Our current work is focusing on conjugation strategies to obtain polymer/AuNRs nanohybrids and their characterization.

References

[1] A. Bordat, T. Boissenot, J. Nicolas, N. Tsapis, Thermoresponsive polymer nanocarriers for biomedical applications, Adv. Drug Deliv. Rev. ***138****, 167-192 (2019).*

[2] A. Nikoletić, M. Maleković, G. Kozalak, C.G. Palivan, O. Tagit, Thermoresponsive Nanocarriers Transduced by Inorganic Nanoparticles: Design Considerations and Applications in Drug Delivery, Helv. Chim. Acta ***108*** *(3), e202400193 (2025).*

Biofunctionalizing scintillating HfO$_2$ nanoparticles for X-ray mediated optogenetics

Project P2207: Targeted scintillator nanoparticles for X-ray mediated optogenetics in behaving mice
Project leaders: A. A. Wanner, J. D. Roo, and C. Padeste
Collaborator: E. Liari (SNI PhD Student)

In conventional optogenetics, optical tools are exploited in order to manipulate the activity and function of neurons in the brain. This is typically achieved by the activation of light switchable transmembrane proteins, such as channelrhodopsin, halorhodopsin or archaerhodopsin, with the assistance of visible light [1,2]. However, the visible light has a penetration depth limited to a few hundred micrometers and thus, to reach deeper brain structures, the light source has to be invasively implanted into the brain. This can lead to problems such as tissue damage and neuroinflammation. In this project, we are developing HfO$_2$ scintillating nanoparticles (SNPs) doped with Tb^{3+}, as an alternative non-invasive means of optogenetics. Utilizing their property of absorbing X-ray radiation due to the high atomic number of Hf (Z= 72) and the subsequent conversion to visible light by Tb^{3+}, we expect to achieve a non-invasive X-ray mediated optogenetic manipulation of brain cells [3].

Synthesizing scintillating nanoparticles (SNPs) for X-ray mediated optogenetics

HfO$_2$ NPs have emerged as an alternative host matrix for Ln^{3+} ions due to their chemical stability, large bandgap and optical transparency in the visible range [4, 5]. Hence, luminescent HfO$_2$:Tb NPs of around 3 nm diameter were synthesized using a typical solvothermal reaction. After synthesis, the particles were further functionalized with the appropriate carboxylate ligand that makes them colloidally stable in non-polar solvents [4]. Further increase of the final photoluminescence properties was achieved by coating the previously synthesized core particles with an additional thin layer of approximately 0.5 nm in thickness of optically inactive HfO$_2$ shell. The shell grows epitaxially on the surface of the particles and its main aim is to protect the quenching of Tb^{3+} luminescence from possible surface defects and surface molecules, such as the surface ligands or the solvent [5]. Characterization of the particles was conducted by means of ^{1}H NMR spectroscopy to verify the surface functionalization, Dynamic Light Scattering (DLS) to confirm the hydrodynamic size and Transmission Electron Microscopy (TEM) to measure the diameter of the inorganic core.

The optical properties of the as-synthesized particles were initially measured using photoluminescence. For the core only particles, the excitation spectrum shows two peaks with the maximum peak at 235 nm and a shoulder at 280 nm. After excitation of the particles at 280 nm, 4 characteristic emission peaks are noticed which correspond to the 4 transitions of Tb^{3+}. The green peak at 545 nm originating from the $^5D_4$ --> $^7F_5$ transition shows the maximum emission. Furthermore, it matches with the excitation range of the opsin that we want to utilize in the final application – ChRmine, a red-shifted channelrhodopsin, with a peak response at 520 nm. In addition, the lifetime measurements showed a decay time in the range of ms, which is characteristic for Ln^{3+}.

On the contrary, the as synthesized core-shell particles show different excitation properties with a broad peak showing a peak maximum at 260 nm. The emission profile is similar to that of the core only particles with the four characteristic peaks showing further splitting, which indicates that surface quenching has been alleviated. Furthermore, the decay time of the 545 nm has been increased and the peak is longer lived compared to the one of the core particles. Overall, the core-shell particles have improved optical properties.

Biofunctionalization of HfO$_2$ scintillating nanoparticles (SNPs)

HfO$_2$ has been shown to be an excellent host matrix for Ln^{3+} due to the chemical stability it possesses [4, 5]. Despite the superior properties of HfO$_2$:Tb, widespread utilization of these particles is limited due to their poor colloidal stability in aqueous environments and at physiological conditions. This is provided by the organic ligands capping the particles. Catecholates provide excellent colloidal stability for metal oxides and specifically for HfO$_2$ NPs [6]. However, we have shown that catecholates quench the luminescence of the particles, which is detrimental for the final application (Fig. 1). Hence, it is crucial to find an alternative ligand which provides equally strong colloidal stability without quenching the luminescence of the particles.

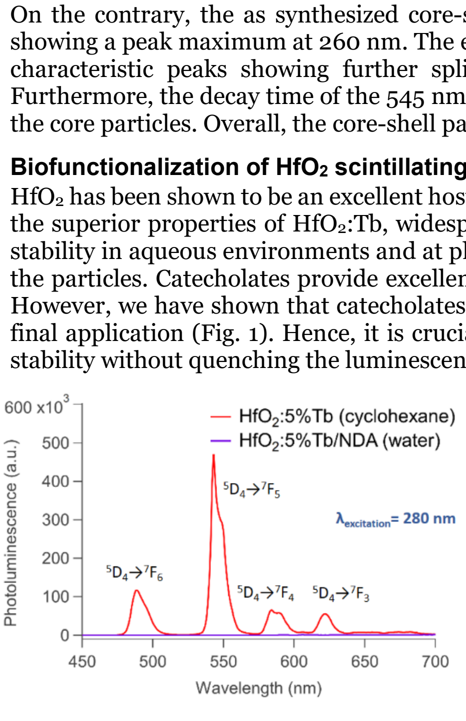

Fig. 1: Emission spectra of HfO$_2$:Tb capped with dodecanoate (red spectrum) in cyclohexane and HfO$_2$:Tb capped with nitrodopamine (NDA) (purple spectrum) in water after excitation at 280 nm. Even though particles with NDA are colloidally stable in water, they show no photoluminescence properties.

Bisphosphonates have been widely used in the literature to provide colloidal stability for a plethora of NPs including $NaYF_4$, which is an alternative host matrix for Ln^{3+} [7, 8]. Hence, we synthesized two bisphosphonate ligands with different ligand chain to validate whether the chain can have a difference on the final colloidal stability of the particles [8]. We studied the ligand binding and thus, the colloidal stability of the particles using non-doped HfO_2 NPs, HfO_2 are compatible with NMR spectroscopy, which serves as the tool to study ligand binding. We were able to quantify the amount of bound ligands on the surface of the NPs by deconvolution of the ^{31}P NMR peaks in different pH ranges in aqueous environment and biologically relevant solutions. Furthermore, we used Z-average and Zeta potential measurements to verify the colloidal stability of the particles. Finally, we performed a ligand exchange reaction with bisphosphonates on the surface of optically active HfO_2:Tb NPs to examine whether bisphosphonates quench the final photoluminescence of the particles.

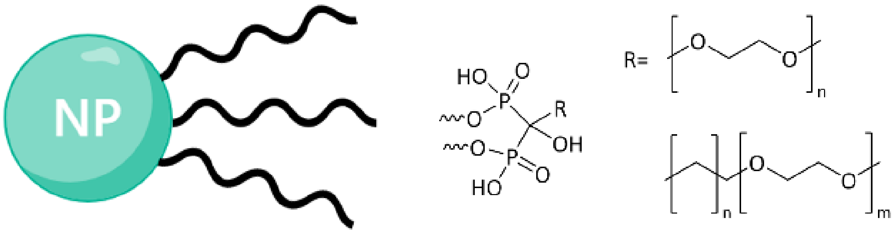

Fig. 2: Schematic representation of HfO_2 NPs capped with bisphosphonate ligands for colloidal stability in aqueous environment and at physiological conditions.

X-ray stimulation of bisphosphonate capped HfO_2:Tb NPs

Verification of the colloidal stability of the NPs provided by bisphosphonates allowed us to functionalize optically active HfO_2:Tb and HfO_2:Tb/HfO_2 NPs. Using a Cu X-ray tube, we were able to show that both the core and core-shell NPs are radioluminescent. Similar to the photoluminescence measurements, X-ray irradiation resulted into the particles showing the 4 characteristic emission peaks of Tb^{3+} with the maximum emission peak at 545 nm. Hence, the NPs show promising characteristics as scintillating nanoplatforms for use in X-ray mediated optogenetics.

Conclusions & Future Perspective

In conclusion, we have synthesized HfO_2:Tb and HfO_2:Tb/HfO_2 SNPs. The NPs are luminescent showing a peak maximum at 545 nm under excitation at 280 nm and its decay is in the ms range. The particles were colloidally stable in aqueous environment and at physiological conditions using bidentate bisphosphonates as ligands, while remaining luminescent. Finally, the NPs show promising radio-luminescent properties under X-ray irradiation.

In the future, we aim to further end-functionalize the bisphosphonate-capped particles with an appropriate moiety that can be chemically attached to specific molecules (e.g. SNAP tags) that will provide linkage of the NPs to the targeted protein in the brain. In addition, we will test whether the SNPs can activate red shifted proteins in vitro under both UV and X-ray activation. Lastly, the NPs will be tested first in vitro in acute coronal slices of mouse brain, where the generated photocurrents will be monitored by electrophysiological recordings and finally, *in vivo* in behaving mice

References

*[1] J. Ditterich, et al., "Microstimulation of visual cortex affects the speed of perceptual decisions" Nature Neuroscience **6**, 891–898 (2003).*

*[2] B. Chen, et al., "Recent advances in cellular optogenetics for photomedicine", Advanced Drug Delivery Reviews **188**, 114457 (2022).*

*[3] A. Kamkaew, et al., "Scintillating Nanoparticles as Energy Mediators for Enhanced Photodynamic Therapy", ACS Nano **10**, 3918–3935 (2016).*

[4] A. Lauria, et al. , "Multifunctional Role of Rare Earth Doping in Optical Materials: Nonaqueous Sol-Gel Synthesis of Stabilized Cubic HfO2 Luminescent Nanoparticles", ACS Nano 7, 7041-7052 (2013).

*[5] C. Seno, et al., "Epitaxial core/shell nanocrystals of (europium-doped) zirconia and hafnia", J. Am. Chem. Soc. **146,** 20550-20555 (2024).*

*[6] L. Deblock, et al., "Mapping out the Aqueous Surface Chemistry of Metal Oxide Nanocrystals: Carboxylate, Phosphonate, and Catecholate Ligands", JACS Au **2**, 711–722 (2022).*

*[7] X. Zhang et al., "Boosting luminance energy transfer efficiency in upconversion nanoparticles with an energy-concentrating Zone" Angewandte Chemie **131**, 12245–12250 (2019).*

*[8] S. Kachbi-Khelfallah, et al., "Towards potential nanoparticle contrast agents: Synthesis of new functionalized PEG bisphosphonates", Beilstein J. Org. Chem. **12**, 1366–1371 (2016).*

NANO-PHOTO: NANOstructured protein material for PHOTOcatalysis

Project P2301: NANO-PHOTO: NANOstructured protein material for PHOTOcatalysis
Project leaders: A. Bunzel, S. Panke and T. Ward
Collaborator: P. Elbers (SNI PhD Student)

Introduction

Humanity faces increasing challenges from rising carbon emissions, while energy production remains heavily dependent on fossil fuels. Natural photosynthesis offers a blueprint for sustainable solar energy conversion by harvesting sunlight to drive chemical reactions. However, despite efficient light harvesting, only ~1–2% of absorbed solar energy is converted into biomass by photosynthesis [1]. In addition, natural photoactive enzymes are generally ill-suited for biotechnological applications such as biohybrid photovoltaics due to limited stability and insufficient control over electron flow [2].

To address these limitations, we exploit computational protein design—particularly at the nanoscale—to engineer photoenzymes for biohybrid photovoltaics. Previously, we generated new-to-nature photoenzymes by computationally designing binding pockets for the photosensitizer eosin Y (EOY) into heme-containing helical-bundle proteins (Fig. 1a). Subsequent improvement by directed evolution yielded EOY4D2.2, which produced photocurrents 2.6-fold higher than those of the photosensitizer alone in a model solar cell [3]. Building on this result, the goal of this project is to engineer the nanoscale assembly of photoenzymes to improve photoefficiency and enable structural characterization. To this end, we are computationally designing 2D nanosheets to densely pack photoenzymes onto solar cells and 3D nanospheres to facilitate cryo-EM structure determination of small photoenzymes (Fig. 1b).

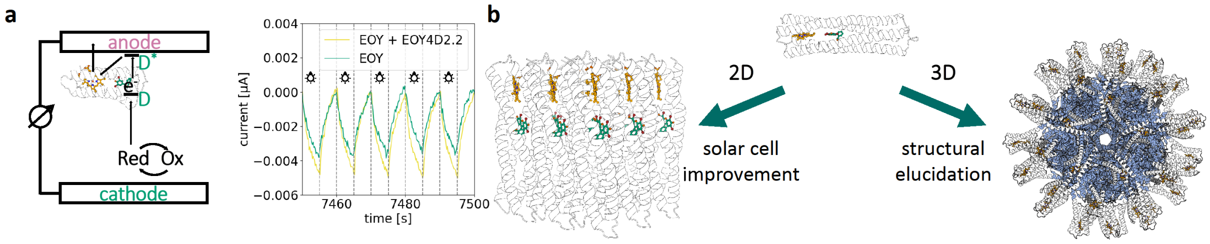

Fig. 1: Photoenzyme nanoscale design may improve photoefficiency and allow structural elucidation. a) *Biohybrid solar cell using a designer enzyme to drive photo currents (eosin Y (EOY): green; heme: orange).* ***b)*** *This work aims to design 2D nanosheets (left) and 3D nanospheres (right) for solar cell improvement and structural elucidation, respectively.*

Main Results

2D Nanosheets: Dye-sensitized solar cells benefit from dense coatings of photoactive molecules to achieve high photoefficiencies. Inspired by this, we aim to use protein design to assemble photoenzymes into 2D nanosheets that can be densely coated onto solar cells. While self-assembling protein lattices have been created [4], their design remains challenging and limited to non-functional proteins. Here, we develop a new approach by redesigning photoenzymes into C4-symmetric tetramers, followed by redesigning into p4-symmetrical 2D lattices. To that end, protein monomers are first forced into tetrameric assemblies by docking. Subsequently, iterative rounds of sequence design using LigandMPNN [5] and validation using Boltz-2 structure prediction [6] were performed. During iteration, the best variants are filtered for low solvent-accessible surface area and high ipTM scores to promote nanosheet assembly (Fig. 2a). Using this iterative pipeline densely packed structures with high confidence in the predicted interfaces were designed (Fig. 2b). These features are consistent with molecular dynamics simulations and other structure prediction tools. Next, we will test the 96 best-scoring designs in high-throughput experiments.

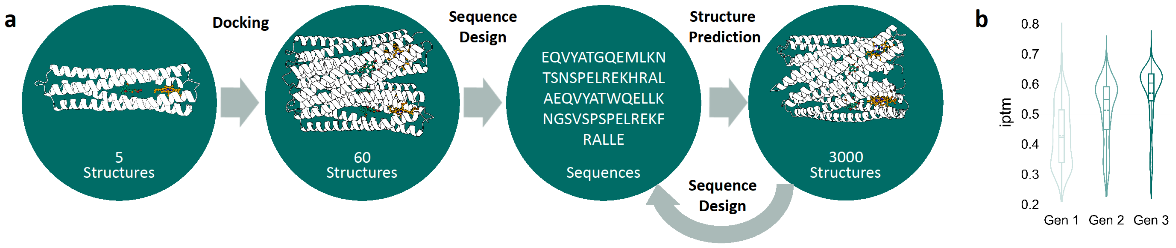

Fig. 2: Design pipeline of 2D nanosheets. a) *Monomeric proteins are docked into tetrameric C4-symmetric structures. Subsequent rounds of sequence redesign and structure prediction yielded structures with improved scores, such as the* ***(b)*** *ipTM score predictive for protein-protein binding.*

3D Nanospheres. The Bunzel group has designed a range of photoenzymes that are structurally related to EOY4D2.2. Atomic structures of these enzymes would substantially aid further engineering. However, structural determination of proteins of the 4D2 family has remained challenging. They often evade crystallization, and NMR suffers from peak broadening due to the paramagnetic iron of the bound heme. Finally, the helical-bundle photoenzymes only range up to 20 kDa, making them too small for atomic-resolution cryo-EM [7].

To overcome the limitations of structural biology, we designed fusion proteins in which helical bundle proteins are rigidly attached to the icosahedral capsid *Aa*LS (*Aquifex aeolicus* lumazine synthase). Our design pipeline relied on AlphaFold2 [8] to predict the structure of a protein nanosphere fused to a helical bundle protein, and on ProteinMPNN to optimize the resulting structure. The developed design pipeline provides a strong foundation for future display of other proteins and a starting point for experimental validation of our approach. The designed 3D nanospheres were successfully produced and purified, and size-exclusion chromatography confirmed the correct size of the megadalton complex. Individual particles of the correct size and shape were clearly visible in cryo-EM. Reconstruction with this dataset led to atomic resolution for the core and 6 Å resolution for the helical bundle attached to the core (Fig. 3b). These results demonstrate the general feasibility of using nanospheres for cryo-EM imaging and lay the groundwork for high-resolution structure determination.

Fig. 3: Design and validation of display approach for 3D nanospheres for structure elucidation. *a) Fusion structures were designed by genetically fusing helical bundle proteins to the C-terminus of AaLS; b) Preliminary density of a designed pentamer showing one helical bundle protein attached to the core.*

Conclusion

This project aims to establish nanoscale protein design as a strategy to control both the organization and function of photoenzymes. By engineering photoenzymes into defined 2D nanosheets and rigid 3D nanospheres, we seek to directly link nanoscale assembly to improved photoefficiency and structural accessibility. Together, these efforts are expected to lay the groundwork for rationally designed, nanostructured protein materials for photocatalysis and biohybrid energy conversion.

References

[1] R. E. Blankenship, et al., Comparing photosynthetic and photovoltaic efficiencies and recognizing the potential for improvement, Science ***332****, 805 (2011).*
[2] E. Musazade, et al., Biohybrid solar cells: Fundamentals, progress, and challenges, J. Photochem. Photobiol. C ***35****, 134 (2018).*
[3] H. A. Bunzel, et al., Photovoltaic enzymes by design and evolution, bioRxiv, 2022.12.20.521207 (2022).
[4] S. Gonen, et al. Design of ordered two-dimensional arrays mediated by noncovalent protein-protein interfaces", Science ***348****, 6241 (2015).*
[5] J. Dauparas, et al., Atomic context-conditioned protein sequence design using LigandMPNN, Nat. Methods ***22****, 717 (2025).*
[6] S. Passaro, et al., Boltz-2: Towards Accurate and Efficient Binding Affinity Prediction, bioRxiv, 2025.06.14.659707 (2025).
[7] Hutchins, G. H. et al., An expandable, modular de novo protein platform for precision redox engineering, Proc. Nat. Acad. Sci. ***31****, 120 (2023).*
[8] Jumper, J. et al. Highly accurate protein structure prediction with AlphaFold, Nature ***596****, 583 (2021).*

Osteogenesis on the nanoscale – an in vitro model based on electrospun PCL/chitosan scaffolds

Project P2302: Elucidating synergistic effects of nano topography and peptide immobilisation on osteogenesis
Project leaders: A. G. Guex and M. Nash
Collaborator: I. Imhof (SNI PhD Student)

Introduction

A healthy tooth is firmly anchored in its socket within the alveolar bone, yet tooth loss can occur in response to disease or trauma. Dental implants are an effective solution for tooth replacement and have generally high survival rates. However, some patients lack sufficient bone volume and quality required for implant placement. Consequently, bone augmentation is needed. To date, autografts remain the gold standard for bone augmentation, followed by xenogeneic and synthetic materials. The present methods each have their own drawbacks, ranging from donor-site morbidity in the case of auto-or allografts to potential inflammatory responses against xenografts. Synthetic materials on the other hand have, at times, poor mechanical properties [1]. Further adding to the challenge, not all patients are eligible for current strategies, highlighting the need for alternative solutions. A better understanding of the bone nanoarchitecture and molecular environment is key to developing regenerative strategies. This project aims to create an *in vitro* model of the alveolar bone's extracellular matrix by electrospinning. This technique uses a high-voltage electric field applied to a polymer solution to generate nanofibrous scaffolds. The scaffolds will be fabricated from a chitosan (CS)/poly(ε-caprolactone) (PCL) composite, wherein PCL is an FDA-approved polymer and CS has been reported to exhibit anti-fouling and osteo-inductive properties [2]. In addition to material selection, the type of cells in regenerative medicine is crucial for clinical success. Here, human dental pulp stem cells (hDPSCs) are cultured on the fabricated scaffolds and stimulated with osteogenic factors to induce differentiation towards bone. hDPSCs exhibit multilineage differentiation potential, including osteogenic, chondrogenic, odontogenic, adipogenic, and neurogenic lineages [3] and can be characterised by the expression of mesenchymal surface markers CD90, CD73, CD105, and CD146; alongside the absence of haematopoietic markers CD11, CD34, CD19, CD45, and HLA-DR [4]. This in vitro approach with hDPSC will enable us to study underlying molecular structures of osteogenesis within a defined, biomimetic extracellular environment with a close link to the clinics.

Main Results

We dissolved a polymer blend of 10% w/v PCL and 1.5% w/v CS (PCL/CS) in 90% acetic acid overnight; pure PCL (10% w/v) served as a control. The following day, we produced nanofibrous scaffolds through electrospinning. The fibre diameter of PCL/CS scaffolds increased (0.277 ± 0.183 µm) compared to pure PCL (0.125 ± 0.06 µm), which was observed with SEM (Fig. 1A). Next, we investigated the presence of CS in various PCL/CS blends, which was confirmed by FTIR with characteristic CS peaks at 1590 cm^{-1} and 3435 cm^{-1} and PCL peaks at 1720 cm^{-1} [5] (Fig. 1B). The CS peaks increased with increasing CS concentration; however, increasing CS concentration increased the brittleness of the scaffold, and therefore limits its suitability for cell culture and clinical applications.

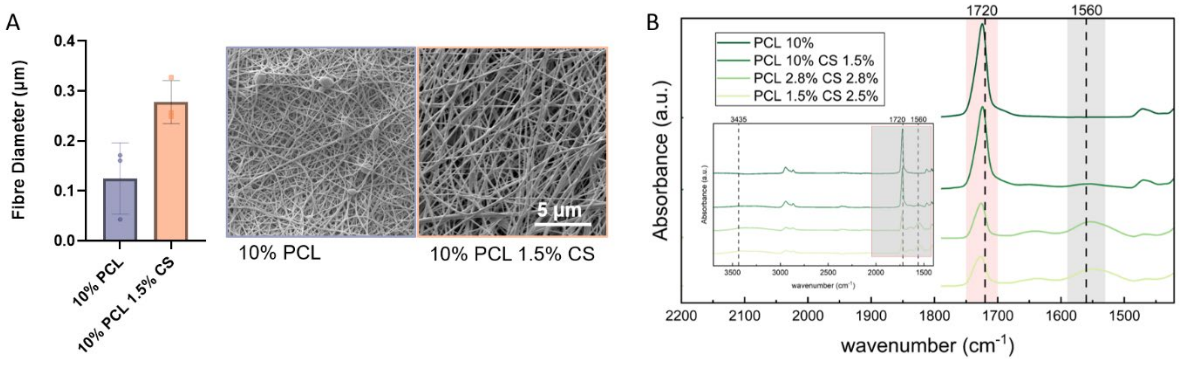

Fig 1. Characterisation of scaffolds with different polymer blends. A) Fibre diameters of PCL or PCL/CS scaffolds. B) FTIR spectra off different PCL/CS blends with characteristic PCL or CS peaks at 1720 cm^{-1} or 1560 cm^{-1}, respectively.

hDPSC were isolated from extracted teeth from patients (for example wisdom teeth) and assessed for their potential to differentiate into bone on the respective scaffolds. Flow cytometry was used to analyse surface markers defined as the international minimal criteria for mesenchymal stem cells [4]. Our preliminary data confirms the absence of haematopoietic markers (hMSC negative lineage cocktail) and the presence of CD90+ and CD73+ surface markers on hDPSCs (Fig. 2A). Subsequently, hDPSC were cultured on the scaffolds, following the scheme outlined in Fig. 2B. Unstimulated hDPSC that only received proliferation medium served as a control group. Mineralisation, a hallmark of osteogenesis, was confirmed in a calcium assay. We found higher Ca^{2+} concentrations of osteo-stimulated hDPSC (0.22 ± 0.05 µg/µl) compared to the control (0.01 ± 0.01 µg/µl). Preliminary data on PCL indicate an upregulation of *COL1A1*, *RUNX2*, and *SPP1* by 1.5-, 2-, and 4-fold, respectively, after 21 days (normalised to day 0). The expression of *BGLAP* was only slightly upregulated, *ALPL* was downregulated, which was expected as it is an early osteogenic marker that should decrease over time (Fig 2C).

Conclusion

These preliminary results indicate that both PCL and PCL/CS scaffolds support hDPSC attachment and osteogenic differentiation, demonstrating that the model effectively mimics key aspects of the bone extracellular matrix. Although the findings are preliminary, the system provides a robust platform to explore donor-specific variations, including potential sex-based differences. Future work will focus on the robustness of the model, refining the scaffold architecture and incorporating non-RGD integrin-binding peptides. RGD is the primary domain for integrin-mediated adhesion, but alternative peptide sequences may provide additional specificity and control over cell–matrix interactions. By integrating these functional peptides, we aim to investigate the molecular pathways that mediate osteogenesis more precisely, ultimately enhancing the translational relevance of this in vitro model for dental tissue engineering and regenerative applications.

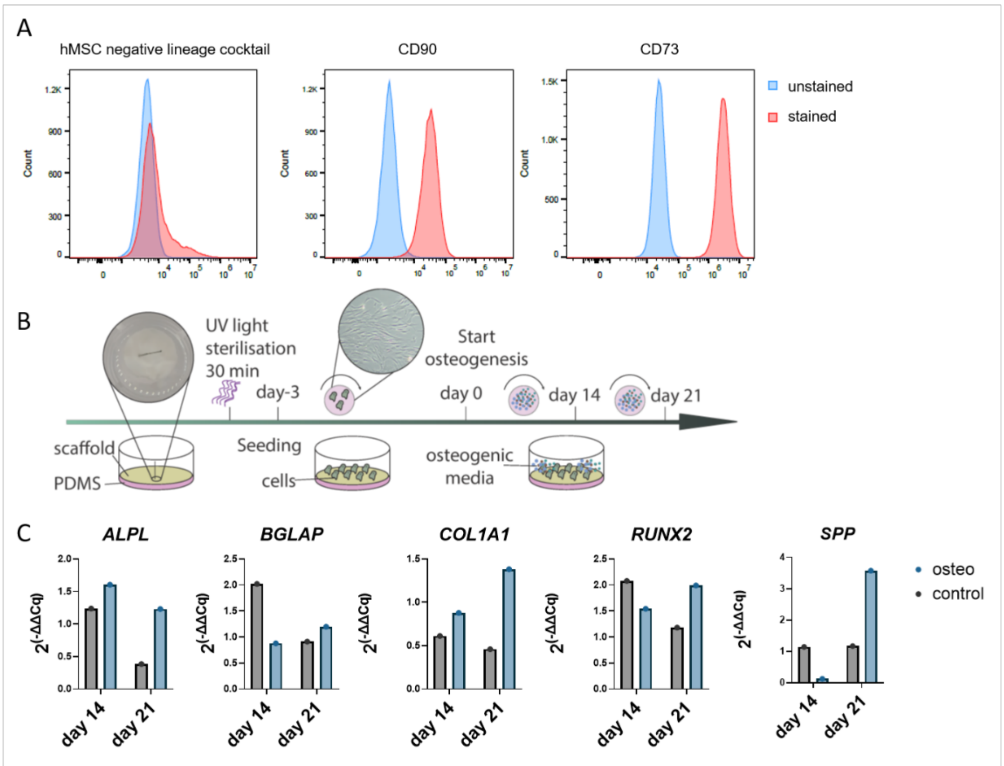

Fig 2. Biological characterisation of hDPSCs on scaffolds. A) Flow cytometry for characteristic MSC markers. Cells are negative for haematopoietic markers and positive for CD90 and CD73. B) graphical visualisation of osteogenic differentiation on nanofibrous scaffolds. C) Gene expression profile of hDPSCs on pure PCL scaffold after 14 and 21 days (n=1).

References

[1] *S. G. Kim, "Advancements in Alveolar Bone Grafting and Ridge Preservation: A Narrative Review on Materials, Techniques, and Clinical Outcomes", Maxillofac Plast Reconstr Surg **46** (1), 14(2024).*

[2] *W. Xu, X. Gao, M. Zhang, Z. Jiang, X. Xu, et al.," Electrospun Polycaprolactone-Chitosan Nanofibers on a Zinc Mesh as Biodegradable Guided Bone-Regeneration Membranes with Enhanced Mechanical, Antibacterial, and Osteogenic Properties for Alveolar Bone-Repair Applications", Acta Biomater **187**, 434–50 (2024).*

[3] *W. Zhang, X. F. Walboomers, S. Shi, M. Fan, and J. A. Jansen, "Multilineage Differentiation Potential of Stem Cells Derived from Human Dental Pulp after Cryopreservation", Tissue Eng **12** (10), 2813–23 (2006).*

[4] *M. Dominici, K. Le Blanc, I. Mueller, I. Slaper-Cortenbach, Fc Marini, et al., "Minimal Criteria for Defining Multipotent Mesenchymal Stromal Cells. The International Society for Cellular Therapy Position Statement", Cytotherapy **8** (4), 315–17 (2006).*

[5] *L. Van der Schueren, I. Steyaert, B. De Schoenmaker, and K. De Clerck, "Polycaprolactone/Chitosan Blend Nanofibres Electrospun from an Acetic Acid/Formic Acid Solvent System", Carbohydr. Polym. **88** (4), 1221–26 (2012).*

Vertical Quantum Dots in Coupled Ge Quantum Wells

Project P2303 : Vertical Quantum Dots in Coupled Ge Quantum Wells
Project leaders: A. Hofmann and I. Zardo
Collaborator: D. Nieri Orfatti (SNI PhD Student)

Introduction

High-quality semiconductor heterostructures build the basic ingredient enabling quantum transport experiments including the promising field of semiconductor spin qubits. The material used for the quantum well (QW) determines the properties of the confined quantum states. Ge QWs have recently emerged as a suitable platform for fast spin qubits [1, 2, 3], due to a low effective mass (relaxing fabrication constraints), large spin–orbit interaction (SOI) (enabling electrical spin-manipulation), low hyper fine interaction (reducing magnetic noise) and large mobilities (ballistic transport) [4]. This platform is furthermore interesting as it allows to investigate low-dimensional valence band states ("holes"), which are much less studied than conduction band states ("electrons"). Typically, such a heterostructure consists of a Ge QW sandwiched between two SiGe barriers, thus confining the Ge states into two dimensions [5]. Lower-dimensional states are then constructed with electric fields induced by nm-scale electrodes patterned on top of the heterostructure. Quantum dots (QDs) are prominent examples of zero-dimensional states formed in this way. Here, we will take a next step and expand the platform from the two-dimensional states available in a single QW to a vertical 2 × 2D playground emerging when coupling two Ge QWs grown in the same heterostructure. Similar systems are used, for example, for electrons in GaAs to answer basic research questions about exiton condensates [6]. In more practical terms, this layout will pave a path towards solving the scalability problem of semiconductor qubits: the two QWs could be used to couple double-QDs vertically instead of horizontally [7, 8]; or to vertically stack the qubit and the readout layer instead of squeezing everything into one layer.

Simulations

To better understand the system, we performed simulations using the software NextNano, a Poisson-Schrödinger solver. Specifically, we wanted to understand how to build the heterostructure in a way that allows accumulation of both QWs and leads to a tunnel-coupling between the two quantum wells. This will be crucial for enabling tunnelling between two vertical QDs. Keeping the Ge concentration of the barrier and quantum well layers at 80 % and 100 %, we vary the thickness and the concentration of the layer that separates the two QWs. Fig. 1 shows how the anticrossing energy of the lowest states decreases rapidly as a function of both decreased Ge concentration increased width of the separation layer. Including the natural limitations set by the growth of such heterostructures, for our first device, we aimed at a 3 nm thick separation layer consisting of 80 % Ge.

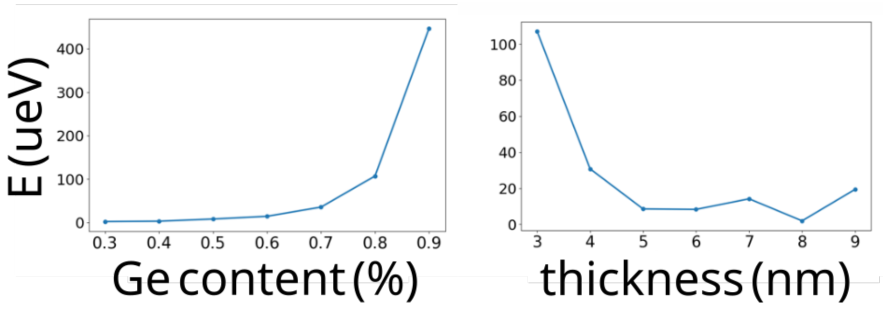

Fig. 1: Anticrossing energy E as a function of Ge content (left) and thickness (right) of the separation layer.

Growth

Even though long down-times of the growth chamber due to various upgrades and fixes lead to unforeseen delays, first double-QW samples have been grown successfully. In a first attempt (referred to as DQW1 in the following), the bottom QW was much thicker than anticipated. Adjustments ofthe growth parameters enabled growing a sample(DQW2) as shown in Fig. 2. The definition of bothQWs is extremely sharp, and the layers came outas 14 nm, 3 nm, 6 nm for the bottom QW, separationand top QW, respectively.

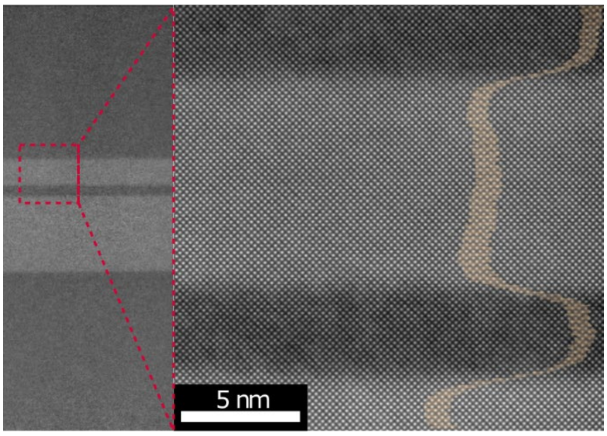

Fig. 2: High-resolution scanning tunnelling electron micrograph of the double-QW sample. The orange data in the magnified image indicates the Ge content in each layer.

Fabricatoin and Measurements

While fabrication recipes could mostly be transferred directly from our single QW processing steps, the ohmic contacts have to reach lower into the heterostructure in order to contact both QWs. Using transmission electron microscopy, we found a one-to-one correspondence between the amount of metal deposited and the depth of the PtSiGe contacts after annealing. First hallbar samples have been fabricated on DQW1, and cooled down to 10 mK in a dilution refrigerator. Standard DC and lock-in magnetotransport measurements revealed a Landau Fan as shown in Fig. 3. Clearly, the data shows the quantization into Landau Levels as expected for a single-QW, which we believe forms in the top QW. Some additional features are visible, which we attribute to the second QW. Using DQW2, we fabricated not only hallbars but also QDs and simple transistor-like devices. Measurements on these devices are ongoing.

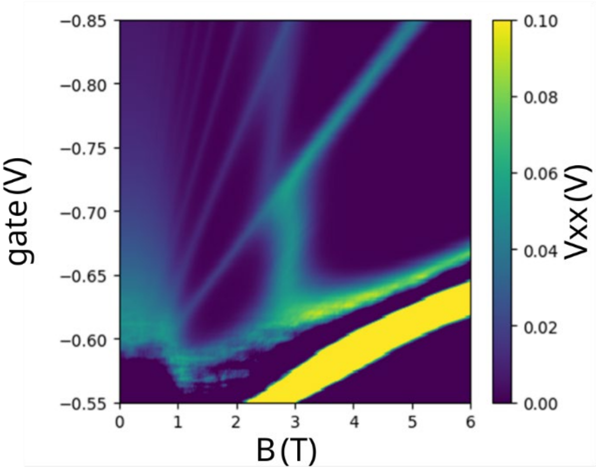

Fig. 3: Landau fan obtained by measuring the longitudinal voltage drop (Vxx) as a function of gate voltage and magnetic field B.

Outlook

The next steps include measurements of the hallbar of DQW2, which will clarify the participation of both QWs to transport measurements. Further, we will measure the QD devices to characterize parallel transport through both

References

[1] *D. Jirovec, et all, "A singlet-triplet hole spin qubit in planar Ge", Nature Materials* ***20,*** *1106 (2021).*

[2] *N. W. Hendrickx, et al., "Fast two-qubit logic with holes in germanium ", Nature* ***577****, 487 (2020).*

[3] *N. W. Hendrickx, et al., "A four-qubit germanium quantum processor" Nature* ***591****, 580 (2021).*

[4] *A. Sammak, et al., "Shallow and Undoped Germanium Quantum Wells: A Playground for Spin and Hybrid Quantum Technology" Advanced Functional Materials* ***29****, 1807613, (2019).*

[5] *M. Myronov. "Molecular Beam Epitaxy of High Mobility Silicon, Silicon Germanium and Germanium Quantum Well Heterostructures", Molecular Beam Epitaxy, pp. 37–54. (2018.).*

[6] *J. Eisenstein. "Exciton Condensation in Bilayer Quantum Hall Systems", Annu. Rev. Condens. Matter Phys.,* ***5,*** *159 (2014).*

[7] *H. Tidjani, et al. "Vertical gate-defined double quantum dot in a strained germanium double quantum well", Phys. Rev. Applied* ***20****, 054035 (2023).*

[8] *H. Tidjani, et al. A Three-Dimensional Array of Quantum Dots., arXiv:2512.01634v1 (2025).*

Programmable Origami for Regulated Exchange (PORE-X): Nuclear Pore Complex-Inspired DNA Nanopores

Project P2304: Selective new-to-nature nanopores enabled by biomolecular condensation
Project leaders: R. Y. H. Lim and M. Hondele
Collaborator: L. Beckert (SNI PhD Student), E. Cao, C. Lin, D. Overwijn, and K. Baumann

Drawing inspiration from nature: The Nuclear Pore Complex

The nuclear pore complex (NPC) mediates selective macromolecular exchange between the nucleus and cytoplasm [1]. Selectivity arises from intrinsically disordered phenylalanine–glycine nucleoporins (FG Nups), which interact rapidly and transiently with nuclear transport receptors (karyopherins, Kaps) to enable passage of receptor-bound cargo [2]. In contrast, nonspecific cargo is excluded by a permeability barrier located within the pore interior. This barrier is commonly attributed to a dynamic network of FG Nups and Kaps concentrated in the pore center [3]. Beyond the NPC, RNA and proteins can assemble into highly dynamic, liquid-like biomolecular condensates in vitro and into membraneless organelles in cells, which exert multivalent interactions to discriminate between specific binding partners (clients) and inert molecules [4].

Our objective is to examine how transient binding under nanoconfinement regulates transport using multivalent RNA–protein interactions as a minimal physical principle. Towards this goal, we engineer NPC-inspired DNA origami nanopores with RNA scaffolds tethered to the pore lumen. By probing how RNA-binding proteins reorganize the confined molecular environment and quantifying the resulting permeability changes in membrane-spanning pores, we derive design principles for selective transport in synthetic nanopores.

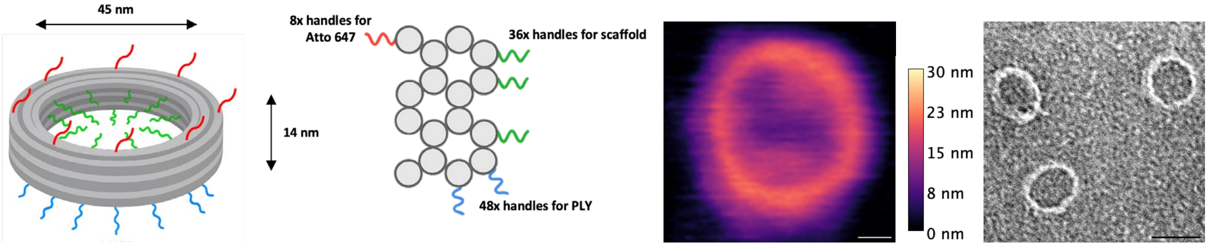

Fig. 1: PORE-X schematic. DNA origami nanopore (≈ 45 nm inner diameter, ≈ 14 nm height) featuring 48 handles for DNA-conjugated pneumolysin (PLY; blue) membrane anchors, 36 inward-facing handles for lumenal scaffold attachment (e.g. RNA; green), and 8 handles for fluorophore labeling (red). High-speed AFM image of PORE-X after RNA-functionalization showing dynamic fluctuations and a physical barrier within the lumen (scale bar: 10 nm). TEM image of the empty PORE-X confirming the pore architecture (scale bar: 50 nm).

From concept to structure: Engineering DNA origami nanopores

At the core of our work is PORE-X, a modular DNA origami nanopore for controlled membrane insertion and quantitative transport measurements. PORE-X consists of a rigid DNA origami ring that enables precise spatial control over functionalization. DNA origami is based on the programmed self-assembly of a long single-stranded DNA scaffold with short complementary staple strands, allowing nanostructures with defined geometry and addressable binding sites [5]. Membrane insertion is achieved by recruiting pneumolysin (PLY). PLY is a cholesterol-dependent cytolysin that binds cholesterol-containing membranes and assembles into large transmembrane pores, providing a robust route to span lipid bilayers. A high local density of pore-forming units is generated by 48 outward-facing DNA handles on the origami ring that hybridize with DNA-conjugated PLY, resulting in efficient and stable bilayer perforation. The pore lumen is independently functionalized via 36 inward-facing handles that tether defined scaffold molecules. In addition, 8 external handles are used for fluorophore labeling, enabling optical visualization (Fig. 1).

Unveiling inner pore dynamics by High-Speed AFM and interaction studies

High-speed atomic force microscopy (HS-AFM) [7] revealed the dynamic fluctuations of RNA-scaffold molecules within individual PORE-Xs in real time. These fluctuations may reflect short-lived structural rearrangements or localized interactions. Such behaviour aligns with the properties of the NPC, where flexibility and transient binding are key to the speed and bidirectionality of selective transport. Complementary insights were obtained through surface plasmon resonance (SPR) studies, which quantified the interaction kinetics of RNA scaffolds and Fused In Sarcoma (FUS). FUS was chosen as a client molecule due to its well-characterized RNA-binding domain and its role in exerting multivalent, transient interactions within biomolecular condensates.

Membrane insertion and quantitative transport assays

To connect the lumen organization to a functional permeability readout, we implemented a Giant Unilamellar Vesicle (GUV)-based transport assay using PLY-functionalized PORE-X constructs. In the assay, GUVs are generated by gel-assisted swelling using a defined lipid composition (DOPC with ~30% cholesterol and a fluorescent Liss Rhodamine PE lipid). PLY-functionalized PORE-Xs are incubated with GUVs, and permeability is quantified by monitoring time-resolved uptake of fluorescent dextran tracers (FITC-dextran, 20–70 kDa) into the vesicle lumen by confocal imaging and Fluorescence Recovery After Photobleaching (FRAP) (Fig. 2). Current data show that RNA-tethered pores exhibit reduced dextran influx relative to empty pores, consistent with a passive barrier formed by the confined RNA network. Upon addition of FUS, we detect an increase in fluorescence intensity at the GUV membrane that co-localizes with the PORE-X-associated fluorescent signal. This membrane-enriched protein signal is consistent with FUS recruitment to membrane-inserted PORE constructs and suggests FUS accumulation at the pore location, with likely enrichment within the pore lumen. In parallel, we observe a further reduction in FITC-dextran influx.

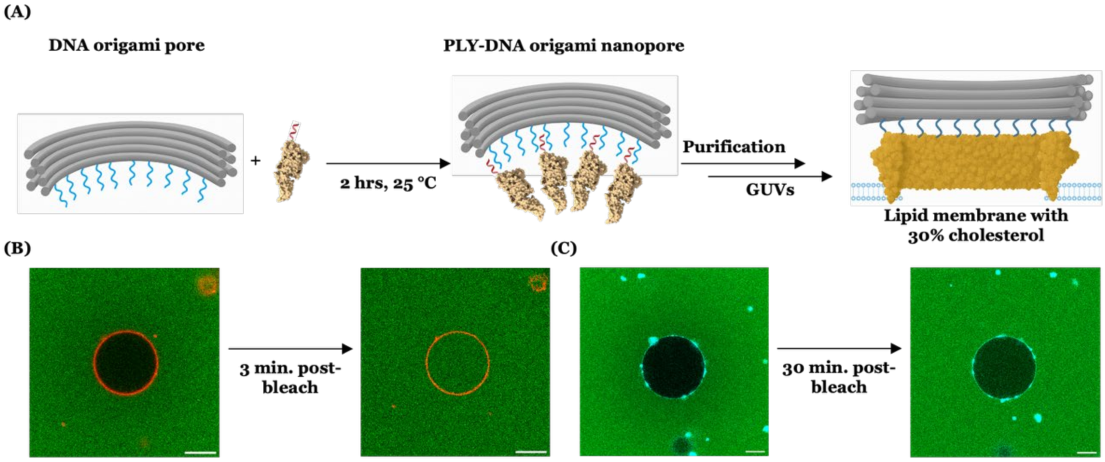

Fig. 2: (A) DNA origami pores are incubated with DNA-conjugated PLY (2 h, 25 °C), purified, and added to GUVs (30% cholesterol) to enable membrane insertion. (B) PLY–DNA channel without lumen scaffold: FITC–dextran 70 kDa (green) and Alexa 647–labeled DNA channel (red), 3 min post-bleach. (C) PLY–PORE with 75-nt RNA and 1000 nM wtFUS–mCherry (cyan): FITC–dextran 70 kDa (green); wtFUS signal remains non-equilibrated after 30 min. Scale bar, 10 µm.

Concluding remarks

This project advances the engineering of NPC-inspired selective transport in a fully synthetic system. Our programmable PORE-X system leverages nanopore confinement to couple dynamic scaffold–client interactions to measurable permeability changes across lipid membranes. By establishing a direct link between nanoscale organization (HS-AFM, SPR) and a functional transport readout (transport assays), we provide an experimentally tractable route to dissect how transient, multivalent interactions generate transport selectivity. These principles are transferable to engineered nanopores beyond the NPC context and support future applications in molecular sorting, diagnostics, and targeted delivery.

References

[1] B. W. Hoogenboom et al., "Physics of the Nuclear Pore Complex: Theory, Modeling and Experiment", Phys Rep 921, 1-53 (2021).

[2] L. E. Kapinos, et al., "Karyopherin-Centric Control of Nuclear Pores Based on Molecular Occupancy and Kinetic Analysis of Multivalent Binding with FG Nucleoporins", Biophysical Journal 106, 1751-1762 (2014).

[3] T. Kozai et al., „ Karyopherins remodel the dynamic organization of the nuclear pore complex transport barrier", Nat Cell Biol (2025).

[4] G. Gao et al., "Nanoscale domains govern local diffusion and aging within FUS condensates", bioRxiv (2025).

[5] P. W. Rothemund et al., "Folding DNA to create nanoscale shapes and patterns", Nature 440, 297-302 (2006).

[6] Q. Shen et al., "Functionalized DNA-Origami-Protein Nanopores Generate Large Transmembrane Channels with Programmable Size-Selectivity", J. Am. Chem. Soc. 145, 1292–1300 (2023).

[7] Q. Feng et al., "Channel width modulates the permeability of DNA origami-based nuclear pore mimics", Sci. Adv. 10, eadq8773 (2024).

Synthesis of a novel carcerand suitable for metal ion encapsulation

Project P2306: Enabling the challenging separation of radionuclides via the entrapment inside molecular containers
Project Leaders: K. Tiefenbacher and P. Steinegger
Collaborator: A. Kharchenko (SNI PhD Student)

Introduction

The field of nuclear medicine requires highly efficient and durable methods for the separation of radionuclides. Traditional 44Ti/44Sc generators, which utilize adsorption-based separation techniques, encounter significant obstacles such as limited chemical stability, radiolysis, and a decline in separation efficiency over time. To address these limitations, a novel molecular encapsulation/destruction strategy for radionuclide separation has been proposed. This method involves the irreversible encapsulation of radionuclides within a molecular container, followed by the degradation of that container (the carcerand) during the process of radioactive decay, which subsequently releases the daughter product (Figure 1).

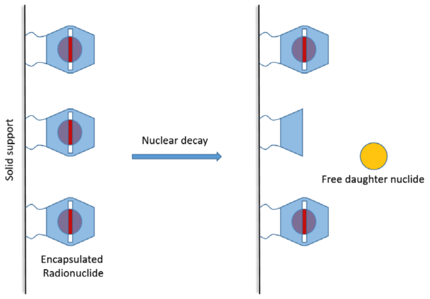

Fig. 1: Proposed molecular encapsulation/destruction method for radionuclide separation.

Based on the reported detection of Cs+ encapsulation in resorcin[4]arene-based carcerands by D. J. Cram, we proposed methanospherophane derivative (1) as a carcerand for metal ion encapsulation [1]. This structure is part of the hypothetical methylene-bridged calixarene polyhedra class of compounds, which were the subject of our perspective published in 2025 [2]. Previously, we achieved the first-ever synthesis of the molecule from this class. Starting from 5,11,17,23-tetrakis(4-hydroxybenzyl)-25,26,27,28-tetrahydroxycalix[4]arene (2), yielding a product carcerand (1) containing dichloromethane (DCM) as a guest in up to 8% yield. However, a high temperature (160 °C) is required, and no other guests were able to be encapsulated. Building on this, we explored alternative synthetic routes to carcerand (1), as well as alternative candidates for metal ion encapsulation.

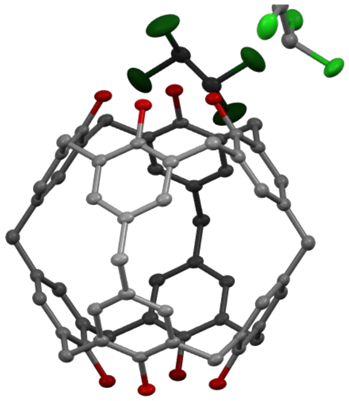

Fig. 2: X-ray structure of obtained carcerand 1.

Improved synthesis of carcerand 1 and expanded guest scope

Since our previous investigations showed that only more preorganized starting materials, such as (2), yielded the desired product, we decided to further increase the preorganization of the starting material by introducing benzylic alcohol groups. This modification was designed to enforce cage closure exclusively via intramolecular condensation. Encouragingly, after optimization, we were able to obtain the corresponding compound (5) in only two steps from commercially available calix[4]arene (2) and 5-(chloromethyl)-2-hydroxybenzaldehyde (3) in a 45% overall yield (Figure 3).

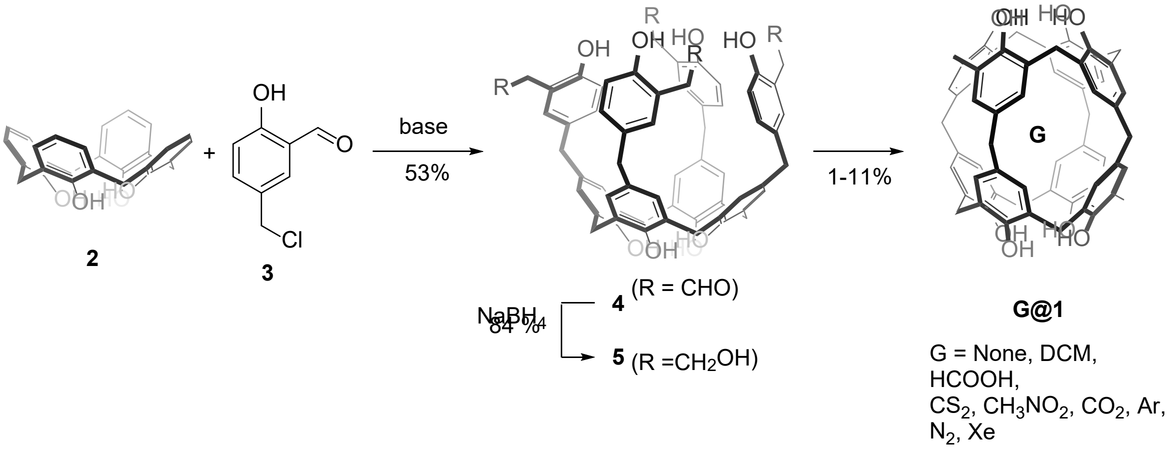

Fig. 3: Synthesis of carcerand 1 and guest screening.

After careful optimization of the reaction conditions, the desired product was obtained in yields of up to 11%. Importantly, this strategy enabled both the formation of the empty carcerand and the encapsulation of a diverse range of guests, including small organic molecules such as formic acid, carbon disulfide, and nitromethane, as well as gases including nitrogen, argon, xenon, and carbon dioxide. When the reaction was carried out in the presence of hydrogen, only the empty carcerand **(1)** was formed, likely because the small size of the hydrogen molecule allows it to escape from the cavity. Reactions performed in the presence of various metal salts similarly led exclusively to the formation of empty carcerand **(1)**, with no evidence for encapsulated metal ions.

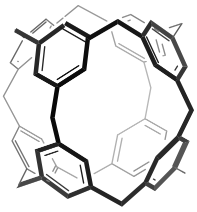

6

Fig. 4: Proposed alternative structures for metal ion binding.

Conclusion

An improved three-step synthesis of carcerand 1 was developed, and its ability to encapsulate a wide range of guests was demonstrated. The first-ever X-ray structure of a member of the methylene-bridged calixarene polyhedral class of compounds was obtained. Stability studies performed on carcerand (1) suggest that the eight hydroxyl groups contribute to a rather high oxygen sensitivity. These substituents may also inhibit metal-ion encapsulation by coordinating to the metals via the lone pairs on the oxygen atoms. Consequently, the unsubstituted methanospherophane **(6)** represents a promising alternative for metal-ion binding (Figure 4), which is currently under investigation

References

[1] *D. J. Cram, S. Karbach, Y. H. Kim, L. Baczynskyj, K. Marti, et al., Host–Guest Complexation: Carcerands and Carcaplexes, the First Closed Molecular Container Compounds, J. Am. Chem. Soc. 110, 2554–2560 (1988).*

[2] *A. Kharchenko, I. Cornu, B. Goldfuss, K. Tiefenbacher, Methylene-Bridged Calixarene Polyhedra: An Elusive Class of Symmetric Molecular Architectures, Helv. Chim. Acta, e00177 (2025).*

Optical coherent feedback control of a nanomechanical oscillator

Project P2307: Coherent feedback control of nanomechanical oscillators
Project Leaders: P. Treutlein and P. Potts
Collaborators: A. Huot de Saint-Albin (SNI PhD Student), M. Bosch Aguilera, G.-L. Schmid, A. Mitchell Galvao de Melo

Introduction

Feedback is a powerful technique for controlling quantum systems. The conventional strategy relies on quantum-limited measurements followed by classical processing and feedback actuation onto the system. However, quantum mechanics also allows coherent feedback of quantum signals. Such coherent feedback may exploit the information contained in non-commuting observables while circumventing the decoherence and backaction noise associated with measurement. Coherent feedback thus has the potential to improve quantum control and provide new capabilities in a broad range of physical systems [1,2]. In this project, we are experimentally investigating coherent feedback control of a nanomechanical oscillator with a quality factor of 141 million in an optical cavity, using novel optomechanical coherent feedback schemes that our group has developed [3]. In a first step, we aim at demonstrating coherent feedback cooling of the mechanical oscillator to its quantum ground state in a parameter regime where conventional cavity dynamical backaction cooling techniques cannot reach the ground state.

Main Results

We use an optical coherent feedback scheme to engineer a cooling force for the vibrations of a nanomechanical membrane oscillator. The membrane vibrations are imprinted as a quantum signal on a beam of light, which is optically processed in a coherent way and sent back to the membrane, exerting a radiation pressure force on it. By controlling the parameters of this optical coherent feedback loop, we can control the feedback force acting on the membrane vibrations and thus steer it to a desired target state.

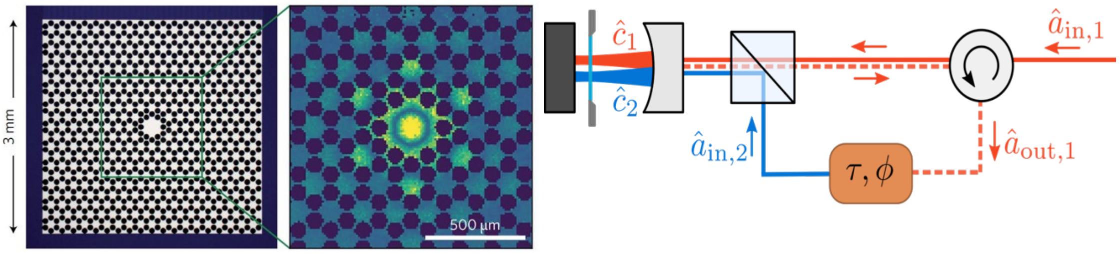

Fig. 1: Nanomechanical membrane oscillator featuring a high-Q mechanical mode in the defect of a phononic crystal pattern. To implement an optomechanical coherent feedback loop, a beam of light is sent twice to an optical cavity containing the membrane oscillator. In the first interaction, the membrane vibrations are imprinted on the light. After optical phase-shifting and time delaying of this quantum signal, the beam sent a second time to the cavity, exerting a feedback force on the membrane vibrations.

A schematic of the setup is shown in Fig. 1. The system comprises a nanomechanical membrane inside an optical cavity that is placed in a cryostat at 10 K. A laser beam is coupled to the cavity so that the membrane vibrations are imprinted on the phase quadrature of the light leaving the cavity. This phase modulation is converted into an amplitude modulation by interfering the reflected light with a local oscillator beam at the same frequency, whose phase can be adjusted to optimize the conversion. The beam is time-delayed using an optical fiber and then sent back to the cavity a second time, where it exerts a radiation-pressure feedback force on the membrane, resulting in cooling of the mechanical vibrations [3].

In a previous experiment, we demonstrated this cooling scheme with a silicon nitride membrane that had a mechanical mode with a quality factor of $Q = 3.2 \times 10^6$ at 20 K. The optical coherent feedback resulted in cooling of the mode to 5 phonons [3]. In order to improve the experiment and reach the ground state, we now replaced the membrane with an improved structure that was fabricated by our collaborators in the Gröblacher group at TU Delft. The new membrane features a “soft-clamped” mechanical mode localized in the defect of a phononic crystal pattern, see Fig. 1, which has a frequency of 2.15 MHz and a mechanical quality factor as high as $Q = 141 \times 10^6$ at 10 K, which is measured by mechanical ringdown measurements, see Fig. 2.

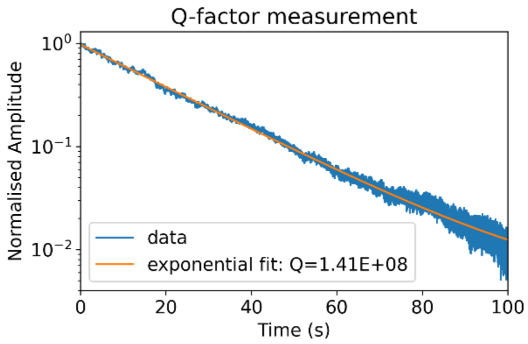

Fig. 2: Ringdown measurement of the membrane vibrations. The amplitude of the membrane vibrations at 2.15 MHz decays on a minute time scale, corresponding to a mechanical quality factor of 141 million.

To characterize the optomechanical interaction, we cool the membrane vibrations using cavity dynamical backaction. In this method, a laser beam that is red-detuned with respect to the cavity resonance is sent to the membrane-cavity system. The reflected beam is then used to measure the membrane vibrations via homodyne detection. We compute the power spectral density (PSD) of the mechanical displacement from this signal, which allows us to determine the number of phonons in the mechanical mode. By adjusting the power of the laser beam, we can cool the mechanical oscillator down to the limit imposed by the radiation-pressure shot noise of the light. For our system, which is in the unresolved sideband regime, this limit prevents mechanical ground-state cooling by cavity dynamical backaction, see Fig. 3. The good agreement with the optomechanical theory allows us to precisely calibrate the parameters of our system.

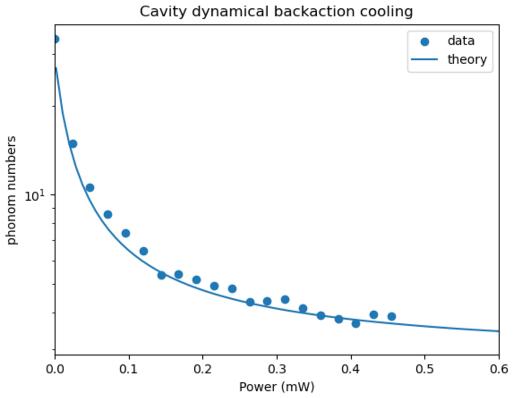

Fig. 3: Cooling of the membrane vibrations by cavity dynamical backaction, reaching an average phonon occupation of 3.7, fundamentally limited by radiation pressure shot noise.

In contrast to cavity dynamical backaction, our coherent feedback cooling scheme can in principle reach the mechanical ground state, as has been shown in a detailed theoretical analysis [3]. We are currently performing experiments to confirm this prediction. Preliminary measurements indicate that phonon numbers around one phonon can be reached, with room for further improvements. We are in the process of improving the optical signal processing and cross-checking the measurement of the phonon occupation using different methods in order to corroborate these results.

Conclusion

We have built an optomechanical system with a patterned SiN membrane that supports a high-Q mechanical mode in the defect of a phononic crystal structure. Characterization measurements demonstrate cavity dynamical backaction cooling of this mode to the radiation pressure shot noise limit. Optical coherent feedback cooling allows us to overcome this limit, potentially reaching the quantum ground state of the mechanical mode. In ongoing coherent feedback cooling experiments, we observe phonon occupations around one phonon. Further optimizations and cross-checking of these results using different optomechanical thermometry methods are ongoing.

References

[1] Seth Lloyd, Coherent quantum feedback, Phys. Rev. A 62, 022108 (2000).

[2] J. Zhang, Y.-xi Liu, R.-B. Wu, K. Jacobs, and F. Nori, Quantum Feedback: Theory, Experiments, and Applications, Phys. Rep. 679, 1 (2017).

[3] M. Ernzer, M. Bosch Aguilera, M. Brunelli, G.-L. Schmid, T. M. Karg et al., Optical Coherent Feedback Control of a Mechanical Oscillator, Phys Rev. X 13, 021023 (2023).

Low-noise diamond membranes in an optical cavity

Project P2308: A diamond-based spin-photon interface
Project Leaders: R. Warburton and P. Maletinsky
Collaborator: M. Obramenko (SNI PhD Student) and Andrea Corazza

Introduction

A colour centre in diamond represents an attractive candidate for an efficient and coherent spin-photon interface. A prototype network consisting of three nodes has already been constructed [1], in this particular case using three NV centres. Many challenges need to be overcome to increase the rate and security of such networks such that the technology can be scaled up. We report here advances in applying a microcavity to boost the light-matter interaction of a colour centre in diamond.

Main Results

The cavity is an open microcavity consisting of a planar bottom mirror and a curved top mirror [2]. A diamond membrane (thickness 500 nm to 2,000 nm) is bonded to the planar mirror via a van der Waals force [2]. Colour centres are best created in the diamond post-fabrication using ion implantation and annealing [3]. Here, NV centres were used.

Previous techniques to create diamond membranes resulted in a wedged shape and roughness at low spatial frequencies [2]. Both are problematic for low-loss operation in a cavity. These problems were remedied by developing a new fabrication protocol [4], Fig. 1. With this protocol, it is now possible to create constant-thickness membranes with sub-nanometre surface roughness, Fig. 2. We constructed an open microcavity with the new membranes and were able to demonstrate extremely high values of finesse, up to 30,000. This is important as a high value of finesse is required to optimise the efficiency of a spin-cavity interface employing an NV centre as the NV centre has a relatively small optical dipole moment.

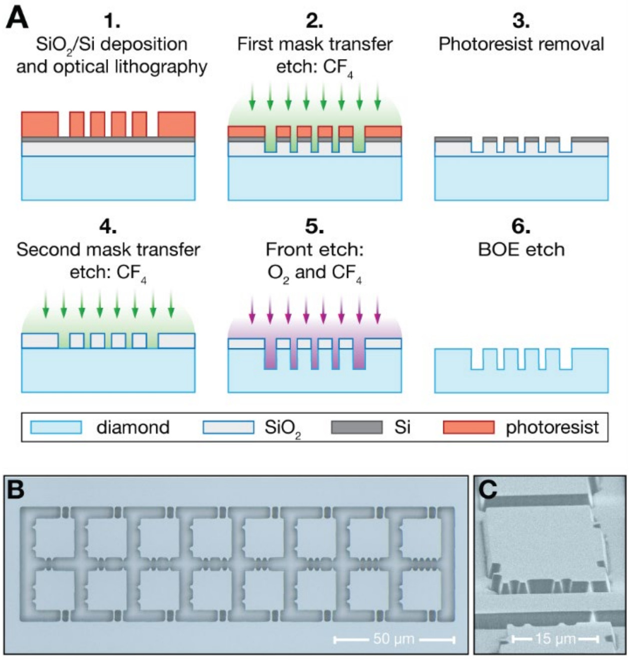

Fig. 1: Diamond membranes fabricated in the SNI's facilities. A: process flow. B: final membranes.

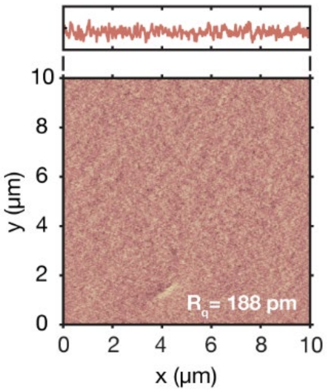

Fig. 2: Atomic force microscopy image of a diamond membrane fabricated using the new process showing a root-mean-square roughness of 0.188 nm.

Operation as a spin-photon interface hinges on the noise. In particular, charge noise results in noise in the emission frequency, a particularly severe problem for the NV centre. To probe the noise, we measured the homogeneous linewidth of a single NV centre in the open microcavity, Fig. 3. This constitutes a detection of resonance fluorescence, a challenging experiment as both laser and NV photons have the same frequency. By working in a dark-field mode (based on polarisation), we have achieved a signal:background ratio of 100:1. The photon flux is sufficient to enable a rapid measurement of the homogeneous linewidth. We find linewidths very close to the transform limit, Fig. 3. On longer timescales, the emission frequency exhibits a small drift, equivalently, noise at low-frequencies. A crucial discovery is that this drift is very sensitive to any residual green laser light. (The green laser is used to reset the NV's charge should it ionise.) Small levels of low-frequency noise could only be achieved by eliminating the green laser light completely.

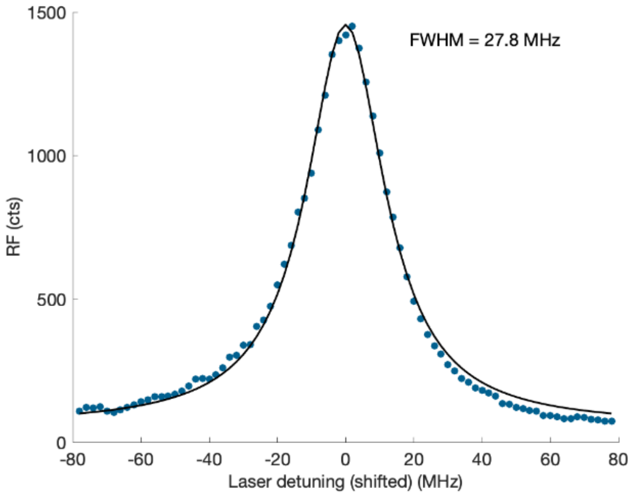

Fig. 3: Resonance fluorescence (RF) of a single NV centre in an open microcavity showing the linewidth (FWHM).

Conclusion

Two crucial steps have been made in the quest to create an efficient and coherent spin-photon interface using a colour centre in diamond: fabrication of constant-thickness ultrasmooth diamond membranes; demonstration of close to transform-limited optical linewidths on a single NV centre in an open microcavity.

References

[1] *M. Pompili et al, "Realization of a multinode quantum network of remote solid-state qubits", Science* ***372****, 259 (2021).*

[2] *Daniel Riedel et al, "Deterministic Enhancement of Coherent Photon Generation from a Nitrogen-Vacancy Center in Ultrapure Diamond", Physical Review X* ***7****, 031040 (2017).*

[3] *V. Yurgens et al, "Spectrally stable nitrogen-vacancy centers in diamond formed by carbon implantation into thin microstructures", Applied Physics Letters* ***121****, 234001 (2022).*

[4] *Andrea Corazza et al, "Homogeneous Free-Standing Nanostructures from Bulk Diamond over Millimeter Scales for Quantum Technologies", Nano Letters* ***25****, 14526 (2025).*

Coupled phonons in graphene nanoribbons

Project P2309: Graphene nanoribbon phonon dynamics
Project Leaders: M. Dimitrievska and M. Calame
Collaborator: Á. Labordet Álvarez (SNI PhD Student)

Introduction

Atomically precise graphene nanoribbons (GNRs) are one-dimensional semiconductors with width- and edge-controlled band gaps, making them promising building blocks for nanoelectronic and optoelectronic devices. For reliable device integration, it is essential to understand how their vibrational and electronic properties are modified by the environment. Our project addresses three tightly linked questions (Fig. 1):

1. **Defects** – how edge defects and "bite" defects [1] change the Raman response of 9-AGNRs and can be detected non-destructively;
2. **Substrate effects** – how metal and oxide substrates influence phonon energies and their temperature dependence;
3. **GNR–GNR interactions** – whether closely packed GNR arrays show collective vibrational behaviour that can be used as an additional tuning knob.

We combine low-temperature and temperature-dependent Raman spectroscopy with DFT calculations and advanced spectral analysis to build a consistent picture across these three aspects.

1. Defect-sensitive Raman modes in 9-AGNRs

Using multi-wavelength angle-resolved polarization Raman spectroscopy (ARPRS) at 70 K, we resolved the first-order Raman spectrum of aligned 9-AGNRs on Au(788) into 14 fundamental modes. Comparison with D_{2h} symmetry analysis and DFT assigns A_g and B_{1g} symmetries and reveals several defect-sensitive modes in the D and C–H regions. Modes near 1340 cm^{-1} (D) and 1240 cm^{-1} (C–H) show angular dependences that deviate strongly from the ideal symmetry behaviour, while backbone G modes follow theory. DFT calculations for pristine versus defected 9-AGNRs show that the D-derived feature around 1340 cm^{-1} and the C–H bending mode around 1240 cm^{-1} localise on edge hydrogens and respond strongly to edge disorder and "bite" defects; oscillator-strength calculations confirm that edge disorder selectively enhances the intensity of these edge-localised modes.

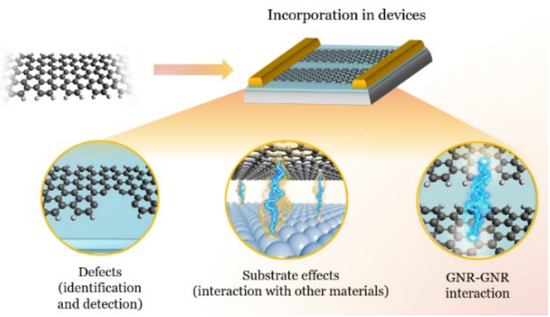

Fig. 1: Schematic overview of the project. Atomically precise 9-armchair graphene nanoribbons (9-AGNRs) are integrated into device structures. We investigate how three key environmental factors – edge "bite" defects and their Raman identification (left), substrate interactions with underlying materials (centre), and GNR–GNR interactions in dense arrays (right) – influence their properties.

Taken together, the RBLM (~310 cm^{-1}, width marker), the edge-localised C–H and D-derived modes in the 1240 cm^{-1} – 1340 cm^{-1} window, and the backbone G mode (~1600 cm^{-1}; Fig. 2c) define a compact Raman fingerprint for defect detection and quality control in 9-AGNRs, which we now use as a rapid screening metric for new samples.

2. Substrate-dependent temperature shifts of phonon modes

In 2025 we performed a systematic Raman study (70–300 K) on a well-defined "sample matrix" of 9-AGNR films (Fig. 2). The matrix comprises five morphologies that span three parameters: coverage (low vs high), in-plane order (aligned vs misaligned), and substrate (Au vs ALD-grown $Al_2O_3/SiO_2/Si$). In the following, each distinct combination of these parameters is referred to as a morphology within this matrix. For all morphologies, the G and D bands red-shift with increasing temperature, whereas the radial breathing-like mode (RBLM) is almost temperature-independent.

By fitting the G-mode shift $\Delta\omega(T)$ with a model including three-phonon anharmonicity and thermal-expansion-mismatch strain, and using literature thermal-expansion data for Au, sapphire and carbon nanotubes as a proxy for the GNR TEC, we find that $\Delta\omega(T)$ is dominated by thermal-expansion-coefficient (TEC) mismatch between substrate and GNR, rather than intrinsic anharmonicity, in our temperature window. Ribbons on Au exhibit larger $|d\omega/dT|$ than transferred films on oxide, consistent with stronger mechanical coupling and larger TEC mismatch. These results provide a quantitative reference for substrate-induced shifts of GNR Raman modes between 70 and 300 K, enabling future device measurements to separate intrinsic ribbon effects from thermal strain imposed by Au and $Al_2O_3/SiO_2/Si$.

3. Inter-ribbon coupling in dense GNR arrays

In high-coverage aligned arrays on Au(788) we observe a non-monotonic (U-shaped) temperature dependence of the G-mode linewidth, together with the appearance of an additional Raman band around 1300 cm^{-1} that is absent in low-coverage and misaligned arrays. The temperature evolution of peak position, intensity and line shape allows us to rule out several standard mechanisms as primary causes of the U-shaped $\Gamma(T)$: (i) unresolved LO/TO shoulders and other double-resonant features, (ii) phonon confinement in very narrow ribbons, (iii) 1D or array-induced zone folding, and (iv) electron–phonon coupling (EPC), for which we refer to standard Raman and linewidth literature [2–5]. Strain inhomogeneity may still contribute, but simple models (static strain distributions or monotonically increasing broadening with T) either produce purely monotonic Γ(T) or fail to reproduce both the U-shaped linewidth and the additional ~1300 cm^{-1} band. Our working hypothesis is that the U-shaped G-mode linewidth reflects phonon signatures of inter-ribbon excitonic coupling in a lateral GNR superlattice. DFT predicts strong lateral π–π overlap and edge-state splitting at our inter-ribbon distances [6], implying a non-negligible electronic (excitonic) coupling J between neighbouring ribbons. At low temperature, when dephasing is weak enough that an optical excitation can delocalise over several ribbons, this coupling can support phase-coherent superpositions of single-ribbon excitations (delocalised excitons), analogous to the extended exciton states in molecular J-aggregates [7]; this low-T regime of delocalised exciton states is what we refer to here as “coherent coupling between ribbons”. Via vibronic coupling, the Raman-active G mode then probes Davydov-split exciton states built from in-phase and out-of-phase combinations of these delocalised excitons, again in analogy to H- and J-aggregates [7]. As temperature increases, phonon-induced dephasing shortens the inter-ribbon exciton coherence length N_{coh}, in line with the decrease of N_{coh} with temperature discussed in Ref. [7]; this progressively suppresses the contribution of the Davydov partner and narrows the G band, before conventional anharmonic broadening dominates at the highest T. Packing density and alignment therefore emerge as key extrinsic parameters controlling phonon lifetimes in dense 9-AGNR arrays. At this stage the main implication is that inter-ribbon coupling cannot be neglected when interpreting Raman spectra of transferred, device-relevant films, where the transfer process can modify spacing and order. In the longer term, improved control over large-area transfer onto device substrates should allow this coupling to be deliberately exploited as an additional degree of freedom to adjust vibrational and transport properties without changing the ribbon chemistry.

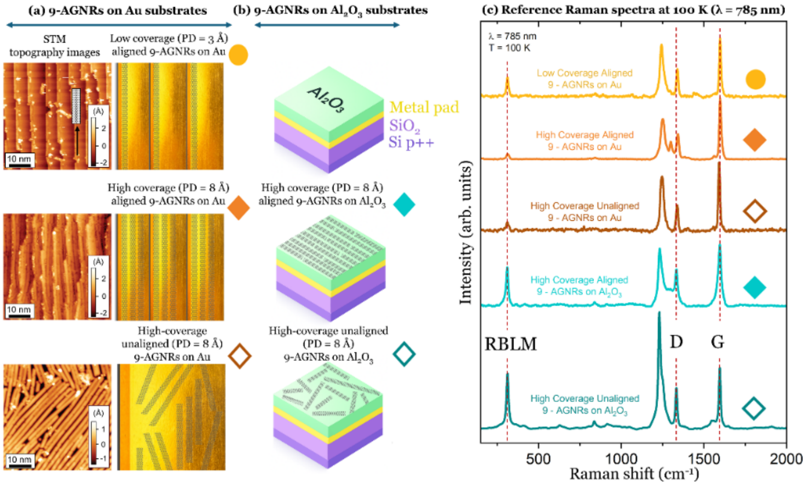

Fig. 2: Sample matrix of 9-AGNR films with controlled coverage, alignment and substrate. (a) STM and schematic images of low-coverage (precursor dose PD = 3 Å) aligned, high-coverage (PD = 8 Å) aligned and high-coverage (PD = 8 Å) unaligned 9-AGNR arrays on Au substrates. The precursor dose PD denotes the integrated monomer exposure during on-surface synthesis, as defined in Ref. [8]. (b) Schematic cross-sections of the corresponding high-coverage aligned and unaligned films transferred onto ALD-grown $Al_2O_3/SiO_2/Si$ stacks. (c) Reference Raman spectra at 100 K (λ = 785 nm) for all morphologies, showing the radial breathing-like mode (RBLM), D and G bands that serve as the main probes of phonon dynamics in this work.

Conclusion

Within this project we have:

- established polarization-resolved Raman fingerprints for defect detection in 9-AGNRs,
- quantified how substrate-induced thermal strain governs temperature-dependent Raman shifts, and
- obtained spectroscopic evidence that GNR–GNR interactions in dense arrays lead to collective phonon behaviour and non-trivial linewidth trends.

These results show that the vibrational response of GNRs is not only a property of an isolated ribbon, but is strongly shaped by defects, substrate and packing. In the next phase we will move to voltage-gated devices based on high-coverage aligned 9-AGNR arrays. We plan to correlate Raman linewidths with conductance (Γ(FWHM) vs G) under gate bias, testing whether injected carriers screen or disrupt inter-ribbon coherence, and to extend our defect-sensitive Raman metrics to study how controlled defect densities affect both phonons and transport. This will directly connect the fundamental phonon physics explored here with device performance.

References

[1] M. Pizzochero, et al., "Quantum electronic transport across 'bite' defects in graphene nanoribbons," 2D Materials, vol. 8, no. 3, p. 035025, 2021.
[2] A. C. Ferrari and D. M. Basko, "Nat. Nanotechnol.," Nature Nanotechnology, vol. 8, pp. 235–246, 2013.
[3] J.-B. Wu, et al., "Raman spectroscopy of graphene-based materials and its applications in related devices," Chemical Society Reviews, vol. 47, no. 5, pp. 1822–1873, 2018.
[4] N. Bonini, et al., "Phonon anharmonicities in graphite and graphene," Physical Review Letters, vol. 99, no. 17, p. 176802, 2007.
[5] M. Lazzeri, et al., "Phonon linewidths and electron-phonon coupling in graphite and nanotubes," Physical Review B: Condensed Matter and Materials Physics, vol. 73, no. 15, p. 155426, 2006.
[6] J. Zhao, et al., "Lateral in-plane coupling between graphene nanoribbons: A density functional study," Journal of Applied Physics, vol. 111, no. 4, 2012.
[7] N. J. Hestand and F. C. Spano, "Expanded theory of H- and J-molecular aggregates: the effects of vibronic coupling and intermolecular charge transfer," Chemical Reviews, vol. 118, no. 15, pp. 7069–7163, 2018.
[8] R. Darawish, et al., "The role of precursor coverage in the synthesis and substrate transfer of graphene nanoribbons," Nanoscale Advances, vol. 7, no. 7, pp. 1962–1971, 2025.

Induced quantum dot microscopy of germanium and graphene quantum devices

Project P2401: Induced quantum dot microscopy of germanium and graphene quantum devices
Project Leaders: A. Hofmann, M. Poggio and F. Braakman
Collaborator: P. Raif (SNI PhD Student)

Introduction

Quantum dots and related quantum devices form the basic ingredients for experiments on quantum computation using spin or charge qubits [1], as well as for experiments exploring fundamental physics, such as studying emergent particles and the physics of unconventional superconductivity [2]. In recent years, planar germanium-based heterostructures have become a leading platform for such experiments, in particular for the implementation of spin qubit processors [3], featuring long coherence times and fast logical operations [4-6]. However, even in such high-quality spin qubit devices, important qubit parameters show significant variations from device to device, and from qubit to qubit. Basic quantities such as pinch-off voltages, tunnel barrier heights, Landé g-factors, spin-orbit lengths, and valley splittings have spatial variations to such an extent that in practice, individual quantum dots and qubits need to be configured one at a time. This necessitates long tuning processes, or worse, trying out different devices until a suitable one is found. Moreover, all these properties are usually only measured at few individual sites, or even averaged over a few sites, through electrical transport and qubit measurements. Such measurements therefore do not yield much spatial information on the variations of the above-mentioned properties. In addition, typical qubit devices go through many fabrication steps, which likely creates even further variation of these parameters due to the application of heat, residues of resists, and the strain of the deposited materials onto the substrate.

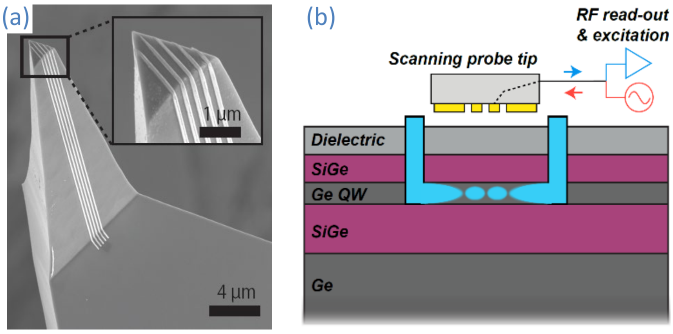

Fig. 1: (a) SEM image of a scanning probe tip patterned with 5 gates. [9] (b) Schematic illustration of a double quantum dot (blue central dots) in a Ge QW, induced by voltage biasing of gates (yellow) on the tip of a moveable scanning probe. Quantum dots can be excited and detected through gate-based dispersive RF read-out, also via the gates on the scanning probe tip. Also shown are two contacts, which could be used for additional on-sample measurements in a Hall bar setup.

Here, we aim to spatially map out these important properties to understand sample-variations and the influence of the fabrication onto the qubit performance. For this, we will use our newly developed scanning multi-gate microscopy operating at mK temperatures and relatively high magnetic fields. Specifically, the multi-gate tips allow creating the desired device potential landscapes, dispersive probing enables read-out via the scanning probe, and the high bandwidth enables such measurements within qubit coherence times. As a substrate, we will focus on Ge quantum well samples, making use of our existing know-how. However, the technique will be material-independent to a large extent and can also be applied to bilayer graphene devices, a promising field of research being investigated by the Hofmann group.

Fabrication and Measurements

The confinement of charges in a quantum dot require size quantization in all three spatial directions. The in-plane confinement is provided by the Ge quantum well. Mesa etching of this quantum well into a one-dimensional wire and finger gates patterned on the scanning probe tip provide the additional confinement. Both of these measures require delicate fabrication recipes. Regarding the mesa etching, a method had to be developed to locally etch the SiGe barrier while protecting the channel itself. We found that, while electron-beam resist usually was hard-baked in the etching process and could not be lifted off, an Al hard mask was well suited for the etching process. An image of the etched mesa channel and its height profile is shown in Fig. 2. In order to test the suitability of this mesa for quantum dot measurements, we went on to fabricate on-chip gates, which will later be replaced by the gates on the

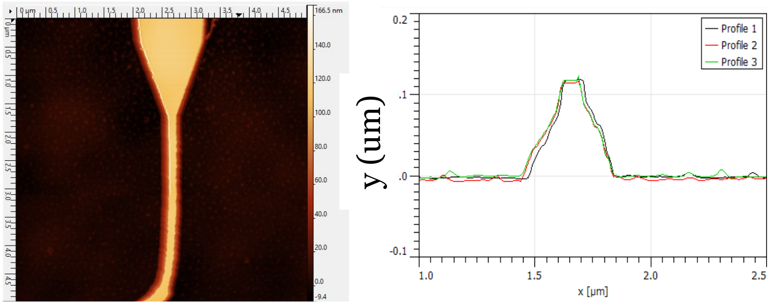

Fig. 2: Atomic force micrograph of the etched channel (left) and its height profile (right).

scanning probe tip. Measurements at 4 K revealed transport through the channel, which could be pinched off by the on-chip gates. However, no clear signatures of a quantum dot were visible. Possible reasons include the comparably (to the charging energy) high measurement temperature and the large width of the finger gates which possibly prevent transport through the channel before properly confining the states into a quantum dot. For this reason, we are currently in the process of down-sizing the finger gate patterns.

Scanning multi-gate microscopy

We have produced several scanning probe cantilevers with 3 to 5 finger gates patterned at the underside, using fabrication techniques detailed in [9]. The gates can be contacted through wire bonding and can thus be voltage-biased. Fig. 3 shows first proof-of-principle measurements taken at a temperature of 4 K, where a multi-gate probe (top left), was used to modulate the current in a contacted InAs nanowire sample. As can be seen in the spatial scans, the current through the nanowire gets reduced when a biased gate is scanned over it, revealing a spatial pattern in the shape of the gate. These results illustrate that each gate of the multi-gate probe is functional and can be used to generate the specific potential landscape at a sample underneath suitable for inducing tunnel barriers and QDs.

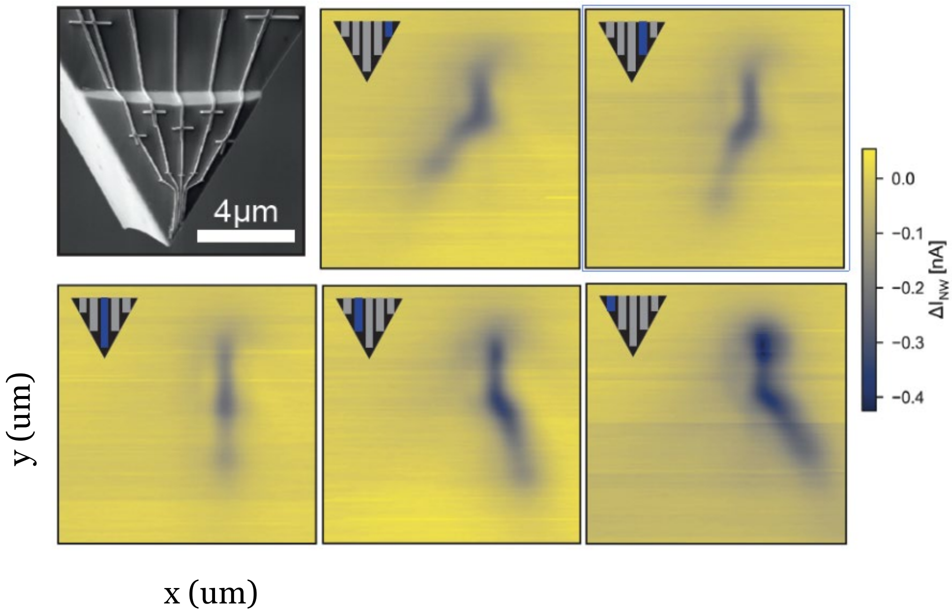

Fig. 3: Top left panel: SEM image of tip of AFM cantilever patterned with 5 nanoscale finger gates. Other images: Constant-z current scanning probe images of a bare InAs nanowire, recorded while biasing one cantilever gate at −2 V (indicated in insets).

Outlook

Having tested the suitability of the etched channel for quantum dot measurements, as well as the functionality of multi-gate cantilevers at 4 K, we will move from on-chip defined to scanning probe defined quantum dot gates. Meanwhile, first steps have been taken to implement induced scanning probe microscopy on bilayer graphene samples.

References

[1] *G. Burkard et al., Semiconductor spin qubits, Rev. Mod. Phys.* ***95****, 025003 (2023).*

[2] *E. Prada et al., From Andreev to Majorana bound states in hybrid superconductor–semiconductor nanowires, Nat. Rev. Phys.* ***2****, 575 (2020).*

[3] *G. Scappucci et al., The germanium quantum information route Nat. Rev. Mat.* ***6****, 926 (2021).*

[4] *N. Henrickx et al., A single-hole spin qubit, Nat. Commun.* ***11****, 3478 (2020).*

[5] *N. Henrickx et al., Fast two-qubit logic with holes in germanium, Nature* ***577****, 487 (2020).*

[6] *D. Jirovec et al., A singlet-triplet hole spin qubit in planar Ge, Nat. Mater.* ***20****, 1106 (2021).*

[7] *A. Denisov et al., Microwave-Frequency Scanning Gate Microscopy of a Si/SiGe Double Quantum Dot, Nano. Lett.* ***22****, 4807 (2022).*

[8] *Y. Shim et al., Induced quantum dot probe for material characterization, Appl. Phys. Lett.* ***114****, 152105 (2019).*

[9] *L. Forrer et al., Electron-beam lithography of nanostructures at the tips of scanning probe cantilevers, AIP Adv.* ***13****, 035208 (2023).*

Spin wave imaging and control at the nanoscale

Project P2402: Spin waves get a twist!
Project Leader: V. Scagnoli and P. Maletinsky
Collaborator: E. Ersoy (SNI PhD Student), K. Wagner

Introduction

Spin waves, which are collective dynamic excitations of magnetic systems, have emerged as a central topic in modern condensed matter physics [1]. By transporting spin information without the motion of charge carriers, they offer promising opportunities for low-power information processing with minimal energy dissipation, contributing to reduced energy consumption and environmentally sustainable computing technologies. In parallel, non-uniform magnetic configurations, such as domain walls, vortices, and skyrmions, have gathered interest due to their potential applications for next generation memory and logic devices [2, 3]. A particularly appealing research direction is to integrate spin waves with such magnetic textures, which can act as scatterers, waveguides, or emitters of spin waves [4]. However, identifying a material platform that simultaneously supports stable, controllable magnetic textures and long-range spin-wave propagation remains challenging. A promising approach is to interface yttrium iron garnet (YIG), a magnetic insulator with exceptionally low damping, with texture-hosting materials. Past works have already demonstrated the steering and scattering of spin waves in decorated YIG samples [5]. Building on these advances, the aim of this project is to design and fabricate YIG-based heterostructures to couple magnetic textures, and to characterize their magnetic properties using advanced imaging techniques.

To image these magnetic systems, this project relies on scanning nitrogen-vacancy (NV) center magnetometry as the primary experimental technique, as depicted in Fig 1(a). This technique provides quantitative, non-invasive measurements of local magnetic stray fields with nanoscale spatial resolution and high sensitivity under ambient conditions [7]. This makes it particularly well suited to imaging nanoscale magnetic textures [8] as key details can often only be revealed for resolutions below 100 nm. In addition to static imaging, NV magnetometry offers powerful capabilities of probing magnetization dynamics, such as the oscillating magnetic fields created by propagating spin waves [9]. This dual sensitivity to static and dynamic magnetic fields makes NV magnetometry a key tool in this project, enabling a unified investigation of spin textures, spin-wave propagation, and their mutual coupling within the same experimental platform.

Main Results

This year, we focused on identifying suitable material systems that host robust and controllable magnetic textures under ambient conditions and are suitable for interfacing with YIG. In our experimental investigations we targeted $NdMn_2Ge_2$, a rare-earth non-collinear antiferromagnet known to host a skyrmion bubble lattice at room temperature without applied magnetic field [10]. These skyrmion bubbles are stabilized by dipolar interaction, since the system has no intrinsic Dzyaloshinskii-Moriya interaction due to its centrosymmetric crystal structure. It has been shown that the skyrmion bubble lattice in this material remains stable over periods exceeding one year, including temperatures up to the material's Curie temperature of 330 K and magnetic fields reaching 160 mT [11].

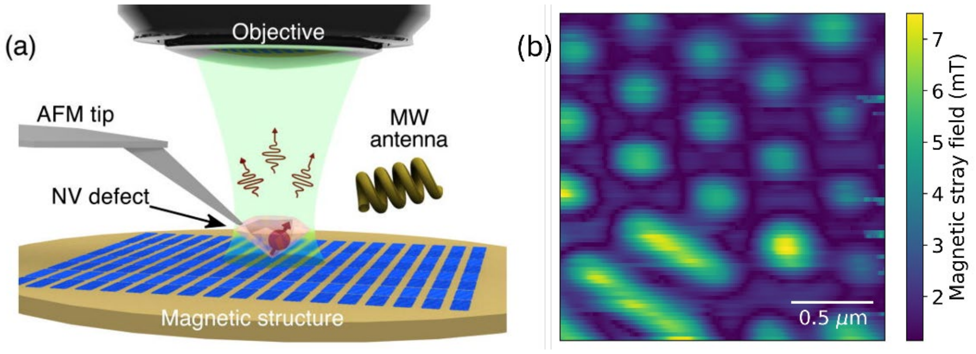

Fig. 1: (a) Simplified scheme of scanning NV magnetometry. Figure taken from [6]. (b) The skyrmion bubble lattice in $NdMn_2Ge_2$ imaged by scanning NV magnetometry.

The sample studied here is a 190 nm thick circular $NdMn_2Ge_2$ lamella of 4 μm diameter that was cut from a bulk crystal. The skyrmion bubble lattice is initialized via the following protocol, developed in an earlier SNI PhD project.

First, a current is applied to heat the sample above its Curie temperature, $T_C = 330\ \mathrm{K}$. Second, an out-of-plane magnetic field of 40 mT is applied while the sample is still heated. Then, the current is turned off to stop the heating while the external field is maintained. Finally, once the sample cools down to ambient temperature, the external field is removed. After this protocol, the sample is stabilized in the skyrmion bubble lattice configuration, which is then imaged using scanning NV magnetometry. The measurements are performed by scanning a diamond probe hosting a single NV center over the sample at a lift height of approximately 240 nm. At each position, the local magnetic stray field is quantitatively measured using optically detected magnetic resonance. A representative image is shown in Figure 1(b), revealing a stable triangular skyrmion bubble lattice. Beyond imaging, we demonstrate the ability to locally manipulate the magnetic texture using focused laser pulses as shown in Figure 2. Microsecond-long pulses delivered through the diamond tip allow for localized heating within a confined area. Following this excitation, the magnetic configuration reveals a modification of the lattice, where several skyrmion bubbles near the target location merge to form larger magnetic domains. Although at an early stage, this local manipulation ability highlights the potential for on-chip spin-texture engineering.

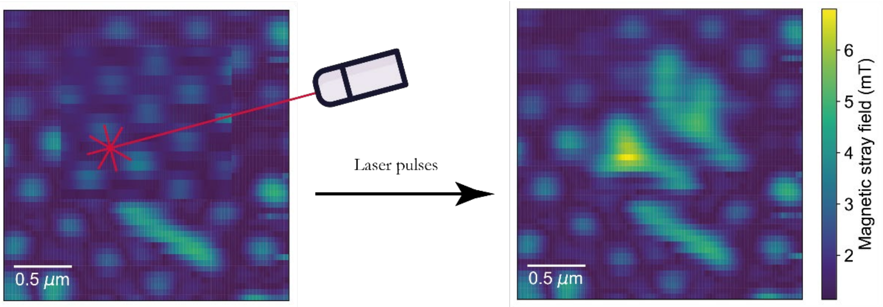

Fig. 2: Demonstration of skyrmion bubble lattice manipulation in $NdMn_2Ge_2$ by laser pulses. The figures on the left and right show the magnetic configuration before and after the laser pulses respectively.

Conclusion

In this work, we have established scanning NV center magnetometry as a powerful tool to image magnetic textures in materials hosting skyrmions at room temperature. Using $NdMn_2Ge_2$, we demonstrated the stabilization and high-resolution imaging of a skyrmion bubble lattice under ambient conditions, as well as preliminary control over its local configuration. These results provide an important experimental foundation for the next stage of the project, which aims to combine texture-hosting materials with low-damping platforms such as YIG in engineered heterostructures. Such systems will enable systematic studies of spin wave–texture interactions, including scattering and guiding. While the present manipulation capabilities remain at an early stage and require improved precision, they open the door to in situ control of magnetic textures within a single reconfigurable device. Future studies will also explore dynamic spin textures, such as gyrating skyrmions, as potential sources of spin-wave emission [12], further enriching the potential in hybrid magnetic systems combining spin waves with magnetic textures.

References

[1] A. V. Chumak, V. I. Vasyuchka, A. A. Serga, B. Hillebrands, Magnon spintronics, Nat. Phys. ***11****, 453 (2015).*

[2] S. S. P. Parkin, M. Hayashi, L. Thomas, Magnetic domain-wall racetrack memory, Science ***320****, 190 (2008).*

[3] A. Fert, V. Cros, J. Sampaio, Skyrmions on the track, Nat. Nanotechnol. ***8****, 152 (2013).*

[4] H. Yu, J. Xiao, H. Schultheiss, Magnetic texture based magnonics, Phys. Rep. ***905****, 1 (2021).*

[5] T. X. Zhou, J. J. Carmiggelt, L. M. Gächter, I. Esterlis, D. Sels, et al., A magnon scattering platform, Proc. Natl. Acad. Sci. U.S.A. ***118****, e2019473118 (2021).*

[6] L. Rondin, J.-P. Tetienne, P. Spinicelli, C. Dal Savio, K. Karrai, et al., Nanoscale magnetic field mapping with a single spin scanning probe magnetometer, Appl. Phys. Lett. ***100****, 153118 (2012).*

[7] L. Rondin, J.-P. Tetienne, T. Hingant, J.-F. Roch, P. Maletinsky, et al., Magnetometry with nitrogen-vacancy defects in diamond, Rep. Prog. Phys. 77, 056503 (2014).

[8] Y. Dovzhenko, F. Casola, S. Schlotter, T. X. Zhou, F. Büttner, et al., Magnetostatic twists in room-temperature skyrmions explored by nitrogen-vacancy center spin texture reconstruction, Nat. Commun. ***9****, 2712 (2018).*

[9] T. van der Sar, F. Casola, R. Walsworth, A. Yacoby, Nanometre-scale probing of spin waves using single-electron spins, Nat. Commun. ***6****, 7886 (2015).*

[10] S. Wang, Q. Zeng, D. Liu, H. Zhang, L. Ma, et al., Giant topological Hall effect and superstable spontaneous skyrmions below 330 K in a centrosymmetric complex noncollinear ferromagnet NdMn2Ge2, ACS Appl. Mater. Interfaces ***12****, 24125 (2020).*

[11] S. K. Treves, V. Ukleev, A. Apseros, J. R. Massey, K. Wagner, et al., Investigating skyrmion stability and core polarity reversal in NdMn2Ge2, Sci. Rep. ***15****, 461 (2025).*

[12] J. Chen, J. Hu, H. Yu, Chiral emission of exchange spin waves by magnetic skyrmions, ACS Nano ***15****, 4372 (2021).*

Quantum Sensing Towards Direct Observation of Dynamics in Biomolecules

Project P2403: Quantum Sensing of Biomolecules and Their Chemical Stimuli
Project Leader: S. Schmid and P. Maletinsky
Collaborator: R. Liu (SNI PhD Student)

Introduction

The goal of this project is to employ quantum sensing based on nitrogen-vacancy (NV) centers in diamond nanopillars for the detection of single biomolecules and their transient interactions and cooperativity behaviour. The measurement setup, including a confocal microscope and microwave delivery, is constructed from the ground up based on state-of-the-art equipment.

To interface biological targets with the NV sensor, we implement a new surface functionalization strategy inspired by Li [1] and Xie [2], based on photo-catalyzed charge-state conversion [3]. This chemistry minimizes the NV–protein distance while ensuring covalent immobilization of individual biomolecules on the nanopillar tip. We focus on metalloproteins as biological model systems for studying sequential ion binding, cooperativity, and multi-step magnetic signatures.

Setup Construction

We completed construction and optimisation of a confocal microscope for this project and achieved stable NV fluorescence detection on reference samples, establishing the foundation for spin-based measurements. Fully synchronized control electronics — combining microwave delivery, pulse sequencers and photon-counting detection — have been integrated to allow optically detected magnetic resonance (ODMR) and T_1 relaxometry.

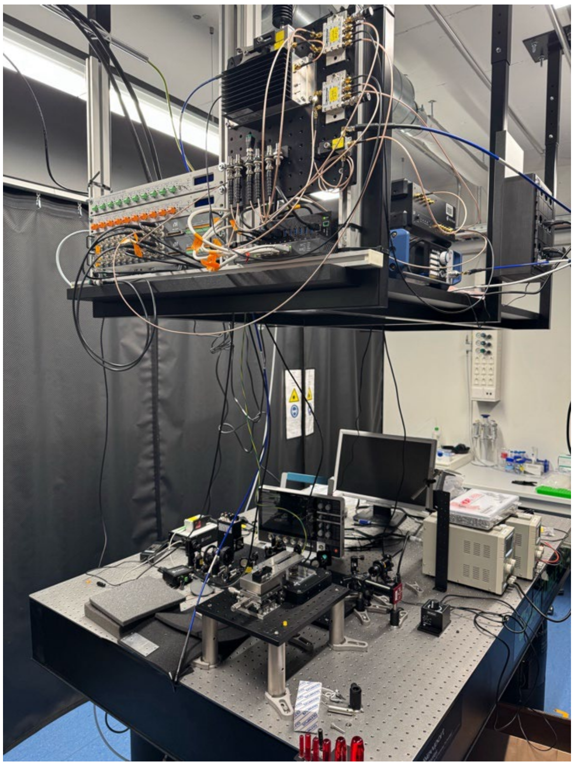

Figure 1. Integrated quantum sensing setup combining confocal microscopy, synchronized microwave control, AOM-modulated laser excitation, and APD fluorescence detection. Left: photograph of the assembled system. Right: electronic and optical schematics of the control architecture.

Reference NV samples have been used to validate the confocal microscope performance and fiber-coupling efficiency. In addition, the beam quality of the excitation path was characterized using the razor-blade method, confirming a near-Gaussian intensity profile with an ellipticity of 1.039. From the measured $1/e^2$ beam waists, we further extracted the effective numerical aperture of the objective under experimental conditions. The resulting NA closely matches the optical acceptance of the diamond nanopillar waveguide, ensuring efficient coupling of the pump light into the pillar and thereby reliable optical initialization and readout of shallow NV centers.

Surface Functionalization Strategy

Achieving reliable single-molecule sensing requires minimizing the NV–protein distance while ensuring chemical robustness. Based on mild oxygen termination and photo-catalyzed charge-state conversion [3], we propose a localized covalent immobilization strategy that avoids unnecessary spacer layers and reduces steric barriers typical in polyethylene-glycol(PEG)-based approaches.

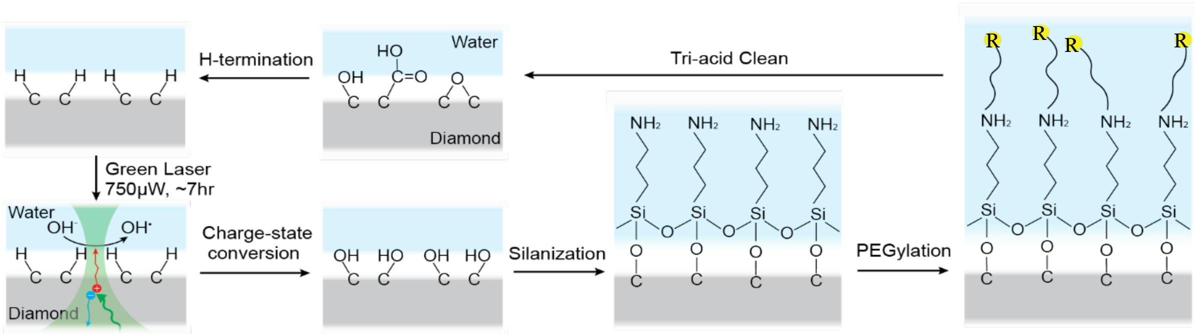

Figure 2: Surface functionalization strategy for single-protein immobilization on diamond nanopillars. After tri-acid cleaning and H-termination, prolonged laser irradiation induces photo-catalyzed charge conversion that locally oxidizes surface groups to –OH. The hydroxylated region enables efficient silanization and subsequent PEGylation for covalent attachment of the target biomolecule, while the surface can be fully restored by acid cleaning.

A Biomolecular Model System for Metal-ion Sensing

Transient interactions between biomolecules and ions drive essential functions in living organisms, with key biomedical and biotechnological implications. No current technique directly observes such transient events. To address this, we use trivalent lanthanid-binding biomolecules as models to pioneer novel quantum biosensing technology. These ions produce strong paramagnetic noise, enabling direct readout via NV “T_1 relaxometry”. Multiple binding sites cause multi-step changes in magnetic noise amplitude, thereby modulating the NV relaxation rate. We expect to convert T_1 sensing into a fast binary “state detector” for individual binding events. Together with theoretical modeling, we will estimate achievable time resolution for different NV-protein distances, explicitly incorporating realistic rotational correlation times of the protein-ion complex, which govern fluctuation spectra and thus relaxometry contrast.

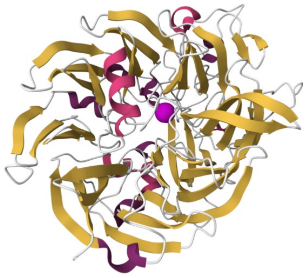

Figure 3. Structure of a metallo-protein with lanthanide-binding site (center). PDB: 6OC5

Conclusion

We have constructed the optical, electronic, and software framework for a NV-based quantum sensing platform, and proposed a new surface functionalization approach based on locally photo-catalyzed charge conversion, and designed the workflow for observing multi-step metal-ion binding applicable to diverse biomolecules. The project has strong synergistic effects between the Schmid and Maletinsky groups: know-how about the quantum sensing setup and NV creation has been fully transferred to the Schmid group, where the project is predominantly hosted, while the latter is contributing single-molecule biophysics expertise and bio-interfacing know-how.

In the coming year, we will finalize the microwave chain and ODMR calibration to enable spin manipulation, and establish a reversible metal-binding model system to validate sequential binding detection. We will complement these experiments with theoretical estimates of achievable time resolution and SNR at different NV–protein distances.

References

[1] M. Li et al., arXiv, 2506.20714 (2025).
[2] M. Xie et al., Proceedings of the National Academy of Sciences, 119, (2022).
[3] Lila et al., Proceedings of the National Academy of Sciences, 121, (2024).

Engineering proteins with multinuclear metal complexes as cofactors

Project P2404: Recruiting synthetic metal oxo nanoclusters as enzyme cofactors
Project Leaders: F. P. Seebeck, J. De Roo
Collaborator: I. Nonikashvili (SNI PhD Student)

Introduction

Metalloclusters bound to proteins drive some of biology's most essential reactions, such as nitrogen fixation, photosynthetic oxygen evolution, and metabolic pathways like the citric acid cycle. Given their chemical flexibility and spontaneous self-assembly, iron-sulfur clusters are thought to have been crucial to the origins of life, allowing even primitive heritable catalysts like ribozymes to perform the complex chemistry needed to construct cellular components from simple geochemical precursors [1].

While numerous enzymes containing multinuclear metal cofactors are known—catalyzing diverse reactions with clusters of varying sizes and geometries—natural evolution has explored only a narrow subset of the vast chemical landscape accessible through transition metal cluster chemistry. This constraint likely stems from the limited bioavailability of many transition metals in Earth's crust, their low solubility under biological conditions, and kinetically unfavorable assembly pathways. Consequently, natural evolution has never had the opportunity to develop a wide array of potentially useful catalysts.

In this project we explore new approaches to combine polynuclear metal complexes with designed proteins as possible starting points to develop biocatalysts. In pursuit of this goal, we have established protocols for the production of designed recombinant proteins, and we have developed key techniques to study their ability to combine with synthetic metal clusters.

Main Results

The results we have gathered since June 2025 give us strong confidence that we will achieve the goals described in the proposal. We have established a highly collaborative working relationship between the De Roo and Seebeck labs, including frequent joint meetings with the PIs and PhD student, exchange of materials, and insights into analytical methodologies. Iya Nonikashvili has trained in techniques for recombinant protein production, spectroscopic analysis of metal complexes, and synthesis of inorganic compounds. In addition, protein crystallography has emerged as a central tool for understanding the structure of metal-loaded proteins. Iya has therefore begun crystallizing proteins and will spend the next three months (February–April 2026) working in a structural biology laboratory at the Helmholtz-Zentrum für Infektionsforschung to train in protein crystallography.

Conclusion

Our preliminary results from the biochemical analysis of metal-bound proteins provide strong evidence that the general concept underlying this research project will likely prove fruitful. These early findings demonstrate that our protein scaffolds are indeed capable of coordinating the designed metal complexes, and initial characterization suggests that the resulting hybrid species exhibit the anticipated properties. However, our work has also revealed that creating these novel chemical entities presents significant analytical challenges that were not fully anticipated at the project's outset.

Specifically, the unique nature of these protein-metal hybrids—which combine characteristics of both biological macromolecules and inorganic coordination complexes—requires analytical techniques that bridge traditional biochemistry and inorganic chemistry. Standard protein characterization methods must be adapted or complemented with specialized spectroscopic and structural approaches to fully elucidate the metal coordination environment, oxidation states, and dynamic behavior of these systems. Furthermore, assessing the stability of these species under physiologically relevant conditions requires careful optimization of experimental protocols.

We have come to recognize that the development of robust analytical approaches to determine the structure, stability, and functional properties of our novel protein-metal species will constitute an important and valuable outcome of this SNI project in its own right. The methodologies we establish will not only enable us to characterize our target systems but will also provide a foundation for future research in this emerging area of protein-inorganic chemistry. These analytical tools and protocols will be broadly applicable to other researchers working at the interface of bioinorganic chemistry and protein engineering.

References

[1] C. Rees, "GREAT METALLOCLUSTERS IN ENZYMOLOGY", Annu. Rev. Biochem ***71****, 221 (2002).*

Lipid-core polymer-shell hybrid nanoparticles for the delivery of mRNA against bacterial infections

Project P2405: Novel mRNA nanotherapeutics against antibiotic-resistant pulmonary infections
Project Leaders: O. Tagit, N. Khanna and D. Bumann
Collaborator: T. Flathmann (SNI PhD Student)

Introduction

The increase of antimicrobial resistance (AMR) in hospital- and community-acquired bacterial infections and the decreasing effectiveness of existing antibiotics is a global health concern. By 2021, about 1.14 million deaths worldwide were caused directly by AMR, and this number is predicted to increase by another 68% by the end of the decade [1]. As the number of pathogens acquiring resistance against last-resort antibiotics such as Carbapenem is rising, exploring innovative treatment options is of utmost importance.

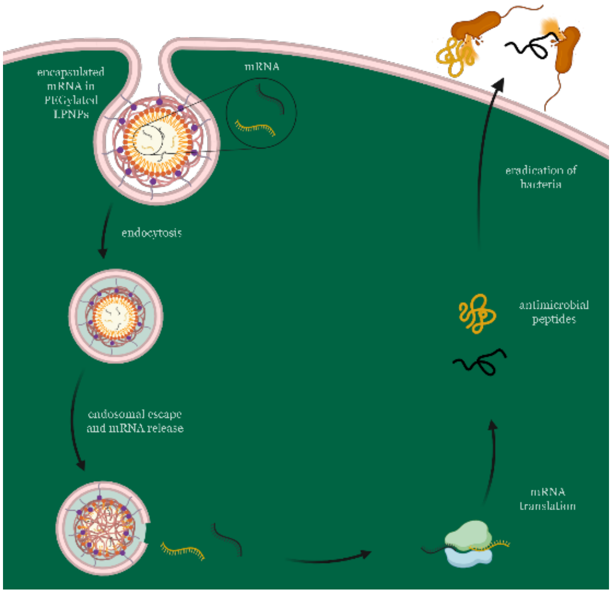

Fig 1: Proposed working principle of mRNA-loaded LPNPs to fight infections. Particles are taken up via endocytosis; mRNA is translated to AMPs after endosomal escape; AMPs are excreted from cells and eradicate bacteria. Created in BioRender.com.

Antimicrobial peptides (AMPs) offer a promising alternative. These short, often cationic peptides are produced naturally by most living organisms and act upon multiple targets in Gram-positive and -negative bacteria. Most AMPs kill bacteria in an unspecific manner, by disrupting their membranes, circumventing existing molecular resistance pathways and reducing the risk of resistance development. However, they are prone to proteo- and hydrolytic degradation and are often toxic or immunogenic in vivo [2].

The aim of this project is to develop novel mRNA therapeutics to synthesize AMPs directly at the infection site. Once translated, the encoded AMPs can act on both intracellular and extracellular infections (Scheme 1). As nanocarrier, we have developed a novel class of lipid-polymer hybrid nanoparticles (LPNPs) made from distearoylphosphatidylcholine (DSPC), poly-(lactic-co-glycolic acid) (PLGA), polyethylene glycol (PEG) and cationic lipid 1,2-dioleoyl-3-trimethylammonium propane (DOTAP). The carrier combines the benefits of efficient mRNA encapsulation in the cationic lipid core with the superior stability of a polymeric shell, making it the ideal candidate for our case.

LPNP Manufacturing process

We used a TAMARA microfluidic system (Inside Therapeutics) to prepare LPNPs with optimal particle properties in a reproducible manner. Briefly, in a first step, the lipid components, comprised of DSPC, DOTAP and PEG are dissolved in an organic phase and mixed in a Herringbone chip with a volume of aqueous solution containing mRNA. The resulting lipid nanoparticle-water dispersion is then reintroduced back into the microfluidic system in a second step and mixed with an organic phase of PLGA solution. By passing the Herringbone chip, the PLGA assembles as a polymer layer surrounding the lipid nanoparticle core. These LPNPs are collected in a 2% aqueous polyvinyl alcohol (PVA) solution, which acts as a surfactant to prevent aggregation of the particles. After washing, we analyzed the LPNPs and lyophilized them for long-term storage. In total, we produced empty LPNPs and LPNPs encapsulating mCherry mRNA and Bodipy (BODIPY™ 493/503) for subsequent analyses.

Characterization of LPNPs

For the approval of therapeutic nanoparticle formulations by regulatory bodies such as the FDA, it is important to provide detailed information on the physicochemical properties of the particles, including morphology, size distribution and to prove batch-to-batch reproducibility of the particles [3].

Scanning transmission electron microscopy (S-TEM) reveals smooth, spherical morphology of LPNPs. Additionally, the distinctly separated inner and outer regions of differing electron density within the particles suggest the presence of the hypothesized core-shell structure (Fig. 1a). Via dynamic light scattering (DLS) analysis, we are able to show strong batch-to-batch consistency, with a mean hydrodynamic diameter of 144 ± 4 nm and a polydispersity index (PDI) of 0.04 ± 0.02 (Fig. 1b). LPNPs loaded with Bodipy or mCherry mRNA show similar behavior. The percent encapsulation efficiency (EE%) of cargo into LPNPs is defined as:

$$\mathrm{EE\%} = {}^{\mathrm{m}_{\text{LPNP cargo}}}\!/\,\mathrm{m}_{\text{total cargo in initial formulation}}$$

In our nanoparticle carrier system, mRNA is encapsulated by electrostatic attraction to the cationic lipid DOTAP. The N/P ratio between positively charged amines in the DOTAP and negatively charged phosphate groups on the mRNA backbone can be adjusted by changing relative amounts of mRNA or DOTAP in the formulation. Using an N/P ratio of 3, we determined the EE% by breaking the particles with 0.5% v/v Triton and performing a Ribogreen® fluorescence assay, where the dye's fluorescence can be directly correlated with the amount of mRNA it complexes with. With this formulation, we found that much of the mRNA remains unencapsulated, as indicated by an EE% of approximately 10%.

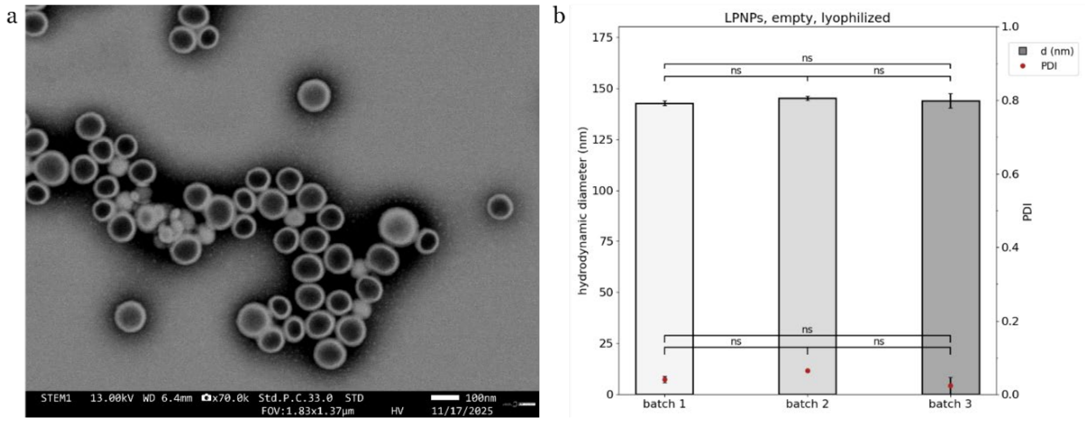

Fig. 2: a. Representative S-TEM micrograph of empty LPNPs after lyophilization and rehydration. Different light and dark regions within the nanoparticles represent areas of differing electron density and confirm a lipid-core polymer-shell-like structure. Negative staining (black halo surrounding the LPNPs) was done with UranyLess EM Stain. b. Hydrodynamic diameter and PDI of three separate batches of lyophilized LPNPs, measured on a LiteSizer DLS (Anton Paar). Pairwise Welch's t-test, corrected via Holm's multiple comparison. ns: $p \geq 0.05$.

Aside from the morphology and physicochemical properties of our LPNPs, we have started to investigate their biological effects. To check for potential cytotoxic effects of the unloaded particles, we performed an *in vitro* MTT assay on HepG2 cells. We observed a concentration-dependent decrease in cell metabolic activity down to 50% for a dose of 4 mg LPNPs per 1×10^6 cells after 48 h. To assess the uptake of LPNPs into target cells, we incubated A549 lung epithelial cells with Bodipy-loaded LPNPs. Uptake of the nanoparticles leads to an accumulation of fluorescence inside the cells. Preliminary flow cytometry experiments reveal successful uptake into the cells as early as 30 min after incubation, with a steady increase in uptake visible until 20 h.

Conclusion and Outlook

Thus far, we have been able to synthesize both empty LPNPs and ones bearing mRNA cargo, with an N/P ratio of 3. We have confirmed their uniform size distribution and mRNA uptake abilities, and analyzed morphology, cell toxicity and -uptake of unloaded particles. As a next step, we will expand the preliminary morphological S-TEM analyses, cell uptake and toxicity tests to mRNA-bearing LPNPs. By increasing the N/P ratio, we hope to enhance the EE%. Using flow cytometry, we will also study the uptake of Bodipy-loaded LPNPs into phagocytotic and endothelial cells. Furthermore, via endosome co-localization in confocal fluorescence live-cell imaging, we will investigate whether the proposed endosomal uptake and release mechanism of nucleic acid cargo holds true for our novel nanoparticle system [4]. Finally, it will be of great importance to determine the minimal inhibitory concentration (MIC), minimal bactericidal concentration (MBC) and bacterial killing kinetics of the target AMP, and empty, AMP-loaded, and mRNA-loaded LPNPs.

References

[1] M. Naghavi, S. E. Vollset, K. S. Ikuta, L. R. Swetschinski, A. P. Gray, et al, "Global burden of bacterial antimicrobial resistance 1990–2021: a systematic analysis with forecasts to 2050", The Lancet ***404****, 10459 (2024).*

[2] N. Chen, C. Jiang, "Antimicrobial peptides: Structure, mechanism, and modification", European Journal of Medicinal Chemistry ***255****, 115377 (2023).*

[3] S. Kumar, A. Javed, B. Sanjula, "Regulatory requirement for the approval of novel, nanotechnology-based biological products." Regulatory Affairs in the Pharmaceutical Industry. Academic Press, 31-45 (2022).

[4] A. Cavegn, S. Waldner, D. Wang, J. Sedzicki, E. Ü. Kuzucu et al., "Intracellular processing of DNA-lipid nanoparticles: A quantitative assessment by image segmentation", Journal of Controlled Release ***382****, 113709 (2025).*

Enzymatic reactions in subzero liquid water by lipidic mesophase nanoconfinement

Project P2406: Artificial Photosynthesis at Sub-zero Temperatures within Cryo-protective Lipidic Mesophase Nanoconfinement
Project Leaders: Y. Yao and F. Juranyi
Collaborator: K. Wang (SNI PhD student)

Introduction

Phytantriol–water–based lipidic mesophases (LMPs) have been shown to maintain water in the liquid state at temperatures as low as −120 °C while still supporting enzymatic activity [1]. The unique nanostructured architecture of these mesophases, consisting of interconnected aqueous channels confined within a lipid matrix, provides a stabilizing environment that suppresses ice crystallization and preserves the mobility of water molecules under extreme supercooling conditions. As a result, LMPs offer a powerful experimental platform for investigating the behavior of water and the functionality of biomolecules in temperature regimes that are typically inaccessible in bulk aqueous systems. Building on this framework, we investigate whether such liquid water stabilized within these nanoconfined environments can sustain enzymatic reactions at even lower temperatures. In particular, we explore whether biochemical activity can persist within the deeply supercooled regime known as the “no man’s land” of water, spanning approximately −40 to −120 °C. This temperature range is generally inaccessible to conventional studies because rapid ice crystallization prevents the observation of liquid water in bulk systems. By exploiting the stabilizing properties of lipidic mesophases, our study aims to probe enzymatic processes under these extreme conditions and to gain new insights into the coupling between water dynamics, confinement effects, and biochemical activity in deeply supercooled environments.

Main Results

We first prepared phytantriol-based lipidic mesophases with different water fractions and characterized their mesophase structures using small-angle X-ray scattering (SAXS). Representative SAXS profiles are shown in Fig. 1. Because our target temperature range lies within the deeply supercooled “no man’s land” of water, we selected two representative temperatures, −40 °C and −60 °C, to examine the structural stability of the mesophases under these extreme conditions. As shown in Fig. 1a, samples with higher water content exhibit a cubic Ia3d phase at room temperature. Upon cooling, a phase transition from the cubic phase to the lamellar phase (L_α) occurs at both −40 °C and −60 °C. In contrast, samples with lower water content display a lamellar phase across the entire temperature range from room temperature down to −60 °C. In this structure, water is confined within nanometer-scale channels between lipid bilayers, forming a highly confined aqueous environment.

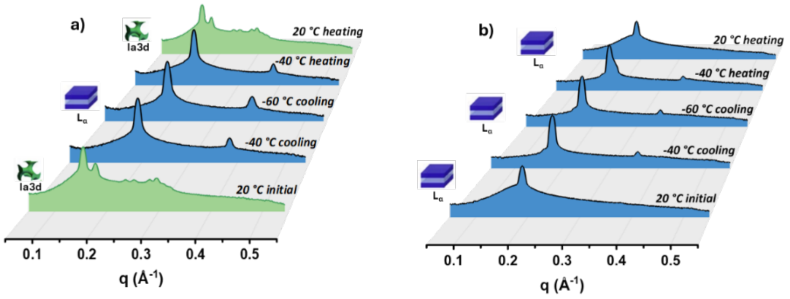

Phy14.8–Enz85.2 **Phy25–Enz75**

Fig. 1: SAXS profiles as a function of temperature of a) Phy14.8-Enz85.2 and b) Phy25-Enz75

The structural stability of the lipidic mesophases at low temperatures provides a suitable framework for investigating enzymatic reactions under supercooled conditions. However, before performing enzymatic studies, it is necessary to understand the crystallization behavior of water within these systems. To this end, we employed both differential scanning calorimetry (DSC) and wide-angle X-ray scattering (WAXS) to analyze ice formation and melting processes.

For samples with higher water content (Phy14.8–Enz85.2), an exothermic peak was observed during cooling in the DSC thermogram, indicating that a fraction of the water crystallizes into ice. Based on the measured enthalpy change, the ice fraction is estimated to be approximately 44%. In contrast, in samples with lower water content (Phy25–Enz75), no crystallization peak was detected during cooling. A small melting peak appears only upon reheating, suggesting that a limited amount of ice forms through recrystallization during the heating process. The estimated ice fraction in this case is only about 26.5%, indicating that most of the water remains in the liquid state down to −120 °C within the lipidic mesophase.

The DSC results are further supported by WAXS measurements. In the Phy14.8–Enz85.2 sample, characteristic diffraction peaks corresponding to crystalline ice are observed during both cooling and heating cycles, and the relatively strong peak intensity indicates a significant fraction of ice formation. In contrast, in the lower water fraction sample (Phy25–Enz75), no ice diffraction peaks are detected during cooling. Only during reheating to approximately −40 °C do weak ice reflections appear, which subsequently disappear upon further heating toward room temperature.

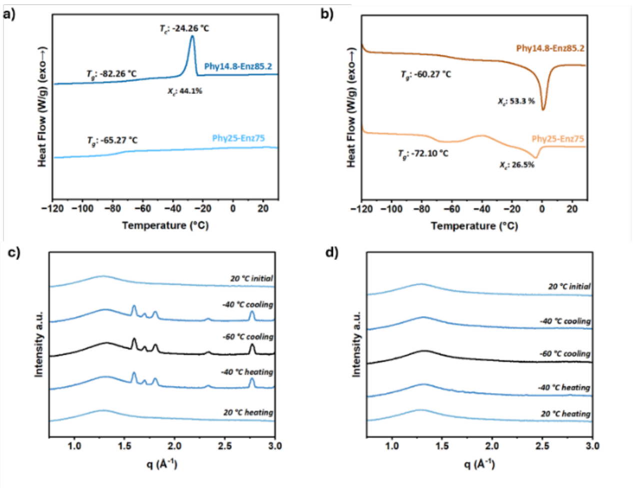

Fig. 2: a) DSC cooling curves of sample Phy14.8-Enz85.2 and Phy25-Enz75 b) DSC heating curves of sample Phy14.8-Enz85.2 and Phy25-Enz75, both measured at a rate of 10 °C/min. c) and d) WAXS profiles at different temperatures of sample Phy14.8-Enz85.2 and Phy25-Enz75, respectively.

Based on the structural and crystallization analysis obtained from SAXS, DSC, and WAXS measurements, we next investigated enzymatic activity in these lipidic mesophase systems. We hypothesized that enzymatic activity would be strongly suppressed in samples where ice forms during cooling, whereas in samples with large fraction of liquid water, enzymatic reactions might still occur even at very low temperatures. Because lipase has previously been shown to remain active in lipidic mesophases down to approximately −10 °C, we selected lipase as a model enzyme to explore whether enzymatic reactions could be extended into the deeply supercooled "no man's land" temperature regime.

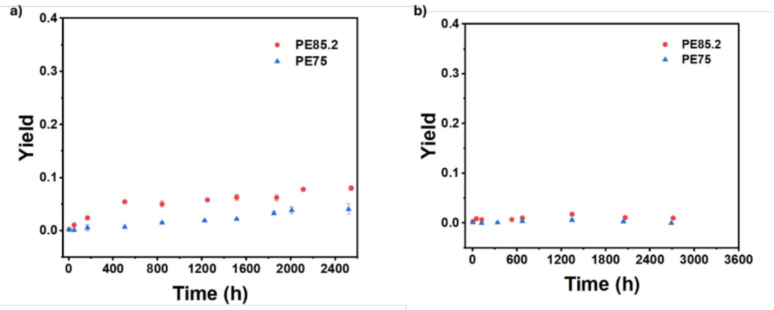

Fig. 3: a) and b) Kinetic curves of the confined enzymatic reaction in Phy14.8-Enz85.2 in comparison to Phy25-Enz75 at -40 °C and -60 °C, respectively.

Enzymatic reactions were therefore carried out in both Phy14.8–Enz85.2 and Phy25–Enz75 samples at −40 °C and −60 °C. The preliminary results are shown in Figure 3. At −40 °C, after more than 2400 hours (approximately three months), a small amount of product formation was detected in both lipidic mesophase systems, although the overall yield remained below 1%. Interestingly, the reaction rate in the sample containing ice (Phy14.8–Enz85.2) was slightly higher than that in the sample where ice formation during cooling was largely suppressed (Phy25–Enz75). When the temperature was further reduced to −60 °C, however, lipase activity appeared to be completely suppressed in both systems, and no detectable product formation was observed.

Conclusion

In summary, phytantriol-based lipidic mesophases provide a stable nanoconfined environment that preserves a significant fraction of liquid water under deeply supercooled conditions down to −120 °C. This unique system might enable enzymatic reactions to occur within the "no man's land" temperature regime, offering new opportunities to investigate biochemical processes and water dynamics at extremely low temperatures.

References

[1] Y. Yao, et al., "Designing cryo-enzymatic reactions in subzero liquid water by lipidic mesophase nanoconfinement, Nat. Nanotechnol. ***16****, 802–810 (2021).*

Smooth focusing mirrors for X-rays

Project A18.1: CAPOFOX (Paul Scherrer Institute, FHNW Muttenz, XRnanotech)
Project leader: H. Schift
Collaborators: S. Saxer, F. Döring

Introduction

During the three-year Nano Argovia project *CAPillary Optics for FOcusing of X-rays* (CAPOFOX), surface smoothening strategies were developed for lithographically engineered 3D structures with the aim of producing optical mirror surfaces with ultra-low roughness. The project was carried out by researchers from the Paul Scherrer Institute PSI, the School of Life Sciences at the University of Applied Sciences and Arts, Northwestern Switzerland (FHNW) and the industrial partner XRnanotech. The objective was to establish a process that produces ellipsoid mirrors suitable for applications ranging from the ultraviolet (UV) and X-rays spectral regions. While for optical wavelengths in the visible range (500 nm) a root-mean-square (RMS) roughness of 5 nm would generate excellent optical quality with less than 1% scattering in grazing incidence, roughness below 1 nm would be required for a wavelength of 13.5 nm extreme UV (EUV) to keep scattering below 2%. Surface scattering not only reduces the intensity in the focal spot of a focusing mirror, but also the contrast. The multilayer-coated EUV-mirrors used in modern lithography tools for chip manufacturing achieve 0.2 nm. However, in comparison to our polymer surfaces, they are manufactured using extensive polishing techniques in hard materials such as Zerodur® (Schott AG).

Main Results

Gray-tone lithography allows to reproduce a 3D surface topography from a computer aided design and could create surfaces, e.g., with parabolic shapes in lateral (x-y) direction, that could focus light more precisely (Fig. 1a). This can be done by exposing photosensitive materials (photoresists) with a scanning laser of rapidly varying laser intensity and then etching the exposed resist away, leading to a ready to use 3D structure. In CAPOFOX, the project team wanted to establish methods that are a) capable of generating such geometries with a limited number of gray values and b) optimize the roughness in the nanometer range, to finally achieve smooth waveguide structures in polymers that are similar or even better than those of glass capillaries. This is, however, only possible if roughness can be characterized with methods that are non-destructive, fast and versatile enough that they assess the roughness in deep concave elements. For the fabrication, the team at PSI led by Dr. Helmut Schift employed a novel resist from micro resist technology GmbH that could be patterned to more than 100 µm depth instead of the 20 µm so far [1]. This was a big step towards designs that would be closer to the capillaries used for curved focusing mirrors. The actual glass capillaries commonly used have diameters of up to 1 mm but narrow down to a few 10's of µm at the end where the light is focused. Therefore, an inverted cylinder ("half-pipe") of over 50 µm height would already allow to come close to such a setup. The design and 3D reproduction of such structure is shown in Fig.1a.

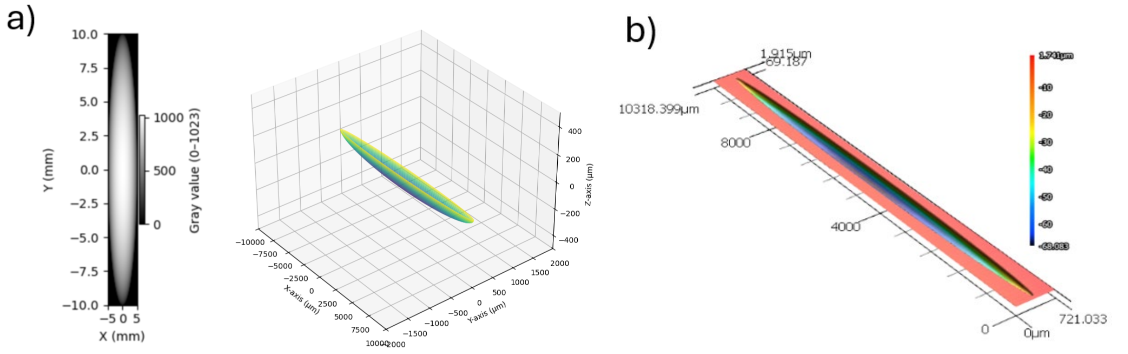

Fig. 1: Half ellipsoidal structure a) on the left, the 2D design as function of gray values from 0 to 1023, on the right the 3D visualization as function of x,y,z coordinates. b) the 3D measurement acquired with the confocal microscope.

Different methods were necessary to reduce roughness, due to the limitations of the design and the materials, but also due to defects that are generated by manufacturing methods. Artifacts due to stitching, i.e., the boundaries of neighboring exposures could be reduced by using staggered exposure. The design is exposed in stripes, and by splitting the exposure into multiple exposures, are all overlayed with a different lateral displacement. Apart from this manufacturing error stemming from the direct write lithography tool DWL 66$^+$ from Heidelberg Instruments, that employs a serial scanning focused laser beam, the limited number of gray values can be enhanced to a maximum of 1024 values and even beyond, smoothening out discrete steps that would result in diffraction pattern due to their regularity. For the designs presented here, these steps would become most severe in areas where shallow structures need to be exposed, since the steps become extended and smoothening processes due to overlay of laser beams typically enable the local redistribution of material. By reducing or even eliminating these systemic errors of the resist structures, this leads to a roughness of down to 4 nm which can be attributed to the photoresist materials used for DWL patterning. This value was measured by confocal microscopy and was validated using atomic force microscopy (AFM), as seen in Fig 2a. However, researchers have shown that by thermal imprint, 0.3 nm high steps can be replicated [2]. This was done using polymethyl methacrylate (PMMA), a polymer well known for its high resolution in electron beam lithography. Here, the nature of the photopolymer comes into play. Novolak molecules are rather large and present in agglomerations. Therefore, we anticipate that the measured 4 nm roughness is a limitation of the used polymer [3]. A replication into a polymer with linear chains such as PMMA was therefore seen as a possibility to reduce the roughness further. However, replication typically does not reduce roughness but at best keeps it. Replication into PMMA by thermal imprint, however, makes it not only possible to use a material whose molecular weight (M_w) and thus chain length can be tailored, but also to selectively modify this chain length by exposure with UV light. The process, called TASTE, is depth confined, i.e., a shallow surface area can be modified by exposure while the rest stays the same [4]. The lower M_w results in a lower glass transition temperature, thus by adjusting the reflow temperature in a way that the top surface can flow while the bulk stays solid, small surface undulations such as steps can be smoothened out. The current measurement would be close to the 0.3 nm, as seen in Fig. 2c achieved so far and – even better – be close to the roughness achieved in EUV-mirrors. And it is far below the target value of 2 nm that we originally presented in the project proposal.

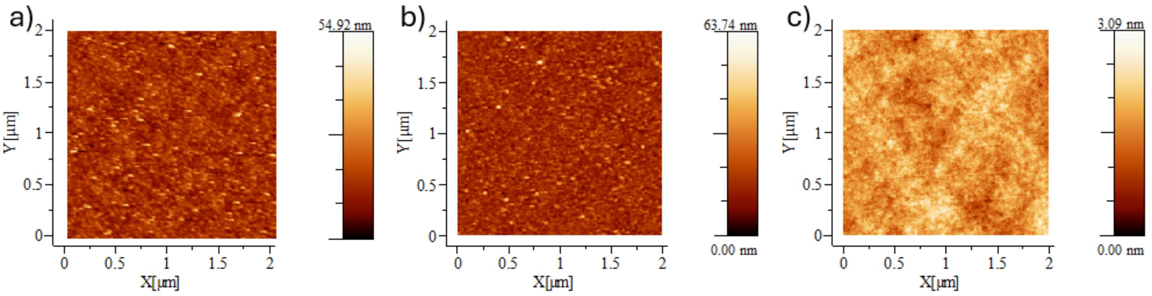

σ = 5.4 nm   σ = 4.7 nm   σ = 0.3 nm

Fig. 2: AFM measurements of a 2x2 µm^2 area of a) mr-P 22G XP resist exposed with DWL, and thermal imprinted PMMA before (b) and after (c) reflow.

Conclusion

The CAPOFOX project demonstrates the fabrication of lithographically defined polymer optics. By combining three-dimensional gray-tone patterning with material-specific post-processing, a viable pathway toward smooth, freeform capillary-like optics has been established. The intrinsic roughness limitation of the photoresist material was addressed through replication into PMMA combined with the depth-confined TASTE process. This approach enabled selective surface reflow without distortion of the overall geometry, resulting in a significant reduction of surface roughness to values as low as 0.3 nm, well below the original project target of 2 nm and approaching the roughness levels of state-of-the-art EUV mirrors.

For application at EUV and X-ray wavelengths, further steps are required to ensure long-term stability under irradiation. Polymers such as PMMA are not the best materials used for X-ray reflection, because they would undergo further modification due to the penetration of X-rays into the material, causing further reduction of M_W. Therefore, two measures are necessary: Coating the surface with a metal layer, thus securing the stability of the shape. And the transfer of the surface once again into a material that is more robust against EUV wavelengths or X-rays. Since transfer by replication means that a concave shape will be converted into a convex shape and vice versa, two replications would be required. Furthermore, measurement techniques must be developed that can be used throughout the process chain. E.g., AFM is slow and has limited ability to measure at slopes or deep trenches. Therefore, the correlation between AFM and confocal microcopy measurement needs to be assessed for different materials. Finally, the devices need to be measured using X-ray focusing. Since we cannot quantify the scattering in the current setup, a comparison between an optimized and non-optimized structure would give an indication how much the roughness improvement we have achieved. The measurement of the roughness itself, at limited areas of the current device, are very promising.

References

[1] C. Schuster, G. Ekindorf, A. Voigt, et al., "Pushing deep greyscale lithography beyond 100 um pattern depth with a novel photoresist" Proc. SPIE 124970 (2023) 14 pp.

[2] G. Tan, et al., "Atomic-scale thermal behavior of nanoimprinted 0.3 nm high step patterns on PMMA polymer sheets", Polym. J. 48 (2016) 225–227.

[3] C.A. Mack, "Line-Edge Roughness and the ultimate limits of lithography", Proc. SPIE 7639 (2010) 763931, 16 pp.

[4] A. Schleunitz, et al., "Novel 3D micro- and nanofabrication method using thermally activated selective topography equilibration (TASTE) of polymers", Nano Convergence 1(7) (2014).

Development of functional nano-layers for Gen 4 anode-less all-solid-state batteries

Project A19.1: BatCoat (PSI Center for Energy and Environmental Sciences)

Project leader: M. El Kazzi

Collaborators: K. Löffel, K. Yalamanchili

Introduction

The BatCoat project aims to address the critical anode-electrolyte interfacial challenges that currently limit the realization of next-generation (Gen4) anode-less lithium metal all-solid-state batteries (AL-ASSBs). Gen4 employ solid electrolytes (SEs) and rely solely on a copper (Cu) current collector (CC) as the anode (Fig. 1), eliminating excess lithium. This architecture offers a compelling pathway to achieve gravimetric energy densities approaching 500 Wh kg^{-1}, while simultaneously reducing cell-level costs to below 80–100 CHF kWh^{-1} and significantly improving safety. For these reasons, AL-ASSBs are widely regarded as a holy grail technology for future rechargeable batteries.

Despite their promise, the practical deployment of AL-ASSBs remains hindered by fundamental interfacial limitations. In particular, achieving highly reversible lithium plating and stripping over more than 500 cycles, with Coulombic efficiencies exceeding 99%, remains a major challenge. Electro-chemo-mechanical instability at the Cu–lithium–SE interface often led to non-uniform Li deposition, interfacial degradation, and premature cell failure.

The primary objective of BatCoat is to explore and validate the integration of nanoscale functional coatings (10–200 nm) deposited directly onto the surface of the Cu CC and evaluated in all-solid-state battery cells. In the second year, PSI focuses on the optimization of a lithiophilic nucleation layer applied to both Cu and stainless- steel surface to promote uniform lithium nucleation and reversible plating/stripping through enhanced lithium wettability. This nucleation layer is further complemented by a second barrier layer designed to exhibit high ionic conductivity while remaining electronically insulating. (Fig. 1).

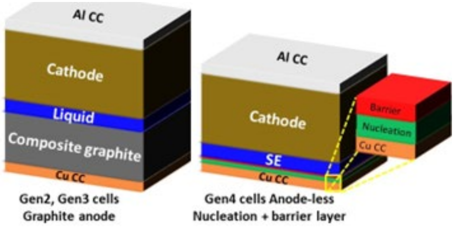

Fig. 1: Sketch of the current Gen2, Gen3 compared to Gen4 cells.

In parallel, FHNW contributes into advanced electro-chemo-mechanical simulations to establish a mechanistic understanding of lithium plating and stripping at the SE interface. These modeling efforts support the interpretation of experimental observations and provide quantitative guidance for coating design and materials optimization. Finally, the industrial partner Oerlikon Metco (OM) evaluates technically robust and economically viable high-throughput coating processes for both nucleation and barrier layers. This effort is essential to enable scalable manufacturing routes and to bridge the gap between laboratory-scale validation and industrial implementation of Gen4 anode-less solid-state battery technology.

Main Results

In the second year, PSI focused on improving the long-term cyclability of conventional Cu and stainless steel (AISI316L) CCs in combination with a bilayer of silver and carbon, achieving excellent areal capacity and capacity retention in NCM8111/Li_6PS_5Cl (LPSCl)/Cu full cells that even surpassed the desired KPI. The main achievements are summarized in Fig. 2. The cells are cycled at room temperature (22 – 25 °C) in galvanostatic mode at an intermediate current density of around 0.3 mA cm^{-2} (C/10) to maximize the capacity delivered by the NCM811 cathode material, being 2.5 mAh cm^{-2} (Fig. 2). As already discovered in the previous year, the uncoated Cu and stainless-steel CCs suffer from inhomogeneous Li plating, contact loss of Li metal to the current collectors, and corrosion with the SE, leading to rapid capacity decay and short circuiting, indicated by a fast specific capacity drop in early cycling. By implementing a thin nucleation layer of silver, a significant improvement in capacity retention for both stainless steel and Cu CCs are visible, which can be attributed to the favorable wettability of silver with Li, homogenizing the Li metal growth. However, for the Cu, after approximately 80 cycles, rapid capacity fading and subsequent short circuiting (cycle 180) can be observed, which is mainly caused by the corrosion of the Cu CC with the SE. By implementing a 10 nm interlayer of carbon between the silver and Cu, the diffusion of Cu through the nucleation layer can be minimized to prevent the formation of Cu sulfide species at the interface of the SE and nucleation layer. While the carbon layer on the Cu alone behaves similarly to the bare current collectors, the combination of both carbon and silver on the Cu can significantly improve the capacity retention further, showing identical behavior to

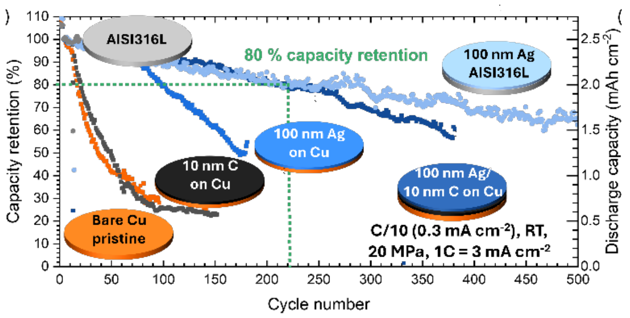

Fig. 2: Galvanostatic cycling of bare and coated CCs vs NCM811 cathode using Ag as a nucleation layer and carbon as a protective interlayer. Capacity retention and capacity vs cycle number.

the stainless-steel current collector with Ag up to 250 cycles. The stainless steel has so far performed the best with a capacity retention of 64% after 500 cycles without short circuiting.

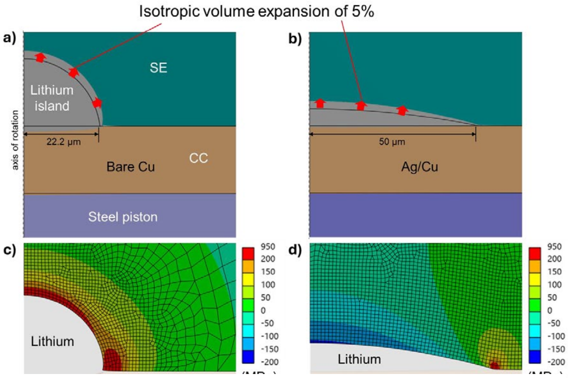

Fig. 3: Simulation results shown with a deformation scale factor of 5 for better visibility. Deformed components in the vicinity of (a) the higher lithium island on bare Cu, and (b) the flat and wide lithium island on Ag/Cu, with the black edges corresponding to the undeformed geometries. Maximum principal stress distribution in the SE around the lithium islands (c) on bare Cu and (d) on Ag/Cu.

In addition to the electrochemical simulations already described in the 1st year report, in the 2nd year FHNW focused on the mechanical simulation of the processes at the interface between the CC and the SE. Understanding the interfacial mechanical stress distribution and the resulting risk of SE cracking in the vicinity of the lithium islands is crucial in order to be able to operate a AL-ASSBs over a high number of cycles without failure. In the mechanical finite element model two predefined lithium island geometries with identical total Li volumes were compared. These two representative island shapes mimic the growth of small and large Li deposits typically observed at the SE|Cu and the SE|Ag/Cu interfaces, respectively. (i) A high, narrow Li island with a contact diameter of 44.4 µm at the CC, exhibiting predominantly vertical growth and little lateral expansion, simulating the poor lithium wettability on Cu (Fig. 3a), and (ii) a flat, wide island with a contact diameter of 100 µm, showing greater lateral expansion and reduced growth in height, corresponding to improved Li wettability on Ag (Fig. 3b). The 2-dimensional model with axial symmetry assumes identical Li volumes when fully revolved. The applied loads include a stack pressure of 20 MPa and an isotropic expansion coefficient of 5% to simulate progressive Li growth. The resulting deformations in the vicinity of Li islands are shown in Fig. 3a and Fig. 3b. Plating-induced cracks into the Li_6PS_5Cl (LPSC) SE originate primarily from regions of high tensile stress, therefore, the maximum principal stress was evaluated. Stress values were used here for qualitative comparison between the two cases.

The simulations reveal that the narrow island on bare Cu generates high tensile stresses of several hundred MPa above the island, indicating a significant risk of cracking (region with maximum principal stress above 200 MPa are highlighted in red in Fig. 3c). In contrast, the flat island on Ag/Cu shows tensile stresses only at the edges and negative stresses (i.e. compressive stresses) across almost the entire upper surface of the island (Fig. 3d). These results demonstrate that a flatter, laterally expanded Li morphology markedly reduces the risk of crack initiation and dendrite penetration into the SE. The mechanical simulations presented in this work corroborate the experimental observations shown in Fig. 2, obtained from full-cell electrochemical measurements and operando X-ray computed tomography. Both experimental and modeling results consistently demonstrate that the use of Ag-coated current CCs leads to a marked improvement in the electrochemical and mechanical performance of the AL-ASSBs. The simulations provide mechanistic insight into how the Ag coating promotes more favorable interfacial contact and stress distribution, thereby enhancing cell stability and performance. This study has been accepted in Small (Wiley) [4].

Conclusion

The BatCoat project successfully met, and in several aspects exceeded, its objectives and KPIs. The results clearly demonstrate the beneficial effect of nanoscale nucleation and barrier layer on Cu CCs, significantly improving the cycling performance of AL-ASSBs. This work validates CCs functionalization as an effective and scalable strategy for enhancing battery stability and performance. The project also highlights the crucial role of coupled electro-mechanical simulations in understanding interfacial processes and guiding coating design and materials optimization. Moreover, the project delivered highly valuable feedback to OM, demonstrating both the technical feasibility and commercial relevance of CC functionalization. It further strengthened the positioning of AL-ASSBs as a highly promising battery technology with substantial potential for future industrial deployment. Over two years, four peer-reviewed publications in high-impact journals were produced [1, 2, 3, 4], confirming both the scientific excellence and strong commercial potential of AL-ASSB technology.

References

[1] *R. N. Wullich, B. Lelotte, V. Pelé, C. Jordy, L. Gubler, et al., "Optimized LiNbO3 Sol-Gel Coatings for Ncm622 in Sulfide-Based All-Solid-State Batteries: Insights into Synthesis, Uniformity, and Electrochemical Performance", Electrochimica Acta* ***536****, 146750 (2025).*

[2] *J. Zhang, R. N. Wullich, L. Xu, V. Siller, T. J. Schmidt, et al., "Impacts of Key Physical Parameters on the Cycling of Thin Metallic Lithium in Sulfide-Based All-Solid-State Batteries", Journal of Power Sources* ***655****, 237999 (2025).*

[3] *J. Zhang, R. N. Wullich, T. J. Schmidt, M. El Kazzi, "Synergistic Effects of Solid Electrolyte Mild Sintering and Lithium Surface Passivation for Enhanced Lithium Metal Cycling in All-Solid-State Batteries", Advanced Science (2025) DOI: 10.1002/advs.202521791.*

[4] *L. Xu, J. L. Houx, V. Kachkanov, J. Zhang, R. N. Wullich, et al., "Operando X-ray Computed Tomography Reveals the Role of Interfacial Nucleation Nanolayers in Suppressing Mechanical Failure in Zero-Excess Lithium All-Solid-State Batteries", Small (2025) DOI: 10.1002/smll.202512284.*

Nano-structured zirconia - do cells like rice crackers?

Project A19.11: ZIRYT (University of Basel, FHNW Muttenz, Straumann)
Project leader: N. Rohr
Collaborators: A. G. Guex, M. de Wild, and R. Wagner

Introduction

Zirconia (ZrO_2) is a high-strength oxide ceramic that is used as dental implant material as well as for patient-specific restorations on implants and natural teeth. Once inserted to the oral cavity, the material is in direct contact with human hard and soft tissue and exposed to thermal, chemical, and mechanical loads. This complex environment imposes significant demands on the material, with surfaces of zirconia to be structured to a) provide an ideal environment to promote cell growth and attachment of fibroblasts and keratinocytes in the gingival region, b) induce differentiation of bone progenitor cells and facilitate osseointegration in the endosseous part without pronounced inflammatory response, and c) to potentially inhibit bacterial attachment along the entire implant surface. To achieve this, major emphasis has been placed on the topographical surface characteristics of zirconia. Traditional structuring approaches used by dental implant manufacturers are sandblasting, acid-etching, laser-ablation or by additive sintering of a ceramic slurry [1]. However, those production steps are hazardous due to the high acid concentration and temperatures needed to structure zirconia. Further, they are labor intense, reduce mechanical strength and significantly increase the final costs for zirconia implants. Therefore, it is of high interest to simplify the production steps without loss of function and performance. In-depth understanding of how surface topography in the nano- to micrometer-spectrum affect material properties and material-cell interaction is lacking to date. Hence, within the ZIRYT project and an interdisciplinary approach we aimed to create different heat-treatment-induced nano-structured topographies on zirconia materials by eliminating macro-roughness. Materials were characterized in terms of their topography, chemistry, crystallography, tribology and mechanical properties. Subsequently, osteogenic mineralization as well as fibroblast spreading, and immune response of macrophages on zirconia materials with nano-structured topographies were assessed using an extensive series of cell culture evaluations.

Main Results

Nano-to micro-structured topographies on zirconia materials were successfully produced by super-polishing the surfaces to a surface roughness value S_a of 11±2 nm followed by a heat-treatment at 1250°C to retrieve the grain structure und nano-topography that vanished during polishing. The size of the grains freshly formed on the surfaces were measured by using the line-intercept method in scanning electron microscope images (Fig. 1). Our findings demonstrated a consistent rise in grain size with rising yttria content (3 - 5mol% yttria-doping: 3YZ, 4YZ, 5YZ). Grain sizes ranged from 190 ± 28 nm for a zirconia implant material that is commercially available (IMP) to 1532 ± 328 nm for a zirconia material doped with 5 mol% yttria (5YZ). The formed crystal grains resembled the appearance of rice crackers. As a higher yttria content in polymorphic zirconia also results in a higher amount of cubic crystal phase found within the bulk material, mechanical properties are also affected. The biaxial flexural strength decreased linearly with increasing yttria content from 1347 ± 127 MPa for a 3 mol% yttria-doped zirconia to 857 ± 125 MPa for a 5 mol% yttria-doped zirconia. The increased proportion of the cubic phase in 4YZ and 5YZ reduces the tetragonal phase's ability to undergo transformation toughening making the surface more brittle. This was observed in increased spalling during tribological scratch tests.

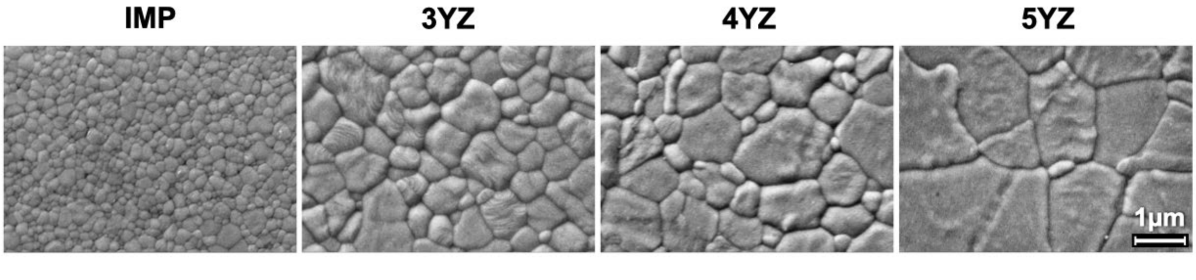

Fig. 1: By super-polishing zirconia materials and subsequent heat-treatment it was possible to create nano- to micro-sized crystal grains resembling the topography of a rice cracker. The size of the grains was controlled by doping zirconia with yttria. IMP is a commercially available zirconia implant material, while 3YZ-5YZ are doped with 3-5 mol% yttria.

Next, cell-material-interactions were evaluated on different time-scales using human cell lines for the simplified representation of soft tissue, hard tissue or first responders of the immune system. Within a few hours of cell seeding, HGF-1 (representing the soft tissue), SaOS-2 (mimicking hard tissue) and THP-1 (representative for macrophages) had attached with equal efficiency to all materials. After 7 days of HGF-1 culture, the cells had colonized and covered all surfaces and deposited fibronectin extracellular matrix, which is an important step in early soft tissue formation. SaOS-2 osteoblast-like cells were cultured under osteogenic conditions for 11 days. The activity of secreted alkaline phosphatase continuously increased during culture. Osteogenic maturation was equally efficient on all materials as evaluated by mineralization assays and expression of osteogenesis-related genes *BGLAP, COL1A1, RUNX2, SP7* and *SPP1*. Lastly, THP-1 were differentiated from monocytes to macrophages for 1 day and cytokine secretion was assessed from day 1-4 (early) or day 4-7 (late). The early phase saw a high secretion of pro-inflammatory cytokines IL-1β and TNF-α, while the late phase was characterized by an increased secretion of anti-inflammatory IL-10 and a significant reduction of pro-inflammatory cytokines. Angiogenesis and healing-stimulating factor VEGF was secreted at high levels of 250-350 pg/mL during both the early and late phase. On all materials, THP-1 had doubled in surface area compared to day 1 (400 vs 200 µm^2) and both pro- and anti-inflammatory phenotype markers (iNOS and Arg1, respectively) were observed.

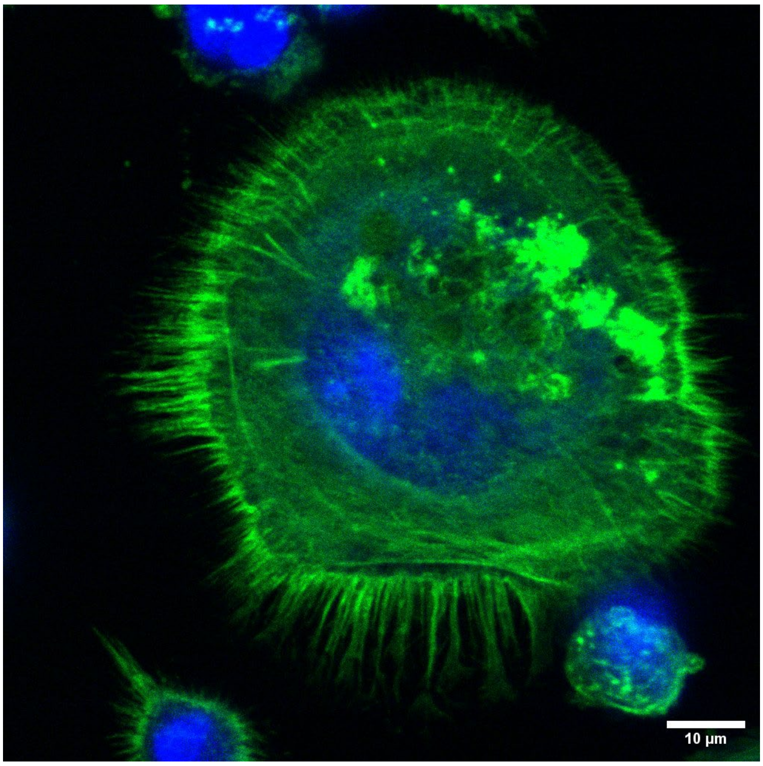

Fig. 2: Fluorescent microscopy Image of a THP-1 macrophage cultured on a nano-structured zirconia surface. The actin skeleton is stained with phalloidin (green), nuclei were labelled with DAPI (blue).

Conclusion

The experiments conducted within the ZIRYT project helped us to significantly broaden our knowledge and further understand parameters influencing material properties of yttria doped zirconia. An interdisciplinary approach was followed to explore the polymorphic behavior of zirconia and how this is affected by factors such as the raw material, yttria concentration and distribution, sintering parameters and processing considering scientific and industrial perspectives. In addition, the project enabled us to establish a variety of cell culture models with osteoblasts, fibroblasts or macrophages to thoroughly characterize cell-material interaction at early and late stage.

Creating nano-to micro-structured topographies on zirconia by eliminating macro-roughness enabled us to solve the long-awaited mystery: Do cells like rice crackers? The answer is: Yes, they do like to grow on them! We demonstrated material coverage with fibroblasts, osteogenic maturation and mineralization of Saos-2, and macrophage polarization without signs of chronic inflammation.

References

[1] Schünemann, et al., "Zirconia surface modifications for implant dentistry", Mater Sci Eng C ***98****,1294–305 (2019).*

Pushing the limits of electron microscopy with high-Z sensors

Project A19.3: HiZfEM (Paul Scherrer Institut, University of Basel, DECTRIS)
Project leaders: D. Greiffenberg and E. van Genderen
Collaborators: K. A. Paton, S. Fernandez, and J.P. Abrahams

Introduction

Hybrid pixel detectors (HPD) have been widely adopted in electron microscopy for diffraction-based experimental modalities thanks to their high dynamic range, fast (>kHz) frames rates, and radiation hardness compared to the current state-of-the-art CMOS cameras. However, compared with CMOS cameras, their spatial resolution is limited by the multiple scattering of primary electrons in their thick ($\geq 300\ \mu$m) silicon sensors, necessary to ensure their radiation hardness [1]. Incident electrons deposit their energy in a stochastic way, tending to deposit most of their energy at the end of their trajectory. Machine learning-based methods, combined with fine energy information are needed to identify the entry point of incident electrons and thereby improve the spatial resolution of detectors with Si sensors [2, 3]. These methods are computationally intensive, and obtaining high quality training data is challenging. Furthermore, the need for precise information about how the incident electrons deposit their energy in the sensor means these methods can only be applied to energy-sensitive HPDs, such as those with charge integrating (CI) architectures, which have more limited frame rates than single quanta counting (SQC) HPDs, the other main variety of HPD.

This project aims to replace the standard, relatively light silicon sensors (atomic number Z=14) with heavier, high-Z sensors, which have greater stopping power due to their increased electron density. GaAs:Cr is a particularly promising sensor material as its average atomic number is sufficiently high to reduce the range of incident electrons but not so high as to cause a significant reduction in detector efficiency due to increased electron backscattering [4]. The reduced spread of signal should permit the use of simpler interpolation methods adapted from photon science [5]. Such methods have been used to enhance the spatial resolution of SQC detectors, the latest generation of which feature multiple counting thresholds that can be set independently, providing the necessary coarse energy information. Combining a GaAs:Cr sensor with a SQC detector and applying interpolation schemes should result in a highly flexible detector that in conditions of lower flux has high spatial resolution while maintaining an extremely high count-rate under high-flux conditions.

Materials and Methods

GaAs:Cr and Si sensors were bonded to the CI readout chip JUNGFRAU1.0 [6], which has a pixel size of 75 x 75 μm^2 (Fig. 1, left). Using a CI chip makes possible measurement of the improvement in performance obtained by using a GaAs :Cr sensor and prediction of the likely performance possible when using a SQC readout chip by post-processing of the data.To test the sensors' response to electrons with energies up to 200 keV, dedicated mechanics were constructed for installing devices on the JEOL JEM F200 (S)TEM located at the Paul Scherrer Institut and operated by the University of Basel (Fig. 1, right).

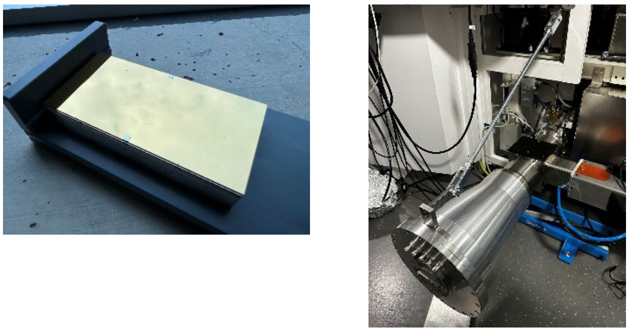

Fig. 1: (left) Picture of a full GaAs:Cr module composed of a single GaAs:Cr sensor (with a thickness of 500 µm and an area of ~ 8x4 cm^2) mounted on eight JUNGFRAU readout chip arranged in two rows of four chips. (right) Photo of the mechanics for testing different detectors installed on the JEOL JEM F200 (S)TEM.

The imaging performance of a detector is quantified by its modulation transfer function (MTF) and detective quantum efficiency (DQE) which describe how well a detector can reproduce the contrast and the signal-to-noise ratio of the image incident upon it as a function of image feature size. Datasets for determining the MTF and DQE using the methods described in reference [4] were acquired with 80 keV, 120 keV and 200 keV electrons under conditions of sparse illumination. The flat field data acquired as part of the MTF and DQE measurements can also be used to produce energy spectra, to better understand the way in which incident electrons deposit their energy in the sensor.

Main Results

Fig. 2 shows the energy spectra recorded by the two detectors for different electron energies. It can be seen that the spectra recorded by the GaAs:Cr for 200 keV electrons the spectra is deformed in a way that suggests that the analogue front-end electronics become saturated when they record a 200 keV electron. This is likely due to the reduced spread in signal in the GaAs:Cr meaning that, on average, pixels in which an electron deposits their energy see a larger proportion of the electron's energy than is the case in the Si sensor, combined with the elevated dark current expected for GaAs:Cr sensors. This means that the energy deposited by 200 keV electrons in some pixels for some events is not accurately recorded in the GaAs:Cr sensor.

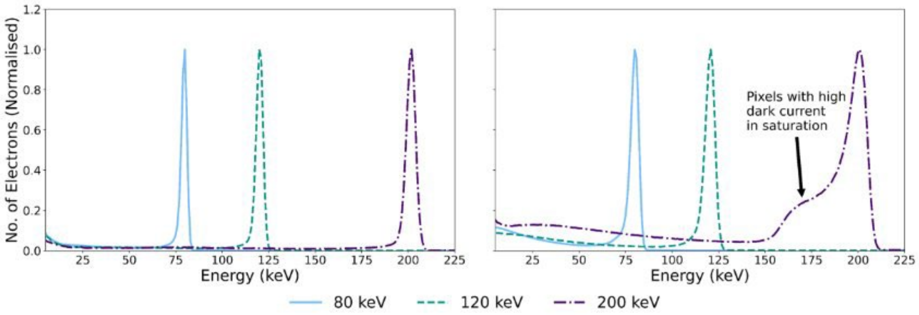

Fig.2: Energy spectra for (left) the Si and (right) the GaAs:Cr sensor for electrons with energies ranging from 80 keV – 200 keV.

Despite this limitation, it can be seen in Fig. 3 that for 200 keV electrons there is a marked improvement in imaging performance when using a GaAs:Cr sensor compared with using a Si sensor, with further improvement in performance obtained via interpolation to an extent not possible with the Si sensor. In Fig. 3,the underlying data has been processed to mimic the performance of a SPC detector with a low counting threshold (such as are available commercially); with the electron hit allocated to the pixel that registers the highest signal in pixel clusters due to individual electrons (equivalent to a SQC with a high counting threshold) and to a virtual pixel one quarter the size of a physical pixel, identified as the weighted centre-of-mass of individual pixel clusters, i.e. the simplest form of interpolation.

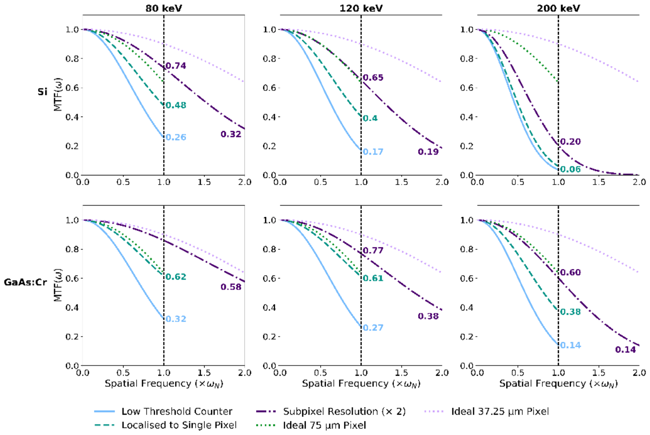

Fig. 3: MTF measurements for the (top) Si and (bottom) GaAs:Cr JUNFRAU assemblies, with comparison made to the performance of an ideal square pixel detector with 75 um and 37.25 um pixel pitch. Also noted are the values of the MTF at Nyquist for different ways of processing the data; for an ideal square pixel detector the MTF is 0.64 at the Nyquist frequency.

Conclusions

We have confirmed an improvement in MTF performance is obtained by using a GaAs:Cr sensor for electrons with energies ranging from 80 – 200 keV, with further improvement possible via basic interpolation schemes to an extent not possible with the Si sensor. At present, we are confirming the results of the DQE measurements and attempting to correct for the effects of saturation in post-processing, which we expect will yield further improvements in the results obtained via interpolation. The data collected is also being used to determine the optimal threshold settings when using a SQC detector with four thresholds, such as the one currently under development at PSI, of which the first full scale chips are expected back from production in Q1 2026.

References

[1] G. Tinti, et al., "Electron crystallography with the EIGER detector", IUCrJ, 5, 190-199 (2018).

*[2] P. van Schayck, et al., "Sub-pixel electron detection using a convolutional neural network", Ultramicroscopy, **218**, 113091 (2020).*

*[3] X. Xie, et al., "Enhancing spatial resolution in MÖNCH for electron microscopy via deep learning", JInst, **19**, C01020 (2024).*

*[4] K.A. Paton, et al., "Quantifying the performance of a hybrid pixel detector with GaAs:Cr sensor for transmission electron microscopy", Ultramicroscopy, **227**, 113298 (2021).*

*[5] A. Bergamaschi, et al., "First demonstration of on-chip interpolation using a single photon counting microstrip detector", JInst, **17**, C11012 (2022).*

*[6] A. Mozzanica, et al., "Characterization results of the JUNGFRAU full scale readout ASIC", JInst, **11**(2), C02047 (2016).*

Nanobiocatalysts for PET Recycling

Project A19.5: NANOdePET (FHNW Muttenz (HLS), FHNW Windisch (HT), INOFEA)
Project leader: P. Shahgaldian
Collaborators: M. Grob and M. R. Correro

Introduction

Polyethylene terephthalate (PET) is used globally in packaging, textiles, and consumer goods, yet current recycling strategies fall short due to declining material properties and high energy requirements. Enzymatic depolymerization has emerged as an attractive alternative, but practical deployment is constrained by low thermostability, limited PET affinity, and limited enzyme reusability. The NANOdePET project addresses these limitations by developing high-performance nanobiocatalysts for efficient PET depolymerization at elevated temperatures. The approach builds on INOFEA's proprietary supramolecular stabilization technology, which encapsulates immobilized enzymes within a porous and soft organosilica layer that enhances mechanical and chemical resistance while enabling repeated use [1]. Recent advances, such as partial shielding achieved by growing protective layers thinner than the enzyme dimensions to improve accessibility for bulky substrates [2], along with the integration of cyclodextrin-based molecular chaperones for enhanced stability [3], have been shown to further elevate catalyst performance. Through a collaboration between HLS, HT, and INOFEA, NANOdePET thrives to engineer next-generation stabilized PET-degrading enzymes capable of converting PET into terephthalic acid (TPA), mono-(2-hydroxyethyl) terephthalate (MHET), and bis-(2-hydroxyethyl) terephthalate (BHET). In parallel, the project benchmarks this technology against current industrial recycling processes to demonstrate its feasibility and competitive advantage.

Main Results

Screening of several PET-degrading enzymes, including leaf compost cutinase wildtype (LCC^{WT}), bacillus lipase 9 (Lip9), candida antarctica lipase B (CalB), an archaeal-type hydrolase (PET46), and humicola insolens cutinase (HiC), identified LCC^{WT} as the most suitable candidate based on its degradation efficiency, industrial-applicability, and immobilization compatibility. LCC^{WT} was immobilized on amino-modified silica nanoparticles (SNPs) via glutaraldehyde coupling, achieving *ca.* 60% loading (33.8 µg enzyme per mg SNP). A tunable organosilica layer was subsequently grown around the immobilized enzyme using tetraethoxysilane (TEOS), aminopropyltriethoxysilane (APTES), α-cyclodextrin-TES (α-CD-TES), and n-propyltriethoxysilane (PTES) as hydrophobic modifier. Three partially shielding formulations were designed: TA_{SNP} (TEOS/APTES), $\alpha\text{-CD}_{\text{SNP}}$ (TEOS + α-CD-TES), and TP_{SNP} (TEOS + PTES) with layer thickness values of 4.0, 3.4, and 3.5 nm, respectively; slightly below the longest enzyme dimension (5.5 nm) to ensure substrate access while providing structural protection.

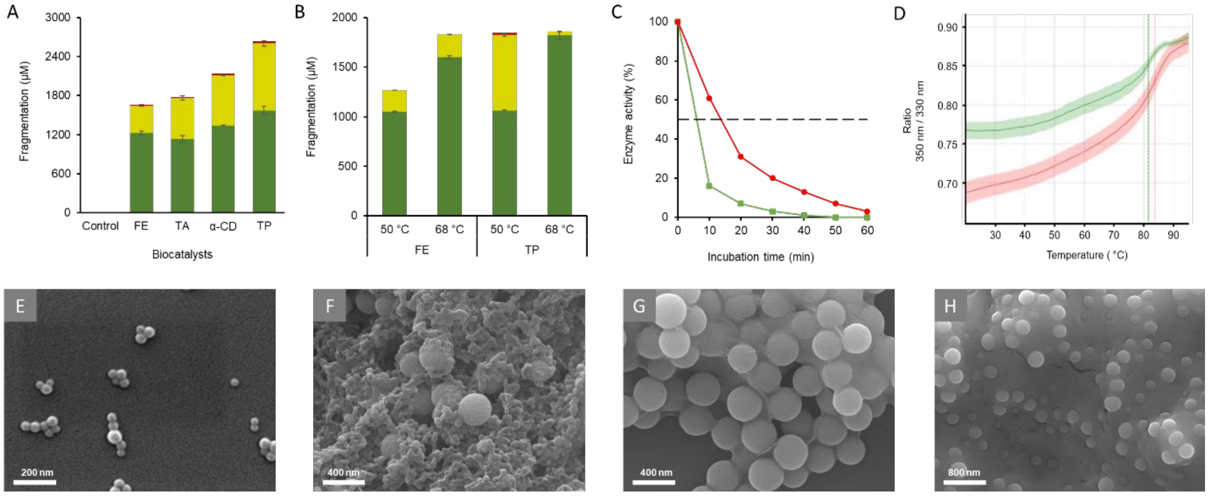

Fig. 1 Fragmentation of PET particles (0.8 mg) into TPA (green), MHET (yellow) , and BHET (red) after 24 h at 50 °C using 2 U of soluble LCC^{WT} (FE) and SNP-based nanobiocatalysts (TA, α-CD, TP) (A), and comparison of FE and TP_{SNP} at 50 °C and 68 °C using 0.4 mg of PET (B). Enzymatic activity at 80 °C (C) and melting points by DSF (D) for FE (green) and TP_{SNP} (red). SEM micrographs of PET particles before (E) and after 3-hour incubation with nanobiocatalysts (F). Panels G and H display the nanobiocatalysts after complete degradation in the reaction matrix. Error bars show standard deviations (n = 3).

To assess the effectiveness of our system, we evaluated the degradation of two distinct PET materials. i) PET nanoparticles, prepared by dissolving a PET-based sock material in hexafluoroisopropanol followed by precipitation into water, with an average diameter of ca. 70 nm and a crystallinity of 11.3%. ii) PET film; a bottle-grade PET film, composed of 100% PET with a crystallinity of 4.8%. Degradation efficiency was evaluated by analyzing the released fragments using high-performance liquid chromatography (HPLC). PET nanoparticles (0.8 mg) were incubated for 24 hours at 50 °C using 2 U of enzyme (Fig. 1A). All nanobiocatalysts outperformed soluble LCC$^{\text{WT}}$, achieving higher fragmentation efficiencies: FE 43%, TA$_{\text{SNP}}$ 46%, α-CD$_{\text{SNP}}$ 55%, and TP$_{\text{SNP}}$ 68%. TP$^{\text{SNP}}$ also produced the highest TPA concentration (1.6 mM), confirming superior catalytic performance. Based on these results, TP$_{\text{SNP}}$ was selected for further experiments using 0.4 mg PET at 50 and 68 °C (Fig. 1B). At 50 °C, TP$_{\text{SNP}}$ achieved complete depolymerization, whereas soluble LCC$^{\text{WT}}$ reached only ~70%. Despite complete degradation, TPA yields remained similar, likely due to MHET retention on the hydrophobic surface and the short reaction time. At 68 °C, both biocatalysts reached almost full-degradation, while TP$_{\text{SNP}}$ retained 95% of its initial activity and achieved near-complete TPA formation (94%), while the soluble enzyme dropped to 45% activity. The thermostability of biocatalysts was assessed by incubation at 80 °C for 60 minutes (Fig. 1C). LCC$^{\text{WT}}$ (FE) and TP$_{\text{SNP}}$ exhibited a half-life of 5.6 and 12.9-minute, respectively; a 2.3-fold improvement. Differential scanning fluorimetry also demonstrated a 2.1 °C increase in melting temperature, confirming enhanced structural stability sustaining catalytic activity at elevated temperatures (Fig. 1D). SEM images showed strong particle-catalyst interactions followed by total disappearance of PET particles, indicating complete depolymerization (Fig. 1E-H).

PET foil degradation was assessed over three days at 50 °C and 68 °C using 4 U of enzymes. At 50 °C, TP$_{\text{SNP}}$ achieved 37% degradation compared to 27% for soluble LCC. At 68 °C, TP$^{\text{SNP}}$ reached nearly 95% total fragmentation (90%; 20 mM TPA) with an activity retention of, whereas soluble LCC completely lost activity (Fig. 2A).

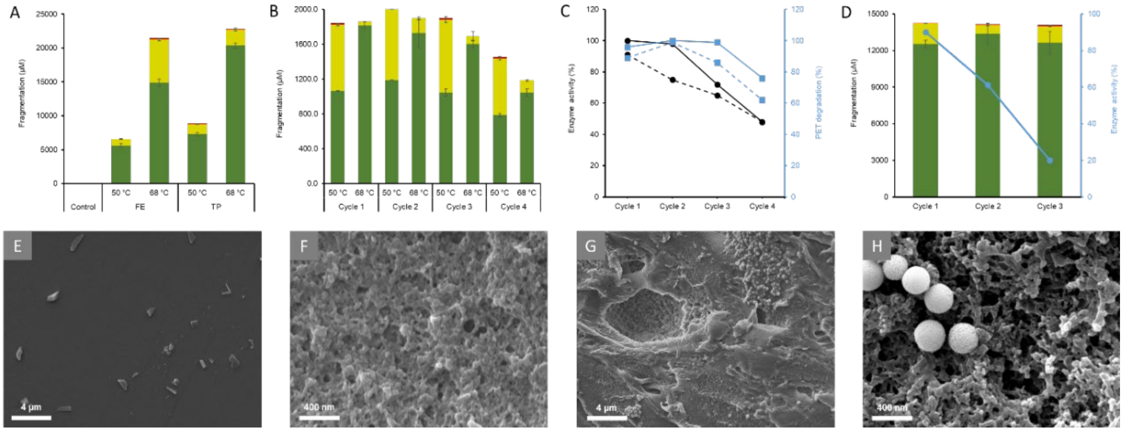

Fig. 2 Fragmentation of PET foil (5 mg) using 4 U of FE and TPSNP over 3 days at 50 °C (A). Fragmentation of PET particles using TP$_{\text{SNP}}$ across four consecutive degradation cycles (B). Degradation efficiency (blue lines) and enzymatic activity (black lines) of nanobiocatalysts over four cycles at 50 (dashed lines) and 68 °C (solid lines) (C). Fragmentation of PET foil (3 mg) after varying incubation times with TP (4 U) at 68 °C across three consecutive degradation cycles, continuing until complete visual degradation was achieved (D) and the corresponding enzymatic activity of TP$_{\text{SNP}}$ after each degradation cycle (blue line) (D). SEM micrographs of PET foil: untreated control (E); after degradation with soluble enzyme (F) and after degradation with TP$_{\text{SNP}}$ (G and H) at 68 °C over 3 days (~95% degradation). Error bars show standard deviations (n = 3).

To evaluate the reusability of the TP$_{\text{SNP}}$, four consecutive degradation cycles were performed with 0.4 mg PET nanoparticles at 50 and 68 °C under the same conditions (Fig. 2B). Complete degradation (100%) was achieved in the first three cycles at both temperatures, with approximately 50% activity retained after the fourth cycle (Fig. 2C). While 50 °C was sufficient to depolymerize PET particles, operation at 68 °C enabled near-complete conversion to TPA in every cycle, providing the highest monomer recovery efficiency. Recyclability was also assessed with PET foil. Three consecutive cycles using 3 mg foil at 68 °C resulted in complete degradation each time, with more than 90% conversion into TPA (Fig. 2D). Activity gradually decreased to about 20% by the third cycle, leading to longer processing times; however, full degradation could still be confirmed visually through the complete disappearance of the foil prior to HPLC analysis. SEM analysis revealed clear differences: soluble enzyme caused surface roughening, whereas TP$_{\text{SNP}}$ produced large holes (up to 10 µm) and extensive erosion (Fig. 2E-H).

Conclusion

Within NANOdePET project, supramolecular stabilization of a PET-degrading enzyme enabled faster product formation, near-complete oligomer conversion into TPA, and full PET depolymerization at elevated temperatures for several cycles. The PTES-modified organosilica layer ensured strong enzyme-PET contact, providing a scalable strategy to durable, reusable, and highly efficient nanobiocatalysts for PET recycling. Of note, increasing enzyme loading would shorten the time required for complete PET degradation and minimize activity loss, ultimately enabling greater number of degradation cycles and supporting a more sustainable enzymatic recycling process.

References

[1] *M. R. Correro et al., "Enzyme Shielding in an Enzyme-thin and Soft Organosilica Layer", Angew. Chem. Int. Ed.,* ***55****, 6285 (2016).*

[2] *M. L. Briand et al., "Partially shielded enzymes capable of processing large protein substrates", Chem. Commun.,* ***56****, 62855170 (2020).*

[3] *A. Foroutan et al., "Exploiting cyclodextrins as artificial chaperones to enhance enzyme protection through supramolecular engineering", Nanoscale,* ***16****, 5123 (2024).*

Advancing Electron Diffraction

Project A19.7: ProtEDinNanoxtals (Paul Scherrer Institute, Biozentrum University of Basel, ELDICO Scientific, leadXpro)
Project leader: V. Panneels
Collaborators: G. Fiorini, E. van Genderen, R. Cheng, J. P. Abrahams, M. Hennig, and G. Steinfeld

Introduction

Electron diffraction (ED) is an emerging technique for the structural determination of proteins, from their nano-sized crystals [1]. Already in the 1970s, a combination of ED and imaging enabled to solve the structure of the membrane protein bacteriorhodopsin, at a resolution of 7 Å [2]. Since then, advances in sample preparation, data collection, and data analysis have broadened the number of samples accessible to structural studies with ED [3,4], thus paving the way for measurements on more protein targets.

Despite recent advancements, protein ED still presents numerous challenges. To obtain usable ED data, crystals need to be thin enough, in the order of hundreds of nanometres [4]. While many scientists and industries already harvest showers of tiny submicron crystals that are too small for X-ray diffraction, membrane protein crystals are often grown in a viscous medium that increases background noise [3]. As a result, extra steps are needed to ensure the sample is properly thinned and suitable for ED data collection. ED is in its early development; therefore, data collection and analysis is often still performed manually, thus reducing the accessibility of the technique to non-experts of the field. Even so, ED offers important advantages. It is particularly useful for very small crystals [5]. It is performed on transmission electron microscopes (TEMs), generally cheaper and easier to maintain than synchrotron facilities. Moreover, because electrons interact strongly with matter, ED has the potential to detect hydrogen atoms effectively.

Importantly, hydrogen atoms and protons are crucial in biological chemical reactions yet visualizing them in proteins is challenging. Spectroscopy struggles due to background noise and difficulties in interpretations of spectroscopic shifts, X-rays do not reveal the exact positions of very light elements like the hydrogen atoms, and neutron crystallography requires large crystals. In this Nano-Argovia project, we aim to establish an ED pipeline and employ it for studying hydrogen roles in protein-ligand interactions, in both soluble and membrane proteins.

Main Results

In the ProtEDinNanoxtals consortium the two partners, UniBas and ELDICO Scientific AG, are ED experts, while PSI and the biotech company leadXpro contribute expertise in protein sample preparation. The goal is to establish an ED workflow using a JEOL F-200 TEM, owned by UniBas and housed at PSI, and to explore the possibility to perform protein ED data collection on the ELDICO electron diffractometer. ELDICO is the first company to commercialize devices designed specifically for small-molecule ED crystallography. Its novel lens-less design minimizes the risk of data distortion due to lens aberration. The recent addition of a cryo-transfer module expands its capability and enables data collection from samples requiring cryo-cooling.

The Nano-Argovia postdoc played a central role in producing and crystallizing multiple proteins, optimizing the nano-sample preparation, collecting and analysing ED datasets, and establishing collaborations with international partners interested in applying the method. Several ED single measurements and data collections were performed on the JEOL F-200 TEM and the ELDICO diffractometer. Structural data were obtained from nanocrystals of DNA-binding enzymes, provided by an external collaborator from the University of Oxford, to 2.1 Å resolution (Fig 1.A). Additionally, to develop a protocol for further thinning of protein crystals, a Focused-Ion-Beam (FIB) milling protocol was established, with support from the BioEM Lab in Basel, using crystals of a light-oxygen-voltage (LOV) domain produced by the postdoc at PSI. Structural data from the resulting LOV lamellae reached 3.5 Å resolution, demonstrating the feasibility of this approach (Fig 1.B).

For the first time, ED measurements on protein were performed successfully on the device from ELDICO using a purpose-built cryogenic adaptor module. Together with the ELDICO team, sample preparation and data collection parameters were optimized, leading to the first protein dataset obtained on the ELDICO device. Nanocrystals of the DNA-binding enzyme, provided by the University of Oxford, diffracted to 3 Å resolution (Fig 2).

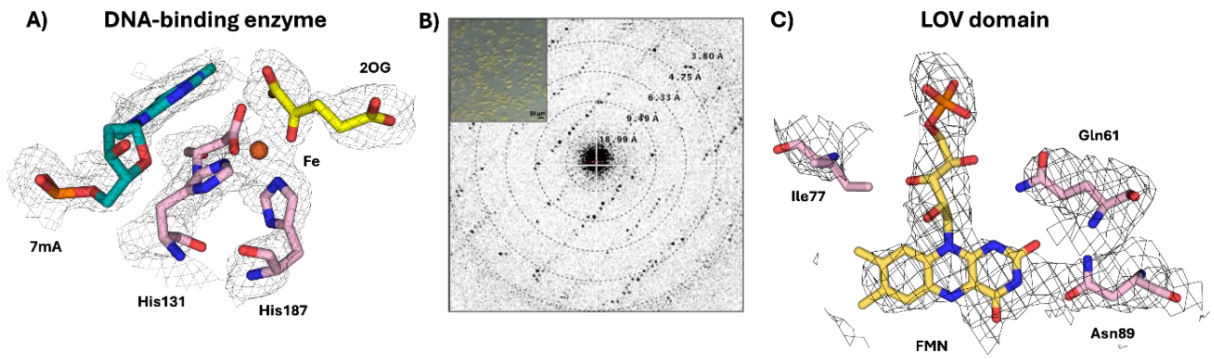

Fig. 1: A) View of the Coulomb potential map, contoured at 1σ, for key amino acids of DNA-binding-enzyme, obtained using ED. B-C) Image showing crystals before milling, lamella diffraction pattern and resulting Coulomb potential map for key amino acids in a LOV domain.

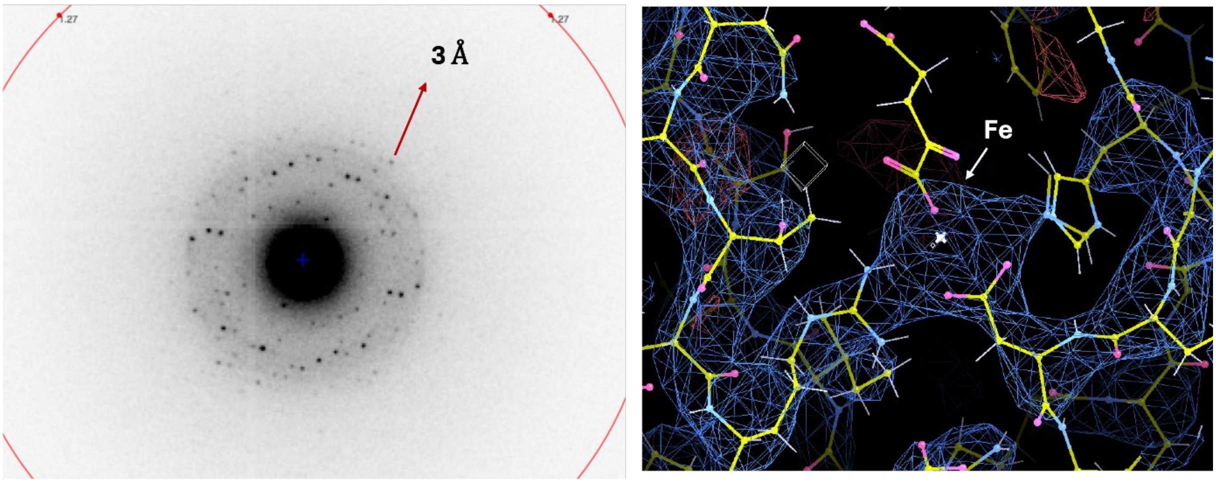

Fig. 2: ED pattern obtained from nanocrystals of a DNA-binding enzyme (molecular weight: 22.3 kDa) using the ELDICO diffractometer and view of the resulting Coulomb potential map, contoured at 1σ, for the metal iron centre (Fe) and other key amino acids in the enzyme.

Conclusion

In our consortium, we collaborate, exchange experience, and collect ED data from nanocrystals and from crystals that have to be precisely nano shaped into lamellae. The protocols we established open the possibility to acquire data from specific/various proteins of interest, including from the drug discovery industrial partner leadXpro. Our collaborative approach is aimed at broadening the expertise across both academia and industry, driving forward our understanding and capabilities in ED and protein crystallography in Switzerland. The results obtained so far lay the foundation for a functioning ED workflow. The forthcoming installment of a newly developed ED-detector at the PSI on the JEOL-F200 TEM, will enable us to push the resolution of our datasets further and ultimately achieve hydrogen localization in proteins.

References

[1] D. Acehan, et al., "Reaching the potential of electron diffraction". Cell Reports Physical Science 5, 102007 (2024).

[2] R. Henderson & P. N. Unwin, "Three-dimensional model of purple membrane obtained by electron microscopy". Nature 257, 28-32 (1975).

[3] M.J Gallenito and T. Gonen "Studying membrane proteins with MicroED". Biochemical Society Transactions 50, 231–239 (2022).

[4] G. Fiorini; G.F.X. Schertler; V. Panneels "Advamces of 3D microcrystals electron diffraction for transmembrane protein structure determination", Biophysical Journal 125, (2025).

[5] M. Gemmi, et al., "3D Electron Diffraction: The Nanocrystallography Revolution". ACS Cent Sci 5, 1315-1329 (2019).

Nano structured Fresnel axicon lens for ultrahigh resolution Optical Coherence Tomography (OCT) and large size, high efficiency gratings for ultrafast chirped pulse amplified lasers

Project A20.3: Nano Diffractive Optics (FHNW Windisch, XRnanotech, Paul Scherrer Institute)
Project leader: B. Resan
Collaborators: M. Zeyen, G. S. Perren, Jan Erjawetz, Valentin Leuthard, and Alexandre Trisorio

Introduction

Many applications, such as Optical Coherence Tomography (OCT), benefit from the use of a Bessel beam. Such a beam can be created using an axicon, a conical lens. For the creation of a narrow Bessel beam, the tip of the axicon plays an important role. Mechanical manufacturing methods are limited by the precision that can be achieved. Within the framework of this project, the concept of a Fresnel lens has been applied to an axicon to create a fraxicon with a submicron precision tip [1, 2]. Furthermore, the project aims to explore DLW lithography, e-beam, and nanoimprint lithography methods for producing high-efficiency optical gratings for UV and IR spectral regions.

Main Results

To the best of our knowledge, a novel optical device called a fraxicon has been designed, manufactured, and characterized. The fraxicon represents the Fresnel lens concept applied to an axicon lens. The diameter of the fraxicon is 2 mm, and the depth of the grooves is 1.4 µm. This fraxicon probe was produced using Direct Laser Writing Lithography (DWL) at XRnanotech and will be tested in an OCT at the FHNW school of engineering. Preliminary tests showed that a narrow Bessel beam with a maximum centre diameter of <2.2 µm has been achieved. The exact diameter has not been measured yet, because the beam was so narrow that it only illuminated a single pixel on the CCD camera.

Fig. 1: Laser Scanning Microscope image of the fraxicon surface showing the periodic structure. The image was taken with a 100x magnification. The scale is 20 µm.

Figures 1 and 2 show the surface of one of the fraxicon samples manufactured and tested. The manufactured samples have a diameter of 2 mm. Further research will focus on the manufacturing of larger samples. The diameter of the beam and therefore the required diameter of the fraxicon, has a direct influence on the propagation distance of the Bessel beam. It is therefore desirable to manufacture fraxicons with a larger diameter [3]. Figure 3 shows the measured propagation of the Bessel beam at different distances between the fraxicon and the sensor (CCD camera). The intensity decreases with increasing distance between the sensor and the fraxicon. At very short distances, the sensor is fully saturated and therefore measures the maximum value. The plot shows the intensity of each pixel across the cross-section of the Bessel beam, demonstrating a highly narrow peak of the Bessel beam with FWHM <2 microns.

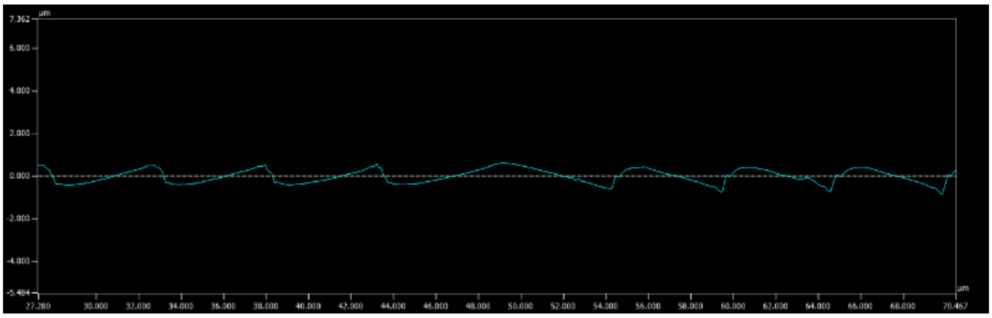

Fig. 1: Surface profile of the fraxcion measured with a Laser Scanning Microscope.

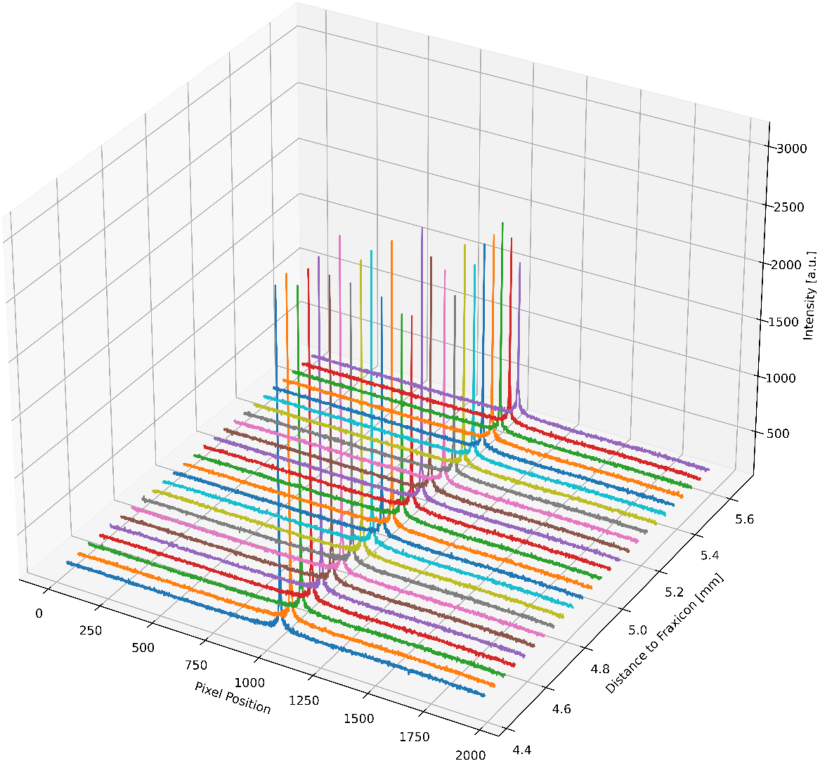

Fig. 3: The measured Bessel beam at various distances between the fraxicon and the sensor.

Conclusion

The fraxicon has successfully been designed, manufactured, and demonstrated to generate a Bessel beam with a propagation length of multiple millimetres. An increase in the fraxicon diameter will further increase the propagation length of the Bessel beam. However, increasing the diameter poses a significant production challenge. Further research aims to implement the fraxicon into an Optical Coherence Tomography System developed and built at the FHNW Schoof of Engineering and Environment, thereby replacing the currently installed axicon. It is expected that the implementation will lead to shorter processing times for OCT scans as well as improved resolution of the images. The experience and technical progress made during the manufacturing of the fraxicon will be valuable in producing highly efficient optical gratings.

References

[1] I. Golub, "Fresnel axicon," Opt. Lett. 31, 1890–1892 (2006).

[2] K. Gourley, I. Golub, and B. Chebbi, "Demonstration of a Fresnel axicon," Appl. Opt. 50, 303-306 (2011).

[3] Z. Ding, H. Ren, Y. Zhao, J. S. Nelson, and Z. Chen, "High-resolution optical coherence tomography over a large depth range with an axicon lens," Opt. Lett. 27, 243–245 (2002).

Nano-Optimized Carrier System for Efficient Laser Tissue Soldering

Project A20.4: Na-LTS (FHNW Muttenz, FHNW Windisch, University of Basel, Thommen Medical)
Project leader: F. Koch
Collaborators: O. Germershaus, L. Kind, M. de Wild, and R. Holtz

Introduction

The project Na-LTS aims to develop a nanoparticle-optimized, adhesive palatal patch for laser tissue soldering (LTS) using a diode laser, in order to enable rapid, safe, and patient-friendly oral tissue closure following mucosal grafting procedures. The project is motivated by the limitations of conventional methods, including mechanical stabilization techniques (e.g. surgical splints, sutures), biostimulatory approaches (e.g. photobiomodulation), physical barriers (resin or acetate stents), resorbable materials (collagen sponges, platelet-rich fibrin (PRF)), as well as adhesive glues (cyanoacrylates) [1][2], which are often associated with infections, pain, or delayed healing.

By combining protein solder with photothermal converters (heat-generating nanoparticles such as gold nanorods (Au-NRs) or indocyanine green (ICG)) embedded in a porous polymer matrix, together with a temperature-controlled laser process, the project pursues an innovative approach that considers clinical efficiency, regulatory requirements, and market viability from the outset [1].

Main Results

During the first project year, various polymer systems have been screened and evaluated based on multiple criteria (such as brittleness, foldability, adaptability, and solubility behavior). A dual polymer mix, based on a synthetic and natural polymer, has been identified as lead candidate due to its good handling properties, biodegradability, and tissue adhesion. Fabrication via phase inversion was successfully established, enabling the production of matrices with variable porosity (see Figure 1) and reproducible structure. Wettability was significantly improved through process optimization and hydrophilic surface coatings. Mechanical testing confirmed a dependence of tensile strength on the polymer content.

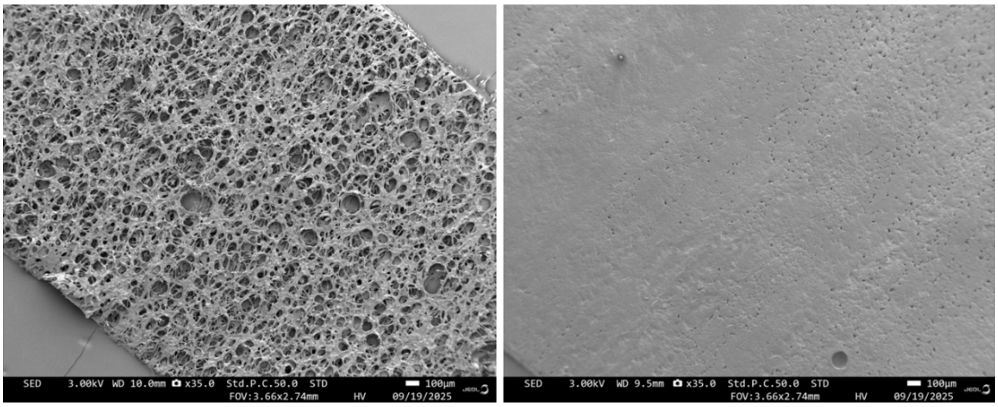

Fig. 1: Polymer matrix with variable porosity, 35x magnification

The photothermal converters (Au-NRs) were reproducibly synthesized using seed-mediated growth, yielding an absorption maximum at 800 nm (for characterization data, see Figure 2. The development of the synthesis protocol simultaneously pursued flexible tuning of the nanorods to other wavelengths and enables the demand-driven production of larger material quantities while ensuring reproducibility

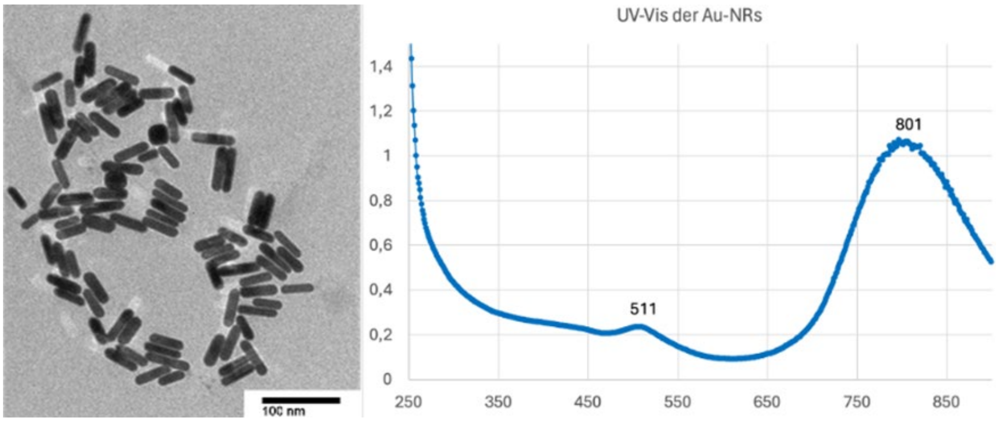

Fig. 2: Left: Transmission Electron Microscopy picture of synthesized gold nanorods. Right: UV-vis spectroscopy of gold nanorods, with absorption maximum at 801 nm

Protein solder (BSA) and photothermal converters (ICG and Au-NRs) were successfully deposited onto the matrix via a coating process. The nano optimized polymer matrix with Au-NR concentrations of 5.6×10^{13} Au-NRs/mL resulted in successful matrix–tissue bonding with porcine gingiva. Since temperature control is a critical factor in the laser tissue soldering (LTS) process, an experimental setup has been established, comprising the laser system, focus control, and temperature monitoring, according to Figure 3. Initial tests on porcine gingiva demonstrated successful matrix–tissue bonding at temperatures of 60–80 °C.

Fig. 3: Experimental setup comprising a laser processing head, infrared camera, motion system, and sample

Conclusion

Within the Na-LTS project, several milestones have already been achieved, including the fabrication of stable polymer matrices with variable porosity, successful commissioning of the laser process, initial ex vivo tissue soldering with mechanical verification, and integration of photothermal nanoparticles. Remaining tasks will focus on the reproducible production of standardized laser samples and optimization of laser parameters for clinical testing. The coating process will be refined to ensure targeted incorporation of Au-NRs, and key objectives include optimizing protein solder and Au-NR content while improving mechanical strength through reinforcing nanocomponents such as silk fibroin.

References

[1] F. D'Ambrosio et al., "Palatal Graft Harvesting Site Healing and Pain Management: What Is the Best Choice? An Umbrella Review ", Appl Sci.,14(13):5614 (2024).

[2] M. Kumar, et al., "Comparison between Silk Sutures and Cyanoacrylate Adhesive in Human Mucosa- A Clinical and Histological Study", J Int Oral Health JIOH, 5(5):95–100 (2013).

Nano-structured absorbable implants for pediatric neurosurgery

Project 20.5: NanoPED (FHNW Muttenz, ANAXAM, KSW, Kairos Medical)
Project leader: R. Marek
Collaborators: M. de Wild, V. Novak, C. Chang, M.-E. Halatsch, A. Alfieri, S. Matter, and L. Berger

Introduction

Craniosynostosis is a congenital pediatric disease in which cranial sutures fuse prematurely, disrupting physiological skull growth and causing progressive skull deformation. Surgical reconstruction is often required to restore skull shape, involving reopening the fused sutures and stabilizing skull segments with an osteosynthesis device, commonly a screw-plate system. Titanium (Ti) implants are the current standard for such interventions due to the materials' strength and ease of use. However, their non-resorbable nature hinders continuous skull growth after implantation and thus necessitates a second surgery for implant removal after 6–12 months. The currently available absorbable options are made of polymers and lack mechanical strength, urging the need for more suitable alternatives [1].

Kairos Medical AG recently introduced a magnesium (Mg)-calcium (Ca)-alloy named “X0” with tunable mechanical response that can be tailored to the distinct mechanical requirements of osteosynthesis screws and plates. This is obtained via the introduction of nm-sized Mg_2Ca-precipitates by adjusting thermo-mechanical process parameters during alloy manufacturing, leading to either high-strength or high-ductility X0 variants [2]. Given the thin cranial plate of infants, osteosynthesis devices used for craniosynostosis surgery need to have filigree structures, and a precise control of the degradation kinetics is essential for clinical implant success. Surface treatments like plasma electrolytic oxidation (PEO), producing a protecting ceramic-like surface layer, are frequently used to improve the initial corrosion resistance of Mg-based implants. However, the influence of the PEO coating on the mechanical performance of implants with highly filigree structures, as well as the influence of the nano-Mg_2Ca-precipitates and the thermo-mechanical conditioning during X0 manufacturing on the alloy´s degradation behavior, are unknown.

Within the NanoPED project, we thus aim at evaluating the influence of the nano-Mg_2Ca-precipitates on the degradation behavior and the mechanical performance of the X0 alloy, allowing the production of a specific osteosynthesis device for craniosynostosis treatment with optimized mechanical and degradation profile (Fig. 1). Furthermore, the impact and effectiveness of a protective PEO coating regarding the described aspects is evaluated.

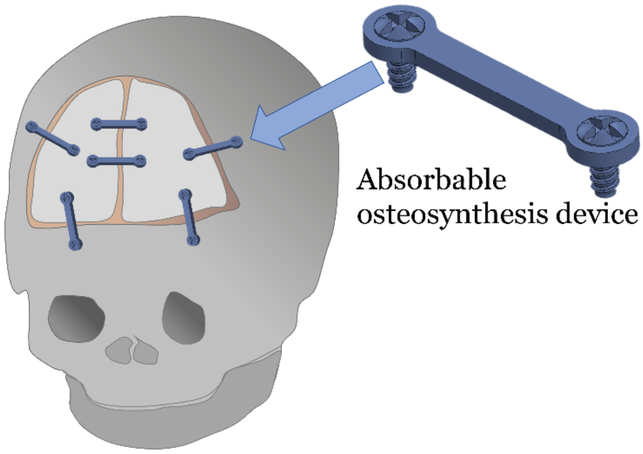

Figure 1: An absorbable osteosynthesis screw-plate device made of the Mg-based alloy “X0” with optimized degradation kinetics and mechanical response is developed for surgical treatment of craniosynostosis.

Main Results

Within the first phase of the NanoPED project, we successfully produced three distinct X0 variants, possessing either high strength (sX0), high ductility (dX0), or intermediate strength and ductility (mX0), by varying the nano- to microstructure of the X0 alloy. Cylinders were manufactured from all three X0 variants for subsequent investigations, while plates were produced from dX0 and mX0 (Fig. 2a), and screws from the sX0 variant only. Additional PEO-coated versions were manufactured from all samples.

First, we investigated the morphological, chemical and crystallographic characteristics of the X0 variants and the PEO coating by means of Scanning Electron Microscopy (SEM) combined with Energy Dispersive X-ray (EDX) spectroscopy, Synchrotron-Radiation-based X-Ray Diffraction (SRXRD) and micro-Computed Tomography (μCT), using cylindrical samples. The PEO coating revealed a highly porous structure (Fig. 2b) with small-sized pores at the bulk-coating conversion interface and a dense outer layer (Fig. 2c), which is characteristic of PEO coatings. Furthermore, the PEO coating revealed good adhesion to the cylinders without delamination during scratch testing (Fig. 2d), which is crucial to avert coating failure during the implantation of the osteosynthesis device, particularly on the screws.

To assess the influence of the nano-Mg_2Ca-precipitates and the PEO coating on the mechanical performance of the osteosynthesis device, we performed 4-point-bending testing of osteosynthesis plates with thicknesses of either 0.6 mm or 0.9 mm, made from mX0 and dX0 variants, with and without PEO coating (Fig. 2a). An increased bending strength and stiffness was measured in case of the thicker plates made of mX0 compared to dX0, as anticipated, while the PEO coating reduced both parameters. Interestingly, we found no influence on the bending properties caused by the nano-precipitates and the PEO coating in the case of the thinner plates.

To elaborate the influence of the nano-Mg_2Ca-precipitates on the degradation kinetics of the X0 alloy, and to test the effectiveness of the PEO coating regarding corrosion protection, we investigate cylinders, screws, and plates in ongoing *in vitro* degradation experiments, by immersing the samples in Hank´s Balanced Salt Solution over different durations at controlled pH levels, temperature and CO_2 atmosphere. Investigating uncoated and PEO-coated cylinders, we observed the formation of a corrosion product layer that covered the entire uncoated cylinder surface after two weeks (Fig. 2e-g). We observed a delayed formation of the corrosion product layer on PEO-coated cylinders, pointing towards decelerated degradation. During subsequent chemical and crystallographic analysis, we identified Ca-phosphates (CaP) being the main elemental components of the corrosion product layer, which is favorable for ongoing osseointegration.

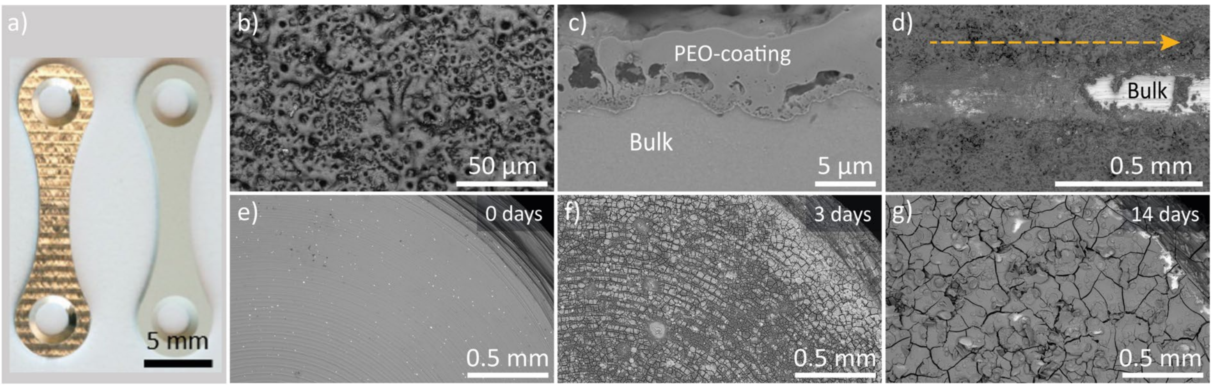

Figure 2: Osteosynthesis plate made of mX0 without (left) and with (right) PEO coating (a). Scanning Electron Microscopy (SEM) investigation of the PEO surface (b) and the ground and polished cross section (c) revealed a highly porous yet well-adhered structure that is typical for PEO coatings. d) No chipping was observed during scratch testing of PEO-coated cylinders. The direction of the scratching with progressive loading is indicated by the orange arrow. During in vitro degradation testing of uncoated X0 cylinders over 0 days (e), 3 days (f), and 14 days (g), the gradual formation of a corrosion product layer was observed, covering the entire cylinder surface after 14 days.

Conclusion

Preliminary findings indicate a potential influence of nano-Mg_2Ca-precipitates and the PEO coating on the mechanical properties of the X0 alloy, which is however dependent on the implant dimensions. Both factors should thus be considered during implant development to obtain the required mechanical profile of the device.

Within the second year of the NanoPED project, we will focus on the influence of the nano-Mg_2Ca-precipitates on the degradation performance of the X0-alloy. The expected results will be combined with the outcomes of the mechanical testing to design an optimized screw-plate system. Ultimately, we strive at developing an osteosynthesis device with customized mechanical properties and predictable degradation behavior, enabling the reliable fabrication of delicate implant structures such as those used in surgical craniosynostosis treatment.

References

[1] B. Zanotti, N. Zingaretti, A. Verlicchi, M. Robiony, A. Alfieri, et al., Cranioplasy : Review of Materials, J. Craniofac. Surg. 27, 2061 (2016).

[2] T. Akhmetshina, L. Berger, I. Basu, S. Montibeller, W. Rubin, et al., High-performance ultra-lean biodegradable Mg–Ca alloys and guidelines for their processing, Acta Mater. 120, 247 (2024).

Quantum-Limited Microwave Amplifier

Project A20.8: QAmp (University of Basel, Paul Scherrer Institute, YQuantum)
Project leaders: C. Schönenberger
Collaborators: D. Sarmah, M. Gabureac, V. Guzenko, C. Jünger, J. Herrmann and A. Hofmann

Introduction

Quantum technologies promise a revolution in sensing, communication and computing. It is a rapidly growing field, generating a new ecosystem of products for “quantum”. QAmp addresses one key component for measuring quantum signals: the first stage amplifier that is supposed to convert a quantum signal with minimal added noise into a classical signal that can then be further processed. The startup YQuantum is developing key microwave components enabling high fidelity quantum control of quantum processors. The startup was inaugurated in 2024 and is located at Park Innovaare next to the PSI. This location has been chosen due to the availability of the new professional cleanroom PICO enabling the fabrication of complex superconducting circuits in collaboration with members from the Laboratory for Nano and Quantum Technologies (LNQ) at PSI on an 8” wafer basis. The target amplifier is a travelling-wave parametric amplifier (TWPA) based on arrays of superconducting Josephson junctions (JJs) with planar capacitors and proprietary integration and packaging [1,2]. We aim to establish a low-noise quantum-limited TWPA that beats the state-of-the-art of currently available amplifiers which only reach “near”-quantum limit adding at least twice as much noise as required by quantum mechanics. The short-to-mid-term application is the readout of quantum states of cryogenic qubits in quantum processor units (QPUs), such as superconducting, charge or spin qubits. Initially, we target a relatively wide frequency bandwidth between 4 GHz and 8 GHz, relevant for the readout of qubits. However, future designs for different applications, such as quantum sensing and imaging, will be considered. To facilitate scaling to many amplifiers, the amplifier module shall be miniaturized and packaged, integrating all required components (amplifier, directional coupler and later also circulator) to be ready to scale readout of QPUs with hundreds of qubits.

Main Results

In QAmp we develop a TWPA based on planar interdigitated capacitors that exhibit ultra-low loss and reaches quantum-limited noise performance. For the fabrication process of the TWPA we work on an all planar (2D) device geometry with a minimal amount of lithography steps. The base material is a highly resistive (undoped) Si wafer that is homogeneously coated with a sputtered superconducting film and then processed into the desired structure as seen in Fig. 1. Initially, we worked with Nb that was sputtered at UBAS, but switched during the first year to Ta, since Ta has shown superior performance in recent literature. Qubits with $T_1 > 1ms$ were presented.

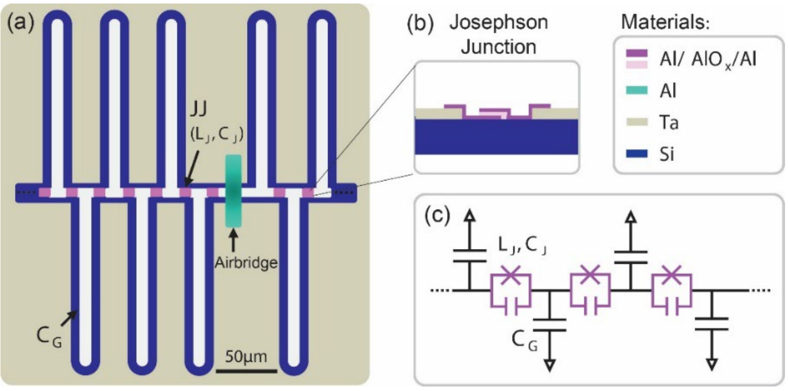

Fig.1: (a) Schematic of the layout of four-unit cells of the proposed TWPA with interdigitated finger capacitors C_G and Josephson junctions (JJs) of inductance L_J and capacitance C_J (purple). The entire TWPA device consists of 1000-2000 such cells. An “air-bridge” is shown in green. It establishes a well-connected ground plane on both sides of the transmission line (TL). (b) Cross section of a JJ showing the superconductor-insulator-superconductor (Al-AlOx-Al) interface indicating also the need for fabrication processes with nanometer precision. (c) Equivalent circuit diagram of the TWPA. One cell consists of L_J, C_J and C_G.

We have found optimized target values for the junction inductor and junction and finger capacitors by minimizing the insertion loss. We have also considered phase-matching in simulations by slightly modulating the parameters periodically along the 1000–2000-unit cells, thereby defining a superlattice with a band stop near 8 GHz [2].

The fabrication and test phase can be split into three main parts: a) high quality superconducting films that enable the engineering of low-loss superconducting circuits, b) the fabrication of superconducting air-bridges which are needed to ensure a good ground plane in the chosen planar geometry, and c) Josephson junctions that can reliably be fabricated with high homogeneity and low variability of junction parameters (junction inductances).

In the first year, we primarily worked on a) and b). Due to space considerations, we only show results for part a), but we mention that we have lately converged to a clean-room fabrication process that yields Al air-bridges with high confidence and ease of manufacturing as all is based on laser-writing with only three-resist steps.

To test the quality of the superconducting film for low-loss application, transmission line resonators (TLR) were structured into the sputter film and then electrically characterized. Initially, we used 160nm thick Nb films that were sputtered at UBAS on 4" wafers. They were ideally suited to get acquainted with the laser writer at PICO (Heidelberg DWL 66+) which allows writing at a wide range of laser intensities. We found an almost perfect match between the designed frequencies of the resonators and the measured ones. The resonance frequencies were obtained by performing lumped element simulations in QUCS (Quite Universal Circuit Simulator) with a coupling capacitance matrix obtained through a Maxwell 3D simulation in Ansys.

As mentioned, we switched from Nb to Ta films that were sputtered at PICO. In Fig. 2 we show the results of four Ta resonators designed as "hangers" capacitively coupled to a feedline. All four resonances are electrically visible, and the circular fits work to a very high degree yielding the resonance frequency, the coupling and internal quality factors as well as an asymmetric parameter. Here, the measured resonance frequency is on average 1% smaller than designed and shows an exceptionally low standard deviation of less than 0.2%. In the first run the quality factors varied between 35'000 and 75'000 with a mean of 48'000 measured at 100mK and photon number $>10^{3}$. In the 2nd run we obtained quality factors between 87,000 to 92,000. While $Qi \approx 10^{5}$ is a good starting point, it is not good enough for achieving low loss amplification. Our target is $Qi = 10^{6}$ and we think that we will achieve this when we are using our new undoped and highly resistive Si substrates, which we recently purchased, and cleaning it properly right before sputtering the Ta film, as well as by adding sufficient and systematic airbridges for proper grounding instead of the manually placed bridges done with the bonder.

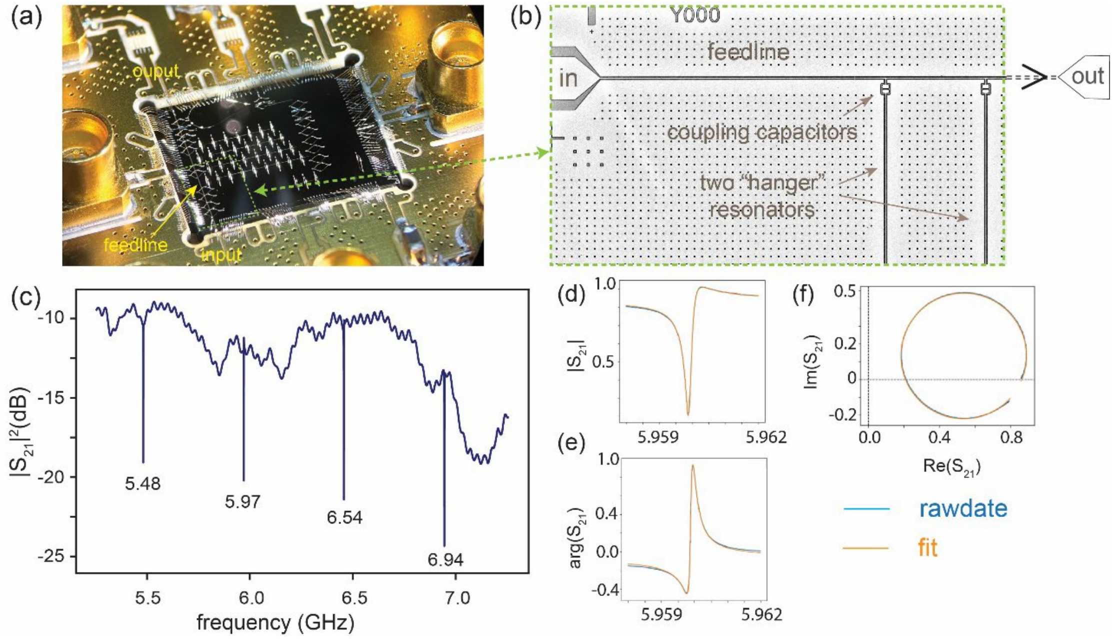

Fig. 2: (a) Chip bonded to a PCB containing 4 "hanger" $\lambda/4$ resonators attached to a feedline, all structured into a superconducting Ta film. A closer view on the device is seen in (b). Note, (b) is rotated by 90° clockwise relative to (a). (c) Measured forward power transmission $|S(f)_{21}|^2$ as a function of frequency f through the feedline. In this example, all four designed resonators show up as sharp dips with their respective designed frequencies. (d-e) Fits to the amplitude and phase and (f) real and imaginary part of the transmission amplitude $S(f)_{21}$.

Conclusion

We have realized low-loss coplanar transmission line resonators in superconducting Ta films and established a simple fabrication process for superconducting air-bridges. In the 2nd year, we will work on the Josephson junctions and then combine all together to establish a TWPA.

In addition to the SNI we acknowledge support by the HTZ, Innosuisse and the Swiss Quantum Initiative. We are grateful to A. Grimm (PSI) and his team for the collaboration. We are also grateful for support from the mechanical workshop at the Department of Physics at UBAS under the lead of Sascha Martin.

References

[1] J. Aumentado,, Superconducting Parametric Amplifiers: The State of the Art in Josephson Parametric Amplifiers, IEEE Microwave Magazine 21 (8), 45-59 (2020).

[2] M. Esposito, A. Ranadive, L. Planat and N. Roch, Perspective on traveling wave microwave parametric amplifiers, Appl. Phys. Lett. 119, 120501 (2021).

Selective Nano Magnetic Detector for Water Pollution

Project A20.9: SENAMAG (FHNW Muttenz, FHNW Windisch, MEMS)
Project leader: J. Pascal
Collaborators: O. Tagit, S. Gorenflo, and D. Matter

Introduction

Water quality is fundamental to human health and ecosystem sustainability. Water pollution originates from diverse sources (industries, agriculture, etc.). For instance, some industries release heavy metals as well as persistent chemicals such as PFAS, which accumulate in rivers and groundwater. Traditional water analysis relies on advanced laboratory techniques, like chromatography or mass spectrometry. These methods offer ultra-low detection limits and analyze multiple pollutions simultaneously. Their implementation requires skilled personnel, facilities, and significant financial resources and their limitations in terms of portability and turnaround time highlight the need for complementary on-site solutions. On-site water quality analysis aims to bridge the gap between laboratory precision and the need for real-time monitoring. Tools such as electrochemical sensors or turbidity meters provide immediate results, are cost-effective and easy to deploy. However, their sensitivity is lower than lab-based methods, and they can be susceptible to environmental interferences. Despite challenges, on-site analysis plays a crucial role in rapid decision-making. Our SENAMAG detector concept aims to complete the available portfolio for water quality monitoring. By leveraging different magnetic technologies, SENAMAG is designed to operate autonomously within water networks, delivering reliable daily measurements without maintenance for several years. The system's distributed architecture allows for localized detection of targeted contaminants, enabling fast responses to pollution events. SENAMAG's core innovation lies in its ability to combine selectivity, sensitivity, and scalability. The core technology we intend to develop first relies on the use of magnetic nanoparticles (MNP) functionalized to bind specifically targeted pollutant molecules. The detector then employs a magnetic manipulation system to capture, concentrate and manipulate the clusters. Finally, magnetometers measure their magnetic response which thus provides a direct indication of pollutant presence. The concept aims to offer a new way to detect pollution efficiently.

Main Results

During the first year of the project, we worked on each block of the system (MNP, manipulation, detection) separately. Our initial experiments with MNPs focused on their functionalization to selectively capture target pollutants in water. Our initial focus is on glyphosate, a widely used herbicide with significant environmental and health concerns. The aim was to create MNPs capable of binding specifically to glyphosate molecules, but they should also be able to bind to a coated surface for storage before use. We started by working on the process of conjugating antibodies to the surface of the MNPs. We began by biotinylating the anti-glyphosate antibody, because our MNPs are coated with streptavidin (Fig.1a). This process involved attaching biotin molecules to the antibody, enabling its sub-sequent binding to streptavidin-coated MNPs (Fig. 1a). Using the HABA assay, we quantified the biotinylation efficiency, determining an average of 0.78 biotin molecules per antibody. The next step was to bind the biotinylated antibody to streptavidin-coated MNPs, leveraging the exceptionally strong and specific streptavidin-biotin interaction. This binding process resulted in the formation of a stable complex between the antibody and the MNPs. To confirm the successful conjugation, we used Dynamic Light Scattering (DLS), which revealed an increase in the diameter of 31 nanometers after antibody binding (Fig. 1b). This increase provided clear evidence of the antibody's attachment to the MNPs, as the larger size reflected the presence of the antibody layer on the MNPs surface. To further validate the conjugation, we labeled the biotinylated antibody with Fluorescein isothiocyanate. The appearance of an absorbance peak confirmed that the antibodies were effectively bound to the MNPs (Fig. 1c). Finally, we conducted an aggregation assay by mixing our functionalized MNPs and MNPs functionalized with glyphosate molecules to evaluate their specific binding interaction. This experiment confirmed the selective recognition and clustering (Fig. 1d, sample 1). However, control sample 3 showed nonspecific binding between glyphosate and streptavidin molecules (Fig. 1d). This is a phenomenon that must be eliminated to ensure the selectivity of the detector, and it is therefore our top priority for the second year at the MNP level. The second part of the chemistry work involves functionalizing a surface to store the MNPs before they encounter pollutants. To this end, several tests were conducted during this first year. Glass functionalization emerged as a promising solution for achieving stable and reproducible surface. In this approach, microscope glass slides were functionalized using APTES followed by the attachment of glyphosate molecules. The goal was to create a surface that could selectively bind MNPs functionalized with glyphosate-specific antibodies. However, we encountered challenges with the specificity of the APTES coating. To address these issues, we transitioned to using silane-PEG-amine, a more robust and versatile functionalization agent. Hydrophilic PEG chains prevent non-specific absorption. This modification significantly improved the binding efficiency and stability of the MNPs on the slide surface.

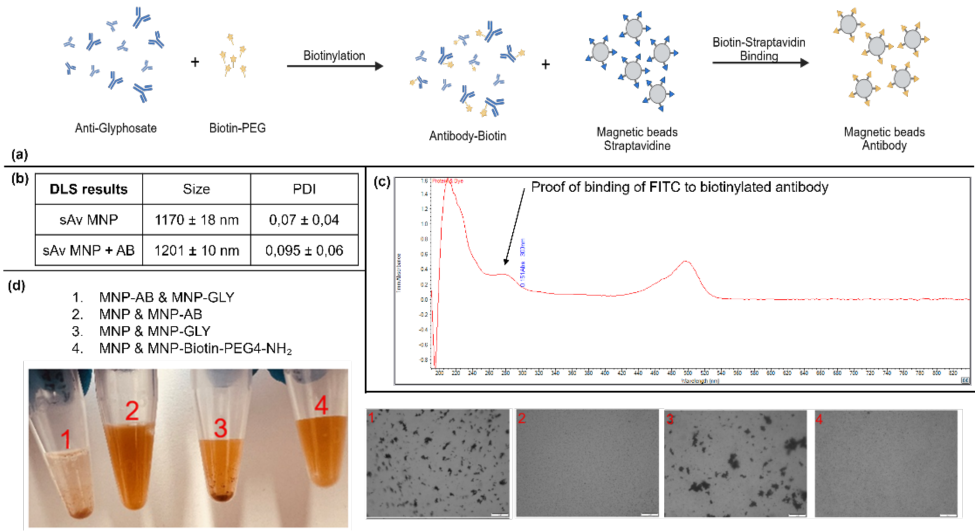

DLS results	Size	PDI
sAv MNP	1170 ± 18 nm	0,07 ± 0,04
sAv MNP + AB	1201 ± 10 nm	0,095 ± 0,06

Fig. 1: (a) MNPs functionalization strategy (b) DLS results (c) Absorbance measurement results (d) Aggregation assay

Regarding the manipulation of the MNPs, the first year was devoted to developing a current source with three outputs that will subsequently be used to power the coils used to manipulate the MNPs (Fig. 2a). The source has been tested and is fully functional. As a result, the second year will be devoted to developing the coils. For the detection part, the first part of the work was to select a miniaturized magnetic sensor technology capable of detecting clusters of MNPs that are manipulated at a controlled frequency. Optically Pumped Magnetometers and Magneto-Impedance (MI) have been identified as the most promising candidates. Simple tests carried out with MI sensors on moving MNPs led to the detection of 25 µg. During the second year of the project, we will work to lower this detection limit as much as possible. To do this, we will implement a synchronous detection. This will be done by using a lock-in amplifier, a powerful signal processing technique designed to extract weak, periodic signals buried in noise. This method works by multiplying the input signal by a reference signal at the same frequency, followed by low pass filtering to isolate the component of interest. By focusing on a specific frequency, synchronous detection effectively suppresses random noise and interfering signals, significantly enhancing the signal-to-noise ratio (SNR). By employing lock-in amplification, we can precisely isolate the magnetic response of the MNPs. This approach is essential for achieving the high sensitivity required to monitor trace levels of contaminants in real-world conditions, where noise and interference are inevitable. We began testing this technique during the first year with a simple setup consisting of a coil fed with a dynamic signal of ± 5 mA (Fig. 2c), blue curve) and an MI sensor located 70 cm away (Fig. 2b). As a result, we are in a situation where the magnetic signal is drowned out by ambient noise (Fig. 2c, red curve). After implementing lock-in, we can detect the period during which the signal is emitted (Fig. 2c, green curve). These initial results are promising, and we will continue along this path for the second year.

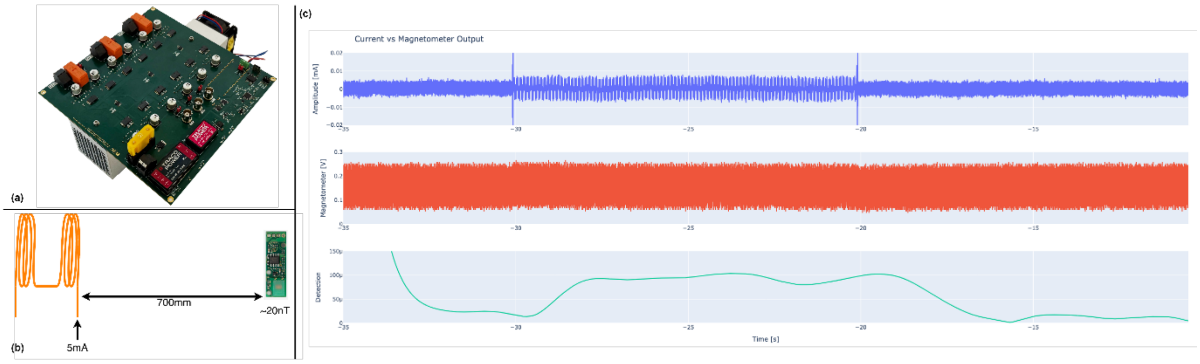

Fig. 2: (a) Developed current source (b) Experimental setup (c) Results of lock-in detection

Conclusion

In conclusion, our initial results start demonstrating the feasibility of the SENAMAG concept at different levels. In addition to demonstrating the technology of each block separately, we also seek to select techniques that will subsequently enable scalability and low cost. For instance, the glass functionalization strategy not only provided a stable platform for MNP binding but also offered a scalable and cost-effective solution for real-world applications. While challenges remain for the second year, such as improving SNR, our findings from the first year lay a solid foundation for the development of a full proof of concept of a SENAMAG system in 2026.

Publications

[1]

J. H. Ungerer et al., “A dephasing sweet spot with enhanced dipolar coupling,” Commun Phys, vol. 8, no. 1, p. 306, Jul. 2025, doi: 10.1038/s42005-025-02216-9.

[2]

T. Weber et al., “Advanced SQUID-on-lever scanning probe for high-sensitivity magnetic microscopy with sub-100-nm spatial resolution,” Phys. Rev. Appl., vol. 24, no. 5, p. 054041, Nov. 2025, doi: 10.1103/6s24-vz3k.

[3]

J. Fernández de Santaella, N. G. Koch, L. Widmer, and M. A. Nash, “Amber Codon Mutational Scanning and Bioorthogonal PEGylation for Epitope Mapping of Antibody Binding Sites on Human Arginase-1,” ACS Chem. Biol., vol. 20, no. 4, pp. 791–801, Apr. 2025, doi: 10.1021/acschembio.4c00692.

[4]

P. A. Lehner et al., “Architecture and conformational dynamics of the BAM-SurA holo insertase complex,” Science Advances, vol. 11, no. 14, p. eads6094, Apr. 2025, doi: 10.1126/sciadv.ads6094.

[5]

V. Hutskalova and C. Sparr, “Aromatic ring-opening metathesis,” Nature, vol. 638, no. 8051, pp. 697–703, Feb. 2025, doi: 10.1038/s41586-024-08472-z.

[6]

R. S. Nielsen et al., “BaZrS3 Lights Up: The Interplay of Electrons, Photons, and Phonons in Strongly Luminescent Single Crystals,” Advanced Optical Materials, vol. 13, no. 26, p. e00915, 2025, doi: 10.1002/adom.202500915.

[7]

Z. Liu, A. Hinaut, T. Glatzel, U. Aschauer, and E. Meyer, “Chemical Coordination Induced Fullerene Dimers on Hot Pt(111),” Angewandte Chemie International Edition, vol. 64, no. 33, p. e202505101, 2025, doi: 10.1002/anie.202505101.

[8]

S. Honrath et al., “Closing the gap: Nonviral TFAMoplex transfection boosted by bZIP domains compared to AAV-mediated transduction,” Molecular Therapy Nucleic Acids, vol. 36, no. 2, p. 102526, Jun. 2025, doi: 10.1016/j.omtn.2025.102526.

[9]

G. De Sousa, P. Bakhshinezhad, B. Annby-Andersson, P. Samuelsson, P. P. Potts, and C. Jarzynski, “Continuous feedback protocols for cooling and trapping a quantum harmonic oscillator,” Phys. Rev. E, vol. 111, no. 1, p. 014152, Jan. 2025, doi: 10.1103/PhysRevE.111.014152.

[10]

Y.-W. Chang et al., “Correlated Magnetic and Electrical Phenomena in Epitaxially Weaved Manganite Lateral Homostructures,” Small, vol. 21, no. 11, p. 2411424, 2025, doi: 10.1002/smll.202411424.

[11]

R. S. Eggli et al., “Coupling a high-Q resonator to a spin qubit with all-electrical control,” Phys. Rev. Res., vol. 7, no. 1, p. 013197, Feb. 2025, doi: 10.1103/PhysRevResearch.7.013197.

[12]

V. Hutskalova, C. Jandl, A. Prescimone, and C. Sparr, “Determination of the Absolute Configuration by 3D ED to Elucidate the Atroposelectivity in Aromatic Ring-Opening Metathesis,” CHIMIA, vol. 79, no. 4, pp. 255–258, Apr. 2025, doi: 10.2533/chimia.2025.255.

[13]

P. Jasko, M. Bina, D. Frey, C.-A. Schoenenberger, C. G. Palivan, and R. A. Kammerer, “Diphtheria toxin T-domain as a tool for inducing lipid vesicle fusion,” Commun Chem, vol. 8, no. 1, p. 355, Nov. 2025, doi: 10.1038/s42004-025-01738-1.

[14]

C. Drechsel et al., “Discharge and electron correlation of radical molecules in a supramolecular assembly on superconducting Pb(111),” Nanoscale Horizons, vol. 10, no. 10, pp. 2365–2373, 2025, doi: 10.1039/D5NH00462D.

[15]

J. Kost, N. Peyer, J. Huwyler, and M. Puchkov, “Drug loading mechanism of hollow hydroxyapatite microcapsules,” European Journal of Pharmaceutics and Biopharmaceutics, vol. 214, p. 114785, Sep. 2025, doi: 10.1016/j.ejpb.2025.114785.

[16]

K. N. Baumann, E. Bertosin, A. Barth, C. Dekker, and R. Y. H. Lim, “Elucidating the nanoscopic organization and dynamics of the nuclear pore complex,” Nucleus, vol. 16, no. 1, p. 2510106, Dec. 2025, doi: 10.1080/19491034.2025.2510106.

[17]

S. Fatemeh Mousavi et al., “Emergence of conformational diversity and complexity of supramolecular structure by the interaction of a simple molecule with a uniform surface,” Commun Chem, vol. 8, no. 1, p. 214, Jul. 2025, doi: 10.1038/s42004-025-01607-x.

[18]

S. F. Mousavi et al., “Emergence of Conformational Diversity in the Supramolecular Assembly of Porphyrins on Uniform Surface Substrates,” Meet. Abstr., vol. MA2025-01, no. 17, p. 1266, Jul. 2025, doi: 10.1149/MA2025-01171266mtgabs.

[19]

J. P. Coats et al., “Engineering pH-Responsive Nanocarriers via an Optimized Synthesis of PMOXA-b-PDPA Amphiphilic Diblock Copolymers,” Macromolecular Rapid Communications, vol. 46, no. 20, p. e00418, 2025, doi: 10.1002/marc.202500418.

[20]

J. Spring et al., “Engineering the Magnetic Transition Temperatures and the Rare Earth Exchange Interaction in Oxide Heterostructures,” ACS Nano, vol. 19, no. 15, pp. 14652–14660, Apr. 2025, doi: 10.1021/acsnano.4c07252.

[21]

M. Governale, C. Schönenberger, P. Scarlino, and G. Rastelli, “Entangled Photon-Pair Emission in Waveguide Circuit QED from a Cooper Pair Splitter,” PRX Quantum, vol. 6, no. 2, p. 020339, May 2025, doi: 10.1103/PRXQuantum.6.020339.

[22]

M. Weegen, P. N. Fountas, M. Poggio, and S. Willitsch, “Experimental implementation of an ion-nanowire hybrid system,” Rev. Sci. Instrum., vol. 96, no. 6, p. 063203, Jun. 2025, doi: 10.1063/5.0260410.

[23]

E. Rahimi, P. Mesquida, T. Glatzel, Y. G. Garcia, and A. Mol, “From electrostatics to electrochemistry: rethinking volta potential in nowadays and future in-situ kelvin probe studies,” Electrochimica Acta, vol. 545, p. 147702, Jan. 2026, doi: 10.1016/j.electacta.2025.147702.

[24]

Z. Zhou et al., “Gate-tunable double-dome superconductivity in twisted trilayer graphene,” Nat. Phys., vol. 21, no. 11, pp. 1773–1779, Nov. 2025, doi: 10.1038/s41567-025-03040-2.

[25]

S. Haldar et al., “High-efficiency microwave photodetection by cavity-coupled double quantum dots with single-cavity-photon sensitivity,” Phys. Rev. Appl., vol. 24, no. 4, p. 044074, Oct. 2025, doi: 10.1103/jlxt-19h9.

[26]

H. Gunstheimer, G. Fläschner, J. D. Adams, H. Hölscher, and B. W. Hoogenboom, “High-Speed Quantitative Nanomechanical Mapping by Photothermal Off-Resonance Atomic Force Microscopy,” Small, vol. 21, no. 40, p. e07640, 2025, doi: 10.1002/smll.202507640.

[27]

A. Corazza et al., "Homogeneous Free-Standing Nanostructures from Bulk Diamond over Millimeter Scales for Quantum Technologies," Nano Lett., vol. 25, no. 40, pp. 14526–14533, Oct. 2025, doi: 10.1021/acs.nanolett.5c03083.

[28]

T. A. Butcher et al., "Imaging ferroelectric domains with soft-x-ray ptychography at the oxygen K-edge," Phys. Rev. Appl., vol. 23, no. 1, p. L011002, Jan. 2025, doi: 10.1103/PhysRevApplied.23.L011002.

[29]

M. Z. Khan et al., "Imaging magnetic order in a two-dimensional iron-rich phyllosilicate," Commun Mater, vol. 6, no. 1, p. 217, Oct. 2025, doi: 10.1038/s43246-025-00936-7.

[30]

A. J. Healey et al., "Imaging Magnetic Switching in Orthogonally Twisted Stacks of a van der Waals Antiferromagnet," ACS Nano, vol. 19, no. 50, pp. 42140–42147, Dec. 2025, doi: 10.1021/acsnano.5c12297.

[31]

N. Sangwan et al., "Impact of Surface Treatments on the Transport Properties of Germanium 2DHGs," ACS Appl. Electron. Mater., vol. 7, no. 19, pp. 8844–8849, Oct. 2025, doi: 10.1021/acsaelm.5c01069.

[32]

C. Li et al., "Individual Assembly of Radical Molecules on Superconductors: Demonstrating Quantum Spin Behavior and Bistable Charge Rearrangement," ACS Nano, vol. 19, no. 3, pp. 3403–3413, Jan. 2025, doi: 10.1021/acsnano.4c12387.

[33]

B. Raveh et al., "Integrative mapping reveals molecular features underlying the mechanism of nucleocytoplasmic transport," Proceedings of the National Academy of Sciences, vol. 122, no. 42, p. e2507559122, Oct. 2025, doi: 10.1073/pnas.2507559122.

[34]

T. Kozai et al., "Karyopherins remodel the dynamic organization of the nuclear pore complex transport barrier," Nat Cell Biol, vol. 27, no. 12, pp. 2089–2101, Dec. 2025, doi: 10.1038/s41556-025-01812-9.

[35]

R. Jha et al., "Large Tunable Kinetic Inductance in a Twisted Graphene Superconductor," Phys. Rev. Lett., vol. 134, no. 21, p. 216001, May 2025, doi: 10.1103/PhysRevLett.134.216001.

[36]

C. Pellet-Mary et al., "Lateral exchange bias for Néel-vector control in atomically thin antiferromagnets," Nat Commun, vol. 16, no. 1, p. 9725, Nov. 2025, doi: 10.1038/s41467-025-64700-8.

[37]

H. Wu et al., "Laterally π-Extended Polyhelicenes," J. Am. Chem. Soc., vol. 147, no. 47, pp. 43842–43849, Nov. 2025, doi: 10.1021/jacs.5c15494.

[38]

H. Ohlin, B. Benz, L. Romano, and U. Vogt, "Lift-off free catalyst for metal assisted chemical etching of nanostructured silicon zone plates in vapour phase," Nano Ex., vol. 6, no. 1, p. 015019, Apr. 2025, doi: 10.1088/2632-959X/adbd5b.

[39]

A. R. Unniram Parambil, J. Pulparayil Mathew, M. J. Parammal, and J. De Roo, "M6O8 metal oxo clusters: A key structural motif across the periodic table," Coordination Chemistry Reviews, vol. 546, p. 216967, Jan. 2026, doi: 10.1016/j.ccr.2025.216967.

[40]

Q. Li et al., "Macro-scale, scaffold-assisted model of the human bone marrow endosteal niche using hiPSC-vascularized osteoblastic organoids," Cell Stem Cell, vol. 32, no. 12, pp. 1941-1958.e8, Dec. 2025, doi: 10.1016/j.stem.2025.10.009.

[41]

N. Abdollahi, D. Messmer, V. Mihali, and C. G. Palivan, "Magnetically Controlled Polymer Giant Unilamellar Vesicles," Small, vol. 21, no. 31, p. 2502552, 2025, doi: 10.1002/smll.202502552.

[42]

J. A. Wilcox et al., "Magnetically controlled vortex dynamics in a ferromagnetic superconductor," Commun Mater, vol. 6, no. 1, p. 108, May 2025, doi: 10.1038/s43246-025-00833-z.

[43]

P. Hiret et al., "Measurements of RF plasma sheath thickness in magnetic field up to 500 mT using a floating spiral probe," Phys. Plasmas, vol. 32, no. 9, p. 093510, Sep. 2025, doi: 10.1063/5.0277005.

[44]

A. Kharchenko, I. Cornu, B. Goldfuss, and K. Tiefenbacher, "Methylene-Bridged Calixarene Polyhedra: An Elusive Class of Symmetric Molecular Architectures," Helvetica Chimica Acta, vol. n/a, no. n/a, p. e00177, doi: 10.1002/hlca.202500177.

[45]

L. Marot et al., "Mirror dual cleaning of ITER equatorial diagnostic Wide Angle Viewing System," Fusion Engineering and Design, vol. 214, p. 114892, May 2025, doi: 10.1016/j.fusengdes.2025.114892.

[46]

S. Huang et al., "Moiré Energy Dissipation Driven by Nonlinear Dynamics," ACS Nano, vol. 19, no. 18, pp. 17365–17373, May 2025, doi: 10.1021/acsnano.4c16817.

[47]

P. Qi et al., "Monolithic X-ray achromat," Opt. Express, OE, vol. 33, no. 12, pp. 26578–26589, Jun. 2025, doi: 10.1364/OE.557328.

[48]

S. Boult, P. Pacak, B. Yang, H. Liu, V. Vogel, and M. A. Nash, "Multi-state catch bond formed in the Izumo1:Juno complex that initiates human fertilization," Nat Commun, vol. 16, no. 1, p. 7952, Aug. 2025, doi: 10.1038/s41467-025-62427-0.

[49]

C. L. Alter et al., "Nano Plasma Membrane Vesicle-Lipid Nanoparticle Hybrids for Enhanced Gene Delivery and Expression," Advanced Healthcare Materials, vol. 14, no. 1, p. 2401888, 2025, doi: 10.1002/adhm.202401888.

[50]

F. Bersano et al., "Nanomole Process: Enabling Localized Metallic Back-Gates for Enhanced Cryogenic Front-to-Back Coupling in FDSOI Quantum Dots," IEEE Journal of the Electron Devices Society, vol. 13, pp. 210–218, 2025, doi: 10.1109/JEDS.2025.3545661.

[51]

T. A. Butcher et al., "Nanoscale domain-wall dynamics in micromagnetic structures with weak perpendicular anisotropy," Phys. Rev. B, vol. 111, no. 22, p. L220409, Jun. 2025, doi: 10.1103/2y4r-my27.

[52]

I. Efe et al., "Nanoscale electrostatic control in ferroelectric thin films through lattice chemistry," Nat Commun, vol. 16, no. 1, p. 6131, Jul. 2025, doi: 10.1038/s41467-025-60176-8.

[53]

G. Navarro-Marín et al., "Non-covalent Molecular Wires of Double Thiahelicene on Cu(111): A nc-AFM Study at Room Temperature," J. Phys. Chem. C, vol. 129, no. 11, pp. 5637–5644, Mar. 2025, doi: 10.1021/acs.jpcc.4c07662.

[54]

A. Chacko et al., "On tailoring structural and optoelectronic properties of TiO2 thin films synthesized via 'room' temperature high power impulse magnetron sputtering (HiPIMS)," J. Phys. Energy, vol. 7, no. 3, p. 035017, Jun. 2025, doi: 10.1088/2515-7655/ade289.

[55]

R. Pawlak et al., “On-Surface Synthesis and Characterization of Radical Spins in Kagome Graphene,” ACS Nano, vol. 19, no. 4, pp. 4768–4777, Feb. 2025, doi: 10.1021/acsnano.4c15519.

[56]

P. D’Astolfo et al., “On-Surface Synthesis and Cryogenic Exfoliation of Sterically Frustrated Atropisomers,” ACS Nano, vol. 19, no. 14, pp. 13805–13816, Apr. 2025, doi: 10.1021/acsnano.4c16645.

[57]

H. Nicolas et al., “Operational Amplifier Circuits for Magnetic Sensing Using Perpendicular Low-Coercivity Nanoscale Spin Transfer Torque Magnetic Tunnel Junctions,” IEEE Sensors Journal, vol. 25, no. 6, pp. 9550–9559, Mar. 2025, doi: 10.1109/JSEN.2025.3537700.

[58]

J. Post et al., “Optical microcavity characterization via resonance spectra and modes,” Phys. Rev. A, vol. 112, no. 3, p. 033537, Sep. 2025, doi: 10.1103/y63l-zwr5.

[59]

K. Prech et al., “Optimal Time Estimation and the Clock Uncertainty Relation for Stochastic Processes,” Phys. Rev. X, vol. 15, no. 3, p. 031068, Sep. 2025, doi: 10.1103/rpls-mp8z.

[60]

J. H. Hwang et al., “Optimized Synthesis and Device Integration of Long 17-Atom-Wide Armchair Graphene Nanoribbons,” ACS Nano, vol. 19, no. 42, pp. 37230–37240, Oct. 2025, doi: 10.1021/acsnano.5c11981.

[61]

R. S. Nielsen et al., “Parallel exploration of the optoelectronic properties of (Sb,Bi)(S,Se)(Br,I) chalcohalides,” J. Mater. Chem. A, vol. 13, no. 37, pp. 31727–31739, Sep. 2025, doi: 10.1039/D5TA05011A.

[62]

N. Larreina Vicente, M. Srinivas, and O. Tagit, “Perfluorocarbon-Loaded Poly(lactide-co-glycolide) Nanoparticles from Core to Crust: Multifaceted Impact of Surfactant on Particle Ultrastructure, Stiffness, and Cell Uptake,” ACS Appl. Polym. Mater., vol. 7, no. 5, pp. 2864–2878, Mar. 2025, doi: 10.1021/acsapm.4c03360.

[63]

D. Lotter, A. Huber, J. Wellauer, O. S. Wenger, and C. Sparr, “Photoinduced Energy Transfer via an Atropisomeric Molecular Bridge,” Helvetica Chimica Acta, vol. 108, no. 1, p. e202400163, 2025, doi: 10.1002/hlca.202400163.

[64]

A. M. Dmitriev, Y. Wang, T. C. Sousa, L. Marot, L. Moser, and E. Meyer, “Platinum as a first mirror material for fusion applications: a comparison with rhodium,” Nucl. Fusion, vol. 65, no. 3, p. 036012, Feb. 2025, doi: 10.1088/1741-4326/adb0dc.

[65]

L. Heuberger et al., “Polymeric Giant Unilamellar Vesicles Support Longevity of Native Nuclei in Protocells,” Small Science, vol. 5, no. 6, p. 2400622, 2025, doi: 10.1002/smsc.202400622.

[66]

R. Hamaguchi, D. A. Graf, K. Kinbara, and T. R. Ward, “Programmable Artificial-Cellular Membrane Dynamics via Ring-Closing Metathesis,” J. Am. Chem. Soc., vol. 147, no. 43, pp. 39204–39211, Oct. 2025, doi: 10.1021/jacs.5c10187.

[67]

M. Brüderlin, M. Kolesnikov, F. Röthlin, R. Y. H. Lim, and M. Basler, “Pseudomonas aeruginosa assembles H1-T6SS in response to physical and chemical damage of the outer membrane,” Science Advances, vol. 11, no. 10, p. eadr1713, Mar. 2025, doi: 10.1126/sciadv.adr1713.

[68]

E. Maksimova, D. E. Salazar Marcano, and J. De Roo, “Quantification of Azides on the Surface of Nanoparticles: Toward Precise Bioconjugation,” Small Structures, vol. 6, no. 8, p. 2500083, 2025, doi: 10.1002/sstr.202500083.

[69]

P. Adams, J. Bühler, Á. Labordet Álvarez, S. D. Tilley, and M. Dimitrievska, “Raman and IR signatures of [Mo3S4]4+ and [Mo3S13]2− molybdenum sulphide molecular catalysts for solar hydrogen evolution,” J. Phys. Mater., vol. 9, no. 1, p. 015001, Nov. 2025, doi: 10.1088/2515-7639/ae199e.

[70]

K. Prech, P. P. Potts, and G. T. Landi, “Role of Quantum Coherence in Kinetic Uncertainty Relations,” Phys. Rev. Lett., vol. 134, no. 2, p. 020401, Jan. 2025, doi: 10.1103/PhysRevLett.134.020401.

[71]

J. Harrison et al., “Room Temperature Control of Axial and Basal Antiferromagnetic Anisotropies Using Strain,” ACS Nano, vol. 19, no. 50, pp. 42118–42127, Dec. 2025, doi: 10.1021/acsnano.5c12282.

[72]

Z. Li, X. Wen, S. B. Bolotova, and F. P. Seebeck, “Short-Circuiting the SAM-Cycle in Escherichia coli,” J. Am. Chem. Soc., vol. 147, no. 51, pp. 47690–47700, Dec. 2025, doi: 10.1021/jacs.5c17370.

[73]

M. Aldeghi et al., “Simulation and Measurement of Stray Fields for the Manipulation of Spin Qubits in One- and Two-Dimensional Arrays,” Nano Lett., vol. 25, no. 5, pp. 1838–1844, Feb. 2025, doi: 10.1021/acs.nanolett.4c05037.

[74]

A. Ahsan et al., “Single Sheet Metal-Organic on-Surface Networks: An Artificial 2D Material Comprising Periodically Coupled Quantum Wells for the Engineering of Localized and Delocalized Electronic States,” Meet. Abstr., vol. MA2025-01, no. 15, p. 1137, Jul. 2025, doi: 10.1149/MA2025-01151137mtgabs.

[75]

F. Baruffaldi et al., “Single-photon counting pixel detector for soft X-rays,” Commun Phys, vol. 8, no. 1, p. 321, Aug. 2025, doi: 10.1038/s42005-025-02240-9.

[76]

A. Nikoletic, E. Natsaridis, T. Flathmann, D. P. C. Quadros, N. Gogniat, and O. Tagit, “Soft Nanocarriers as Antimicrobial Co-Delivery Systems to Combat Resistant Infections,” Advanced Healthcare Materials, vol. 14, no. 21, p. 2404540, 2025, doi: 10.1002/adhm.202404540.

[77]

T. A. Butcher et al., “Soft x-ray ptychography with SOPHIE: Guide and instrumentation,” Rev. Sci. Instrum., vol. 96, no. 12, p. 123704, Dec. 2025, doi: 10.1063/5.0303529.

[78]

J.-C. Liu et al., “Spin Excitations of High Spin Iron(II) in Metal–Organic Chains on Metal and Superconductor,” Advanced Science, vol. 12, no. 7, p. 2412351, 2025, doi: 10.1002/advs.202412351.

[79]

G.-L. Schmid et al., “Squeezing light with optomechanical and spin-light quantum interfaces,” Comptes Rendus. Physique, vol. 26, no. G1, pp. 641–657, 2025, doi: 10.5802/crphys.265.

[80]

A. Nigro et al., “Strain Engineering of Ge Quantum Wells in Planar Ge/Si1 − xGex Heterostructures,” Advanced Materials Interfaces, vol. 12, no. 24, p. e00620, 2025, doi: 10.1002/admi.202500620.

[81]

L. K. Träger et al., “Structural basis for cooperative ssDNA binding by bacteriophage protein filament P12,” Nucleic Acids Res, vol. 53, no. 5, p. gkaf132, Mar. 2025, doi: 10.1093/nar/gkaf132.

[82]

A. Hinaut et al., “Superlubricity of Borophene: Tribological Properties in Comparison to hBN,” ACS Nano, vol. 19, no. 41, pp. 36536–36543, Oct. 2025, doi: 10.1021/acsnano.5c11587.

[83]

S. Jia, H. Guo, R. Y. H. Lim, and S. Tsujino, "Surface-Acoustic-Wave-Driven Acoustic Tweezing in a Silicon Microfluidic Chip," IEEE Transactions on Ultrasonics, Ferroelectrics, and Frequency Control, vol. 72, no. 8, pp. 1005–1014, Aug. 2025, doi: 10.1109/TUFFC.2025.3581642.

[84]

D. Broka et al., "Targeted apoptotic immune modulator for the treatment of metastatic EGFR-positive solid tumors," Proceedings of the National Academy of Sciences, vol. 122, no. 22, p. e2500489122, Jun. 2025, doi: 10.1073/pnas.2500489122.

[85]

E. Bertiaux et al., "The luminal ring protein C2CD3 acts as a radial in-to-out organizer of the distal centriole and appendages," PLOS Biology, vol. 23, no. 12, p. e3003519, Dec. 2025, doi: 10.1371/journal.pbio.3003519.

[86]

R. Darawish et al., "The role of precursor coverage in the synthesis and substrate transfer of graphene nanoribbons," Nanoscale Advances, vol. 7, no. 7, pp. 1962–1971, 2025, doi: 10.1039/D5NA00017C.

[87]

A. Nikoletić, M. Maleković, G. Kozalak, C. G. Palivan, and O. Tagit, "Thermoresponsive Nanocarriers Transduced by Inorganic Nanoparticles: Design Considerations and Applications in Drug Delivery," Helvetica Chimica Acta, vol. 108, no. 3, p. e202400193, 2025, doi: 10.1002/hlca.202400193.

[88]

A. S. Hegde, P. P. Potts, and G. T. Landi, "Time-Resolved Stochastic Dynamics of Quantum Thermal Machines," Phys. Rev. Lett., vol. 134, no. 15, p. 150402, Apr. 2025, doi: 10.1103/PhysRevLett.134.150402.

[89]

R. Pawlak et al., "Toward Gate-Tunable Topological Superconductivity in a Supramolecular Electron Spin Lattice," Nano Lett., vol. 25, no. 42, pp. 15206–15214, Oct. 2025, doi: 10.1021/acs.nanolett.5c03396.

[90]

A. Sileo et al., "Toward Origami-Inspired In Vitro Cardiac Tissue Models," ACS Biomater. Sci. Eng., vol. 11, no. 3, pp. 1583–1597, Mar. 2025, doi: 10.1021/acsbiomaterials.4c01594.

[91]

F. Huber, H. P. Lang, A. Marten, J. A. Bielicki, E. Meyer, and C. Gerber, "Ultra-Sensitive Biosensors for Medical Applications Based on Nanomechanics: From Detection of Synthetic Biomolecules to Analysis of Sepsis in Pediatric Patients," Biosensors (Basel), vol. 15, no. 4, p. 217, Mar. 2025, doi: 10.3390/bios15040217.

[92]

Y. Yao et al., "Unraveling the Interfacial Properties of Twisted Single-Crystal Au(111)/MoS2 Heterostructures: A Pathway to Robust Superlubricity," Advanced Science, vol. 12, no. 21, p. 2415884, 2025, doi: 10.1002/advs.202415884.

[93]

Y.-C. Shen, V. Wyss, A. Shabnam, and M. F. Delley, "Versatile Strategy for Organic Surface Modification of Cobalt Phosphide Using Iodonium Salts Enables Systematic Tuning for Hydrogenation Catalysis," J. Am. Chem. Soc., Dec. 2025, doi: 10.1021/jacs.5c18966.

[94]

D. Zenelaj, P. Samuelsson, and P. P. Potts, "Wigner-function formalism for the detection of single microwave pulses in a resonator-coupled double quantum dot," Phys. Rev. Res., vol. 7, no. 1, p. 013305, Mar. 2025, doi: 10.1103/PhysRevResearch.7.013305.

University of Basel

Annual Report 2025 Supplement
Swiss Nanoscience Institute

Cover image: Protein foam

The open-pored structure consists of natural albumin and forms a stable, biocompatible protein network. Its highly cross-linked pore structure provides an optimal microenvironment for cell adhesion and tissue integration, making it a promising scaffold for bone and cartilage regeneration.
(Image: S. Zaugg, University of Applied Sciences and Arts Northwestern Switzerland and University of Basel)

Educating
Talents
since 1460.

University of Basel
Petersplatz 1
P.O Box 2148
4001 Basel
Schwitzerland

www.unibas.ch

Swiss Nanoscience Institute
University of Basel
Klingelbergstrasse 82
4056 Basel
Switzerland

www.nanoscience.ch